

# The crystal chemistry of hibonite: an indicator for oxygen fugacity during Solar nebula condensation?

## Dissertation

Von der Graduiertenschule für Mathematik und Naturwissenschaften (BayNAT)  
der Universität Bayreuth

zur Erlangung der Würde eines  
Doktors der Naturwissenschaften

– Dr. rer. nat. –

Vorgelegt durch

**Mattia Giannini, M.Sc.- Chem.**

aus Costa di Mezzate, Italien



UNIVERSITÄT  
BAYREUTH

Bayreuth, 2014





This doctoral thesis was prepared at the Bayerisches Geoinstitut at the University of Bayreuth from 02/2010 until 07/2014 and was supervised by Prof. Dr. Falko Langenhorst and Dr. Tiziana Boffa Ballaran.

This is a full reprint of the dissertation submitted to obtain the academic degree of Doctor of Natural Sciences (– Dr. rer. nat. –) and approved by the Bayreuth Graduate School of Mathematical and Natural Sciences (BayNAT) of the University of Bayreuth.

Date of submission: 4th July 2014

Date of defence: 28th August 2014

Acting director:

Prof. Dr. Franz-Xaver Schmid

Doctoral committee:

Prof. Dr. Falko Langenhorst (1st reviewer)

Prof. Dr. Daniel Frost (2nd reviewer)

Prof. Dr. Leonid Dubrovinsky (Chairman)

Dr. Katharina Marquardt

# Table of contents

<i>Summary</i>	vii
<i>Zusammenfassung</i>	xi
<i>Acknowledgements</i>	xv
<b><i>I Introduction &amp; Methodology</i></b>	<b>1</b>
<b>1 Introduction</b>	<b>2</b>
1.1 Formation and composition of chondrites . . . . .	3
1.1.1 Carbonaceous chondrites . . . . .	7
1.1.2 Calcium-aluminium-rich inclusions . . . . .	9
1.1.2.1 Ti <sup>3+</sup> in minerals of refractory inclusions . . . . .	10
1.2 The mineral hibonite . . . . .	14
1.2.1 State of art on hibonite synthesis . . . . .	17
1.3 Aim of the thesis . . . . .	18
<b>2 Samples and experimental methods</b>	<b>20</b>
2.1 Natural samples . . . . .	20
2.2 Synthetic samples . . . . .	21
2.2.1 Starting materials . . . . .	21
2.2.1.1 Oxide precursors . . . . .	21
2.2.1.2 Sol-gel synthesis . . . . .	22
2.2.2 Piston-cylinder synthesis . . . . .	25
2.2.3 Experiments with the gas-mixing furnace . . . . .	27
2.3 Scanning electron microscope and electron probe micro analysis . . . . .	28
2.4 Powder X-ray diffraction . . . . .	29
2.5 Single crystal X-ray diffraction . . . . .	32

---

2.6	Transmission electron microscope observation . . . . .	34
2.6.1	Sample preparation . . . . .	34
2.6.1.1	Argon ion milling . . . . .	35
2.6.1.2	Focused ion beam . . . . .	36
2.6.2	Energy electron loss spectroscopy . . . . .	39
2.7	Optical absorption spectroscopy . . . . .	44
 <b>II Characterisation of synthetic samples - Results &amp; Discussion</b>		<b>48</b>
3	<b>Chemistry and structure of synthetic hibonites</b>	<b>49</b>
3.1	Microscopic observation on synthetic hibonites . . . . .	49
3.1.1	Piston-cylinder run products . . . . .	49
3.1.2	Gas-mixing furnace run products . . . . .	53
3.2	Chemical analysis of synthetic hibonites . . . . .	59
3.3	X-ray diffraction of synthetic hibonites . . . . .	63
3.3.1	Unit cell parameters variation . . . . .	65
3.3.2	Site distribution of Ti . . . . .	68
3.3.3	Structural variations due to Ti-Mg substitution . . . . .	69
4	<b>Energy electron loss spectroscopy on synthetic hibonite</b>	<b>78</b>
4.1	The energy electron loss spectrum of Ti in hibonite . . . . .	78
4.2	Measurement of Ti <sup>3+</sup> in hibonite using energy electron loss spectroscopy . . . . .	80
4.2.1	Application of a previous calibration method based on titanium oxides . . . . .	80
4.2.2	Ti <sup>3+</sup> in hibonite: a new calibration for energy electron loss spectroscopy . . . . .	87
5	<b>Optical absorption spectroscopy on hibonite</b>	<b>102</b>
5.1	The UV/Vis spectrum of Ti in hibonite . . . . .	102
5.2	Quantitative analysis of the absorbance peaks in the UV/Vis spectra of hibonite . . . . .	107
5.3	Assignment of the absorption bands in the UV/Vis spectra of hibonite . . . . .	111
 <b>III Characterisation of natural samples &amp; Conclusions</b>		<b>113</b>
6	<b>Characterisation of natural hibonites</b>	<b>114</b>
6.1	Electron microscope observation on natural hibonites . . . . .	114
6.2	Quantification of Ti <sup>3+</sup> in natural hibonites . . . . .	121

<b>7</b>	<b><i>Concluding remarks</i></b>	<b>126</b>
7.1	Site distribution and valence state of Ti in hibonite . . . . .	126
7.2	The crystal chemistry of hibonite . . . . .	128
7.3	The oxygen fugacity in the Solar Nebula . . . . .	130
	 <i>References</i>	 132
	 <i>Erklärung</i>	 141

## *Summary*

Meteorites represent the main source of materials which can give information on the early history of our Solar System. In particular, Calcium-Aluminium-rich inclusions (CAIs), which are usually found in carbonaceous chondrites, yielded the oldest measured ages of our Solar System. CAIs can contain records of the conditions and the events that characterised their formation, therefore they can provide essential information on the early Solar Nebula, which is believed to have been an environment so reducing to allow the occurrence of  $\text{Ti}^{3+}$ . For these reasons, the oxidation state of titanium in different minerals present in CAIs has attracted considerable attention over the years as it could be used to constrain the oxygen fugacity,  $f\text{O}_2$ , at the time of Solar Nebula condensation. CAIs contain minerals which appear earlier in the condensation sequence of a hot gas having Solar composition. Among these minerals, Ti-rich clinopyroxenes,  $\text{Ca}(\text{Mg},\text{Al},\text{Ti})(\text{Si},\text{Al})_2\text{O}_6$ , and hibonite,  $\text{Ca}(\text{Al},\text{Mg},\text{Ti})_{12}\text{O}_{19}$ , have been used to estimate the  $f\text{O}_2$  during the Solar Nebula condensation, producing contradictory results, with pyroxenes suggesting reducing and hibonite oxidising conditions.

The particular interest on hibonite is due to the fact that it is, together with corundum, the very first mineral to condensate in the Solar Nebula. Therefore, as compared to clinopyroxenes, which have formed subsequently, hibonite potentially carries information on the earliest stages of the Solar System formation. However, little is known on the crystal chemistry of hibonite, on the influence on hibonite structure of the  $\text{Ti}^{3+}$ - $\text{Ti}^{4+}$  incorporation, and on the possible interactions of Ti with other cations substituting for Al such as, for example, Mg. The aim of this thesis is, therefore, to correctly determine the cation distribution of Ti in synthetic and meteoritic samples and to quantify their  $\text{Ti}^{3+}/\text{Ti}^{\text{tot}}$  ratios from spectroscopic data. Correlating the information on the crystal chemistry and the  $\text{Ti}^{3+}/\text{Ti}^{\text{tot}}$  ratios with the  $f\text{O}_2$  at which the hibonite samples formed would then allow testing whether hibonite is a sensible oxybarometer and possibly explaining the large difference in nebular oxygen fugacities obtained using different minerals.

To this end, hibonites with different Ti and Mg contents have been synthesised at different oxygen fugacities and temperatures adopting two different approaches. In the first case polycrystalline hibonite was synthesised in air at 1600 °C from a mixture of oxides and then used as starting material for piston-cylinder experiments performed at 15 kbar and at temperatures ranging from 1450 to 2000 °C. In the second case a citrate-based sol-gel procedure aimed at the synthesis of end-member hibonite has been modified in order to obtain Ti-Mg-bearing sol-gel precursors. These materials were subsequently fired at different temperatures and at variable oxygen fugacities in a gas mixing furnace in order to obtain hibonite samples. Whereas all but one of the piston-cylinder runs resulted in polycrystalline samples containing small sized crystals, most of the sol-gel starting materials produced large single crystals of hibonite.

Chemical analyses performed on synthetic hibonites by means of microprobe (EPMA) indicate that most of the samples have a  $\text{Ti}^{\text{tot}}/\text{Mg}$  ratio close to 1, suggesting that the coupled substitution mechanism  $2\text{Al}^{3+}=\text{Ti}^{4+} + \text{Mg}^{2+}$  is the major incorporation mechanism for Ti and Mg in hibonite, independently of oxygen fugacity. Only for samples synthesised at very reducing conditions the substitution of  $\text{Ti}^{3+}$  takes place according to the substitution  $\text{Al}^{3+}=\text{Ti}^{3+}$ .

X-ray diffraction (XRD) investigations on both polycrystalline and single crystals hibonites indicate that the unit cell volume increases linearly with Ti and Mg content, according to the empirical relationship:  $V = 8.2(2) \cdot (\text{Ti}^{\text{tot}} + \text{Mg}^{2+})_{a.p.f.u.} + 586.1(2)$ . Fourier analysis of single crystal XRD intensity datasets revealed that the Ti atoms occupy exclusively two sites in the structure of hibonite, a trigonally distorted octahedral site occurring as face-sharing pairs, *M4*, and a trigonal bipyramid site, *M2*. The refined occupancy factor on these two sites clearly indicates that Ti partitions preferentially at the *M4* site where Ti is four times more abundant than at the *M2* site. Analysis of bond distances and thermal displacement parameters also suggests that both  $\text{Ti}^{4+}$  and  $\text{Ti}^{3+}$  are present at both *M4* and *M2* sites. It also has been confirmed that divalent species such as  $\text{Mg}^{2+}$  occupy the tetrahedral *M3* site.

Energy electron loss spectroscopy (EELS) in a transmission electron microscope (TEM) has been used to measure the  $\text{Ti}^{3+}/\text{Ti}^{\text{tot}}$  ratios on synthetic hibonite. Due to the low concentration of Ti in hibonite, which does not allow to determine with sufficient accuracy the absolute energy of the EELS peaks, it was not possible to use the EELS calibration already available in the literature which have been derived from EELS of titanium oxides. Therefore, a hibonite-specific calibration for quantifying  $\text{Ti}^{3+}$  in hibonite has been developed, taking into account the

information obtained from XRD. In fact, the knowledge of the exact site distribution of Ti in hibonite allowed to better understand the fine structure of the EEL spectra. Broadening of the four peaks constituting the titanium  $L_{2,3}$  edge of hibonite has been correlated with the presence of  $Ti^{3+}$  via (dynamic) Jahn-Teller effect. The peak broadening has been quantified using the autocorrelation method as well as introducing a new quantity defined as the *net peak height*, which links the relative intensity of the different peaks to their width. The EELS calibration method has been based on the values of net peak height of two reference synthetic hibonites assumed to contain either only  $Ti^{4+}$  or only  $Ti^{3+}$ . The measured  $Ti^{3+}$  contents in different synthetic samples confirmed that the  $Ti^{tot}/Mg$  ratio play a fundamental role in determining the amount of  $Ti^{3+}$  present in hibonite, whereas oxygen fugacity becomes a determining factor only at very reducing conditions or for those samples for which Mg is absent.

UV/Vis optical spectroscopy measurements have been performed on oriented single crystals of synthetic hibonite. The spectra of hibonites are characterized by the presence of a prominent absorption peak centred around 715 nm, except in the case of sample synthesised in air for which the absence of absorption of light confirms that they exclusively contain  $Ti^{4+}$ . The intensity of this absorption band at 715 nm has been found to linearly correlate with the product of the concentrations of  $Ti^{3+}$  and  $Ti^{4+}$  determined from the EELS measurements. This indicates that this absorption band originates from a  $Ti^{3+}$ - $Ti^{4+}$  intervalence charge transfer (IVCT) transition. Such transition requires that the involved atoms occupy edge or face-sharing coordination polyhedra. This is indeed the case for Ti in hibonite which has been found, based on the structural refinements, to occupy preferentially the M4 site (*i.e.* a pair of face-sharing octahedra). The linear correlation observed between the absorbance and the concentrations of  $Ti^{3+}$ - $Ti^{4+}$  pairs taken from EELS validates the newly developed EELS calibration and the assumptions on which it is based.

The values of  $Ti^{3+}$  obtained from EELS were used to construct  $Ti^{3+}$ - $fO_2$  relationships for different  $Ti^{tot}/Mg$  ratios which were then used to interpret the EELS measurements performed on natural specimens. Previous to EELS analysis, the chemical compositions of the natural hibonite grains were measured with EPMA and subsequently the crystals were prepared for TEM analysis using the focused ion beam (FIB) technique. The  $Ti^{3+}$  contents in natural hibonites indicate that these samples have been likely exposed during their formation and accretion in the Solar Nebula to oxygen fugacities several orders of magnitude more oxidising than expected from thermodynamic calculations. These results can be interpreted in the frame

of a recently published model which proposes the occurrence of transient oxidising conditions accompanying thermal processing of nebular precursors. According to this model, at the very high temperatures at which hibonite condensed, the  $fO_2$  conditions might have been temporarily oxidising thus favouring the presence of  $Ti^{4+}$ . Once hibonite formed, its crystal chemistry might have played a major role in stabilising the  $Ti^{4+}$  even after more reducing conditions were re-established. The present results explain the discrepancy between  $fO_2$  estimations based on clinopyroxenes and hibonites, since clinopyroxenes, which condense at lower temperature, were not exposed to transient high temperature events and therefore are more likely to have recorded the reducing conditions predicted by thermodynamic calculations.

# Zusammenfassung

Meteoriten stellen die Hauptquelle des Materials dar, das uns Informationen über die Frühgeschichte unseres Sonnensystems liefert. Insbesondere Kalzium-Aluminium-reiche Einschlüsse (sog. CAIs), die sich normalerweise in kohligen Chondriten finden, ergaben die ältesten gemessenen Alter in unserem Sonnensystem. CAIs können Nachweise für die Bedingungen und die Ereignisse während ihrer Bildung enthalten und daher wichtige Informationen über den solaren Nebel liefern, der vermutlich so reduzierende Bedingungen aufwies, dass Titan in seiner dreiwertigen Oxidationsstufe ( $\text{Ti}^{3+}$ ) vorlag. Aus diesen Gründen hat der Oxidationszustand von Titan in unterschiedlichen Mineralen der CAIs im Laufe der Zeit grosse Aufmerksamkeit erfahren, da er möglicherweise dazu benutzt werden kann, die Sauerstoff fugazität,  $f\text{O}_2$ , zu Zeit der Kondensation des solaren Nebels zu bestimmen. CAIs enthalten Minerale, die sehr früh in der Kondensationsabfolge eines heissen Gases mit solarer Zusammensetzung auftreten. Unter diesen Mineralen wurden Ti-reiche Klinopyroxene,  $\text{Ca}(\text{Mg},\text{Al},\text{Ti})(\text{Si},\text{Al})_2\text{O}_6$ , und Hibonite,  $\text{Ca}(\text{Al},\text{Mg},\text{Ti})_{12}\text{O}_{19}$ , mit widersprüchlichen Resultaten zur Abschätzung des  $f\text{O}_2$  während der Kondensation des solaren Nebels benutzt, da die Pyroxene reduzierende und die Hibonite oxidierende Bedingungen ergaben.

Das besondere Interesse an Hibonit resultiert daraus, dass er zusammen mit Korund das erste Mineral ist, das aus dem solaren Gasnebel kondensiert. Daher enthält der Hibonit im Gegensatz zum später kondensierenden Klinopyroxen Informationen über die frühesten Stadien der Bildung des Sonnensystems. Allerdings ist sehr wenig über die Kristallchemie von Hibonit bekannt, z.B. über den Einfluss der Kristallstruktur von Hibonit auf den Einbau von  $\text{Ti}^{3+}/\text{Ti}^{4+}$  sowie über mögliche Wechselwirkungen von Ti mit anderen Kationen, die Al in der Hibonitstruktur ersetzen können, wie z.B. Mg. Das Ziel der vorliegenden Arbeit war es daher, die Kationenverteilung von Ti in synthetischen und meteoritischen Hiboniten korrekt zu bestimmen und ihre  $\text{Ti}^{3+}/\text{Ti}^{\text{tot}}$  Verhältnisse mithilfe von spektroskopischen Messungen zu quantifizieren. Die Korrelierung der Kristallchemie und den  $\text{Ti}^{3+}/\text{Ti}^{\text{tot}}$  Verhältnissen mit

dem  $f_{\text{O}_2}$  der Hibonitsynthese erlaubt dann zu bestimmen, ob Hibonit ein funktionierendes oxybarometer darstellt und würde möglicherweise die grossen Unterschiede in den bisherigen Bestimmungen der Sauerstoffugazität im solaren Gasnebel erklären, die mit unterschiedlichen Mineralen gewonnen wurden.

In dieser Arbeit wurden Hibonite mit variablen Ti- und Mg-Gehalten bei verschiedenen Sauerstoffugazitäten und Temperaturen mit zwei unterschiedlichen Ansätzen synthetisiert. Im ersten Fall wurde polykristalliner Hibonit in Luft bei 1600 °C aus einer Mischung von Oxiden hergestellt und dann als Ausgangsmaterial für Experimente mit der Stempel-Zylinderpresse bei 15 kbar und 1450-2000 °C verwendet. Im zweiten Ansatz wurde ein Citrat-basiertes Sol-Gel-Verfahren zur Herstellung von reinem Endglied-Hibonit modifiziert, um Ti-Mg-haltige Sol-Gel-Vorläufer zu erhalten. Diese wurden dann bei unterschiedlichen Temperaturen und Sauerstoffugazitäten in einem Gasmischofen gefeuert, um die Hibonitproben zu erhalten. Während mit Ausnahme von einer alle Proben der Stempelzylinderexperimente feinkörnig polykristallin waren, ergaben die Proben aus dem Sol-Gel-Verfahren grosse Einkristalle von Hibonit.

Chemische Analysen der synthetischen Hibonite mithilfe der Elektronenmikrosonde (EP-MA) ergaben, dass die meisten Proben ein  $\text{Ti}^{\text{tot}}/\text{Mg}$  Verhältnis nahe 1 haben, was darauf hindeutet, dass die gekoppelte Substitution  $2\text{Al}^{3+} = \text{Ti}^{4+} + \text{Mg}^{2+}$  unabhängig von der Sauerstoffugazität der Hauptmechanismus für den Einbau von Ti und Mg in Hibonit ist. Einzig Proben, die unter stark reduzierenden Bedingungen synthetisiert wurden, zeigen einen Einbau von  $\text{Ti}^{3+}$  durch die Substitution  $\text{Al}^{3+} = \text{Ti}^{3+}$ .

Röntgenbeugungsexperimente (XRD) an polykristallinen Proben als auch an Einkristallen von Hibonit zeigen, dass das Volumen der Einheitszelle linear mit dem Ti- und Mg-Gehalt ansteigt mit der empirisch bestimmten Beziehung:  $V = 8.2(2) \cdot (\text{Ti}^{\text{tot}} + \text{Mg}^{2+})_{a.p.f.u.} + 586.1(2)$ . Die Fourieranalyse der Intensitäten der Einkristall-Röntgenreflexe ergab, dass die Ti Atome exklusiv zwei Gitterpositionen in der Hibonitstruktur besetzen: einen trigonal verzerrten Oktaederplatz, der in Oktaederpaaren mit einer gemeinsamen Fläche auftritt,  $M4$ , und einen trigonalen Bipyramidenplatz,  $M2$ . Die verfeinerten Besetzungsfaktoren für diese beiden Plätze zeigen deutlich, dass Ti bevorzugt den  $M4$  einnimmt, wo es viermal häufiger auftritt als auf dem  $M2$  Platz. Die Analyse der Bindungsdistanzen and thermischen Faktoren deutet auch darauf hin, dass sowohl  $\text{Ti}^{4+}$  als auch  $\text{Ti}^{3+}$  auf beiden Gitterplätzen  $M4$  und  $M2$  auftreten. Ausserdem wurde bestätigt, dass Mg den Tetraederplatz  $M3$  besetzt.

Elektronenenergieverlust-Spektroskopie (EELS) im Transmissionselektronenmikroskop (TEM) wurde eingesetzt, um das  $\text{Ti}^{3+}/\text{Ti}^{\text{tot}}$  Verhältnis in synthetischem Hibonit zu messen. Aufgrund der niedrigen Konzentration von Ti in Hibonit, die es nicht erlaubt, die absolute Energie der EELS Peaks mit ausreichender Genauigkeit zu bestimmen, war es nicht möglich, die schon in der Literatur vorhandene EELS Kalibrierung zu nutzen, da diese an Titanoxiden erstellt wurde. Daher wurde eine Hibonit-spezifische Kalibrierung zur Quantifizierung von  $\text{Ti}^{3+}$  in Hibonit unter Berücksichtigung der XRD Resultate entwickelt. Tatsächlich half das Wissen über die exakte Gitterplatzverteilung von Ti in Hibonit, die Feinstruktur der EELS Spektren besser zu verstehen. Die Verbreiterung der vier Maxima, die die Titan  $L_{2,3}$  Kante des Hibonits bilden, wurde mit dem Vorhandensein von  $\text{Ti}^{3+}$  über den (dynamischen) Jahn-Teller Effekt korreliert. Die Peakverbreiterung wurde sowohl mit der Autokorrelationsmethode quantifiziert als auch mit der Einführung einer neuen Quantität, definiert als abzugslose (netto) Peakhöhe, die die relative Intensität der verschiedenen Peaks mit ihrer Breite verknüpft. Die EELS Kalibrierungsmethode stützt sich auf die Werte der abzugslosen Peakhöhe für zwei synthetische Referenz-Hibonite, für die angenommen wird, dass sie jeweils nur  $\text{Ti}^{4+}$  bzw.  $\text{Ti}^{3+}$  enthalten. Die gemessenen  $\text{Ti}^{3+}$  Gehalte in verschiedenen synthetischen Proben bestätigen, dass das  $\text{Ti}^{\text{tot}}/\text{Mg}$ -Verhältnis eine fundamentale Rolle für die Konzentration von  $\text{Ti}^{3+}$  in Hibonit spielt, während die Sauerstoffugazität nur bei sehr reduzierenden Bedingungen oder bei Mg-freien Proben ein bestimmender Faktor ist.

UV/Vis-optische Spektroskopiemessungen wurden an orientierten Einkristallen von synthetischem Hibonit durchgeführt. Die Spektren der Hibonite sind durch ein prominentes Absorptionsband bei 715 nm charakterisiert, mit der Ausnahme von in Luft synthetisierten Proben, für die die Abwesenheit von Absorptionsbändern bestätigt, dass sie exklusiv  $\text{Ti}^{4+}$  enthalten. Die Intensität des Absorptionsbandes bei 715 nm korreliert linear mit dem Produkt der Konzentrationen von  $\text{Ti}^{3+}$  und  $\text{Ti}^{4+}$ , bestimmt durch EELS Messungen. Das deutet darauf hin, dass dieses Band durch einen  $\text{Ti}^{3+}$ - $\text{Ti}^{4+}$  Intervallenz-Ladungsübergang (IVCT) verursacht wird. Solch ein Übergang erfordert, dass die beteiligten Atome benachbarte Koordinationspolyeder besetzen, die gemeinsame Kanten oder Flächen haben. Dies ist tatsächlich der Fall für Ti in Hibonit, für den mithilfe der Röntgenstrukturverfeinerungen gefunden wurde, dass er bevorzugt den  $M4$  Gitterplatz besetzt (d.h. in einem Paar Oktaeder mit einer gemeinsamen Fläche). Die beobachtete lineare Korrelation zwischen der Absorption und den Konzentrationen der  $\text{Ti}^{3+}$ - $\text{Ti}^{4+}$  Paare aus den EELS-Messungen validiert die neu entwickelte EELS Kalibrierung und die damit verbundenen Annahmen.

Die aus der EELS-Analyse erhaltenen Werte von  $Ti^{3+}$  wurden dazu benutzt,  $Ti^{3+}$ - $fO_2$  Beziehungen für verschiedene  $Ti^{tot}/Mg$  Verhältnisse zu konstruieren, und wurden dann verwendet, um die EELS Messungen an natürlichen Proben zu interpretieren. Der Chemismus der natürlichen Proben wurde mit EPMA gemessen, anschließend wurde von jeweils einer Messstelle eine Orts-spezifische TEM Probe mittels der fokussierten Ionenstrahl (FIB) Methode für die EELS Analysen präpariert. Die  $Ti^{3+}$  Gehalte in natürlichen Hiboniten deuten darauf hin, dass diese Proben während ihrer Bildung und Akkretion im Solarnebel wahrscheinlich Sauerstoffugazitäten ausgesetzt waren, die mehrere Grössenordnungen oxidierender waren als man von thermodynamischen Berechnungen her erwarten würde. Diese Ergebnisse können im Rahmen eines kürzlich veröffentlichten Modells interpretiert werden, dass das Auftreten vorübergehender oxidierender Bedingungen vorhersagt, die eine thermische Aufarbeitung von nebulären Vorläufern begleiten. Nach diesem Modell waren die  $fO_2$  Bedingungen bei den hohen Temperaturen, bei denen Hibonit kondensierte, vorübergehend deutlich stärker oxidierend, so dass das Vorhandensein von  $Ti^{4+}$  favorisiert war. Nach der Bildung von Hibonit könnte seine Kristallchemie eine wichtige Rolle bei der Stabilisierung von  $Ti^{4+}$  gespielt haben, selbst als wieder deutlich reduzierendere Bedingungen vorherrschten. Die vorgestellten Resultate erklären die Diskrepanz zwischen  $fO_2$  Abschätzungen, die auf den verschiedenen Mineralen Klinopyroxen und Hibonit basieren, da Klinopyroxene, die bei tieferen Temperaturen kondensieren, nicht den vorübergehenden Hochtemperaturereignissen ausgesetzt waren und daher wahrscheinlich die reduzierenden Bedingungen aufgezeichnet haben, die von den thermodynamischen Berechnungen vorhergesagt werden.

## *Acknowledgements*

I am extremely grateful to Prof. Dr. Falko Langenhorst and Dr. Tiziana Boffa Ballaran for providing me the opportunity to work on this challenging project. This thesis would have not been possible without their valuable supervision, great patience and friendly encouragement. Acknowledgements are due to the Deutsche Forschungsgemeinschaft for supporting this work through the Schwerpunktprogramme 1385 and the Leibniz program under the grants BO2550 4-1, BO2550 4-2, LA830-14 and LA830-15. I also thank the Elitenetzwerk Bayern for providing travel funding and Prof. Dr. Addi Bischoff (University of Münster) for loaning the natural samples analysed in this study.

Working at the BGI has been a truly rewarding experience thanks to the professional and kind help that I have received from all colleagues. My gratitude goes in particular to Dr. Nobuyoshi Miyajima for introducing me to TEM, Prof. Dr. Hans Keppler for helping me with UV/Vis spectroscopy, Dr. Dennis Harries for assisting me with FIB sample preparation, and Dr. Florian Heidelberg for translating to German the abstract of this thesis and for assisting me with EBSD measurements. I also thank Dr. Catherine McCammon for fruitful discussions, Dr. Matteo Masotta, Dr. Katharina Marquardt and Dr. Bob Myhill for their help for during final polishing of the thesis. I appreciate BGI's staff invaluable support for skilful and prompt sample preparation, Hubert Schulze and Raphael Njul, for microprobe calibration, Detlef Krauß, and for administrative and general help, Stefan Keyssner, Petra Buchert, Lydia Kison-Herzing and Gerti Golner. I am also grateful to Drs. Michele Zema and Serena Tarantino who pointed me towards Bayreuth in the first place.

In the course of the years spent in Bayreuth, I met many Ph.D. students and Postdocs, their friendship and the time spent together during barbecues, parties and sport activities have made my stay very enjoyable, thank you all! I also thank my friends in Italy and across Europe for the nice time spent together during short visits.

Last but not least, a heartfelt thank you goes to my family.

*Ultimo ma non meno importante, un grazie di cuore va alla mia famiglia per aver sostenuto le mie scelte ed avermi aiutato in questi anni nonostante le difficoltà legate alla distanza.*

*The story so far:  
In the beginning the Universe was created.  
This has made a lot of people very angry  
and been widely regarded as a bad move.*

– Douglas Adams, 1980 –

*Part I*

*Introduction*

*&*

*Methodology*

# 1 Introduction

The observation of stars and planets has always fascinated humanity, in fact, planetary astronomy is likely to be one of the oldest natural sciences. This field of science, from its beginning in ancient times, has progressed enormously through the centuries, leading to a better understanding of the structure of our Solar System and its location in the wider frame of the Milky Way and the Universe. In recent times, the ground-based astronomical observations have been combined with space exploration missions like, for example, the Hubble space telescope (Chaisson and Villard, 1990) aiming at unveiling great details of the Universe. Significant effort has been spent in studying other star systems which can host Earth-like planets. To date the discovery of more than 1400 exoplanets has been confirmed (Wright et al., 2011) and an even greater number of planets is expected to be found with upcoming missions, for example with the CoRoT satellite (Moutou et al., 2013). Together with fully formed extra solar systems, these observations also allow capturing images and spectra of birthplaces for new planets, *i.e.* protoplanetary disks orbiting around young stars (Bally et al., 1996). These exciting discoveries have further stimulated the scientific community to investigate the processes involved in planetary formation and evolution in order to better understand the early history of our Solar System. Despite the fact that the current structure of the Solar System has been well characterised, the present understanding of the physical and chemical conditions at the beginning of its history is still relatively limited. Some of the most important questions regarding the first few million years of our Solar System that are still open can be identified as follows.

How did the first solids form? Where and when did those processes occur?

What were the chemical and physical conditions during formation of these solids?

How did the first solids accreted together to start the formation of larger bodies?

What was the timescale for planetesimal formation and differentiation?

Analysis of the extraterrestrial materials that were produced in the early stages of the Solar System may help to find an answer to these questions. The main sources of these materials are meteorites (from asteroids, the Moon and Mars), micrometeorites (from asteroids and comets)

as well as samples returned by space missions such as those from the historical Apollo and Luna missions together with more recent ones like STARDUST (Anderson et al., 2003). The new frontiers in the study of asteroids and comets also involve on-site analyses of parent bodies carried out by spacecraft, examples of which are DAWN (Rayman et al., 2006) and ROSETTA (Hechler, 1997) missions.

The study of meteorites, in particular, relies on the great amount of extraterrestrial material that falls daily on Earth. Some meteorites are observed as they enter Earth's atmosphere and are collected shortly after their impact with the ground, these are classified as *falls*; all other meteorites are indicated as *finds* and are recovered from cold and hot deserts, where it is easier to spot them. In both cases these meteorites are catalogued and made available for scientists to study; to date the Meteoritical Society database counts more than 48000 valid meteorite names (Garvie, 2012), including meteorites never studied so far, unique and very primitive ones. Mineralogical, chemical, isotopic and spectroscopic measurements performed on primitive meteorites and their components may allow revealing fundamental details on their formation and evolution scenarios in the early Solar System. However, without accurate constrains on the structure-property relationship of the minerals forming meteorites, these data are very difficult to interpret.

### 1.1 *Formation and composition of chondrites*

Generally, meteorites are named after the locality where they are found and are classified both on the basis of mineralogical and petrographic observations and on whole-rock chemical and oxygen isotopic analyses. According to the most recent classification proposed by Weisberg et al. (2006), meteorites are divided into chondrites, achondrites and primitive achondrites. Chondrites are stony meteorites that are characterised by the presence of chondrules, which are mm- to cm-sized spherical droplets that were partially or completely molten in the Solar Nebula, *i.e.* the ensemble of dust and gases rotating around the young Sun, and crystallised within hours prior to accretion in the parent body. They are a well characterised type of meteorites which are further divided into three classes containing fifteen groups (Fig. 1.1). Achondrites are the result of high-degree melting of chondrites, while the relationship between primitive achondrites and chondritic meteorites remains unclear.

Each chondrite group corresponds to a different parent body from which the meteorites were ejected. Chondrites that cannot be assigned to any existing group may represent the first members of new groups. Some chondrite groups are chemically and mineralogically

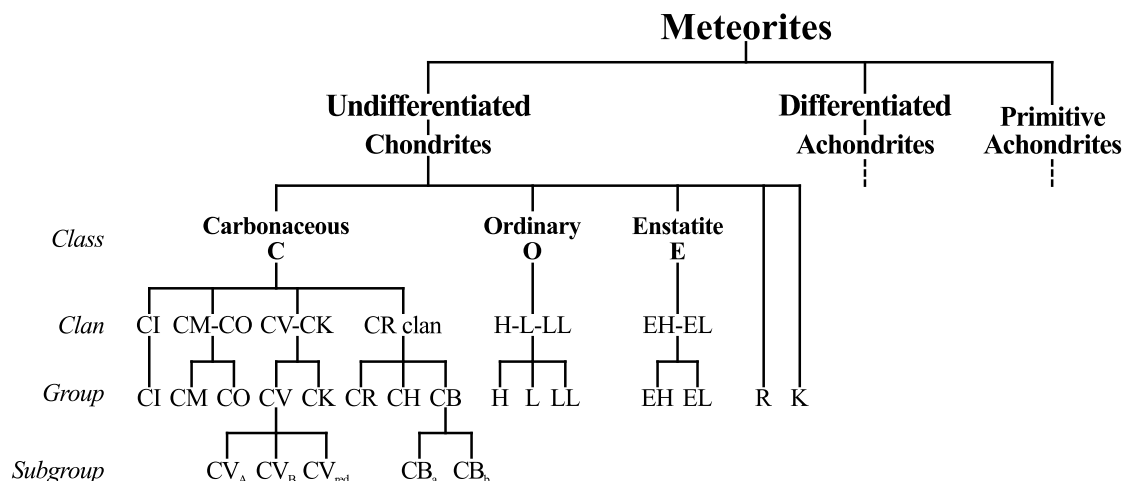


Figure 1.1: Systematics of meteorite classifications showing the different classes, clans and groups of chondrites (modified after Weisberg et al., 2006).

related so they have been grouped into clans, however, the reason for these similarities remains poorly understood. Furthermore, some groups are split into subgroups, which are thought to originate from processes taking place in different asteroids originating from a single parent body (Weisberg et al., 2006).

Chondrites originate from asteroids that did not undergo melting, thus they contain materials that are mainly unaltered and represent the most pristine matter of the Solar System. These materials are chondrules, fine-grained matrix and refractory inclusions; Fe-Ni alloys and sulfides are also present as minor components (Table 1.1). The different components of chondrites formed at different times, places and conditions in the Solar Nebula and accreted together to form the asteroidal parent bodies.

Chondrules are mainly composed by olivine,  $(\text{Mg}_x\text{Fe}_{1-x})_2\text{SiO}_4$ , and low-Ca pyroxene,  $\text{Mg}_x\text{Fe}_{1-x}\text{SiO}_3$ , with  $x$  being the  $\text{Mg}/(\text{Mg}+\text{Fe})$  ratio (Scott and Krot, 2005b). The origin and formation scenarios of chondrules have been debated in the scientific community for decades. Initially, chondrules were thought to be direct condensation products of the Solar Nebula (Wood, 1963; Grossman and Larimer, 1974). However, experimental investigations highlighted that complex mineralogies, isotopic anomalies and inhomogeneities observed in chondrules were not compatible with such hypothesis, and suggested that chondrules have experienced a complex thermal history (Wood, 1988). Further experimental investigations seem to indicate that chondrules originated from multiple flash heating events which involved rapid melting, quenching, evaporation and recondensation of fine-grained dust aggregates as well as accretion of melted, partly melted or solid objects (Wasson et al., 1995; Rubin, 2000; Scott and Krot, 2005b). Despite some controversies (Kerr, 2001), this idea is still generally accepted in the

Table 1.1: Proportions of the different components present in chondrites, modified after Scott and Krot (2003) and sources therein.

Group	Type	Refract. incl. (% <sub>vol</sub> )	Chondr. (% <sub>vol</sub> )	Chondr. diam. (mm)	Fe-Ni metal (% <sub>vol</sub> )	Matrix (% <sub>vol</sub> )	Fall <sup>‡</sup> (%)	Examples
<i>Carbonaceous</i>								
CI	1	<0.01	<5	-	<0.01	95	0.5	Orgueil
CM	1-2	5	20	0.3	0.1	70	1.6	Murchison
CO	3	13	40	0.15	1-5	30	0.5	Ornans
CV	2-3	10	45	1.0	0-5	40	0.6	Vigarano Allende
CK	3-6	4	15	0.8	<0.01	75	0.2	Karoonda
CR	1-2	0.5	50-60	0.7	5-8	30-50	0.3	Renazzo
CH	3	0.1	70	0.05	20	5	0	ALH 85085
CBa	3	<0.1	40	5	60	<5	0	Bencubbin
CBb	3	<0.1	30	0.5	70	<5	0	QUE 94411
<i>Ordinary</i>								
H	3-6	0.01-0.2	60-80	0.3	8	10-15	34.4	Dhajala
L	3-6	<0.1	60-80	0.5	3	10-15	38.1	Khohar
LL	3-6	<0.1	60-80	0.6	1.5	10-15	7.8	Semarkona
<i>Enstatite</i>								
EH	3-6	<0.1	60-80	0.2	8	<0.1-10	0.9	Qingzhen
EL	3-6	<0.1	60-80	0.6	15	<0.1-10	0.8	Hvittis
<i>Other</i>								
R	3-6	<0.1	>40	0.4	<0.1	35	0.1	Rumuruti
K	3	<0.1	20-30	0.6	6-9	70	0.1	Kakangari

<sup>‡</sup>observed falls frequencies based on 918 falls of classified chondrites and achondrites.

scientific community.

The fine-grained matrix mostly consists of olivine, low-Ca-pyroxenes and amorphous silicates with typical grain sizes in the range from 10 nm to  $\sim 5 \mu\text{m}$ . These highly heterogeneous materials coat the chondrules and fills the space between the different components present in chondrites. The matrix and the chondrules are chemically complementary with respect to the Mg/Si ratio, furthermore, there are evidences supporting the hypothesis that they were exposed to the same thermal processing in the nebula, suggesting a common origin for these two components (Huss et al., 2005; Hezel and Palme, 2010).

Refractory components found in chondrites are Calcium-Aluminium-rich inclusions (CAIs) and amoeboid olivine aggregates (AOAs). CAIs are the subject of study in this dissertation and are described in detail in Section 1.1.2. AOAs are fine-grained, irregularly shaped objects mostly composed by forsterite ( $\text{Mg}_2\text{SiO}_4$ ), Fe-Ni metal, and refractory components such as aluminium-diopside ( $\text{Ca}[\text{Mg},\text{Al}][\text{Si},\text{Al}]_2\text{O}_6$ ), spinel ( $\text{MgAl}_2\text{O}_4$ ) and anorthite ( $\text{CaAl}_2\text{Si}_2\text{O}_8$ ) (Scott and Krot, 2003).

The relationship between the different components found in chondrites can be effectively visualised by considering a diagram of mineral stability as a function of temperature in a cooling gas of solar composition at a total pressure of  $10^{-3}$  bar (Fig. 1.2). The relative stabilities for the different minerals were calculated using thermodynamic models, which consider that the initial conditions are hot enough to have vaporised components and assume equilibrium between coexisting solids and vapours, effectively defining a condensation sequence as a function of temperature (Grossman, 1972). The Solar Nebula was a dynamic and energetic environment in which the local dust/gas ratio and the temperatures were perpetually changing (Wood, 1988). These fluctuations have an influence on the order in which minerals condense; however, at total pressures ranging from  $10^{-3}$  to  $10^{-6}$  bar, these effects are minor (Grossman and Larimer, 1974; Yoneda and Grossman, 1995). The results of these studies show that the minerals present in refractory inclusions (CAIs and AOAs) are stable at temperatures above  $\sim 1400$  K while those found in chondrules and matrix are stable below this temperature (Fig. 1.2).

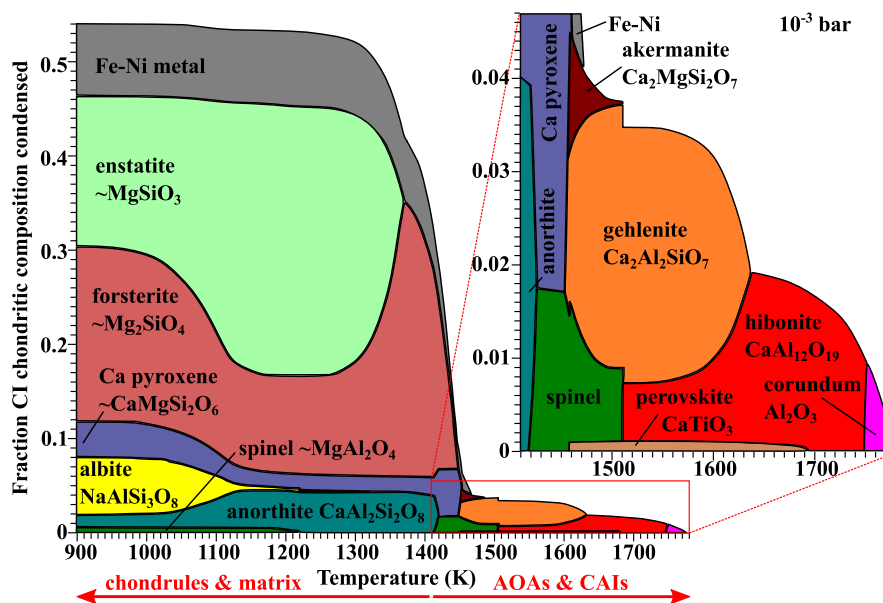


Figure 1.2: Equilibrium diagram for the Solar Nebula at  $10^{-3}$  bar showing the minerals stable above 900 K, modified after Davis and Richter (2003). The minerals found in chondrules and matrix are stable below  $\sim 1400$  K while the minerals of AOAs and CAIs are stable above this temperature.

The condensation processes took place during multiple transient heating events occurred in the Solar Nebula, as proposed in *shock-wave* models, according to which the amorphous interstellar dust was transformed at high temperatures into the chondrite-forming materials (Scott and Krot, 2005a; Desch et al., 2005; Scott and Krot, 2005b). Different hypotheses have

been formulated to explain the origin of the shock waves, and, in spite of the uncertainties, these models are widely accepted as they give plausible explanations for different chemical and mineralogical features observed in chondrules, CAIs and matrices of chondrites (Krot et al., 2009, and references therein). A schematic representation of the Solar Nebula as it would appear in the frame of the shock wave model is shown in Fig. 1.3. Observations on short- and long-lived isotopes indicate that the refractory inclusions were the first solids to form in the Solar Nebula. Their condensation happened either in the hot region in the very proximity of the proto-Sun (<0.1 AU) or throughout the inner protoplanetary disk (<4 AU) due to shock waves (Simon et al., 2005; Kita et al., 2005). Chondrules and fine-grained matrices formed and accreted up to 4 Myr after CAIs in the region between 1 and 4 AU while CAIs were present as free-floating objects. For a long time it has been believed that there has been a time gap of about 1 Myr between CAIs and chondrule formation, however, a recent study by Connelly et al. (2012) showed that these processes may have started simultaneously.

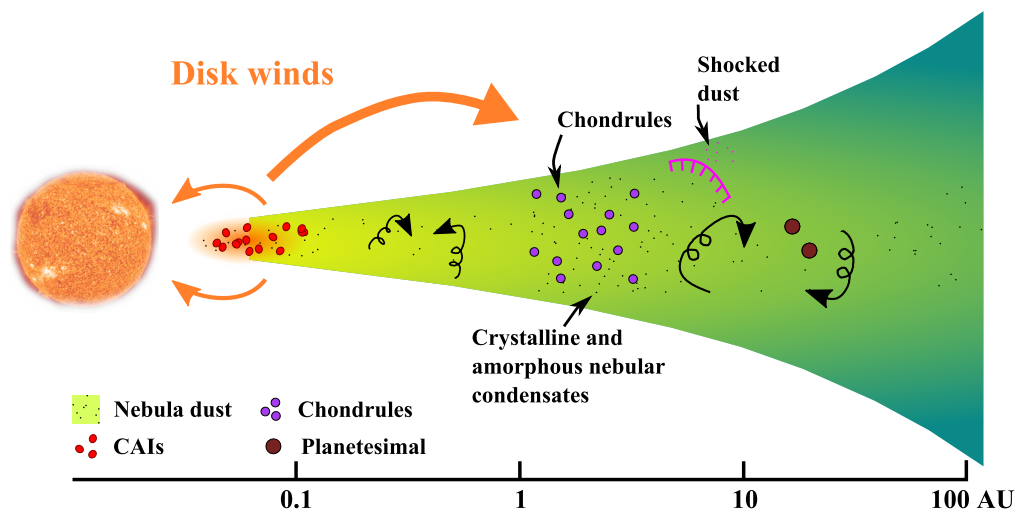


Figure 1.3: Schematic representation of the processes operating in the nebular disk shortly after the formation of the Sun, modified after Scott and Krot (2005a). Crystalline and amorphous nebular dust and condensates are thermally processed through shock waves, transformed into chondrites components and transported across the disk by winds and turbulences.

### 1.1.1 Carbonaceous chondrites

Among chondrites, the carbonaceous class is the one which is more volatile- and organic-rich. This suggests that these meteorites are mostly unaltered and have never experienced during accretion temperatures above 250-300 °C (Huss et al., 2006). For this reason they may have retained information about the first million years of our Solar System and therefore carbonaceous chondrites and their components are described in details in this thesis.

The different groups of chondrites are chemically classified according to their elements ratios. CI chondrites (Table 1.1) are used as reference because their composition matches that of the solar photosphere, which represents the best estimate for the bulk composition of the protoplanetary disk that evolved into the components of the Solar System (Lodders, 2003). The chondrites belonging to the carbonaceous class stand out in this kind of classification because of their elevated carbon and water contents, up to 6 and 10 %, respectively. However, the most distinctive chemical property of carbonaceous chondrites is their abundances of refractory elements, for example Mg/Si ratios in carbonaceous chondrites are similar to that of the Sun, while Al/Si ratios are significantly higher (Fig. 1.4).

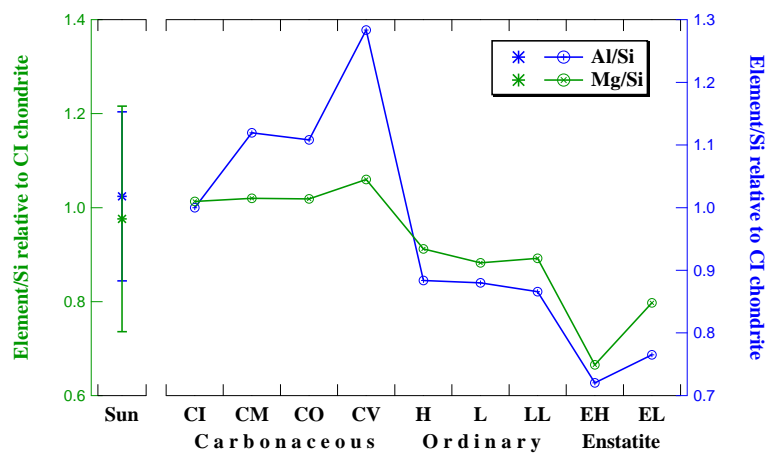


Figure 1.4: Element over Si ratios relative to mean CI values for 9 chondrite groups ordered by decreasing O content and for solar concentrations, modified after Palme and Jones (2003).

A secondary classification for chondrites is the *petrologic type*, which is a number ranging from 1 to 7 indicating the degree of alteration (Van Schmus and Wood, 1967). The most relevant types for the primitive carbonaceous chondrites are 3 and 2. Type 3 represents materials characterised by low degrees of alteration and unequilibrium mineral assemblages, while type 2 corresponds to low degrees of aqueous alteration, observed in meteorites having hydrated minerals, abundant fine-grained matrix and Ni-bearing sulfides.

The carbonaceous chondrite taken into consideration in this study belong to the groups CH, CR, CO and C-ung (ungrouped), having petrologic types 3 and 2 (Section 2.1, Table 6.1). The CH group includes metal-rich chondrites that contain up to 20%<sub>vol</sub> Fe–Ni metal in the form of tiny chondrules; CAIs are also quite small (up to ~0.02 mm). These meteorites generally show a low degree of aqueous alteration and their components are believed to have been formed very close to the sun and subsequently blown away from solar wind toward cooler regions of the system, thus preserving a very primitive state and pristine information

(Grossman and Olsen, 1974; Meibom et al., 1999).

CR chondrites are named after Renazzo, an Italian location where the first meteorite of this group fell in 1824. They are closely related to CH chondrites as they are metal-rich and contain up to 50%<sub>vol</sub> of chondrules and a low amount of small-sized CAIs. They normally show a higher degree of aqueous alteration compared to CH chondrites, are formed by abundant free Fe-Ni metal and sulfides (10%<sub>vol</sub>) together with fine-grained matrix (Bischoff et al., 1993b; Schrader et al., 2011).

CO chondrites are named after Ornans, the French town in which the first of this meteorites fell in 1868. They contain around 50%<sub>vol</sub> of small chondrules and refractory inclusions packed in a dense matrix and they form a well-documented metamorphic series (Scott and Jones, 1990) as they have experienced various degrees of aqueous alterations in the CO parent body (Greenwood and Franchi, 2004).

C-ung are meteorites that once thoroughly studied could not be fit into one of the already existing groups; in other word, they are unique specimens of a parent body not yet identified.

### 1.1.2 Calcium-aluminium-rich inclusions

CAIs are believed to be the first condensates of the Solar Nebula, thus they have been and are the subject of a multitude of chemical, isotopic, mineralogical, petrologic and experimental investigations aiming at understanding the formation and evolution of the early Solar Nebula (Grossman and Clark Jr., 1973; Clark and Reid, 1995).

One of the main evidences for CAIs to be very early condensates from the Solar Nebula is based on radiogenic element measurements. The  $^{26}\text{Al}$ - $^{26}\text{Mg}$  system is particularly important because the decay of  $^{26}\text{Al}$  to  $^{26}\text{Mg}$  has a half-life  $t_{1/2} = 0.73$  Myr and it allows obtaining information on the processes operating in this short time span after the formation of the Solar Nebula. Measured excesses of  $^{26}\text{Mg}$  in bulk CAIs and individual minerals, *e.g.* hibonite ( $\text{CaAl}_{12}\text{O}_{19}$ ), have been used to demonstrate that these materials have condensed very early in the history of the Solar System (Hinton et al., 1988; Ireland, 1990). Such measurements on CAIs seem to indicate that their condensation lasted less than 0.3 Myr or even less than 0.1 Myr (Kita et al., 2005). Another important analytical technique based on long-lived radiogenic elements is the Pb-Pb dating method (Nier et al., 1941), which is based on the decay of U and Th to Pb:  $^{238}\text{U} \longrightarrow ^{206}\text{Pb}$  ( $t_{1/2} = 4.47$  Byr),  $^{235}\text{U} \longrightarrow ^{207}\text{Pb}$  ( $t_{1/2} = 0.704$  Byr) and  $^{232}\text{Th} \longrightarrow ^{208}\text{Pb}$  ( $t_{1/2} = 14.01$  Byr). Pb-Pb dating on CAIs yield the oldest measured ages of any Solar System material, being 4.5647(6) Byr and 4.5672(6) Byr for CAIs from CR and CV chondrites, respectively (Amelin et al., 2002).

CAIs consist mainly of melilite, spinels, perovskite, hibonite, calcium pyroxenes, metal, anorthite and olivine (MacPherson, 2003). Many of the minerals found in CAI have compositions similar to those predicted by equilibrium condensation theory and some CAI are believed to have been formed by vapour-to-solid condensation in the nebula (Grossman and Olsen, 1974; Allen et al., 1978). Although corundum ( $\text{Al}_2\text{O}_3$ ) is predicted to be the first major phase to condensate from a hot solar gas, it is found rarely in CAI inclusions; instead the most Al-rich phase found in CAIs is hibonite and it has been postulated that this mineral is either the primary condensate instead of corundum or replaced corundum at lower temperatures. Some hibonite-bearing CAIs appear, according to their textural and chemical data, to have crystallised from a liquid (Blander and Fuchs, 1975; Macpherson and Grossman, 1984). It is now recognised that CAIs are not simply pristine aggregates of high-temperature nebular condensate grains but have experienced multiple episodes of melting, impact-induced shock and secondary mineralisation during accretion in the nebula and in asteroid parent bodies. In fact the abundance of low-temperature secondary phases in CAIs (Blander and Fuchs, 1975) and the presence of mineralogical distinct rims (Wark and Lovering, 1977) indicate that the refractory inclusions were not isolated from the nebula at high temperature but continued to react with the nebular gas at temperatures below 1000 K (Hutcheon and Newton, 1981).

### 1.1.2.1 $\text{Ti}^{3+}$ in minerals of refractory inclusions

The oxygen fugacity calculated for a gas of solar composition is quite low (Fegley Jr. and Palme, 1985), up to 7 log units below the  $f\text{O}_2$  buffer defined by the iron-wüstite (IW) redox couple (Frost, 1991). These extremely reducing conditions ( $\sim\text{IW}-7$ ,  $\log f\text{O}_2 \simeq -19.0$  at 1503 K and  $1 \times 10^{-3}$  bar) allow the occurrence of  $\text{Ti}^{3+}$ . For this reason, the oxidation state of titanium in different minerals present in the refractory inclusions (RI) of carbonaceous chondrites has attracted considerable attention over the years as it could be used to constrain the oxygen fugacity ( $f\text{O}_2$ ) conditions during Solar Nebula condensation. The minerals so far considered for the estimation of  $f\text{O}_2$  from the measurement of  $\text{Ti}^{3+}$  contents have been pyroxenes, hibonite, spinel and members of the olivine solid solution, including refractory forsterite (RF).

The first studies of this type were conducted crystallising under controlled temperature and  $f\text{O}_2$  glasses having a composition typical of Allende fassaites (Ti-rich clinopyroxenes)  $\text{Ca}(\text{Mg},\text{Al},\text{Ti})(\text{Si},\text{Al})_2\text{O}_6$  (Stolper, 1982). The  $\text{Ti}^{3+}$  content in these synthetic pyroxenes was estimated by means of electron microprobe analyses (EPMA, Section 2.3) and used to construct a calibration curve. Similarly estimated  $\text{Ti}^{3+}$  contents in the corresponding natural pyroxenes

were compared to that of the synthetic ones, giving possible Solar Nebula  $fO_2$  values ranging from about -17.5 to -22.5 log units at 1503 K, which is up to 4 orders of magnitudes more reducing than what is expected for a gas of solar composition. It has to be noted, however, that such calculations based on EPMA measurements have to be interpreted with caution because, especially at relatively low Ti contents, their precision and accuracy are sensitive to small errors in the analyses and to non-stoichiometry of the analysed samples.

Similar experiments performed by Beckett and Grossman (1986) on pyroxenes with slightly different compositions with respect to those of Stolper (1982) lead to a more narrow range of experimentally estimated  $fO_2$ , being up to 1.5 order of magnitude more reducing than expected for a gas of solar composition.

Besides pyroxenes, also the mineral hibonite usually contains significant amounts of transition metal cations. In particular it can incorporate up to 7%<sub>at</sub> of titanium and therefore it can be used in principle as oxybarometer for the Solar Nebula. In fact, the oxidation state of Ti in hibonite has been qualitatively related to the oxygen fugacity at which it has formed and evolved in the Solar Nebula (Ihinger and Stolper, 1986). These authors have synthesised a number of samples equilibrated at different oxygen fugacities using as starting material an oxide mixture with a composition similar to that of the natural hibonite known as *Blue Angel* (Armstrong et al., 1982) and studied them using UV/Vis absorption spectroscopy. They have then used the absorption intensity of a broad peak observed at 715 nm to obtain a qualitative calibration curve as a function of the  $fO_2$  conditions during the syntheses. By comparing the absorption value measured on a specimen of the natural *Blue Angel* with this calibration curve, they concluded that *Blue Angel* might have formed at conditions 4 to 5 orders of magnitude more oxidising than those calculated (Fegley Jr. and Palme, 1985) for the early Solar Nebula (Fig. 1.5).

Considering the results previously obtained by Stolper (1982) on pyroxenes, those of Ihinger and Stolper (1986) are quite striking because they suggest relatively oxidising conditions of the Solar Nebula. However, these measurements on hibonite also have to be considered with caution because the composition of the synthetic hibonites was just inferred from the starting materials, the thickness of the section used to acquire the UV/Vis spectra was just roughly estimated and only unpolarised spectra were collected .

A more quantitative approach to this subject was chosen by Beckett et al. (1988). These authors used Electron Spin Resonance (ESR) spectroscopy to measure more accurately the concentration of  $Ti^{3+}$  in the same synthetic and meteoritic hibonites analysed by Ihinger and Stolper (1986). However, since the ESR analyses are sensitive to the symmetry of the structural site occupied

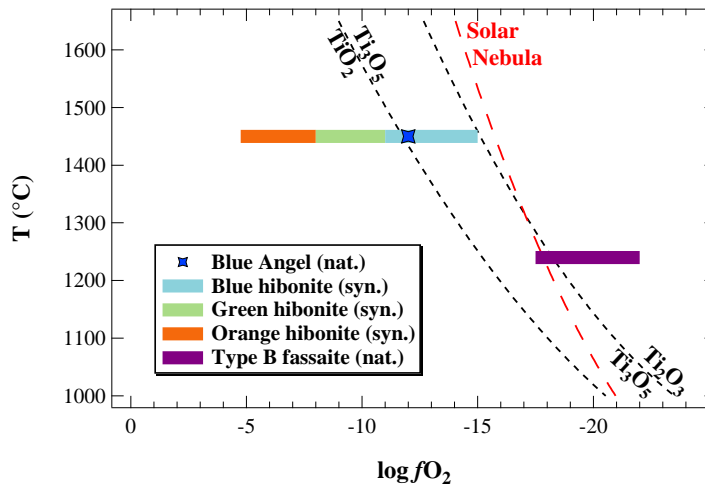


Figure 1.5: Summary of the  $T$ - $fO_2$  relations observed on synthetic and natural (Blue Angel) hibonites, modified after Ihinger and Stolper (1986). The  $fO_2$  range given for fassaites is taken from the experimental study of Stolper (1982).

by  $Ti^{3+}$ , a quantitative estimate of equilibrium oxygen fugacity based on the measured  $Ti^{3+}$  content requires the knowledge of the cation distribution and site occupancy of Ti on the structure of hibonite. This information is accessible through single crystal X-ray diffraction, but was not available to Beckett et al. (1988) at the time of publication. Nevertheless, on account of the number of observed ESR peaks, of their fine structure and of their intensity variation as a function of the angle between the magnetic field  $\vec{H}$  and the crystallographic orientation of the hibonite samples, the authors were able to conclude that  $Ti^{3+}$  in both synthetic and natural hibonites is occupying a distorted site which has an axial symmetry and which is compatible with an ESR signal having a component parallel to the  $c$  axis,  $g_{\parallel}$ , and one perpendicular to it,  $g_{\perp}$ . In the interpretation given by Beckett et al. (1988) these characteristics are referred to a site having a 5-fold coordination environment, which corresponds to the trigonal bipyramidal site M2 present in the structure of hibonite (described in more details in the Section 1.2).

After this initial flourishing of publications focused on the  $Ti^{3+}$ - $fO_2$  relationship in RI, not much has been done for years, possibly due to the still limited number of techniques suitable for the determination of trivalent titanium. In more recent times, with the development of synchrotron radiation facilities, X-ray Absorption Near Edge Spectroscopy (XANES) has become a progressively more popular techniques suited for measuring the valence state of transition metals in solids. Initially this technique was not extensively adopted due to limitations in the spatial resolution that was possible to achieve. Further development have contributed to make XANES a widely used technique which is capable of detecting core-to-rim variations in  $Ti^{3+}$  and which has been used on RI minerals (Table 1.2). However, to be able to translate these

measurements into absolute  $\text{Ti}^{3+}$  concentrations, appropriate calibrations have to be constructed. In the absence of such calibrations, several assumptions need to be made in order to estimate the relative amount of Ti having different valence states (Simon et al., 2009).

Table 1.2: Summary of the XANES measurements performed on minerals of refractory inclusions. RF = refractory forsterite, hib = hibonite, sp = spinel, ol = olivine.

Minerals	Sample (group)	References
RF (isolated grains)	Tagish Lake (C2-ung)	Simon et al. (2007b)
hib, hib-sp (CAI)	Murchison (CM)	Simon et al. (2009)
ol (AOA)	Allende (CV3) Efremovka (CV3)	Simon et al. (2010b)
sp (CAI)	Allende (CV3)	Simon et al. (2010a) Paque et al. (2013)

In recent years also electron microprobe analysis has benefited from technological advancements, allowing researchers to repeat experiments similar to those conducted by Stolper (1982) and Beckett and Grossman (1986) in order to obtain more accurate and precise datasets. In particular, Grossman et al. (2008) have performed crystallisation experiments on liquids having composition similar to those of natural refractory inclusions and derived the  $\text{Ti}^{3+}$  contents in fassaite-clinopyroxenes and melilite pairs by means of microprobe analyses. They have shown, by matching their data from synthetic samples with those of the corresponding natural ones, that the considered phase assemblages are in equilibrium with a solar gas having  $\log f\text{O}_2 = -19.8$  at  $\sim 1509$  K, which is in good agreement with calculated values (Grossman et al., 2008).

The concentration of  $\text{Ti}^{3+}$  has been studied not only in minerals found inside RI, but also in those that are found around RI, which typically appear in the form of Wark-Lovering (WL) rims (Wark and Lovering, 1977). These rims are formed by micrometer-thick layers following a characteristic mineralogical sequence that is independent of differences among CAIs. The characterisation of WL rims allows obtaining information on the history and the evolution of CAIs in the Solar Nebula after their initial formation. Studies focused on the  $\text{Ti}^{3+}$  content in pyroxenes of WL rims conducted using different techniques gave discordant results (Simon et al., 2007a; Dyl et al., 2011; Simon et al., 2012; Young et al., 2012), indicating how sensitive are the measurements to uncertainties and assumptions.

## 1.2 The mineral hibonite

Hibonite has the structure of the magnetoplumbite group minerals with general formula  $AM_{12}O_{19}$ , space group symmetry  $P6_3/mmc$  and unit cell parameters  $a \approx 5.5 \text{ \AA}$ ,  $c \approx 22.0 \text{ \AA}$  (Utsumomiya et al., 1988). The structure is based on six cationic sites ( $A, M1 - M5$ ) and five oxygen ( $O1 - O5$ , Table 1.3). These atoms form 10 layers of close-packed oxygen atoms perpendicular to the  $c$  axis of the hexagonal cell with a sequence which can be expressed as  $chhhcchhhc$  where  $c$  stands for cubic and  $h$  for hexagonal close-packed layers. The stacking of the  $c$  layers results in a spinel-like structural block indicated with  $S = [M_6O_8]^{2+}$ , while the stacking of  $h$  layers gives hexagonal close-packed block  $R = [AM_6O_{11}]^{2-}$ . These blocks alternate in the structure of hibonite according to the sequence  $RSR'S'$  where the prime  $'$  indicates a 2-fold rotation around the  $c$  axis (Bermanec et al., 1996). The large  $A$  atoms (mainly Ca in the case of hibonite) occupy two of these layers in a 12-fold coordinated site, whereas the  $M$  ions are distributed over five different sites: three with octahedral, one with tetrahedral and one with bipyramidal coordination (Fig. 1.6).

The  $M1$  site is a quite regular octahedron, whereas the  $M2$  site is a five-fold coordinated trigonal bipyramid. The  $M2$  cation is displaced from the central position and its dynamical disorder is modelled with a split position located slightly above and below the mirror plane at  $z = \pm 1/4$  and having half occupancy. The  $M3$  site is nearly a regular tetrahedron and the  $M4$  sites are trigonally distorted octahedra which occur in pairs sharing a face. The  $M5$  is a distorted octahedron located between the layers containing the  $A$  cations and the tetrahedral layers (Table 1.3).

Table 1.3: Crystal structure of hibonite: atomic position and coordination polyhedra.

name	Site		Wyckoff letter	Coordination polyhedra
	symmetry	coordinates		
$A$	$\bar{6}m2$	$1/2, 2/3, 3/4$	$2d$	12-fold coordination
$M1$	$\bar{3}m.$	$0, 0, 0$	$2a$	Regular octahedra
$M2$	$\bar{6}m2$	$0, 0, z$	$2b$	Trigonal bipyramid
$M3$	$3m.$	$1/3, 2/3, z$	$4f$	Nearly regular tetrahedron
$M4$	$3m.$	$1/3, 2/3, z$	$4f$	Trigonally distorted octahedra
$M5$	$.m.$	$x, 2x, z$	$12k$	Distorted octahedra
$O1$	$3m.$	$0, 0, z$	$4e$	/
$O2$	$3m.$	$1/3, 2/3, z$	$4f$	/
$O3$	$mm2$	$x, 2x, 1/4$	$6h$	/
$O4$	$.m.$	$x, 2x, z$	$12k$	/
$O5$	$.m.$	$x, 2x, z$	$12k$	/

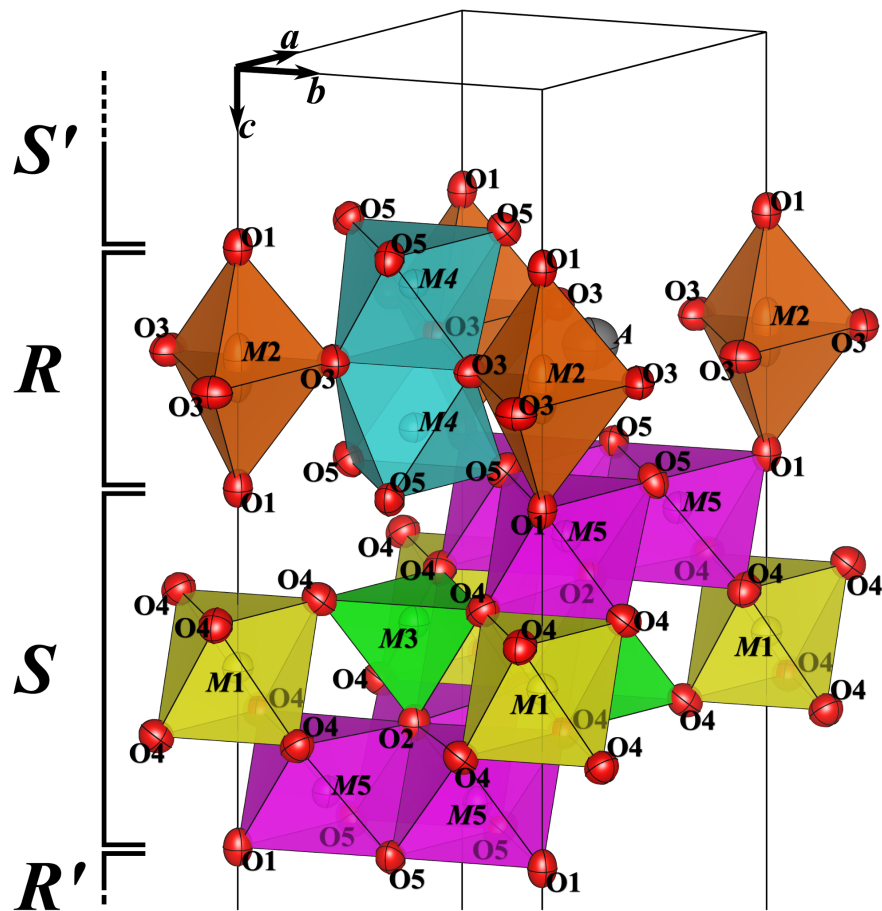


Figure 1.6: Crystal structure of hibonite showing the coordination polyhedra (*A*, *M1* – *M5*) and the repetitive blocks ( $S = [M_6O_8]^{2+}$  and  $R = [AM_6O_{11}]^{2-}$ ). The 12-fold coordinated *A* site is occupied by Ca while Al, Ti and Mg ions are distributed over different sites: one with bipyramidal (*M2*), one with tetrahedral (*M3*) and three with octahedral (*M1*, *M4*, *M5*) coordination.

As mentioned, hibonite is the earliest phase to condensate from the Solar Nebula (Grossman, 1972), thus having the potential to give information on the oldest oxygen fugacity record of the Solar System. Consequently the attention on hibonite is focused on the presence in its structure of Ti, which in principle can substitute for Al on most of the structural sites of this mineral. The knowledge of the site symmetry of Ti can considerably help interpreting the spectroscopic properties of hibonite described in the previous section. Single crystal X-ray diffraction measurements are essential for obtaining key information on the crystal chemistry and substitution mechanisms in hibonite.

Hibonites found in chondrites typically have small grain sizes ( $< 50 \mu\text{m}$ ), hence there are no single crystal structural studies regarding these samples, given the difficulties related to sample extraction and the need of synchrotron radiation for the measurements. The structural data reported so far in the literature concern therefore synthetic hibonite end-member as well as few terrestrial occurrences of hibonite that allowed a structural characterisation by means of single

crystal X-ray diffraction. The first among these studies was carried out on synthetic  $\text{CaAl}_{12}\text{O}_{19}$ , confirming  $P6_3/mmc$  as the correct space group for this material, providing a first structural model for hibonite and reporting the presence of significant thermal disorder at the  $M2$  site (Utsunomiya et al., 1988).

The first X-ray diffraction characterisation of a terrestrial hibonite from Madagascar was reported by Bermanec et al. (1996). The authors first determined the composition of their hibonite specimen by means of microprobe analysis, revealing that the terrestrial sample contained significant amounts of Ti, Fe and Mg similar to chondritic samples, with the addition however of minor quantities of Si and REE. Based on structural refinements performed on X-ray diffraction datasets, Bermanec et al. (1996) provided important information on the crystal chemistry and site occupancy in hibonite. In particular, they reported that the  $M2$  site is displaced from the central position of the trigonal bipyramid, suggesting a dynamic disorder model for this atomic position. It also appears that both  $M1$  and  $M5$  sites are mainly occupied by Al whereas cation substitution occurs at the other structural sites. The authors indicated the possible presence of heavy atoms on the  $M4$  site and suggested that the  $M3$  site is likely to be occupied by divalent cations.

This last hypothesis is also supported by  $^{57}\text{Fe}$  Mössbauer spectroscopy measurement on terrestrial (Madagascar) and Fe-bearing synthetic hibonites (Holtstam, 1996) which clearly indicate the presence of  $\text{Fe}^{2+}$  on the tetrahedral  $M3$  site.

Single crystal X-ray diffraction measurements on pure end-member and terrestrial hibonite from Madagascar were also reported by Hofmeister et al. (2004). The chemical analyses revealed the presence in the natural sample of substantial amounts of Ti, Fe, Mg, Ce and La as well as minor contents of Si, Th and Nd. The structural refinements confirmed the results presented in the early studies. Moreover, the authors also acquired vibrational spectra (IR, Raman) on both their synthetic and natural samples. These measurements have important implications for meteoritic hibonite because it is shown that the IR data from synthetic samples are a good match for astronomical observations from the NGC 6302 proto-planetary nebula, indicating the presence of hibonite and grossite in such environments, which reflect the early stages of the Solar System.

The most recent study on terrestrial hibonite has been carried out on gem-quality samples from Myanmar for which microprobe analyses and single crystal X-ray diffraction at room temperature are presented together with a temperature-dependent structural characterisation (Nagashima et al., 2010). The authors have studied a sample containing mostly Ti and Mg with minor concentrations of Zn and Fe, making this hibonite the most chondritic-like among

those reported in the literature. This represents the first study in which the site occupancy of Ti substituting for Al has been refined in a crystallographic site. In particular the structural refinements indicate that most of the Ti is occupying the *M4* octahedra occurring in face-sharing octahedra while a smaller fraction also substitutes for the *M2* site. Moreover, it is proposed that the *M4* cations are collocated off the centre of the octahedral site due to repulsion between the neighbouring  $\text{Ti}^{4+}$  cations. It has also been confirmed that the atomic site *M2* is split into two positions according to a dynamic disorder model (Nagashima et al., 2010).

However, these samples are not ideal proxies for studying chondritic hibonites due to the fact that they contain large amounts of rare Earth elements (REE) and that the Ti present is all in its oxidised state, *i.e.* 4+. On the other hand, hibonites with compositions relevant for chondritic materials can be synthesised, but usually present very small grain sizes. This is the case for the samples studied by Ihinger and Stolper (1986) and Beckett et al. (1988), as well as for those reported in a very recent contribution on the characterisation of hibonite structure based on Neutron Powder Diffraction (NPD; Doyle et al., 2014). In this study the presence of Ti has been refined on both the *M4* and the *M2* sites, and  $\text{Ti}^{3+}$  has been reported to occupy only the octahedral *M4* site on the basis of Density Functional Theory (DFT) calculations.

### 1.2.1 State of art on hibonite synthesis

To date the methods available for synthesising hibonite in the form of single crystals are very limited in number. The first attempt to synthesise an hibonite-like compound was reported by Mateika and Laudan (1979). In this study large single crystals of  $\text{BaAl}_{12}\text{O}_{19}$  were obtained by means of Czochralski method. A similar technique was later adopted by Utsunomiya et al. (1988), resulting in the first synthesis of pure end-member hibonite. The authors used a travelling solvent floating zone method with a solvent having composition  $\text{CaO} \cdot 4\text{Al}_2\text{O}_3$  and two halogen lamps as heat source, obtaining large platelets of hibonite.

In the frame of an investigation on the enthalpies of formation of calcium aluminates, Geiger et al. (1988) have performed few preliminary attempts to synthesise hibonite by means of piston-cylinder apparatus. The authors sealed an homogenised stoichiometric mixture of  $\text{CaCO}_3$  and  $\text{Al}_2\text{O}_3$  in Pt capsules and run them at 15 kbar and 1450 °C for several hours, however, the run products were mostly unreacted corundum and this technique was abandoned in favour of room pressure syntheses.

Finally, it has been reported that large single crystals of pure end-member hibonite as well as grossite ( $\text{CaAl}_4\text{O}_7$ ) can be obtained by laser-heating pellets of  $\text{CaO-Al}_2\text{O}_3$  mixtures (Hofmeister et al., 2004).

No synthesis of large single crystals of hibonite containing both  $\text{Ti}^{3+}$  and  $\text{Ti}^{4+}$ , *i.e.* under controlled  $f\text{O}_2$ , has been attempted so far.

### 1.3 Aim of the thesis

The knowledge of  $\text{Ti}^{3+}/\text{Ti}^{\text{tot}}$  ratios in hibonite can potentially provide important information on the oxygen fugacity of the Solar Nebula. The determination of  $\text{Ti}^{3+}$  can be performed using spectroscopic techniques which, in order to be correctly interpreted, require the knowledge of the exact coordination environment for Ti in hibonite. However, little is known on the crystal chemistry of hibonite, *i.e.* what is the site distribution of the elements substituting for Al and what are the interactions between atoms of these different species. Moreover, what are the site distribution and the incorporation mechanisms for  $\text{Ti}^{3+}$  and  $\text{Ti}^{4+}$  in hibonite remains an open question.

The principal aim of this research is to determine the distribution of Ti in synthetic and meteoritic hibonites and to quantify their  $\text{Ti}^{3+}/\text{Ti}^{\text{tot}}$  ratios. To this end, synthesis of Ti- and Mg-bearing single crystals of hibonite under controlled  $f\text{O}_2$  are necessary in order to gain crucial information on the crystal chemistry of hibonite. In fact the oxidation state of any cation in a mineral depends not only on temperature, pressure and oxygen fugacity but also on the phase assemblage, *i.e.* the activities of all components in the structure, and on the crystal structure. A particular oxidation state may be favoured if the cation having a specific charge has just the right radius for a given structural site. An instructive example is given by Al- and Fe-bearing silicate perovskite,  $(\text{Mg},\text{Fe}^{2+})(\text{Si},\text{Al},\text{Fe}^{3+})\text{O}_3$ , that shows very high oxidation states, even when it coexists with metallic iron. The current knowledge on the overall oxygen budget and oxygen fugacity of the Earth interior, and the presence of metallic iron in the lower mantle (Frost et al., 2004; McCammon, 2005) are based on this crystal chemical property.

A correct determination of the cation distribution in chondritic hibonite is not only important for assessing its influence on the oxidation state of the substituting cations, but also it can help to better interpret spectroscopic data, which in the specific case of this thesis will be obtained by means of Energy Electron Loss Spectroscopy (EELS) and UV/Vis spectroscopy. In particular, EELS is analogous to XANES but has the practical advantage that instead of requiring a large-scale synchrotron facility can be performed *in-house* using a Transmission Electron Microscope (TEM). Moreover, a method for the estimation of the valence state of Ti by means of EELS has been made available recently (Stoyanov et al., 2007).

The information gathered from single crystal X-ray diffraction and the spectroscopic techniques would then allow testing whether hibonite is a sensible oxybarometer and possibly explain the large difference in nebular oxygen fugacities between estimations based on hibonite (Ihinger and Stolper, 1986) and pyroxenes (Stolper, 1982; Beckett and Grossman, 1986; Grossman et al., 2008).

## 2 Samples and experimental methods

The study of the crystal chemistry of hibonite required the preparation and the analysis of numerous samples. In this chapter the methods used to synthesise polycrystalline and single crystal hibonites are presented together with the techniques adopted for preparing the specimens for analysis. Details are also given on the different analytical techniques used to characterise both synthetic and natural hibonites.

### 2.1 Natural samples

The natural samples that were analysed in this study belong to, and were selected among, the Meteorite collection of the Institut für Planetologie, Westfälische Wilhelms-Universität Münster, curated by Prof. Dr. Addi Bischoff. The sample lot consisted of six petrographic thin sections of carbonaceous chondrites containing a total of seven CAIs (Table 6.1), some of which have been previously studied by Bischoff et al. (1993a); Weber and Bischoff (1994); Weber et al. (1995); Weber (1995). Petrographic microscope observations and electron microscope analyses (Section 2.3) were carried out on all the studied CAIs (Fig. 2.1) in order to characterise them mineralogically and chemically, as presented in Section 6.1.

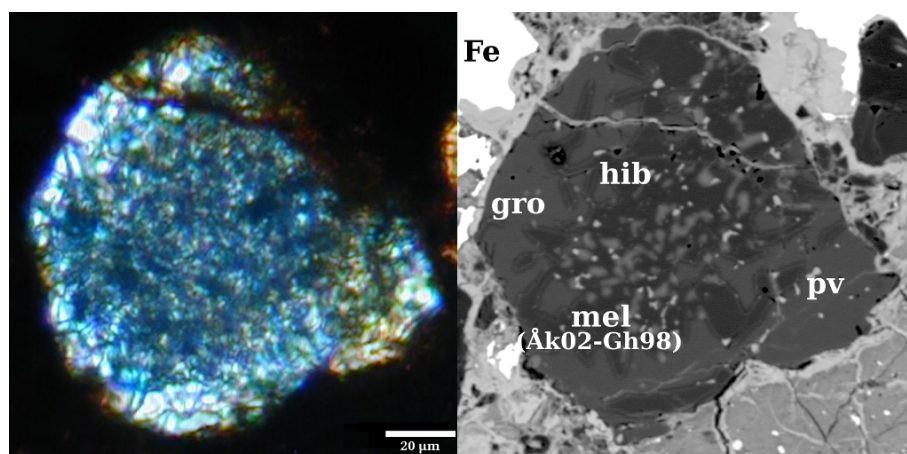


Figure 2.1: Optical transmission image (left) and back-scattered electron image (right) of Acfer 182-3 CAI. hib = hibonite, pv = perovskite, gro = grossite, mel = melilite (åkermanite-gehlenite), Fe = Fe-Ni metal.

For each CAI, one hibonite grain has been selected and extracted by means of focused ion beam milling (Section 2.6.1.2).

## 2.2 *Synthetic samples*

Synthetic hibonites were prepared by means of solid state reactions using piston-cylinder press and gas-mixing furnace apparatuses. In the former case only oxide mixtures were used as starting materials while in the latter sol-gels were also used as precursors.

### 2.2.1 *Starting materials*

#### 2.2.1.1 *Oxide precursors*

Stoichiometric mixtures of  $\text{CaCO}_3$  or  $\text{CaO}$ ,  $\text{MgO}$ ,  $\text{TiO}_2$  or  $\text{Ti}_2\text{O}_3$  and  $\text{Al}_2\text{O}_3$  were used as starting materials for solid state synthesis. The initial compounds were commercially available materials that were fired prior to utilisation in order to desiccate or activate them:  $\text{Al}_2\text{O}_3$  was fired at  $1400^\circ\text{C}$  for 4 h;  $\text{MgO}$  was annealed at  $1500^\circ\text{C}$  for 3 h;  $\text{TiO}_2$  (Anatase),  $\text{Ti}_2\text{O}_3$  and  $\text{CaCO}_3$  were dried at  $150^\circ\text{C}$  for 2 h. The oxides were weighted in batches of 1 to 1.5 g and homogenised by means of milling for 30 to 40 min in an agate mortar using ethanol as lubricant. The dried mixtures were subsequently transferred into a platinum crucible and decarboxylated by heating them up to  $1000^\circ\text{C}$  over 12 h; the powders were then ground one last time for 15 to 20 min. Note that  $\text{Ti}_2\text{O}_3$  was added to the oxide mixtures after decarboxylation.

An et al. (1996) reported that the use of  $\text{CaO}$  (lime) instead of  $\text{CaCO}_3$  enhances the reactivity towards  $\text{Al}_2\text{O}_3$ , so the former has been used in some cases.  $\text{CaO}$  was prepared by decarboxylating  $\text{CaCO}_3$  with the same procedure adopted for the oxide mixtures. Given its high hygroscopicity,  $\text{CaO}$  was kept in a vacuumed desiccator and, before utilisation, it was tested with Powder X-ray diffraction (Section 2.4) to ensure that it did not transform into  $\text{Ca}(\text{OH})_2$  (portlandite). For such samples, the mixtures containing  $\text{MgO}$ ,  $\text{TiO}_2$  and  $\text{Al}_2\text{O}_3$  were weighted and ground as described above;  $\text{CaO}$  was then added before the last grinding cycle.

A summary of the nominal compositions and synthetic conditions for the samples synthesised from oxide precursors is reported in Table 3.2 together with the run products which were obtained from high temperature sintering.

### 2.2.1.2 Sol-gel synthesis

The sol-gel synthesis is a commonly used process for the preparation of ceramic materials, including hexaluminates (Cinibulk, 1998; Lessing, 1989). Solid state reaction from sol-gel precursor are advantageous compared to the reaction of metal oxide because the starting material is a mixture of solid particles highly dispersed in a continuous liquid solution (sol), which guarantees a high level of homogeneity.

In general, the sol-gel synthesis can follow two routes: inorganic (metal salts in aqueous solution) or metal-organic (metal alkoxides in organic solvent). The former route is quicker and easier to realise, but the latter allows having a better control over the stoichiometry of the final products, and therefore was chosen to synthesise the samples for this study, adopting the citrate-based sol-gel method described by Cinibulk (1998). The general outline of the synthesis can be schematised as follows.

- Formation of the sol-gel precursor (Fig. 2.2);
  - preparation of the sol (Fig. 2.3);
  - polymerisation of the sol to produce the gel (Fig. 2.4);
- Firing of the gel to form an amorphous material (Fig. 2.5).

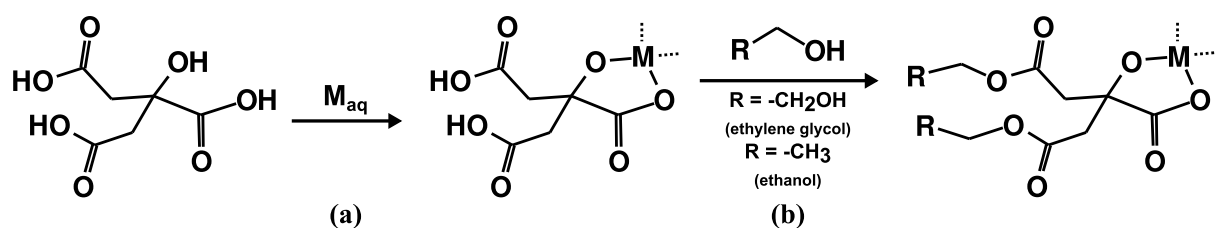


Figure 2.2: Reaction for the formation of metal-citrate complexes in the sol (a) and the subsequent polymerisation to form the gel (b).

The reagents used for the preparation of the sol-gel were: calcium acetate  $\text{Ca}(\text{C}_2\text{H}_3\text{O}_2)_2 \cdot \text{H}_2\text{O}$ , aluminium nitrate  $\text{Al}(\text{NO}_3)_3 \cdot \text{H}_2\text{O}$ , magnesium nitrate  $\text{Mg}(\text{NO}_3)_2 \cdot 6 \text{H}_2\text{O}$  and titanium isopropoxide  $\text{Ti}[\text{OCH}(\text{CH}_3)_2]_4$  as sources for Ca, Al, Mg and Ti, respectively. In addition, citric acid  $\text{C}_6\text{H}_8\text{O}_7 \cdot \text{H}_2\text{O}$  and ethylene glycol  $\text{C}_2\text{H}_6\text{O}_2$  were used as complexing/polymerising agents and ethanol  $\text{CH}_3\text{CH}_2\text{OH}$  as the solvent.

It has to be noted that Cinibulk (1998) prepared a sol corresponding to pure hibonite which was doped with individual metal cation in the form of fine-grained oxides; this resulted in a drastic decrease in hibonite yield. In this study, in order to synthesise Ti-Mg-bearing hibonites, the above mentioned chemicals were used as dopant agent because they can be fully incorporated into the sol-gel and eventually into the structure of the amorphous starting material.

The sol was formed by completely and sequentially dissolving in ethanol, under constant stirring, the appropriate amounts of aluminium nitrate, magnesium nitrate, citric acid and calcium acetate. When the dissolution of the acetate, aided by mild heating up to  $\sim 50^{\circ}\text{C}$ , was complete, titanium isopropoxide and ethylene glycol were added to the mixture. At this point, the solution was heated up to the boiling point ( $\sim 82^{\circ}\text{C}$ ) and it was allowed to reflux for 6 h using the apparatus shown in Fig. 2.3.



Figure 2.3: Experimental setup used to prepare the sol.

During this time the metallic cations dissolved into the alcoholic solution react with citric acid to form metallic citrates, as shown in reaction (a) of Fig. 2.2. The molar ratios of the reactants represent a crucial parameter for the completeness of the complexation reaction and the stability of the final sol-gel. In this study a 1 : 2 ratio for nitrates : citric acid and a 1 : 1 ratio for nitrates : glycol were used in order to obtain a sol containing  $30 \text{ g l}^{-1}$  of hibonite. The product obtained at the end of the 6 h was a pale yellow transparent sol. It could happen, especially for samples having an elevated content of dopants, that the sol turns turbid, in these cases nitric acid  $\text{HNO}_3$  (0.2 mol per 1 mol of Ti-isopropoxide) could be used as clarifying agent, as suggested by Yoldas (1986). Small aliquots of the sol (10 to 20 ml) were then transferred into a Teflon beaker and heated up to  $\sim 150^\circ\text{C}$  under a fume hood. During heating, a part of the solvent is removed and the metal-organic complexes initially segregate (gelification) and then start to polymerise as illustrated in reaction (b) of Fig. 2.2, in which residual ethanol and ethylene glycol react to form an interconnected network. These processes are accompanied by the decomposition to  $\text{N}_x\text{O}_y$  of the nitrates still present in the solution, which causes the release of red gases. Further heating to  $\sim 200^\circ\text{C}$  resulted in the removal of all the solvents, leaving a yellowish resin-like solid (xerogel, Fig. 2.4).

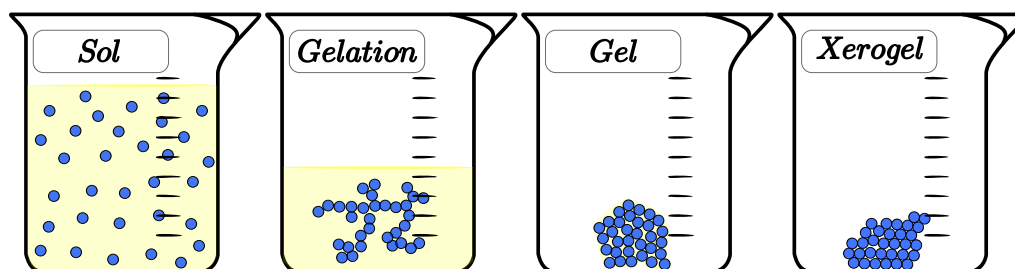


Figure 2.4: Schematic representation for the formation of the gel precursor.

Firing the xerogel up to  $600^\circ\text{C}$  over  $\sim 60$  min results in the removal of all the organics by releasing  $\text{CO}_2$ , yielding an amorphous material in which the cations are, ideally, uniformly dispersed on an atomistic scale throughout the sample. A sequence of X-ray diffraction patterns for sample gel0 (Table 3.3) is plotted in Fig. 2.5, showing the amorphous gel before and after firing, as well as the final product (hibonite) after sintering (Section 2.2.3).

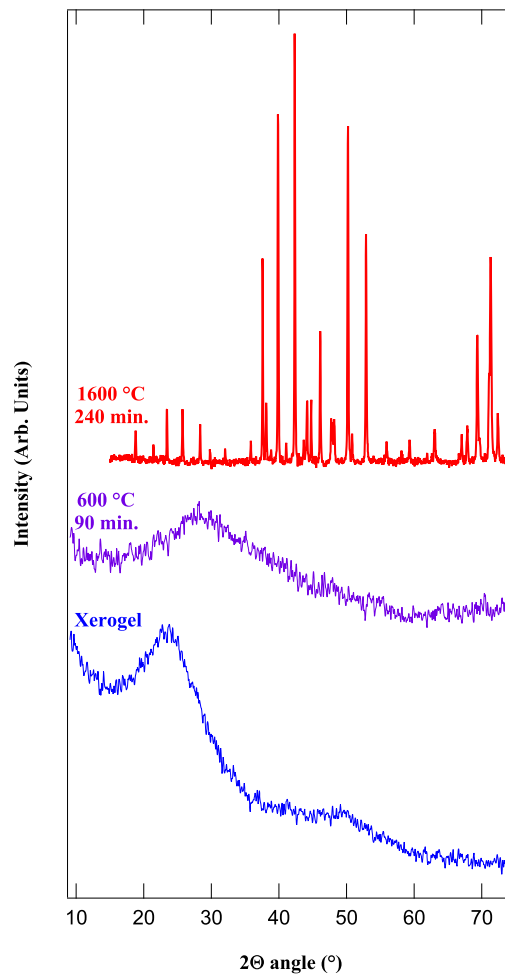


Figure 2.5: X-ray diffraction patterns of different intermediate products for sample gel0.

### 2.2.2 Piston-cylinder synthesis

Following the attempt made by Geiger et al. (1988), which has been described in Section 1.2.1, the piston-cylinder apparatus was used to produce hibonite by a two-stage synthesis method. First polycrystalline hibonite was synthesised at room pressure (Sections 2.2.1.1 and 2.2.3) and then used as starting material for high-pressure and high-temperature experiments carried out by means of piston-cylinder apparatus available at the Bayerisches Geoinstitut.

The piston-cylinder was first developed by Boyd and England (1960). It basically consists of two hydraulic rams: the lower ram transmits pressure, through a bridge, to a tungsten carbide piston while the top ram provides a confining end load. The piston applies force to the high-pressure chamber which is constituted by a water-cooled steel bomb having a tungsten carbide core with a hole of either  $3/4$ " or  $1/2$ " for pressures up to 15 kbar and 40 kbar, respectively.

The sample assembly (Fig. 2.6), which sits in the high-pressure chamber, is constituted of a three-layer cylinder formed by closely fitting sleeves of different materials, which serve specific purposes. The external talc sleeve acts as pressure medium, the second pyrex sleeve forms an insulating layer and the third one is the graphite furnace.

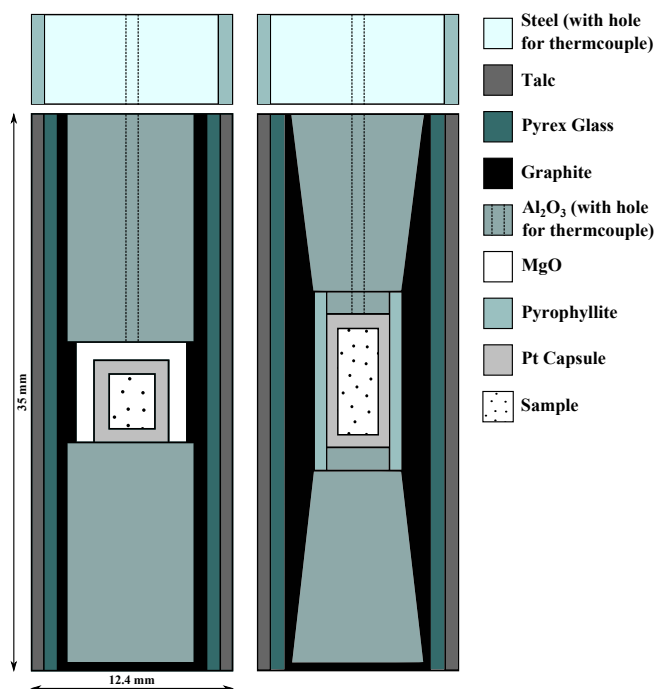


Figure 2.6: Schematic representation of the assemblies used to perform experiments with piston-cylinder apparatus.

Two different designs were used for the furnace, with stepped and wedged profiles; the former, which has been used for the experiments performed at higher temperature, is more robust and generates less thermal gradients. The furnace is heated by passing an electrical current through it. The electrical contact is realised at the top of the assembly by a steel plug and a retaining plate stacked on top of the bomb, while a steel disk placed at the bottom of the assembly ensures the closure of the circuit. During the experiments the temperature was monitored using a type D (W-3% Re/W-25% Re) thermocouple (T/C) and an Ar flux was blown through a Teflon tube at the top of the assembly in order to prevent oxidation and deterioration of the thermocouple wires. The piston-out technique was adopted: the assembly was cold pressed for 30 min at a pressure 2 kbar higher than the target one, then heated up to the running temperature with a  $100\text{ }^{\circ}\text{C min}^{-1}$  slope and finally decompressed to the target pressure over 5 min.

Fluxes like water, CO<sub>2</sub> in the form of CaCO<sub>3</sub> and even PbO (Gasparik, 1984) were used in different experiments in order to facilitate growth of large single crystals. The Pt capsules were welded at both sides while being cooled in liquid nitrogen, in order to avoid the escape of fluids due to the local heating of the welding process.

The products of the piston-cylinder runs consisted of well sintered pellets of crystalline aggregates. A detailed description of the run products is reported in Section 3.1.1.

### 2.2.3 *Experiments with the gas-mixing furnace*

In order to perform high-temperature synthesis under controlled redox conditions, a vertical gas-mixing furnace has been used. The oxygen fugacity has been controlled by changing the CO/CO<sub>2</sub> ratio of the gas mixtures in the range from 1 : 1 to 100 : 0.5. The furnace can operate at temperatures up to 1600 °C and is equipped with a fast quench system for achieving cooling rates in the order of hundreds of Celsius per second, while maintaining the sample still in a reducing environment. During the experiments the temperature was not directly monitored with a thermocouple, but the thermal profile inside the furnace has been characterised and the thermal controller has been calibrated against a temperature measurements with a type S thermocouple (Pt/Pt-10% Rh).

The furnace is usually kept at temperatures not lower than 1000 °C; this initial condition was then used for the synthesis experiments in which the starting materials were oxide mixtures. In the case of pre-fired sol-gel precursors, the temperature of the furnace was temporarily lowered to 800 °C in order to avoid crystallisation of the sample before conditioning the furnace with the gas mixture. In both cases, the temperature was raised to the working set point with an heating rate of  $\sim 100\text{ }^{\circ}\text{C min}^{-1}$ . The experimental setup allows controlling the temperature and the oxygen fugacity within an uncertainty range of 15 °C and 0.3 log units, respectively (Audétat, 2011).

The starting materials for these experiments, whether in the form of oxide mixtures or amorphous material from sol-gel processes, were pressed into 1/2" pellets weighing 300 to 500 mg. The pellets were suspended in the hot spot of the furnace through a thin platinum wire loop (quenching wire) attached to two electrodes formed by a two-hole alumina rod in which thick Pt wires are inserted. The rapid quench is realised by passing high current through the electrodes so that the quenching wire melts allowing the sample to drop into a quenching vessel located at the bottom of the furnace.

In the case of experiments conducted in air, the sample pellets were introduced into a Pt crucible which was subsequently inserted into a furnace. Similarly to the experiments with the gas-mixing furnace, the initial temperature at which the samples were introduced into the furnace was either 800 or 1000 °C, depending on the starting material. The experiments were quenched removing the Pt crucible from the furnace as quickly as possible and cooling it in air; the quench rates are comparable with those of the gas-mixing furnace.

Part of some of the run products were further milled for 30 to 40 min in an agate mortar using ethanol as lubricant, pressed into a 1/2" pellet and re-equilibrated at high temperature and at a specific oxygen fugacity.

The recovered samples typically appeared as well sintered ceramics with colours ranging from creamy white to blue to dark/blackish-blue as a consequence of progressively reducing conditions. The colours reported in Tables 3.2 and 3.3 are referred to hibonites from the interiors of the sintered pellet because, as reported by Ihinger and Stolper (1986), due to unavoidable oxidation during quenching, sometimes the surface of the pellet showed patches of different colours. The characterisation of the gas-mixing furnace run products is given in details in Section 3.1.2.

### 2.3 *Scanning electron microscope and electron probe micro analysis*

The Scanning Electron Microscope (SEM) is a common technique used for micro-structural, textural and chemical examination of materials (Reed, 2010). The electron gun of a SEM generates a beam of electrons having energies up to 30 kV which are focused and scanned across the surface of the sample. The highly energetic electrons interact strongly with the atoms composing the specimen, resulting in the generation of different emissions. The secondary electrons (SE) have relatively low energies and are emitted from the near surface region of the sample, thus they provide three dimensional morphological information. The back-scattered electrons (BSE) have much higher energies than the secondary ones, they come from a larger and deeper volume of interaction and their intensity is proportional to the atomic number  $Z$  thus providing information on the chemistry of the sample.

The electron beam also removes electrons from the atomic shells of the atoms which then emit characteristic X-ray lines. In a conventional SEM these X-rays are detected with an Energy Dispersive X-ray Spectrometer (EDXS) and are used to identify phases and perform fast, semi-quantitative chemical analyses.

In order to perform accurate quantitative analysis, it is necessary to collect the X-ray emission lines using a Wavelength Dispersive X-ray Spectrometer (WDXS), carrying out Electron Probe Micro Analysis (EPMA), which is commonly referred to as *microprobe analysis*. The chemical compositions of hibonites were measured with a JEOL JXA 8200 electron probe, fully automated with five WDX spectrometers. The polished samples were coated with about 10 nm of amorphous carbon to avoid charging of the surface and studied at acceleration voltages of 15 kV and probe currents ranging from 15 to 20 nA, measuring 10 s the pre- and post-peak backgrounds and 20 s the peak position. The analytical standards used for the calibration of the energy positions of the analysed elements were:  $\text{CaSiO}_3$  (wollastonite) for Ca,  $\text{Al}_2\text{O}_3$  for Al, MgO for Mg,  $\text{MnTiO}_3$  for Ti, enstatite ( $\text{MgSiO}_3$ ) for Si,  $\text{Pb}_5(\text{VO}_4)_3\text{Cl}$  (vanadinite) for V and metallic iron for Fe.

For each sample 20 to 40 points were measured on different hibonite crystals and averaged. The chemical composition of the synthetic samples are reported in Tables 3.4 and 3.5, whereas those of the natural hibonites analysed in this study are listed in Table 6.2.

#### 2.4 Powder X-ray diffraction

Powder X-ray diffraction (PXRD) is a relatively quick technique that allows obtaining bulk structural information from polyphasic samples (Giacovazzo, 2002). In the present study it has been used to identify the phases present in all the run products recovered from the high-temperature syntheses (Tables 3.2 and 3.3). A small fragment of the recovered pellets was ground using ethanol as lubricant and, once powdered, a silicon internal standard (Si NIST SRM 640c) was added in the proportion of about  $\sim 30\%_{vol}$ . The mixture was homogenised, allowed to dry and then uniformly dispersed onto the surface of a zero-diffraction background Si single crystal sample holder, accurately levelled with the sample stage. Diffraction datasets were collected using a Philips X'Pert Pro diffractometer operating in reflection mode ( $\theta - 2\theta$  configuration) with  $\text{Co}_{K\alpha_1}$  monochromated radiation in the  $2\theta$  range from 6 to  $110^\circ$ , using  $0.03^\circ$  step size,  $1.8^\circ \text{ min}^{-1}$  scan speed and rotating the sample stage at a speed of 1 revolutions per minute (rpm). The diffractometer is equipped with a primary  $\text{Ge}_{(111)}$  monochromator and a Philips X'celerator detector.

The interaction of the sample with the X-rays creates typical cones of diffracted intensities; the opening angle of these cones is related to the interplanar spacings in the crystalline powders according to the law named after Bragg (1913):

$$2d \sin \theta = n\lambda \quad (2.1)$$

where  $d$  is the interplanar spacing,  $\theta$  is the diffraction angle,  $\lambda$  is the wavelength of the X-ray source and  $n$  is an integer.

The intensity of each diffracted beam depends on how the atoms are accommodated into the structure of each phase. The diffraction pattern, *i.e.* an *Intensity vs.  $2\theta$*  plot of the measured diffraction intensities, for a polyphasic and polycrystalline material is the superposition of the diffraction patterns of all the phases present in the mixture. The relative intensities of the diffraction peaks for each phase are proportional to its volume fraction.

In order to obtain the unit cell lattice parameters of the phases present in each run product, Rietveld refinements were performed using the program suite EXPGUI (Toby, 2001) based on the refinement algorithm GSAS (Larson, A. C. and Von Dreele, R. B., 2004). The structural models for hibonite, corundum, Ca-Ti-perovskite and spinel, were taken from Bermanec et al. (1996); Oetzel and Heger (1999); Sasaki et al. (1987); Grimes et al. (1983), respectively. An example of a refined diffraction pattern for the sample gel3-3 is shown in Fig. 2.7 while the unit cell parameters obtained from the Rietveld refinements performed on the diffraction pattern acquired for all the analysed sample are reported in Table 3.6.

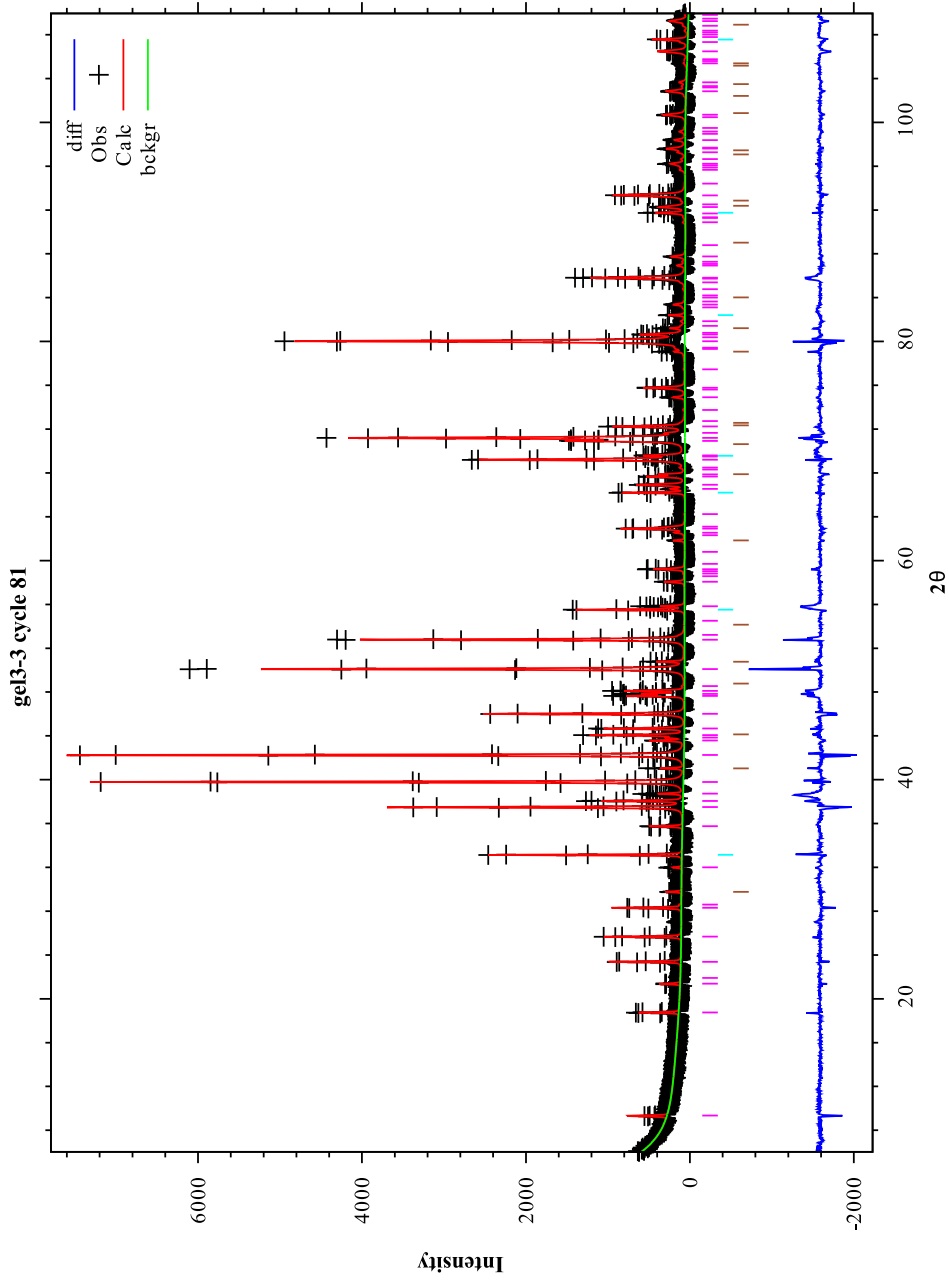


Figure 2.7: Refined diffraction pattern for sample gel3-3 ( $\chi^2 = 6.66$ ). The coloured tick marks correspond to the peaks for the different refined phases: magenta for hibonite, cyan for the Si standard and brown for corundum.

## 2.5 Single crystal X-ray diffraction

Single crystal X-ray diffraction (SCXRD) is a very powerful technique for studying the structure of crystalline materials. It also is based on Bragg's Law (Eq. 2.1) but allows sampling and collecting 3-D diffraction intensities from the whole reciprocal space. This is the main difference with PXRD where all the information are condensed into a 1-D plot. The completeness and the redundancy of the single crystal diffraction datasets is such that even structures containing a large number of independent atoms can be solved (Giacovazzo, 2002).

Hibonite single crystals were chosen for XRD characterisation on the basis of their size, morphology and optical properties (Fig. 2.8).

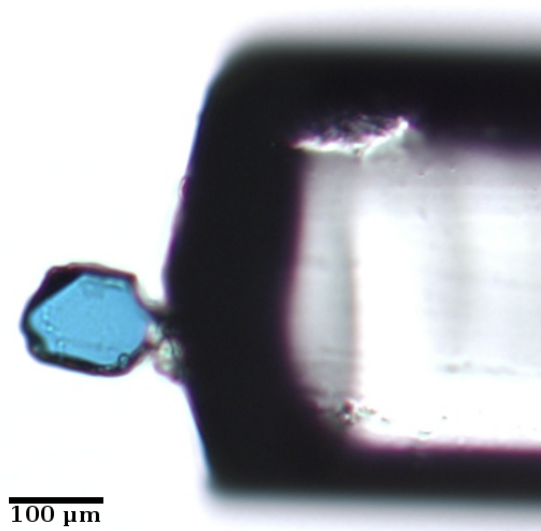


Figure 2.8: Optical transmission image of the single crystal analysed for sample gel6-3. The specimen, glued at the tip of a glass fibre, has the typical platy morphology for hibonite and is free of voids.

Preliminary data sets were collected on a 4-circle  $\kappa$ -geometry Xcalibur diffractometer equipped with CCD detector and monochromatic Mo  $K_{\alpha}$  radiation. The crystals showing strong diffraction intensities were subsequently measured on a Huber SMC9000 4-circle diffractometer equipped with point detector and Mo  $K_{\alpha}$  radiation. The crystals yielding Bragg reflections with Full Width at Half Maximum (FWHM) of  $\omega$  profiles smaller than  $0.12^{\circ}$  were further analysed (Fig. 2.9).

Accurate unit cell parameters were measured on the Huber diffractometer using the 8-position centring procedure (King and Finger, 1979; Angel and Finger, 2010) on a set of selected independent reflections. The measurements and the subsequent least square refinement to calculate the symmetry constrained unit cell parameters were performed with the software SINGLE04 (Angel and Finger, 2010) and are reported in Table 3.7.

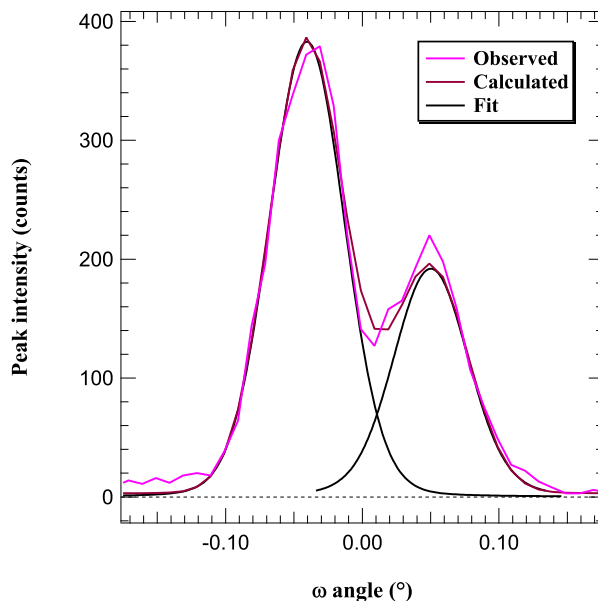


Figure 2.9: X-ray diffraction profile measured in  $\omega$ -scan for the 220 reflection of sample gel6-3. The reflection is centred at  $29.5^\circ 2\theta$  and has an average FWHM of  $0.062(4)^\circ$ . At this high diffraction angle it is possible to completely resolve the contributions from the  $K_{\alpha_1}$  and  $K_{\alpha_2}$  lines of the Mo radiation.

Complete datasets of diffracted intensities for the selected crystals were measured on the Xcalibur diffractometer at room temperature with optimised number of frames collected in  $\omega$ -scan (in one case combined with  $\phi$ -scan) using  $0.5^\circ$  scan width. Data reduction and integration were performed using the CrysAlisPro software (Agilent Technologies, 2012), which also includes the packages used for analytical absorption correction (Clark and Reid, 1995) and empirical multi scan correction ABSPACK (Agilent Technologies, 2012).

The structural refinements were carried out on squared structure factors ( $F_o^2/c$ ) adopting the scattering curves for neutral atoms published on the International Tables for X ray Crystallography (Hahn, 2005) and using the program suites WinGx (Farrugia, 1999) and ShelXle (Hübschle et al., 2011), which are based on the refinement algorithm SHELX (Sheldrick, 2008). All the refinements were performed in the space group  $P6_3/mmc$  (N° 194) assuming a model for pure hibonite end member based on the atomic coordinates proposed by Bermanec et al. (1996). Atomic coordinates and anisotropic displacement factors were refined for all samples, as well as an overall scale factor and a 2-term weighing scheme. The Ti occupancy also was refined as described in Section 3.3.2. Further structural analyses were performed considering the parameters describing distortions of coordination polyhedra, *i.e.* octahedral angle variance (OAV), as defined by Robinson et al. (1971) which were calculated using the software XtalDraw (Downs and Hall-Wallace, 2003).

Data collection and refinements details, refined atomic positions and thermal displacement factors, bond distances and distortion parameters are reported in Tables 3.7, 3.9 and 3.10.

## **2.6 *Transmission electron microscope observation***

The transmission electron microscope (TEM) is a powerful technique that allows performing structural and chemical characterisation at the micro- to nano-scale (Williams and Carter, 1996). A conventional TEM is equipped with an electron gun operating at accelerating voltages up to 300 kV which generates a highly energetic electron beam that is focused using different electromagnetic lenses and transmitted through a thin specimen. After travelling through the sample, the electron beam can be collected as unscattered (the direct beam), elastically scattered as a result of diffraction and inelastically scattered at very low angles. The first two cases are used to generate contrast for imaging while the latter case is relevant for energy electron loss spectroscopy (EELS, Section 2.6.2).

Typical imaging techniques are based on amplitude contrast in which the image is generated by placing an aperture, the objective aperture, in the back focal plane of the objective lens in order to allow passing only the direct beam or one or more diffracted electron beams. In the first case bright field (BF) images are obtained while the latter case corresponds to dark field (DF) imaging. These techniques can be used to visualise microstructural features, imperfection and defects in the observed samples. Examples of BF images are given for synthetic and natural samples in Sections 3.1.2 and 6.1, respectively.

### **2.6.1 *Sample preparation***

The TEM-EELS analysis requires adequately prepared samples, which must be electron transparent. Moreover, since the hibonite samples analysed in this study contain low amount of Ti, the acquisition of EEL spectra must be performed minimising the signal to noise ratio as much as possible. This can be achieved, other than optimising the instrumental parameters and the collection times, having specimens as thin as possible. The sample preparation is therefore a critical step for obtaining high quality, high resolution EELS.

### 2.6.1.1 Argon ion milling

One of the common procedures for TEM sample preparation consists in dispersing a finely ground material on to a Cu grid which sustains a holey amorphous carbon net. This technique, while being very practical and quick, does not allow controlling the thickness of the sample before TEM analysis and could result in specimens which are relatively thick for TEM-EELS investigation. Moreover, the grinding of the sample could produce stress-induced defects. Therefore the argon ion milling technique was adopted since it can provide samples having relatively large areas, free of any contamination and with a final thickness down to less than 100 nm.

The Gatan Duomill precision ion milling system (PIPS) machine available at the Bayerisches Geoinstitut is equipped with two argon ion guns in which a stream of Ar gas is ionised and accelerated with energies up to 7 kV. The Ar<sup>+</sup> beams are focused onto the lower and upper surfaces of the sample, which are eroded as a consequence of the impact with the highly energetic ions. The sample is rotated during the milling process at speeds ranging from 1 to 5 rpm and the angle between the normal to the sample and the direction of the ion beam can be changed independently from 0 to 10° for the two guns.

For all synthetic samples, a fragment of sintered pellet was prepared as double polished thin section less than 30 µm thick, which was glued onto a TEM Mo grid and subsequently thinned with PIPS. The initial thinning was performed with an acceleration voltage of 5 kV, resulting in beams currents from 8 to 12 µA and at a glancing angle of 8°. The thickness of the sample was checked periodically by optical microscopy and after few micrometers of thinning the glancing angles were lowered to 6° and 7° for the upper and the lower gun, respectively. In the final stage of milling, milder ion beams were used (3 kV energy and 4 to 6 µA currents) in order to reduce amorphisation and damage caused by the beam on the sample. Throughout the preparation, the sample stage was rotated at relatively high speed (5 rpm) and the ion beams were slightly defocused with the purpose of obtaining larger uniform thin areas. An example of a specimen after Ar milling preparation is shown in Fig. 2.10.

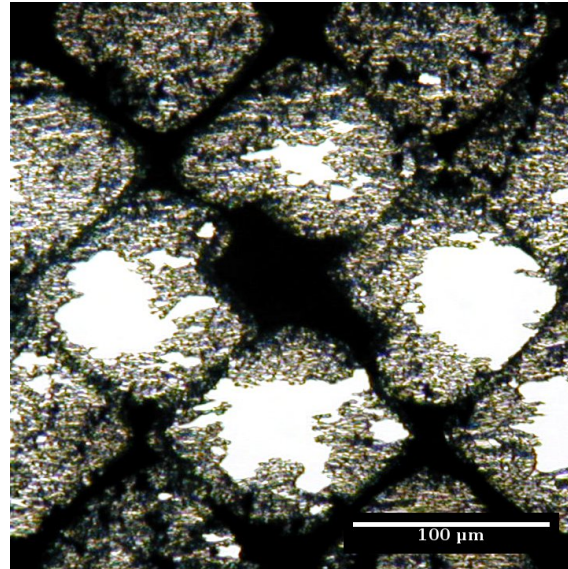


Figure 2.10: Optical transmission image of FIB2S1B sample after Ar ion milling preparation.

#### 2.6.1.2 Focused ion beam

The Focused Ion Beam (FIB) milling is a modern and powerful technique for the preparation of electron transparent thin foils (lamellæ) to be analysed in a TEM (Volkert and Minor, 2007). The lamellæ prepared with this technique are not quite as thin as the samples obtained with the PIPS, but the great advantage is that the sample preparation is combined with SEM observation so it is very site-specific and just a small volume of the sample is lost due to the milling, as illustrated in Fig. 2.11.

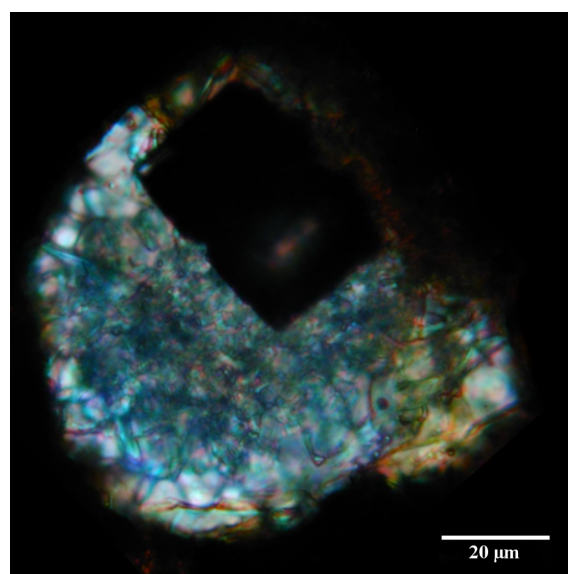


Figure 2.11: Optical transmission image of Acfer 182-3 CAI after FIB preparation. The pit excavated during the sample preparation measures about  $15 \times 30 \times 15 \mu\text{m}$ .

The FIB machine is equipped with a gallium ion source which is heated up to melting point in order to produce liquid Ga flowing to the tip of a tungsten needle. At the extremity of the needle a strong electrical field is capable of ionising the Ga ions which are subsequently extracted and accelerated with energies up to 30 kV.

The  $\text{Ga}^+$  beam is focused and targeted onto the surface of the sample. The transfer of energy due to the collision of the metal ion with the target material results in the latter being eroded while emitting secondary electrons, which are collected for imaging.

The procedure for the preparation of an electron transparent lamella starts with the identification of the selected grain by normal SEM observation. Once identified, the area is protected by the deposition of a 2 to 3  $\mu\text{m}$  platinum strip. The Pt layering is obtained by streaming gaseous  $\text{MeCpPtMe}_3$  (methylcyclopentadienyl-trimethyl-platinum) onto the surface of the sample while scanning with the ion beam, resulting in the decomposition of the organics and deposition of Pt (Fig. 2.12-a). An ion beam with currents from 7 to 15 nA is used then to cut a trench on both sides of the protective Pt strip. The two sides of the forming lamella are then polished in-situ down to  $\sim 1 \mu\text{m}$  using progressively lower beam currents, down to 3 to 5 nA (Fig. 2.12-b).

At this point the lamella is partially cut free and a very thin tungsten tip connected to a micro-manipulator is inserted into the chamber, brought to contact with the sample foil and fixed to it by deposition of Pt. The lamella can now be cut completely free, lifted off the surface of the sample and attached to a Cu-TEM grid by depositing Pt (Fig. 2.12-c).

Afterwards the lamella is thinned down to electron transparency with acceleration voltages from 30 to 5 kV and ion probe currents between 500 to 16 pA. The final results are  $\sim 10 \times 10 \times 0.1 \mu\text{m}$  lamellæ ready for TEM observation (Fig. 2.12-d).

In this study this technique was used to prepare one lamella from each one of the CAIs listed in Table 6.1 using a FEI Quanta 3D Field Emission Gun FIB installed at the Institut für Geowissenschaften, Friedrich-Schiller-Universität in Jena.

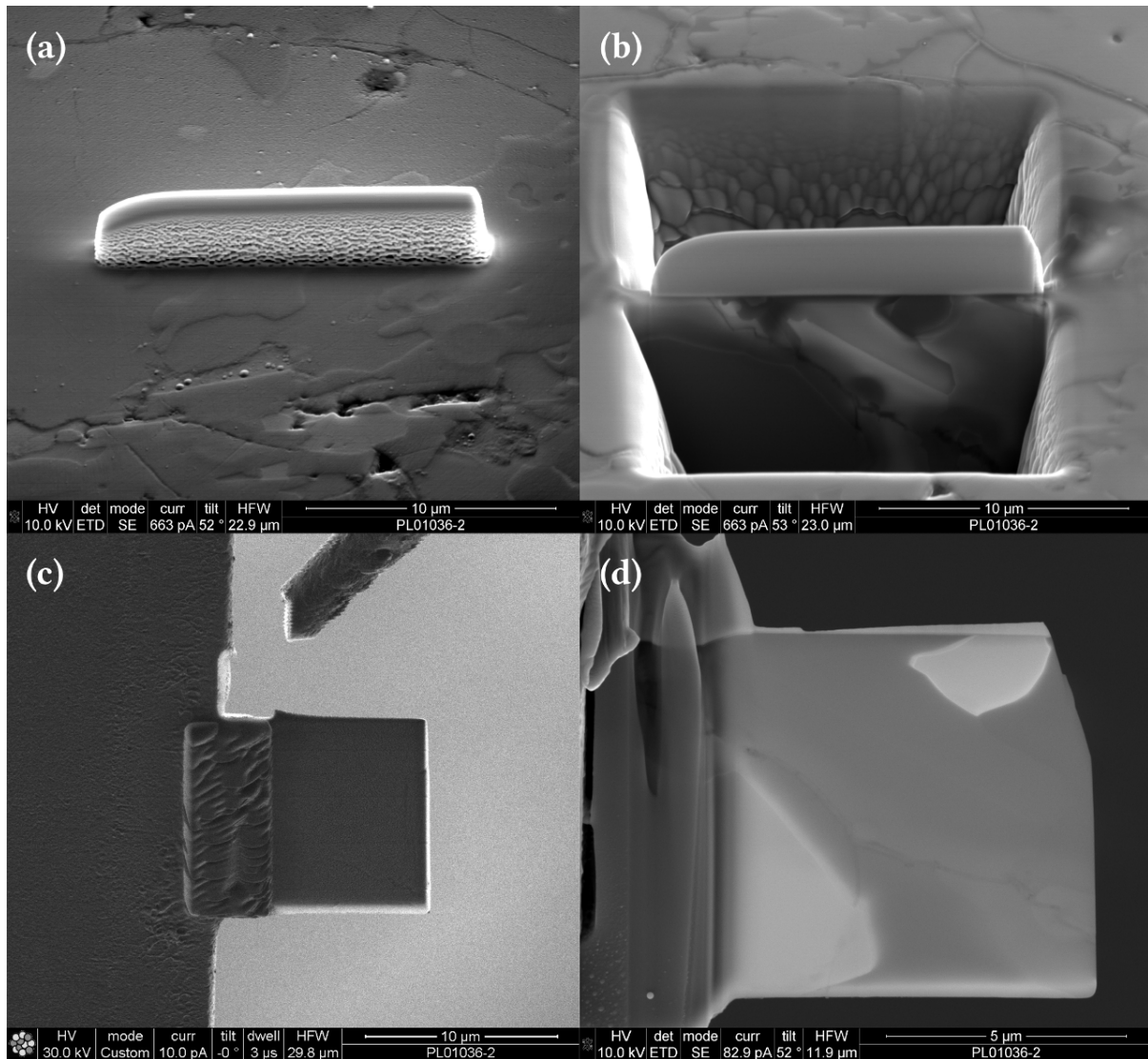


Figure 2.12: SE images of some of the stages for the preparation of a TEM lamella from the sample Acfer 182-2. (a) The hibonite grain selected for analysis is protected by the deposition of a Pt strip. (b) Lateral view of the lamella after trench cutting and in-situ thinning. (c) The lamella as seen after lift-out and welding on to the Cu grid. (d) Final polished sample.

### 2.6.2 Energy electron loss spectroscopy

Energy Electron Loss Spectroscopy (EELS) is an analytic technique which can provide chemical information about the coordination environment, the type of bonding and the valence state of the analysed atomic species (Egerton, 1996).

As already mentioned, EELS is based on the inelastic scattering of the electron transmitted through the specimen. This is, theoretically, a single-particle process in which, due to the interaction of the electron beam with the thin specimen, one of the electrons occupying the inner atomic shells, *i.e.* the valence band, receives enough energy to be transferred to the conduction band, above the Fermi level ( $E_f$ ). The Fermi level is the value of energy of the highest occupied molecular orbital, representing then the separation between occupied and unoccupied states. For semiconductors and insulators the  $E_f$  is located between the fully filled valence band and the empty conduction band, while in metals, where the two bands overlap, it corresponds to some energy level in the conduction band (Egerton, 1996).

The process associated with EEL corresponds to an actual atomic ionisation in which one of the electrons from the inner shells receives enough energy to be ejected out of it; the critical amount of energy required for the transition to happen corresponds to the ionisation energy  $E_c$ ; this makes EELS a very element-sensitive analytic techniques. Most importantly, given that the ejected electron has a very high probability to fill empty states in the valence band, whose energies are extremely sensitive to changes in bonding, coordination environment or valence state, it can provide a great amount of information about the electronic and atomic structure of analysed species (Williams and Carter, 1996).

In case of light elements and most of the transition metals, the electronic transitions originate from the  $K, L, M$  and  $N$  shells, corresponding to the energy levels associated with the principal quantum number  $n = 0, 1, 2$  and  $3$ , respectively. The different EEL edges are then differentiated according to the angular momentum quantum number  $l = 0, 1, 2, 3$ , representing the different atomic orbitals  $s, p, d, f$  from where the ejected electron comes (Fig. 2.13). After the electron core-loss with corresponding excitation, the ionised atom typically relaxes by means of X-ray or Auger electron emission.

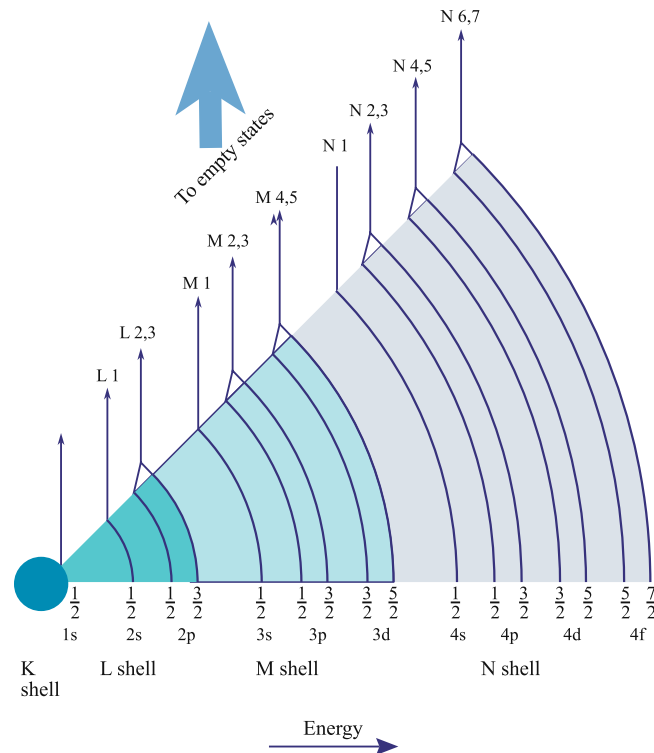


Figure 2.13: Range of possible edges in EELS due to inner shell ionisations and associated nomenclature, modified after Williams and Carter (1996).

The typical EEL spectrum can be divided into two parts, the low- and the high-loss energy regions; the boundary between these two regions is arbitrarily and loosely collocated at 50 eV. In the high-loss region are recorded the processes described above, while the low-loss region comprises the zero-loss and the plasmon peaks (Fig. 2.14).

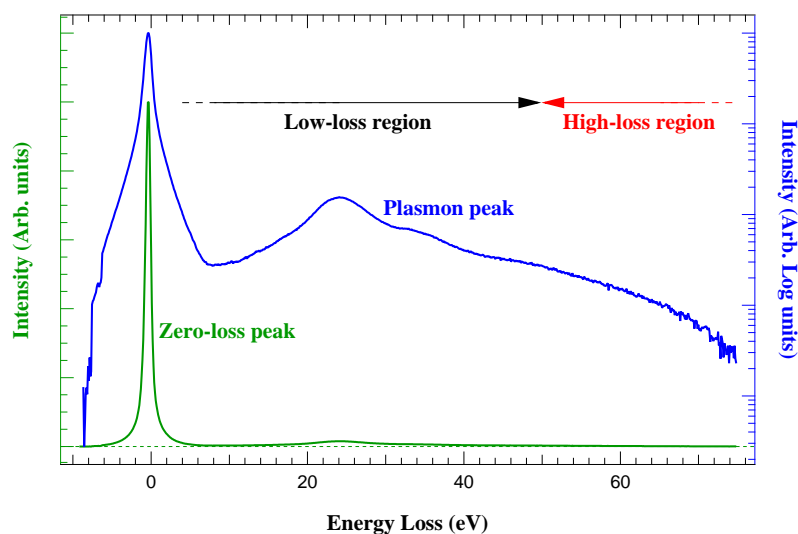


Figure 2.14: Low-loss spectrum of sample gel4-2 plotted with linear intensity scale on the left axis (green) and with logarithmic scale on the right axis (blue) in order to better visualise the zero-loss peak and the plasmon peak, respectively. The boundary between low- and high-loss energy regions is indicated.

The zero-loss peak originates from electrons that have not lost energy after passing through the sample, *i.e.* the direct beam having energy  $E_0$ . The full width at half maximum of the zero loss peak corresponds to the resolution of the measurement and depends mostly on instrumental factors.

The plasmons are collective excitations of quasi-free electrons which oscillate longitudinally in wave-like form. They have a lifetime of  $\sim 10^{-15}$  s and they are localised to areas smaller than 10 nm; their decay results in the emission of either photons or phonons (lattice vibrations equivalent to heating of the sample). The energy loss associated with the production of plasmons is given by the following equation:

$$E_p = \frac{h}{2\pi} \omega_p = \frac{h}{2\pi} \left( \frac{ne^2}{\epsilon_0 m} \right)^{\frac{1}{2}} \quad (2.2)$$

where  $h$  is Planck's constant,  $\omega_p$  is the frequency of the plasmon,  $n$  is the free-electron density,  $e$  and  $m$  are electron's charge and mass,  $\epsilon_0$  is the electrical permittivity in vacuum (Williams and Carter, 1996). The intensity ratio between the plasmon peak ( $I_p$ ) and the zero loss peak ( $I_0$ ) is directly related to the thickness of the specimen  $t$  through the following equation:

$$t = \lambda_p \frac{I_p}{I_0} \quad (2.3)$$

where  $\lambda_p$  is the plasmon mean free path, having typical values of 100 nm in the operative conditions of a TEM.

Energy electron loss spectra were measured from both meteoritic and synthetic hibonites using a field emission gun (FEG) Philips CM20 scanning TEM operating at 200 kV. The microscope is equipped with a Gatan PEELS 666 parallel electron spectrometer having a 1024 channels photo-diode array detector operated at energy dispersion of 0.05, 0.1, 0.2 and 0.3 eV per channel, which correspond to a measurable energy loss range of about 50, 100, 205 and 305 eV, respectively. The measurements were performed at maximum acceleration voltage, using relatively large illumination  $\alpha$  of the electron beam and a 2 mm entrance aperture before the EELS detector, corresponding to 3 mrad collection semi-angle  $\beta$  (Fig.2.15); the acquisition was done in diffraction mode, away from any zone-axis in order to obtain orientation-independent spectra.

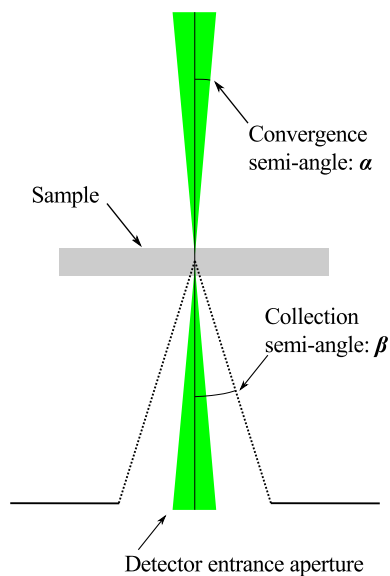


Figure 2.15: Schematic representation of the geometrical conditions for the EELS measurements.

The resulting EEL spectra were corrected for dark current and channel-to-channel gain variation; a typical example of Ti core-loss raw spectrum is shown in Fig. 2.16 (green curve). The actual core-loss signal is superimposed to a large background due to plural scattering events; this background can be described as a negative exponential:

$$I_{bkg} = Ae^{-r} \quad (2.4)$$

which can be modelled and subtracted from the spectrum. The parameters  $A$  and  $r$  are fitted after selecting a  $\sim 5$  eV energy region before the edge of the spectrum in order to extrapolate the background to higher energy losses. The quality of the fit is evaluated ensuring that the extrapolated background do not crosses the spectrum in the post-edge region. An example of fitted background and the resulting spectrum are reported in Fig. 2.16 as magenta and blue curves, respectively.

Despite the fact that EELS is treated as a single-scattering process, in real cases, multiple scattering events occur due both to transmitted electrons interacting with more than one atom and to excited electrons generating more core-loss events instead of being promoted to the conduction band. This results in an experimental spectrum which is the convolution between an ideal single-scattering edge and the plasmon peak, or low-loss spectrum (Williams and Carter, 1996). This gives rise to broadening of the spectrum, which can be removed by applying a plural-scattering deconvolution technique such as the Fourier-ratio method, of which mathematical details are given by Egerton (1996). It has to be noted that, while

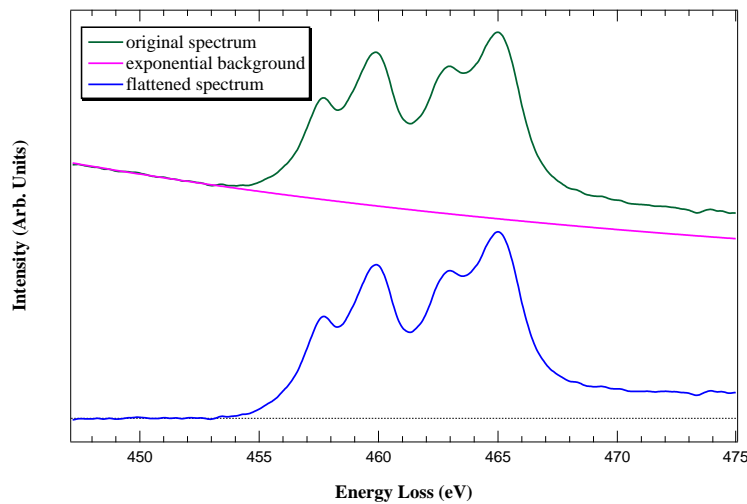


Figure 2.16: Example for the subtraction of the exponential background from the raw spectrum of gel6-3 sample.

processing all the spectra measured in this study, the deconvolution processes have been forced to assume the same FWHM for the zero-loss peaks in order to eliminate differences in the width of the spectra due to the Fourier transformation of EELS.

An example of Ti core-loss spectrum of hibonite after deconvolution is reported as brown curve in Fig. 2.17. As it can be noted, the baseline at the two ends of the spectrum has different heights, this is due to transition to unoccupied continuum states and can be removed adopting the double-arctangent function proposed by Stoyanov et al. (2007):

$$f(\Delta E) = \frac{h_2 - h_1}{2\pi} \left[ \arctan \left( \frac{\pi}{2} (\Delta E - 457.5) \right) + \frac{\pi}{2} \right] + \frac{h_2 - h_1}{2\pi} \left[ \arctan \left( \frac{\pi}{2} (\Delta E - 463.0) \right) + \frac{\pi}{2} \right] \quad (2.5)$$

where  $h_1$  and  $h_2$  are the heights of the baseline before and after the core-loss edge, respectively. An example of double-arctan function subtraction is shown in Fig. 2.17. The exponential background subtraction, the Fourier-ratio deconvolution and the final double-arctan background elimination were performed with the software EELSA, written in Matlab® language by Prescher (2011).

The final EEL spectrum obtained after these procedures (black curve in Fig. 2.17) represents the Ti  $L_{2,3}$  edge for hibonite, showing the two so called *white lines*  $L_3$  and  $L_2$ , which are described in details in Section 4.1 and 4.2.2.

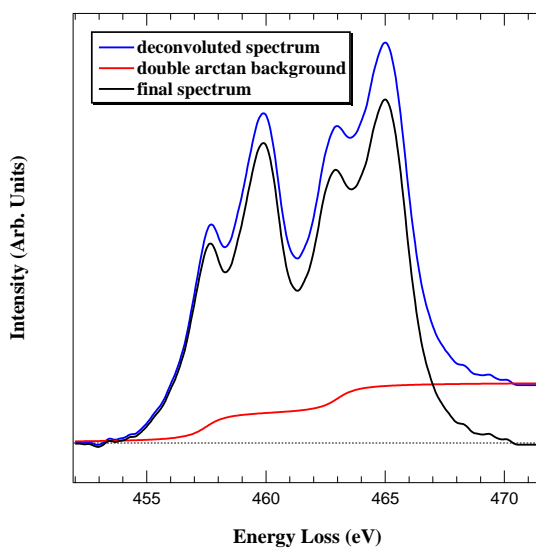


Figure 2.17: Example of the subtraction of the double arctangent background from the deconvoluted spectrum of gel6-3 sample.

## 2.7 Optical absorption spectroscopy

Optical spectroscopy based on the absorption of ultraviolet/visible (UV/Vis) light is a technique that allows obtaining information on the electronic structure and the coordination environment of transition metals.

When light in the range of UV (from 190 to 380 nm) and visible (from 380 to 750 nm) is shone through a transparent sample, part of the radiation can be absorbed and, if the absorbing centre is a transition metal, the process typically involves an electronic transition affecting the electrons occupying the  $d$  orbitals (Wildner et al., 2004). The energy  $E$  involved in the transition is quantised and expressed by Planck's relation:

$$E = \frac{hc}{\lambda} = hc\bar{\lambda} \quad (2.6)$$

where  $h$  is Planck's constant,  $c$  the speed of light in vacuum,  $\lambda$  and  $\bar{\lambda} = 1/\lambda$  are the wavelength and the wavenumber associated with the transition, respectively (Planck, 1901).

In the general description of absorption spectroscopy, a white light is monochromatised and then split into two identical optical paths, one of which is used as reference while the other passes through the specimen which needs to be analysed. It is assumed that the light passing through the sample is either absorbed, causing an electronic transition, or it is transmitted unaltered, while contributions from reflection or scattering are negligible. The amount of radiation that is absorbed in this process can be described by different quantities, one of which

is called *transmittance* ( $T$ ) and it is expressed as a fraction of the absorbed light:

$$T = \frac{I}{I_0} \quad (2.7)$$

where  $I$  and  $I_0$  are the intensities of the transmitted and the reference beams, respectively. Another widely used unit of measure for describing the absorption peak's intensity is the *absorbance* ( $A$ ), which is defined as the negative logarithm of  $T$  and it is used in Lambert-Beer's absorption law:

$$A = -\log_{10} \frac{I}{I_0} = \epsilon cd \quad (2.8)$$

where  $c$  is the molarity of the analysed species,  $d$  is the thickness of the specimens reported in cm and  $\epsilon$  is defined as the (linear) *molar absorption coefficient* (or *molar extinction coefficient*). This quantity is expressed in  $\text{l mol}^{-1} \text{cm}^{-1}$ , and is a characteristic property of the studied material that can be dependent on the orientation of the sample. When light enters into a material, it splits into two orthogonally vibrating components, which are called *E-wave* and *O-wave*. The velocity at which the E- and the O-waves propagate in the sample are indicated as  $v_E$  and  $v_O$ . When the E- and the O-waves exit the crystal, they recombine with a phase shift (retardation) which is a function of the difference in their velocities. The substances through which the E- and O-waves travel with identical velocities ( $v_E=v_O$ ) are defined as optically isotropic; these are generally gasses, amorphous phases or cubic materials and their  $\epsilon$  is the same measured in all directions. In the case of optically anisotropic substances, in which light and its components propagate at different velocities along different direction ( $v_E < v_O$  or  $v_E > v_O$ ), the molar absorption coefficients measured along different directions have distinct values. Optically anisotropic substances are further classified on the basis of the crystal system to which their structure belongs. Materials crystallising in hexagonal, trigonal and tetragonal space groups are defined as optically uniaxial. In these materials the O-wave propagates at the same velocity in all directions while the E-wave has either the highest or the lowest velocity in the direction normal to the crystallographic axis  $c$ ; the so called optical isotropy is achieved when the E-wave travels parallel to  $c$  thus having  $v_E=v_O$  (Raith et al., 2012).

Hibonite crystallises in an hexagonal space group ( $P6_3/mmc$ ) thus it belongs to the group of uniaxial materials. The best condition to measure optical absorption spectra in hibonite therefore, is when the light beam travels across the crystal perpendicularly to the  $c$  axis (defined as the optical axis) while having a direction of polarisation  $E$  parallel to it. To achieve this condition the  $c$  axis of the hibonite crystal must be laying parallel to the glass slide and pointing to the same direction of the selected polarising filter.

In the present study the measurements were performed on a Fourier Transform (FT) Bruker IFS 120 HR high-resolution spectrometer coupled with a Bruker IR microscope. In this configuration a non-monochromated beam from a tungsten source is modulated using a Michelson interferometer equipped with a quartz beam splitter. When the modulated beam passes through a double polished thin section of the sample of interest, it generates an interferogram which is collected with a diode array. The absorption spectrum is a plot of the Absorbance intensity versus the energy of the incident monochromatic beam, which is conveniently expressed in wavenumbers, having the dimension of  $\text{cm}^{-1}$  (Wildner et al., 2004). It is obtained after Fourier transformation of the interferogram and after subtraction of a background spectrum measured through the glass slide and the binding glue used to fix the thin section of the specimens. The spectrometer is equipped with a 15x objective lens and a set of apertures with diameters of 0.3, 0.45 and 0.6 mm, which allow isolating and measuring circular sample's area 20, 30 and 40  $\mu\text{m}$  wide, respectively. Moreover, in order to reduce the contribution to the signal generated from spurious radiation, the samples were covered with a copper foil having a 100  $\mu\text{m}$  hole placed in correspondence of the chosen crystal. The measurements were performed in the range from 8000 to 25000  $\text{cm}^{-1}$ , corresponding to a wavelength range from 1250 to 400 nm, accumulating up to 8000 scans per spectrum.

The thickness of the thin sections, being a very sensible parameter, were accurately measured using a 3D Nanofocus  $\mu\text{Surf}$  custom confocal microscope, equipped with a monochromatic LED source ( $\lambda = 505 \text{ nm}$ ) and a megapixel CCD camera, using a 50x objective lens. This technique is described in detail by Marcilly et al. (1970); Wilson and Sheppard (1984); an example of how the thickness profile was measured from glass slide to glass slide across a thin section is illustrated in Fig. 2.18.

The orientation of hibonite crystals present in the thin sections were determined observing the extinction of polarised light on a petrographic microscope, utilising the conoscopy technique, and on the sample stage of the spectrometer (Raith et al., 2012).

Moreover, in order to confirm the accuracy of the crystal orientation by means of optical methods, the samples also were characterised with electron back-scatter diffraction (EBSD) in a Zeiss Gemini 1530 SEM equipped with a Nordlys2 EBSD detector controlled by the HKL CHANNEL5 software suite from Oxford Instruments.

This technique, which has been described in details by Adams et al. (1993) and Prior et al.

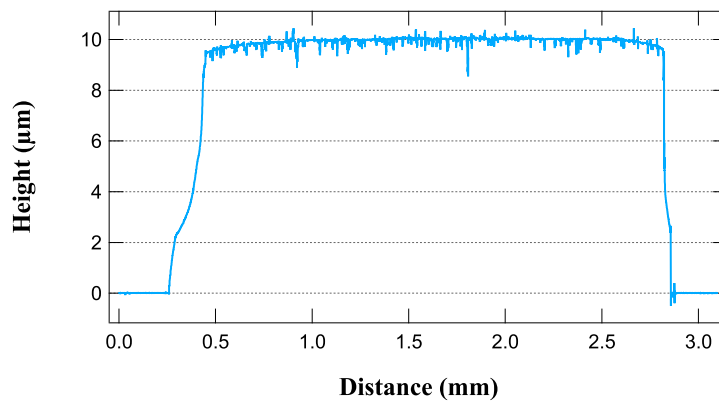


Figure 2.18: Thickness profile for sample gel4-3 measured by means of confocal microscopy.

(1999), allows determining the exact orientation of a crystal by measuring its crystallographic orientation matrix. The BSE generated in a SEM by the interaction of the sample with the electron beam, other than being used for Z-contrast imaging, can also provide a wealth of crystallographic information about the point from which they originate. These electrons are elastically scattered by the lattice planes of the sample's crystalline structure and they have intensities which are function of the scattering angle, according to the Bragg's law (Eq. 2.1). Each lattice plane generates two cones of diffracted electrons that, given the low scattering angle for highly energetic electron, have opening angles close to  $180^\circ$ . When imaged on the EBSD detector, the cones generated by the different lattice planes create a network of bands known as *Kikuchi lines*, which intercept each other in correspondence of *zone axes* (Nishikawa and Kikuchi, 1928). For each crystal individuated by means of conoscopy, several EBSD images were collected from a single point and averaged prior to manual evaluation, which consisted in individuating and marking on the EBSD image several Kikuchi lines. These lines represent the observed diffracted intensities that were matched against a simulated pattern which was calculated from the structural model for hibonite. This allowed obtaining the orientation matrix for the analysed crystal, only those with the *c* axis deviating less than  $5^\circ$  from the direction parallel to the glass slide were taken into further consideration for the UV/Vis measurements.

## *Part II*

### *Characterisation of synthetic samples*

—

### *Results & Discussion*

## 3 *Chemistry and structure of synthetic hibonites*

The hibonite samples synthesised according to the methods described in Section 2.2 were characterised by means of petrographic microscope, SEM, microprobe, TEM. Phase identification and unit cell parameters of all hibonite samples were obtained by means of powder X-ray diffraction (PXRD); moreover, for those runs providing large crystal of hibonite single crystal X-ray diffraction (SCXRD) was used in order to determine the structural variations associated with Ti and Mg substitution.

### 3.1 *Microscopic observation on synthetic hibonites*

#### 3.1.1 *Piston-cylinder run products*

Numerous experiments were performed with the piston-cylinder apparatus in order to explore the possibility of growing large single crystals of hibonite (Table 3.1).

Typical piston-cylinder run products consisted of well sintered samples mostly containing hibonite with crystals having a maximum size of up to 30  $\mu\text{m}$ . An example of piston-cylinder run product is reported in Fig. 3.1-a, showing the back-scattered electron (BSE) image of sample HBMT1\_pc4, which is formed by finely intergrown micrometer-sized hibonite platelets and larger corundum crystals.

In order to attempt enhancing crystal growth, PbO was used as a flux (Gasparik, 1984) in two synthetic runs, HB-MT5\_pc5 and HB-MT1\_pc1. The recovered samples were mostly composed by relatively large corundum crystals surrounded by a Pb-rich glass (Fig. 3.1-b). Hibonite has been observed in these samples mostly at the interface between corundum crystals and the Pb-rich glass. Since hibonite melts incongruently (Chatterjee and Zhmoidin, 1972), these observations suggest that the flux caused a dramatic decrease in the melting point, so that most of the starting material consisting of hibonite melted and subsequently crystallised as corundum and a Ti-Mg-enriched liquid; hibonite formed as a reaction product between these freshly formed corundum and liquid phase.

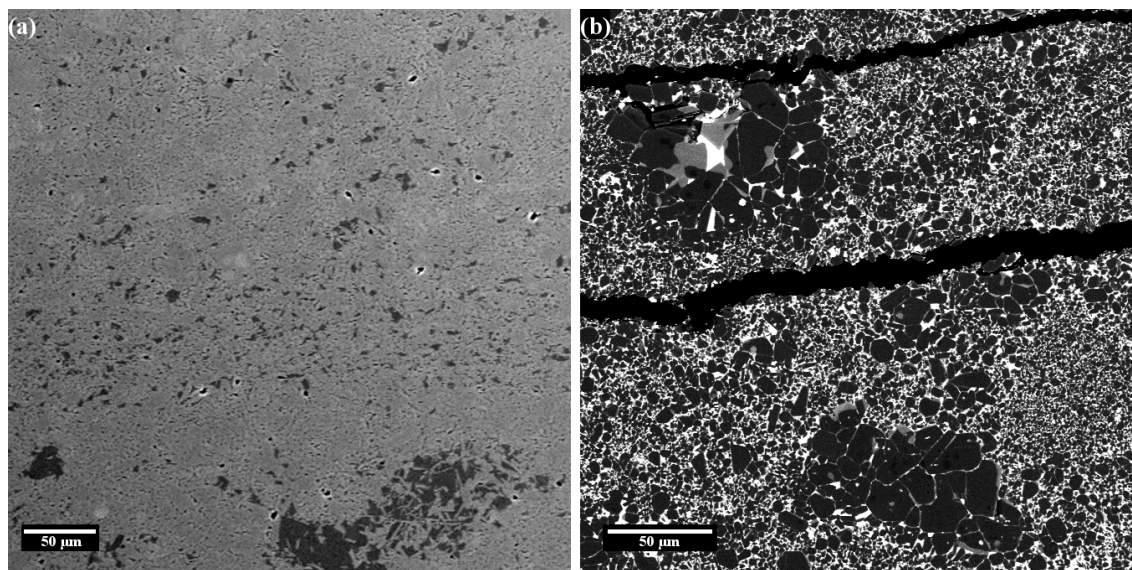


Figure 3.1: BSE image of the run product for the piston-cylinder experiments HBMT1\_pc4 (a) and HBMT5\_pc5 (a). The light grey phase is hibonite and the darker crystals are corundum while the white phase in the right-side image is a Pb-rich glass.

Another common flux which has been tested in some of the piston-cylinder runs is water, which has been introduced as starting material under different forms. In one experiment, bruc\_pc1, brucite ( $\text{Mg}(\text{OH})_2$ ) was used instead of MgO in the starting material. This substitution is equivalent to adding one mole of water per mole of Mg. Unfortunately, also in this run product, corundum was the dominant phase, occupying more than half of the volume of the Pt capsule, and hibonite was formed in the form of equiaxed grains up to 30 μm in size (Fig. 3.2).

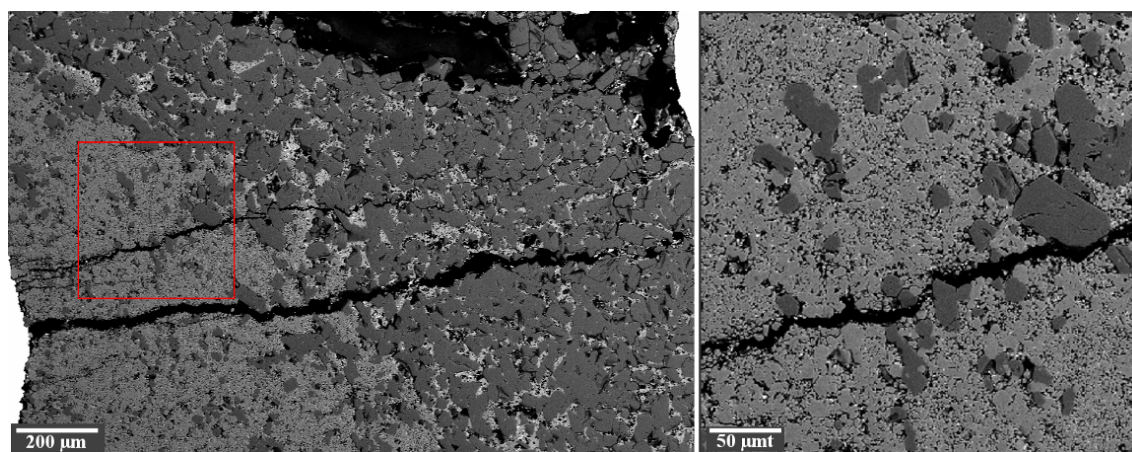


Figure 3.2: BSE image of the run product for the piston-cylinder experiment bruc\_pc1 (left). The light grey phase is hibonite, the darker crystals are corundum and in white is the Pt capsule. The image on the left shows the central part of the Pt capsule while the image on the right is the magnification of the area indicated by the red square.

Only one experiment, HBMT5\_pc3, yielded large hibonite single crystals. The polycrystalline sample HBMT5 with the addition of water in the form of moisture (Table 3.1) was used as starting material. The synthesis was performed at 15 kbar and 1450 °C for 12 h; then, due to a problem with the furnace, the thermal controller increased the amount of power to ~20 % more than the initial value, corresponding to approximately 2000 °C, if a linear dependence of power on temperature is assumed. After about 90 min at such conditions, the assembly was quenched. The recovery of the Pt capsule showed that during such unusual experiment, a part of the sample was lost due to melting of the capsule. In the remaining part, hibonite single crystals up to 200 µm in size crystallised together with small grains of corundum and Ca-Ti-perovskite occupying the interstitial space between the grains of the main phase (Fig. 3.3). The hibonite crystals have platy morphology and blue colour due to the reducing environment controlled by the graphite heater. The oxygen fugacity for this synthesis can be estimated to have varied between  $\log f_{\text{O}_2} = -7.6$  and  $\log f_{\text{O}_2} = -4.9$  during the temperature step from 1450 °C to 2000 °C (Jakobsson and Oskarsson, 1994; Médard et al., 2008). Compared to the Iron Wüstite (IW) buffer (Frost, 1991), these oxygen fugacity conditions at 15 kbar correspond to IW+1 at 1450 °C and IW at 2000 °C, within uncertainties, estimated to be about  $\pm 0.3$  log units (Médard et al., 2008).

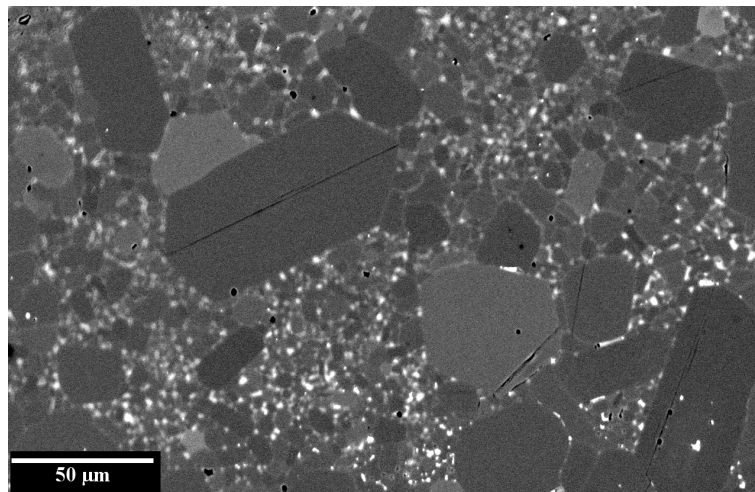


Figure 3.3: BSE image of the run product for the piston-cylinder experiment HBMT5\_pc3. The large grey crystals are hibonite, the small, darker grains are corundum and the white phase is Ca-Ti-perovskite.

Table 3.1: Experimental details of piston-cylinder runs.

Run name	Starting material	Assembly	P (kbar)	T (°C)	time (h)	$fO_2$ (log units)	Run products <sup>#</sup>
HB1_pc1	HB1, 2.55% <sup>wt</sup> H <sub>2</sub> O	WG	15	1450	24	-6.9	hib (<10 µm) + cor
hib1_pc2	HB1_pc2, dry	WG	30	1450	4	-5.8	hib (<10 µm)
hib1_pc3	HB1_pc3, dry	WG	30	1500	4	-5.5	hib (<10 µm) + cor + pv
hib1_pc4	HB-MT1, dry	SH	15	1450	12	-6.9	hib (<10 µm) + cor
				1700	1.5	-5.4	
HB-MT5_pc0 <sup>†</sup>	HB-MT5, dry	WG	15	1450	3	-6.9	hib (<10 µm)
HB-MT5_pc1 <sup>†</sup>	HB-MT5, moist	WG	15	~1450	24	-6.9	hib (<10 µm) + cor
HB-MT5_pc2	HB-MT5, 0.07% <sup>wt</sup> H <sub>2</sub> O	WG	7	1450	9	-7.3	cor + m
HB-MT5_pc3 <sup>§</sup>	HB-MT5, moist	SH	15	1450	12	-7.6	hib (<200 µm) + cor + pv
				~2000	1.5	-4.9	
HB-MT5_pc4	HB-MT5, dry	SH	15	1550	6	-6.2	hib (<20 µm) + cor + pv
HB-MT5_pc5	HB-MT5, 10% <sup>mol</sup> PbO	SH	15	1400	6	-7.2	hib (<20 µm) + cor + pv + m
HB-MT1_pc1	HB-MT1, 20% <sup>mol</sup> PbO	SH	15	1400	6	-7.2	hib (<10 µm) + cor + pv + m
HB-MT1_pc2	HB-MT1_pc2, dry	SH	15	1600	4	-6.0	hib (<30 µm) + cor + sp
HB-MT1_pc3	HB-MT1, 9.5% <sup>wt</sup> H <sub>2</sub> O	SH	15	1600	4	-6.0	hib (<10 µm) + cor
HB-MT1_pc4	HB-MT1, dry	SH	15	1500	12	-6.6	hib (<30 µm) + cor
HB-MT1_pc5	HB-MT1, dry	SH	15	1500	6	-6.0	hib (<10 µm) + cor
				1500	1	-6.6	
HB-MT1_pc6	HB-MT1, dry	SH	15	1500	4	-6.6	hib (<10 µm) + cor
				1700	2	-5.4	
bruc_pc1	bruc	WG	15	1500	8	-6.6	hib (<30 µm) + cor + pv
MgTi_pc1	Mg_Ti, dry	SH	15	1450	13	-6.9	hib (<10 µm) + cor + pv

<sup>†</sup>3/4" assembly; <sup>‡</sup>no T/C, output power set according to a calibration curve; <sup>§</sup>T/C failed after 12 h, successful single crystals growth;

<sup>#</sup>observed with SEM: hib = hibonite (grain size given in brackets), cor = corundum, pv = Ca-Ti-perovskite, sp = spinel, m = melt.

### 3.1.2 Gas-mixing furnace run products

The experimental runs aimed at obtaining hibonite at room pressure from oxide precursors are listed in Table 3.2. Careful SEM analyses of all these samples revealed that hibonite crystals were recovered with sizes of only 20 to 30  $\mu\text{m}$ , which are not suitable for collecting intensity data with an in-house single crystal X-ray diffractometer. Moreover, such run products presented a large chemical variation (Section 3.2).

In order to improve the overall homogeneity of hibonite samples, the sol-gel technique has been adopted in numerous synthesis (Table 3.3). In most cases, after sintering at very high temperature (1550  $^{\circ}\text{C}$ ) the sol-gel precursors led to the formation of single crystals of hibonite up to 100  $\mu\text{m}$  in size. The crystals showed platy-like habit and, in the case of samples prepared under reducing conditions, a nice blue colour. A transmitted polarised light image of sample gel3 synthesised at  $\log f_{\text{O}_2} = -11$  and a BSE photograph of sample gel6 synthesised in air are reported as examples in Figures 3.4-a and 3.4-b, respectively.

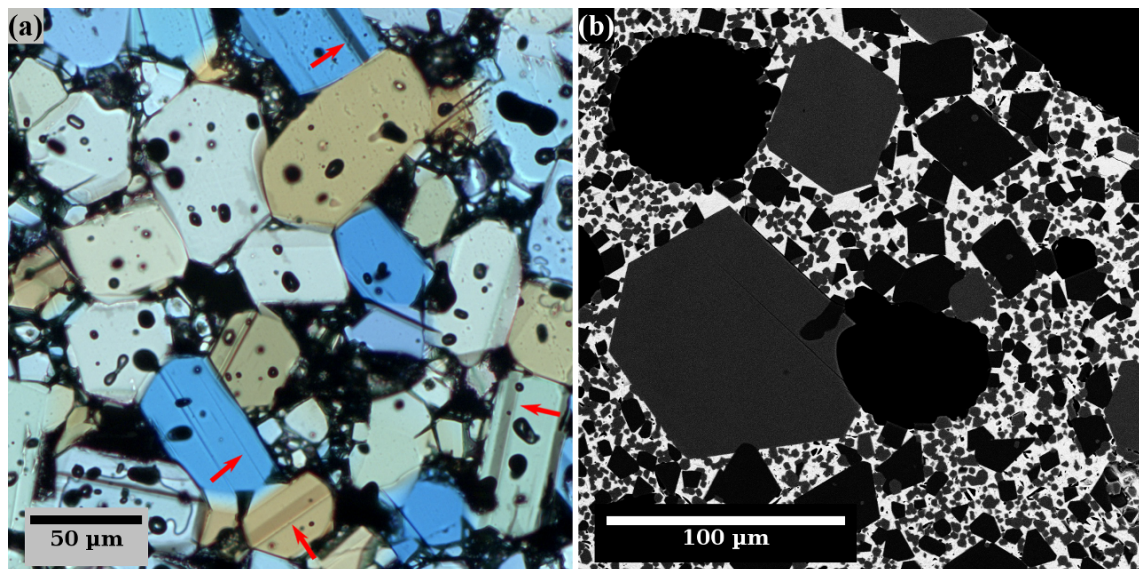


Figure 3.4: Typical run products obtained from sol-gel precursors. (a) Transmitted light image of the sample gel3-3b acquired with nearly parallel polarisers and the lambda plate inserted in order to enhance orientation contrast; the red arrows indicate polysynthetic twins. The round-shaped voids present on hibonite grains are discussed in the text below. (b) BSE image of the sample gel6-1; the grey crystals are hibonite, the dark grains are corundum and the white phase is Ca-Ti-perovskite.

The large hibonite crystals obtained with sol-gel precursors show homogeneous composition with absence of zoning, as illustrated, for example, in the BSE image of sample gel6-1 (Fig. 3.4-b). Optical microscope observations on hibonite samples revealed that, in some cases, they are characterised by the presence of round-shaped voids (Fig. 3.4-a), which are likely associated with the utilisation of sol-gel precursors. In fact, firing the xerogel up to 600  $^{\circ}\text{C}$  produces the

amorphous oxidic material used as sol-gel precursor, which shows a high degree of porosity. Compressing this material into pellets is not sufficient to completely remove the porosity, which is then retained in the final sintered product. Moreover, the differential thermal analysis (DTA) performed by Cinibulk (1998) on sol-gel precursors similar to those of this study shows the presence of an exothermic peak ranging from 785 to 925 °C. This peak corresponds to the transformation from  $\gamma$ - to  $\alpha$ -alumina, which is associated with a volume shrinkage. In order to guarantee that all the chemical and structural transformation, from the starting material to hibonite crystals, would occur under controlled oxygen fugacities, it was chosen to introduce the sol-gel precursor into the gas-mixing furnace prior to the  $\gamma$ - to  $\alpha$ -Al<sub>2</sub>O<sub>3</sub> transformation, resulting in some porosity in the final products for these syntheses. As illustrated in Fig. 2.8, particular care has been taken in order to choose only voids-free hibonite single crystals for X-ray diffraction and spectroscopic analyses.

The transmitted light image of sample gel3-3b also shows the presence of streaks running parallel to the (100) direction of the hibonite grains, which are marked by red arrows in Fig. 3.4-a. This indicates the presence of twinned crystals, "*an aggregate in which different domains are joined together according to a specific symmetry operation, i.e. the twin law*" (Giacovazzo, 2002). The streaking observed in hibonite crystals is typical of *polysynthetic* (or *lamellar*) *twinning* in which three or more individuals are aligned parallel to one another by the same twin law. Example of commonly observed polysynthetic twinning are albite, NaAlSi<sub>3</sub>O<sub>8</sub>, calcite, CaCO<sub>3</sub>, and corundum, Al<sub>2</sub>O<sub>3</sub> (Raith et al., 2012). Polysynthetic twinning has been previously identified on reaction-sintered end-member hibonite (Schmid and De Jonghe, 1983).

Electron microscopy observations of the run products obtained from sol-gel precursors with different amount of Ti + Mg seem to indicate that the grain sizes of hibonite are positively correlated with the concentration of doping elements (Ti and Mg), *i.e.* larger crystals are produced at higher concentrations of Ti and Mg. In fact, whereas gel0 and gel2 have not produced single crystals suitable for XRD measurements, gel4 and gel6 have produced crystals up to 100  $\mu$ m.

The BSE image of the run products obtained for sample gel2-2 is reported in Fig. 3.5-a as an example of a low-Ti-Mg content, fine-grained hibonite sample. The SEM observation revealed the presence of macroscopic grains having neither euhedral nor sub-euhedral morphology. At higher magnifications the surface of these samples appeared to be porous at a microscopic level (Fig. 3.5-a). TEM observation on such samples revealed that they consist indeed of hibonite crystallised in the form of sub-micron platelets, finely intergrown with each other, as shown in Fig. 3.5-b.

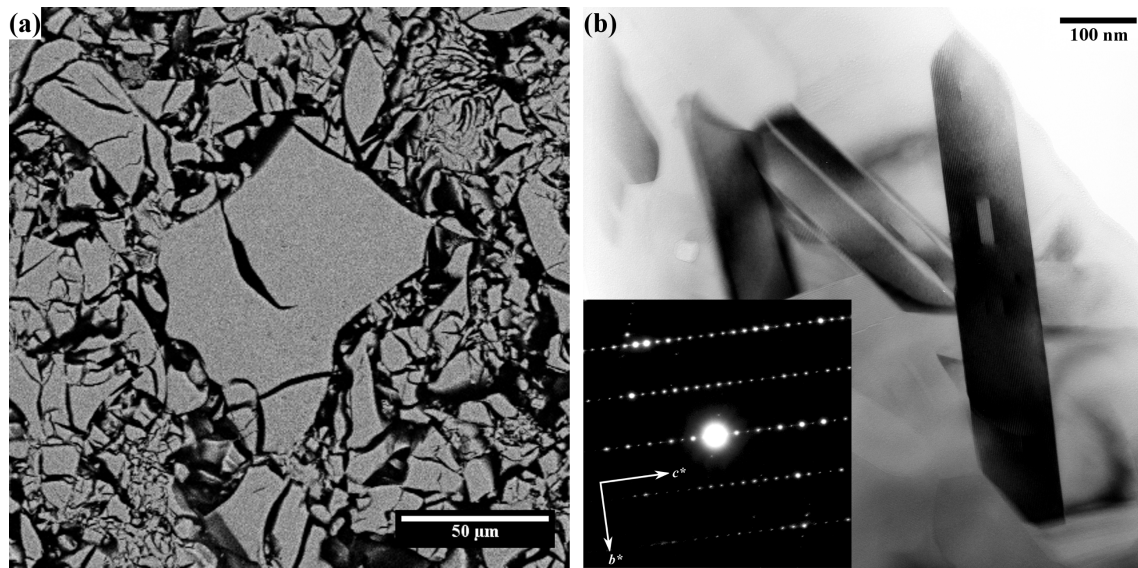


Figure 3.5: Electron microscopy images of sample gel2-2. (a) SEM-BSE image showing micro-porous aggregates of very fine-grained hibonite crystals. (b) TEM bright field image showing sub-micron sized, twinned, hibonite platelets finely intergrown with one another; the inset shows the electron diffraction pattern observed along the zone axis  $[100]$  on the grain appearing darker in the image.

The bright field image of sample gel2-2 (Fig. 3.5-b) shows a  $100 \times 700$  nm hibonite grain which appears dark due to diffraction contrast and exhibits a syntactical intergrowth consisting of a smaller ( $20 \times 80$  nm) hibonite crystal (light grey). Another hibonite grain observed in Fig. 3.5-b appears in partial diffraction contrast, but still allows observing polysynthetic hibonite twins.

The polycrystalline samples obtained at room pressure from oxide precursors are generally formed by well sintered pellets of hibonite having crystals smaller than  $30 \mu\text{m}$ , of which two examples are reported in Fig. 3.6. The morphology of the crystals obtained does not seem to depend on the choice of the starting material, in contrast with what suggested by An et al. (1996), *i.e.* that  $\text{CaCO}_3$  favours platy-like morphology while  $\text{CaO}$  gives equiaxed hibonite grains. In this study platelet crystals were observed even when using  $\text{CaO}$  as starting material (Fig. 3.6).

The TEM observation of several run products from oxide precursors showed that polysynthetic twinning is the only type of defect present in some of the specimens; in all other cases the hibonite samples are defect-free. For example, the bright field images acquired along different zone axes for hibonite grains of samples FIB1S1B and FIB2S1B2 show uniform diffraction contrast (Fig. 3.7).

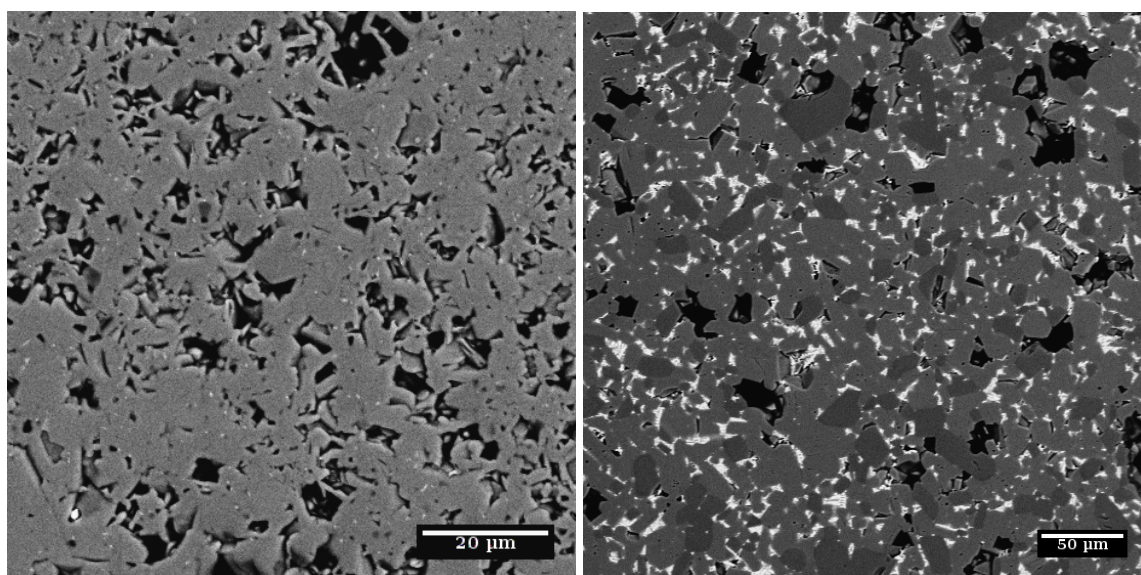


Figure 3.6: BSE images of the run product for the samples FIB3S1B2 (left) and Ti3AS2M (right). The lighter grey grains are hibonite, the darker crystals are corundum and the white phase is Ca-Ti-perovskite.

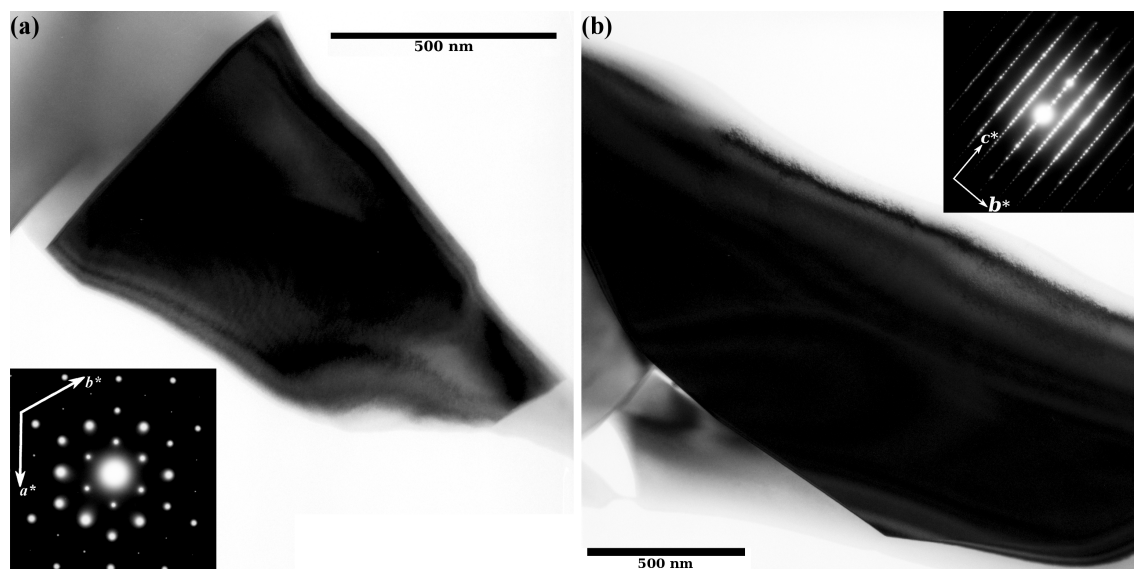


Figure 3.7: TEM-BF image of hibonite grains obtained from oxide precursors. The insets show the electron diffraction patterns used to acquire the images. (a) FIB1S1B observed along the  $[001]$  zone axis. (b) FIB2S1B2 observed along the  $[100]$  zone axis.

Table 3.2: Synthesis conditions and run products of hibonite samples obtained from oxide precursors.

Sample	Temperature (°C)	$f_{O_2}$ (log units)	Time (h)	Nominal composition (%wt)			Products <sup>†</sup>	Colour of hibonite*	
				CaO	Al <sub>2</sub> O <sub>3</sub>	MgO			TiO <sub>2</sub>
HB1	1600	-0.5	4	8.40	91.60	0.00	0.00	hib + cor	white
HB-MT1	1600	-0.5	8	8.30	88.70	2.00	1.00	hib + cor + gro	white
HB-MT5	1600	-0.5	4	8.30	84.70	2.00	5.00	hib + cor	blue
HB-MT5-IW1	1430	-9.3	40					hib + cor	blue
HB-T5B	1430	-11.5	15	5.85	91.45	0.00	2.70	hib + cor	blue
HB-T5M	1430	-0.5	15					hib + cor	white
M2T5Ti3 <sup>+</sup>	1430	-11.0	40	5.85	91.32	0.00	2.83	hib + cor	blue
FIB1S1B	1500	-11.0	14					hib + cor	blue
FIB1S1B2	1500	-16.0	14	5.90	82.52	5.60	5.98	hib + cor	blue
FIB1S1M	1500	-0.5	14					hib + cor	white
FIB2S1B	1500	-11.0	14					hib + cor	blue
FIB2S1B2	1500	-16.0	15					hib + cor	blue
FIB2S1BM*	1500	-0.5	15					hib + cor	white
FIB2S1M	1500	-0.5	14	8.30	86.80	1.20	3.70	hib + cor	white
FIB2S1MB•	1500	-11.0	15					hib + cor	blue
FIB2S2C	1450	-8.0	18					hib + cor	blue
FIB2S2D	1450	-4.0	18					hib + cor	blue
Ti3AS2B2	1500	-16.0	19	8.29	87.46	0.00	4.25	cor + hib + pv	blue
Ti3AS2M	1500	-0.5	19					cor + hib + pv	white
bruc <sup>‡</sup>	1500	-6.6	8	8.20	88.00	1.30	2.50	cor + hib + pv	/
Mg_Ti <sup>†*</sup>	1450	-6.9	13	8.33	86.32	1.80	3.56	cor + hib + pv	/

<sup>†</sup> detected as >5 %wt from PXRD; hib = hibonite, cor = corundum, pv = Ca-Ti-perovskite; <sup>‡</sup> starting material for piston-cylinder experiments only (Table 3.1);

<sup>+</sup> Ti<sub>2</sub>O<sub>3</sub> used instead of TiO<sub>2</sub>; <sup>#</sup> brucite used instead of MgO; \* non-decarboxylated mixture; \* FIB2S1B after re-equilibration; • FIB2S1M after re-equilibration;

\* referred to the appearance of the bulk sample which, for example, can appear white even when the individual grains are colourless.

Table 3.3: Synthesis conditions and run products of hibonite samples obtained from sol-gel precursors.

Sample	Temperature (°C)	$f_{O_2}$ (log units)	Time (h)	Nominal composition (% $_{wt}$ )	Products <sup>†</sup>	Colour of hibonite*
				CaO   Al <sub>2</sub> O <sub>3</sub>   MgO   TiO <sub>2</sub>		
gel0	1600	-0.5	4	8.40   91.60   0.00   0.00	hib	white
gel2-1	1550	-0.5	15		hib + cor	white
gel2-2	1550	-16.0	15		hib + cor	blue
gel2-3	1550	-11.0	15	8.33   86.32   1.80   3.56	hib + cor	blue
gel2-4	1550	-8.0	15		hib + cor	blue
gel2-5	1550	-6.0	15		hib + cor	blue
gel3-1	1550	-0.5	15		hib + cor	white
gel3-1b	1550	-0.5	60		hib + cor	white
gel3-2	1550	-16.0	15		hib + cor	grey
gel3-3	1550	-11.0	15	8.29   87.46   0.00   0.00	hib + cor	blue
gel3-3R <sup>†</sup>	1550	-11.0	15		hib + cor	blue
gel3-3b	1550	-11.0	60		hib + cor	blue
gel3-4	1550	-8.0	15		hib + cor	blue
gel4-1	1550	-0.5	15		hib + cor	white
gel4-2	1550	-16.0	15	8.30   86.02   1.19   4.73	hib	blue
gel4-3	1550	-11.0	15		hib + cor	blue
gel6-1	1550	-0.5	15		hib + sp + pv	white
gel6-2	1550	-16.0	15	7.96   57.91   11.45   22.68	hib + sp + pv	blue/white <sup>§</sup>
gel6-3	1550	-11.0	15		hib + sp + pv	blue
gel6-5	1550	-8.0	15		hib + sp + pv	blue

<sup>†</sup> detected as >5% $_{wt}$  from PXRD: hib = hibonite, cor = corundum, gro = grossite, pv = Ca-Ti-perovskite; <sup>‡</sup>gel3-2 after re-equilibration;

<sup>§</sup>the interior of the sintered pellet appears blue with white patches; repeated attempts at synthesis failed due to problems with the furnace;

\* referred to the appearance of the bulk sample which, for example, can appear white even when the individual grains are colourless.

### 3.2 Chemical analysis of synthetic hibonites

The results of electron microprobe measurements performed on all synthetic runs are reported in Tables 3.4 and 3.5. These tables can be compared with Tables 3.2 and 3.3 to observe, for example, the differences among run products synthesised using different precursors. The samples having a low Ti-Mg content have compositions close to the nominal ones for both oxide and sol-gel precursor starting materials, whereas samples having higher Ti-Mg content have compositions that deviate significantly from the nominal ones. Sol-gel precursors produce, as expected, more homogeneous run products; this is illustrated in Fig. 3.8 where the sum of Ti and Mg substituting for Al is plotted versus the content of Al present in the formula of synthetic hibonites. The individual microprobe measurements acquired from samples FIB2S1B and gel2-3, which have similar compositions and were both synthesised at 1500-1550 °C and  $\log f_{\text{O}_2} = -11$ , show that the sample obtained from sol-gel precursors have a narrower range of concentrations of Ti and Mg (Fig. 3.8-a).

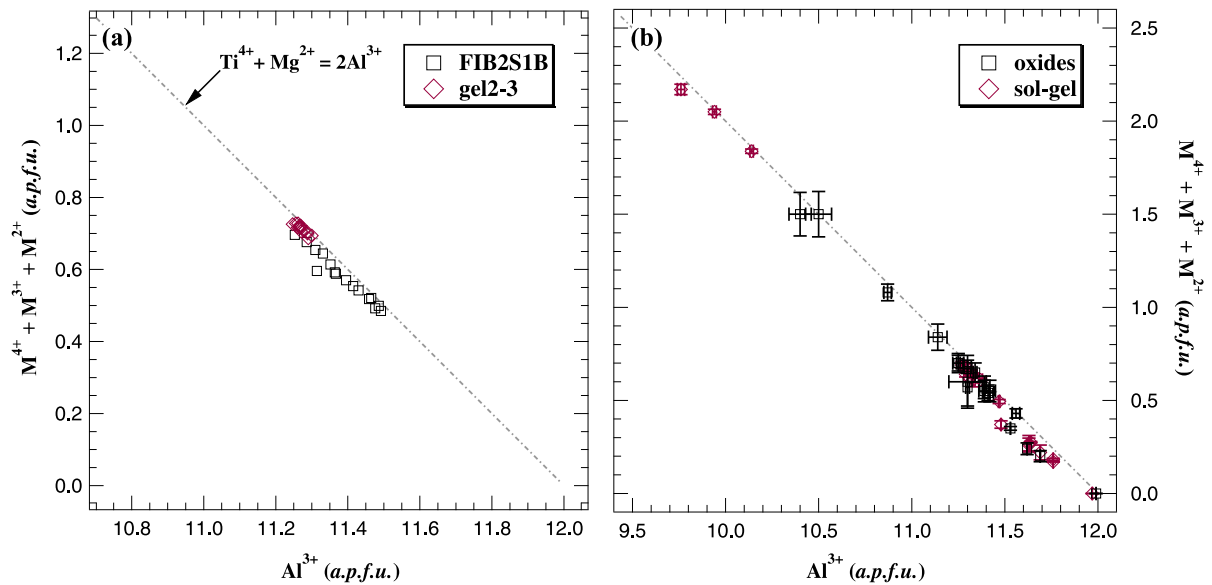


Figure 3.8: Sum of di-, tri- and tetra-valent cations substituting for  $\text{Al}^{3+}$  plotted against  $\text{Al}^{3+}$  for the EPMA performed on synthetic hibonites. The concentrations are given in cations per formula unit, normalised to 19 oxygen. The dashed line is a guide to the eyes representing the indicated coupled substitution mechanism. (a) Individual microprobe measurements acquired from samples FIB2S1B and gel2-3, having comparable compositions and synthesised at similar conditions from oxide and sol-gel precursors, respectively. (b) EPMA averaged over 20 to 40 individual measurements for all synthetic hibonites, the error bars represent one-sigma standard deviations.

Moreover, standard deviations corresponding to the average of individual EPMA for each hibonite sample obtained with the sol-gel technique are smaller than those calculated from the measurements on hibonites synthesised from oxide precursors. This is visible in Fig. 3.8-b, where a compilation of the EPMA performed on all synthetic hibonites (Table 3.5) is reported. Most of the samples plot along the dashed line corresponding to the coupled substitution mechanism



indicating that they have a Ti : Mg ratio that is close to 1 : 1. This suggests that the coupled substitution of Eq. 3.1 is the major incorporation mechanism for Ti and Mg in hibonite.

Only for samples synthesised at low oxygen fugacity, the hibonite structure contains a small excess of Ti with respect to Mg (Table 3.5), *i.e.* more reducing conditions favour the substitution of  $\text{Ti}^{3+}$  according to the substitution



In order to evaluate the effectiveness of these competing equilibria the knowledge of the  $\text{Ti}^{3+}$  contents is required. Given the relatively low bulk content of Ti in the synthetic hibonite samples, EPMA can hardly provide reliable estimation of  $\text{Ti}^{3+}$  concentrations due to the uncertainties in the analyses. A more accurate measure of the  $\text{Ti}^{3+}$  content has been provided by energy electron loss spectroscopy (EELS), as described in Section 4.2.2.

Table 3.4: Chemical composition of synthetic hibonites measured by means of EPMA. The analyses are presented as oxides weight percent. For each sample 20 to 40 individual analyses were performed, the averages are given and the one-sigma standard deviations are indicated in brackets. Fe and Si were probed, however, the corresponding signals were below detection limits for all samples.

Sample	CaO	Al <sub>2</sub> O <sub>3</sub>	MgO	TiO <sub>2</sub>	Tot.
HB1	8.68(5)	92.9(2)	<i>n.d.</i>	<i>n.d.</i>	101.6(2)
HB-MT1	8.47(2)	88.8(3)	1.4(1)	1.1(1)	99.8(2)
HB-MT5	8.5(2)	85.8(7)	1.9(1)	3.9(1)	100.1(3)
HB-MT5-IW1	8.6(2)	84.9(9)	1.9(1)	4.6(5)	100.0(6)
HB-MT5_pc3	8.5(1)	86.3(4)	1.9(1)	4.3(3)	101.0(2)
HB-T5B	9.1(3)	89.0(7)	<i>n.d.</i>	2.8(4)	101.0(4)
HB-T5M	8.9(2)	89.5(6)	<i>n.d.</i>	2.4(3)	100.9(5)
M2T5Ti3	8.7(3)	81.1(7)	3.0(1)	6.6(5)	99.4(8)
FIB1S1B	8.1(1)	78(1)	4.1(4)	10(1)	100.2(8)
FIB1S1B2	8.0(1)	78(1)	4.0(3)	10(1)	100.0(2)
FIB1S1M	8.1(1)	79(1)	4.1(4)	9(1)	100(1)
FIB2S1B	8.5(1)	86.1(6)	1.2(2)	4.1(6)	99.9(4)
FIB2S1B2	8.37(8)	86.4(5)	1.3(2)	3.9(3)	100.0(2)
FIB2S1BM	8.5(1)	86.1(5)	1.2(2)	4.1(5)	100.0(4)
FIB2S1M	8.9(6)	86(2)	1.02(5)	5(2)	100.4(5)
FIB2S1MB	8.9(4)	86(2)	1.0(1)	5(2)	100.2(4)
FIB2S2C	8.4(1)	84.1(0)	2.5(3)	5.1(6)	100.1(3)
FIB2S2D	8.5(2)	86.2(7)	1.46(6)	3.9(7)	100.0(3)
Ti3AS2B2	8.43(7)	87.5(3)	<i>n.d.</i>	4.2(1)	100.1(3)
bruc_pc1	9.1(2)	85.9(8)	2.2(2)	4.1(4)	101.2(7)
gel0	8.7(1)	91.1(2)	<i>n.d.</i>	0.01(1)	99.8(2)
gel2-1	8.35(6)	85.3(3)	1.81(3)	4.17(9)	99.6(3)
gel2-2	8.42(8)	85.6(3)	1.71(7)	4.25(5)	100.0(3)
gel2-3	8.50(7)	85.4(2)	1.83(4)	4.26(9)	100.2(2)
gel2-4	8.52(7)	85.6(3)	1.83(3)	4.1(1)	100.2(2)
gel2-5	8.54(5)	86.1(2)	1.78(3)	3.66(5)	100.1(2)
gel3-1	8.42(6)	89.1(2)	0.02(1)	2.06(5)	99.6(2)
gel3-1b	8.40(6)	89.9(2)	<i>n.d.</i>	2.08(6)	100.4(2)
gel3-2	8.7(1)	87.1(3)	0.01(1)	4.3(2)	100.2(2)
gel3-3	8.5(1)	88.2(5)	0.1(1)	2.9(5)	99.8(3)
gel3-3R	8.6(1)	88.4(6)	0.1(1)	2.7(4)	99.8(2)
gel3-3b	8.39(7)	88.8(3)	0.05(1)	3.16(5)	100.4(3)
gel3-4	8.5(1)	88.6(6)	<i>n.d.</i>	2.6(4)	99.7(1)
gel4-1	8.40(6)	86.7(2)	1.28(2)	3.4(1)	99.7(2)
gel4-2	8.45(7)	85.1(2)	1.35(6)	4.87(9)	99.8(2)
gel4-3	8.5(2)	85.4(7)	1.37(4)	4.2(4)	99.7(2)
gel6-1	8.21(6)	75.4(2)	5.28(6)	10.97(9)	99.9(2)
gel6-3	8.19(7)	72.4(5)	5.7(1)	13.8(2)	100.2(4)
gel6-5	8.08(6)	73.8(2)	5.80(5)	12.3(1)	100.02(8)

Table 3.5: Chemical composition of synthetic hibonites measured by means of EPMA. The analyses are presented as cations per formula unit, normalised to 19 oxygen. For each sample 20 to 40 individual analyses were performed, the averages are given and the one-sigma standard deviations are indicated in brackets. Fe and Si were probed, however, the corresponding signals were below detection limits for all samples.

Sample	Ca <sup>2+</sup>	Al <sup>3+</sup>	Mg <sup>2+</sup>	Ti <sup>4+</sup>	Tot.
HB1	1.02(1)	11.99(1)	<i>n.d.</i>	<i>n.d.</i>	13.01(1)
HB-MT1	1.01(1)	11.65(3)	0.23(2)	0.09(1)	12.98(1)
HB-MT5	1.02(2)	11.34(6)	0.32(1)	0.33(5)	13.00(1)
HB-MT5-IW1	1.04(3)	11.25(8)	0.31(1)	0.39(5)	12.99(1)
HB-MT5_pc3	1.01(1)	11.30(5)	0.32(2)	0.36(3)	12.99(1)
HB-T5B	1.08(4)	11.63(7)	<i>n.d.</i>	0.23(3)	12.95(0)
HB-T5M	1.06(2)	11.69(4)	<i>n.d.</i>	0.20(3)	12.95(1)
M2T5Ti3	1.05(5)	10.87(4)	0.51(2)	0.57(4)	13.00(2)
FIB1S1B	0.99(2)	10.4(1)	0.70(6)	0.8(1)	12.95(3)
FIB1S1B2	0.98(2)	10.5(1)	0.69(4)	0.8(1)	12.97(2)
FIB1S1M	0.99(3)	10.5(2)	0.70(7)	0.8(1)	12.97(2)
FIB2S1B	1.02(1)	11.39(8)	0.20(3)	0.35(5)	12.96(1)
FIB2S1B2	1.01(1)	11.41(6)	0.21(3)	0.33(3)	12.96(1)
FIB2S1BM	1.01(1)	11.42(7)	0.21(3)	0.34(5)	12.98(1)
FIB2S1M	1.07(7)	11.3(2)	0.17(1)	0.4(1)	12.95(3)
FIB2S1MB	1.05(5)	11.3(2)	0.2(1)	0.4(1)	12.95(2)
FIB2S2C	1.01(1)	11.14(0)	0.41(5)	0.43(5)	13.00(1)
FIB2S2D	1.02(2)	11.39(8)	0.24(1)	0.33(6)	12.98(2)
Ti3AS2B2	1.01(1)	11.53(2)	<i>n.d.</i>	0.35(1)	12.89(1)
bruc_pc1	1.08(2)	11.25(6)	0.36(3)	0.34(3)	13.03(1)
gel0	1.04(2)	11.97(1)	<i>n.d.</i>	<i>n.d.</i>	13.01(1)
gel2-1	1.01(1)	11.32(1)	0.30(1)	0.35(1)	12.99(1)
gel2-2	1.01(1)	11.32(1)	0.29(1)	0.36(0)	12.98(1)
gel2-3	1.02(1)	11.29(2)	0.31(1)	0.36(1)	12.98(0)
gel2-4	1.02(1)	11.31(3)	0.31(1)	0.35(1)	12.99(1)
gel2-5	1.03(1)	11.37(1)	0.30(1)	0.31(0)	13.00(1)
gel3-1	1.01(1)	11.76(1)	<i>n.d.</i>	0.17(0)	12.95(0)
gel3-1b	1.00(1)	11.77(1)	<i>n.d.</i>	0.17(1)	12.94(1)
gel3-2	1.04(1)	11.48(3)	<i>n.d.</i>	0.37(2)	12.89(0)
gel3-3	1.02(1)	11.64(8)	0.01(0)	0.25(4)	12.93(2)
gel3-3R	1.02(1)	11.64(7)	0.01(1)	0.24(3)	12.95(2)
gel3-3b	1.00(1)	11.64(1)	0.01(0)	0.27(1)	12.91(1)
gel3-4	1.02(2)	11.69(6)	<i>n.d.</i>	0.22(4)	12.93(1)
gel4-1	1.01(1)	11.47(1)	0.21(1)	0.28(1)	12.98(1)
gel4-2	1.02(1)	11.29(1)	0.23(1)	0.41(1)	12.94(1)
gel4-3	1.03(2)	11.35(8)	0.23(1)	0.36(3)	12.96(1)
gel6-1	1.00(1)	10.14(1)	0.90(1)	0.94(1)	12.99(1)
gel6-3	1.00(1)	9.76(4)	0.98(2)	1.19(2)	12.93(1)
gel6-5	0.99(1)	9.94(1)	0.99(1)	1.06(1)	12.97(1)

### 3.3 X-ray diffraction of synthetic hibonites

A fragment of the pellet recovered from each hibonite synthesis run, after grinding and spiking with Si standard (Section 2.4), was characterised by mean of powder X-ray diffraction in order to carry out phase identification (Tables 3.2 and 3.3) and to measure the unit cell parameters (Table 3.6).

Table 3.6: Refined unit cell parameters obtained by means of Rietveld analysis of the powder X-ray diffraction patterns acquired for the studied hibonite samples. The agreement factors  $\chi^2$  are indicated for each refinement. The sum of Ti and Mg obtained from EPMA (Table 3.5) are also reported.

Sample	Ti <sup>tot</sup> + Mg ( <i>a.p.f.u.</i> )	<i>a</i> (Å)	<i>c</i> (Å)	<i>V</i> (Å <sup>3</sup> )	$\chi^2$
HB1	0	5.55840(4)	21.8999(3)	585.966(7)	2.96
HB-MT1	0.32(2)	5.56463(9)	21.9188(6)	587.79(2)	2.33
HB-MT5	0.65(5)	5.57607(5)	21.9570(4)	591.236(1)	1.76
HB-MT5_pc3	0.68(4)	5.57700(7)	21.9527(5)	591.32(1)	2.80
HB-T5B	0.23(3)	5.56148(4)	21.9430(3)	587.77(1)	4.16
HB-T5M	0.20(3)	5.56164(5)	21.9344(4)	587.57(1)	6.36
FIB1S1B	1.50(6)	5.59392(8)	22.0066(5)	596.37(2)	3.96
FIB1S1M	1.50(7)	5.59252(9)	22.0132(6)	596.25(2)	4.43
FIB2S1B	0.55(6)	5.57277(4)	21.9495(3)	590.34(1)	9.10
FIB2S1B2	0.54(4)	5.57659(7)	21.9593(5)	591.41(1)	2.79
FIB2S1M	0.57(1)	5.56934(3)	21.9468(2)	589.53(1)	4.93
TI3AS2B2	0.35(1)	5.57302(5)	21.9514(4)	590.44(1)	12.92
gel0	0	5.55822(4)	21.9048(2)	586.06(1)	2.26
gel2-1	0.65(1)	5.57563(5)	21.9580(4)	591.17(1)	14.46
gel2-2	0.65(1)	5.57482(6)	21.9801(4)	591.59(1)	4.56
gel2-3	0.67(1)	5.57562(4)	21.9687(2)	591.45(1)	4.73
gel2-4	0.66(1)	5.57588(4)	21.9592(2)	591.25(1)	5.48
gel2-5	0.61(1)	5.57313(4)	21.9632(3)	590.78(1)	4.83
gel3-1	0.17(1)	5.56220(9)	21.9332(6)	587.66(2)	6.21
gel3-2	0.37(2)	5.56237(5)	21.9184(3)	587.298(1)	3.19
gel3-3	0.26(4)	5.56681(7)	21.9398(6)	588.81(2)	6.66
gel3-3R	0.25(3)	5.56962(9)	21.9388(6)	589.38(2)	11.85
gel3-4	0.22(4)	5.56205(5)	21.9430(3)	587.892(1)	6.81
gel4-1	0.49(1)	5.57103(5)	21.9518(3)	590.03(1)	5.98
gel4-2	0.64(1)	5.57742(6)	21.9773(4)	592.07(1)	5.03
gel4-3	0.59(3)	5.57426(4)	21.9556(3)	590.81(1)	5.48
gel6-1	1.84(1)	5.6081(2)	22.073(1)	601.21(4)	12.19
gel6-3	2.17(3)	5.6182(2)	22.099(1)	604.09(4)	10.39
gel6-5	2.05(1)	5.6136(2)	22.094(1)	602.97(3)	7.67

A total of six experimental runs produced hibonite crystals large enough to be characterised by means of single crystal X-ray diffraction. For each sample several single crystals were tested in order to find a high quality specimen suitable for X-ray structural characterisation. The summary of the measurements performed on these representative single crystals is given in Table 3.7.

Table 3.7: Unit cell parameters (u.c.p.), data collection and structural refinements details for synthetic hibonite single crystals.

	HB-MT5_pc3	gel3-1	gel3-3	gel4-1	gel6-1	gel6-3
<b>Crystal size</b>						
Length (mm)	0.175	0.150	0.110	0.06	0.19	0.135
Width (mm)	0.115	0.130	0.090	0.04	0.17	0.095
Height (mm)	0.045	0.050	0.040	0.01	0.09	0.03
<b>U.c.p.</b>						
$a$ (Å)	5.5778(6)	5.5617(8)	5.5663(7)	5.5712(7)	5.6071(4)	5.6192(4)
$c$ (Å)	21.9523(7)	21.9331(8)	21.9377(8)	21.9448(8)	22.0653(4)	22.0945(5)
$V$ (Å <sup>3</sup> )	591.5(1)	587.6(2)	588.6(1)	589.9(1)	600.80(8)	604.18(8)
Reflections	22	22	28	19	11	7
<b>Data collection</b>						
Scan type	$\phi - \omega$	$\omega$	$\omega$	$\omega$	$\omega$	$\omega$
$2\theta_{max}$ (°)	63.66	60.11	64.29	64.2	72.79	72.67
Reflections						
Total	12489	7332	6632	10949	16667	2997
Unique	441	379	443	442	615	596
$F_o > 4\sigma(F_o)$	393	375	420	356	606	515
<b>Refinements</b>						
$R_{int}$ (%)	3.63	3.98	3.9	9.47	4.5	3.17
$R_s$ (%)	3.29	3.18	4.08	5.37	4.14	5.15
$R_1$ (%)	2.78	3.11	3.63	3.82	4.05	3.99
$wR_2$ (%)	7.71	0.088	9.13	9.66	9.88	9.99
Parameters	44	44	44	44	44	44

In the following Sections, unless diversely indicated, all the structural parameters are plotted as a function of the total amount of Ti and/or Mg substituting for Al, as measured with EPMA. Moreover, when plotting the literature data of terrestrial hibonites against Ti and Mg, they are referred to the sum of tri-, tetra-valent and divalent cations, respectively.

### 3.3.1 Unit cell parameters variation

The variation of unit cell parameters and volume of the studied hibonites as a function of the concentration of total Ti and Mg is shown in Fig. 3.9. Solid and open red symbols correspond to the XRD measurements performed on polycrystalline samples from sol-gel and oxides precursors, respectively. Single crystal XRD data are reported as solid blue symbols; SCXRD data from literature are plotted as open black symbols. The unit cell parameters  $a$  and  $c$  have been normalised with respect to those of the end-member hibonite gel0,  $a_0$  and  $c_0$ , respectively.

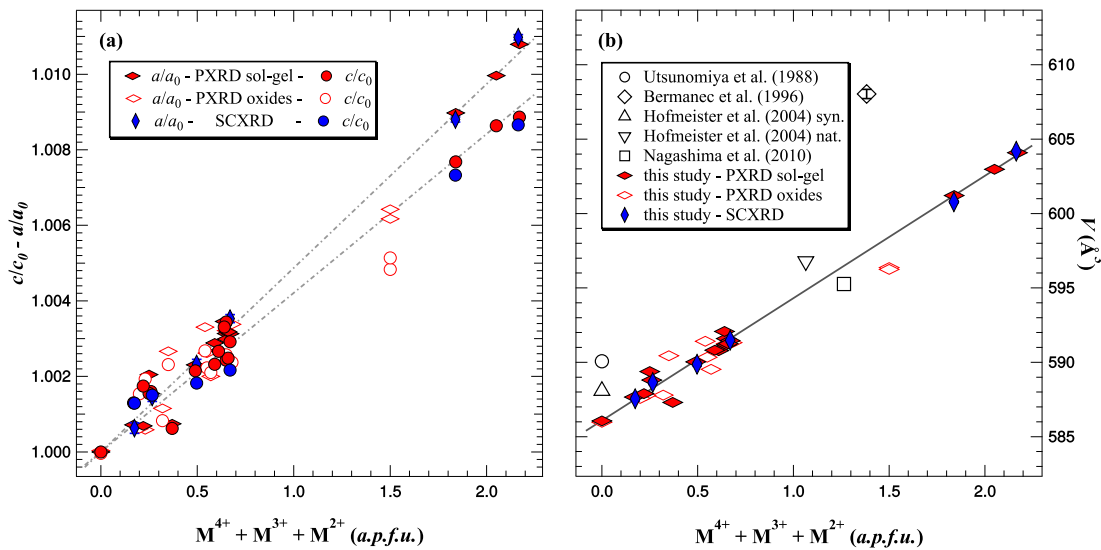


Figure 3.9: Variation of the unit cell parameters of hibonite as a function of the sum of di-, tri- and tetra-valent cations substituting for Al. The data for both PXRd and SCXRD are reported. (a) Unit cell parameters (u.c.p.) normalised with respect to  $a_0$  and  $c_0$ , corresponding to the u.c.p. of end-member hibonite gel0; the dashed lines are guides to the eyes. (b) Unit cell volumes compared to XRD data from literature; the solid line indicates a fit through the PXRd data from hibonites obtained using the sol-gel technique ( $R^2 = 0.99$ ).

The unit cell parameters and volume of hibonite increase linearly with increasing Ti and Mg contents. The expansion of the unit cell parameters can be considered isotropic, *i.e.*  $a/a_0$  and  $c/c_0$  have a similar dependence on the concentration of Ti and Mg. Only for very high contents of these cations the unit cell parameter  $c$  increases slightly less as compared to  $a$ .

The increase of unit cell volume from the end-member hibonite gel0 to the Ti-Mg-rich sample gel6-3 is on the order of 1% and is consistent with an expansion of the oxygen framework as a consequence of the substitution of  $\text{Al}^{3+}$  with larger cations such as  $\text{Mg}^{2+}$ ,  $\text{Ti}^{4+}$  and  $\text{Ti}^{3+}$  (Table 3.8). The data reported in Fig. 3.9-b show that the unit cell parameters measured by means of Rietveld refinements on XRPD data have a high degree of accuracy as they are in excellent agreement with the unit cell parameters obtained from 8-positions centring procedure (Section 2.5) performed on XRD of single crystals. Moreover, it appears that the data corresponding to the samples obtained from sol-gel precursors are closer to the values obtained from SCXRD and are also less scattered as compared to those of the samples from oxide precursors. This is most likely due to the fact that, as shown by microprobe analyses (Section 3.2), the sol-gel samples are more homogeneous in composition thus having more consistent unit cell parameters among the different grains forming the polycrystalline samples. Consequently, the XRPD data from samples synthesised from oxides are not considered for fitting the unit cell volume data of this study represented by the solid line reported in Fig. 3.9-b, which can be expressed with the empirical relationship reported in Eq. 3.3.

$$V = 8.2(2) \cdot (\text{Ti}^{\text{tot}} + \text{Mg}^{2+})_{a.p.f.u.} + 586.1(2) \quad (3.3)$$

The present data are compared with those previously published on SCXRD of synthetic end-members (Utsunomiya et al., 1988; Hofmeister et al., 2004) and terrestrial hibonites (Bermanec et al., 1996; Hofmeister et al., 2004; Nagashima et al., 2010) which, however, have a complex chemistry, containing different transition metals and REE. It can be observed that most of the data reported in the literature lie above the trend determined in this study (Fig. 3.9-b). For the end-member hibonite the unit-cell volume reported by Hofmeister et al. (2004) and Utsunomiya et al. (1988) are 0.35% and 0.70% larger than the unit-cell volume obtained for the end-member hibonite synthesised in this study (gel0). This discrepancy may be due to the different synthesis procedures, which can give rise to varying degree of non-stoichiometry affecting the unit cell parameters, as well as to the accuracy in centring of Bragg reflections, which can result in systematic errors.

The data point from Bermanec et al. (1996) is clearly an outlier, this hibonite has a unit cell volume 1.5% larger than that of the regression line described in this study. This is likely due to the presence in this sample of rare Earth elements (REE) such as  $\text{La}^{3+}$ ,  $\text{Ce}^{4+}$  and  $\text{Nd}^{3+}$  as well as  $\text{Th}^{4+}$ , which have crystal ionic radii much larger than those of  $\text{Al}^{3+}$ ,  $\text{Mg}^{2+}$ ,  $\text{Ti}^{4+}$  and  $\text{Ti}^{3+}$  (Table 3.8). The sample studied by Nagashima et al. (2010), being an unusually REE-free terrestrial hibonite, is in good agreement with the regression line reported in Fig. 3.9-b.

Table 3.8: Crystal ionic radii for 6-fold coordination of the cations present in synthetic samples from this study and in terrestrial hibonites from the literature (Shannon, 1976).

Cation	Radius (Å)
$\text{Al}^{3+}$	0.675
$\text{Mg}^{2+}$	0.860 0.710 <sup>‡</sup>
$\text{Ti}^{4+}$	0.745
$\text{Ti}^{3+}$	0.810
$\text{La}^{3+}$	1.172
$\text{Ce}^{4+}$	1.010
$\text{Nd}^{3+}$	1.123
$\text{Th}^{4+}$	1.080

<sup>‡</sup>radius for 4-fold coordination.

Despite the high degree of accuracy in determining the unit cell parameters, powder X-ray diffraction datasets acquired *in-house* using conventional diffractometers do not allow obtaining information on the structure of hibonite, *i.e.* atom coordinates, thermal displacement factors, site occupancy. In fact, in spite of using adequate functions and parameters for diffraction profiles and background, the quality of the Rietveld refinements was influenced only limitedly by the choice of the structural model used for hibonite.

Therefore, single crystal X-ray diffraction is required in order to fully characterise the structure of hibonite, the results obtained with this technique are presented in Sections 3.3.2 and 3.3.3.

### 3.3.2 Site distribution of Ti

Fourier difference maps were evaluated for each single crystal X-ray diffraction dataset (Table 3.7) in order to estimate the possible location of Ti in the structure of hibonite. Due to the high concentration of Ti in the crystals of gel6-1 and gel6-3, a significant residual electron density was observed at the  $M4$  site, a trigonally distorted octahedron occurring in face sharing pairs. After refining the Ti occupancy into the  $M4$  site, another peak in the Fourier map appeared at the  $M2$  site, a trigonal bipyramid.

At this point a structural model having Ti in both  $M2$  and  $M4$  sites has been used to refine the structure of all other samples, even those whose Ti concentration was too low to give appreciable peaks in the Fourier difference maps, *i.e.* HB-MT5, gel3-1, gel3-3 and gel4-1. In order to consistently check the stability of the structural refinements, they were initially carried out using the model for pure hibonite and subsequently refined introducing Ti first at the  $M4$  site and then also at the  $M2$  site. All steps resulted in convergent refinements with progressively lower agreement factor, *e.g.*  $R_1$ , which reached the values reports in Table 3.7 when refining the occupancy for Ti on both sites, thus justifying the use of this structural model. The sum of the occupancies of Ti and Al at the same site has been constrained to be unitary. The total occupancy of Ti at the  $M4$  and  $M2$  sites has not been constrained to be equal to the Ti contents from EPMA, however, a good agreement between chemical analyses and chemistry from the structural refinements has been obtained in all cases (Tables 3.5 and 3.9). Moreover, it has been observed that for all the refined structures, the amount of Ti occupying the  $M4$  site is consistently larger than that at the  $M2$  site. In particular, the average of the ratios between the Ti present at the  $M4$  and that at the  $M2$  site,  $P_{Ti_{M4}:Ti_{M2}}$ , calculated for the studied samples (Table 3.9), is 4.1(1) indicating that Ti partitions preferentially at the  $M4$  site by a factor of four. The structural refinements for all crystals converged with very good agreement factors between the calculated and observed diffraction intensities. However, many of the datasets included a number of reflections, which were observed in violation of the systematic absence rule  $000l : l = 2n$ , this is typically an indication of the presence of twinning. The most frequently encountered merohedral twin law for hexagonal Laue groups (Eq. 3.4) was introduced into the refinement in order to take into account the systematic absence violations.

$$\mathcal{T} = \begin{pmatrix} 0 & 1 & 0 \\ 1 & 0 & 0 \\ 0 & 0 & \bar{1} \end{pmatrix} \quad (3.4)$$

Applying this twin law all systematic reflections disappeared and the refinements converged to the values reported in Table 3.7.

### 3.3.3 Structural variations due to Ti-Mg substitution

The structural variations due to the substitution of Ti and Mg for Al are investigated by considering the refined parameters (Table 3.9), bond distances and polyhedra distortion parameters (Table 3.10) and their variation as a function of hibonite composition. The representation of the structure of hibonite shown in Fig. 3.10 is a visual aid to locate the individual bonds and the oxygen atoms bridging  $M$  cations.

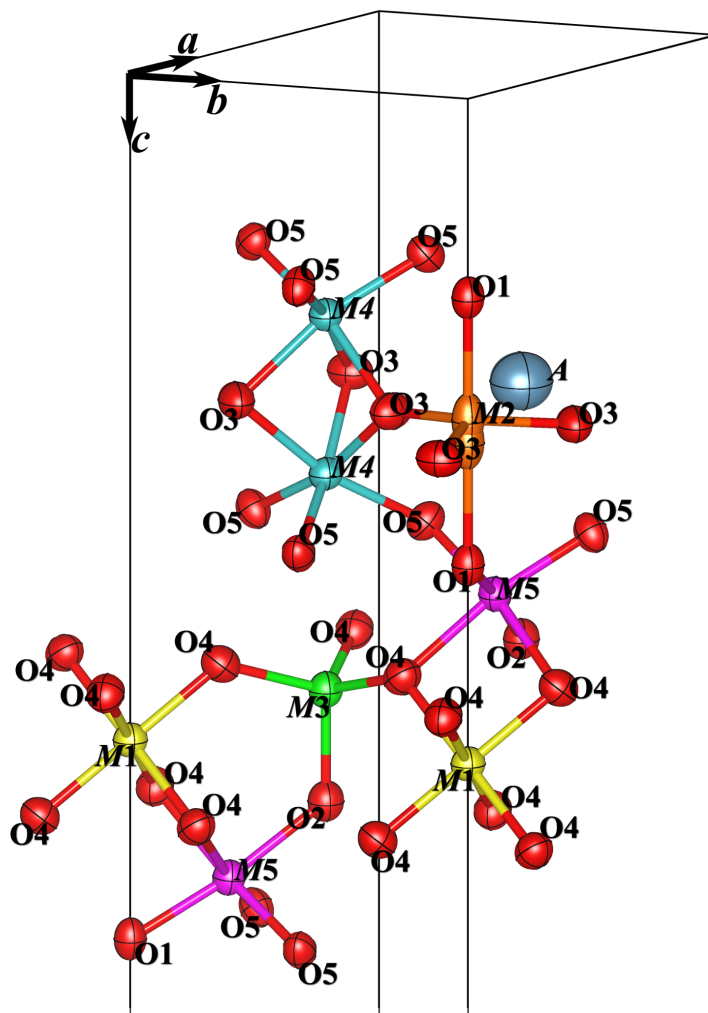


Figure 3.10: Sticks-and-balls structure of hibonite showing the minimum number of atoms necessary to visualise all the  $M-O$  bonds.

Since Ti occupies preferentially the  $M4$  site, the variation of the  $M4-O$  bond distances as a function of Ti content can be expected to present major variations. Changes in the individual bond distance  $M4-O3$  and  $M4-O5$  are reported in Fig. 3.11.

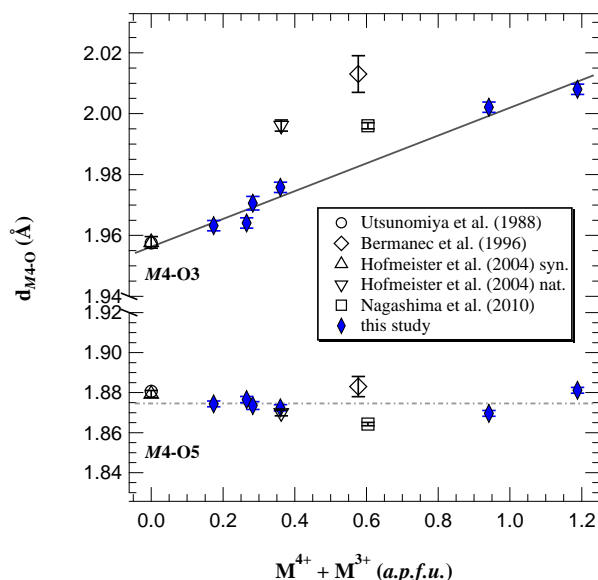


Figure 3.11: Variation of the individual bond distances  $M4-O5$  and  $M4-O3$  as a function of the sum of di-, tri- and tetra-valent cations substituting for Al. The solid line indicates a fit through the data points of this study ( $R^2 = 0.97$ ) while the dashed line is a guide to the eyes.

The bond distance  $M4-O3$  increases as a consequence of Ti substitution, while the  $M4-O5$  remains constant (Fig. 3.11). This in contrast to what reported by Nagashima et al. (2010) who indicated a decrease of the  $M4-O5$  bond distance for increasing Ti contents.

A linear regression through the data from this study gives the following empirical relationship:

$$d_{M4-O3} = 0.46(2) \cdot \text{Ti}_{a.p.f.u.}^{\text{tot}} + 1.956(1) \quad (3.5)$$

The change in  $M4-O3$  bond length is due to the repulsion of the highly charged Ti atoms (mostly present as  $\text{Ti}^{4+}$ ) and their consequent displacement from the central position of the polyhedron along the  $c$  axis. This displacement can be visualised by plotting the variation of the  $M4-M4$  distance with respect to the Ti content (Fig. 3.12). For the present synthetic samples, it can be observed that with increasing amount of Ti the  $M4-M4$  distance increases. Note, however, that this distance is clearly smaller for gel6-3. This is likely due to the fact that this sample contains a larger amount of  $\text{Ti}^{3+}$  with respect to the other samples (Table 4.1) and as a consequence the repulsion between the  $M4$  cations is weaker. The hibonites from Madagascar (Bermanec et al., 1996; Hofmeister et al., 2004) show a larger  $M4-M4$  distance with respect to the trend represented by the samples from this study; this is not surprising given

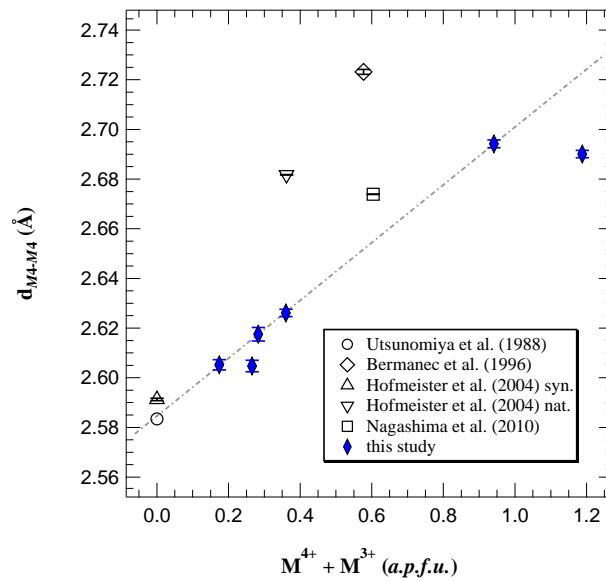


Figure 3.12: Inter-atomic distance  $M4-M4$  as a function of the sum of tri- and tetra-valent cations substituting for Al. The dashed line is a guide to the eyes.

their complex chemistry and the presence in this site of larger REE atoms. More puzzling are the differences between the samples from this thesis and the hibonite studied by Nagashima et al. (2010), which has a much simpler chemical formula. This is likely only an apparent discrepancy because the Ti content (0.52 *a.p.f.u.*) reported as EPMA analysis by Nagashima et al. (2010) is smaller than that calculated from the  $M2$  and  $M4$  site occupancies (0.61 *a.p.f.u.* Ti), listed in their XRD data. This would correspond to about 1 wt% more of  $TiO_2$  in the formula of hibonite by Nagashima et al. (2010), and considering this larger amount of Ti, their data point would be in better agreement with the results from this study.

There is also evidence of some Ti present at the  $M2$  site. Although the axial  $M2-O1$  and equatorial  $M2-O3$  bond distances (Table 3.10) are not clearly dependent on the Ti concentrations, a correlation between the displacement factor along the  $c$  axes,  $M2_{U33}$  (Table 3.9), and the site occupancy factor for Ti at the  $M2$  site,  $Ti_{s.o.f. M2}$ , is observed as shown in Fig. 3.13.

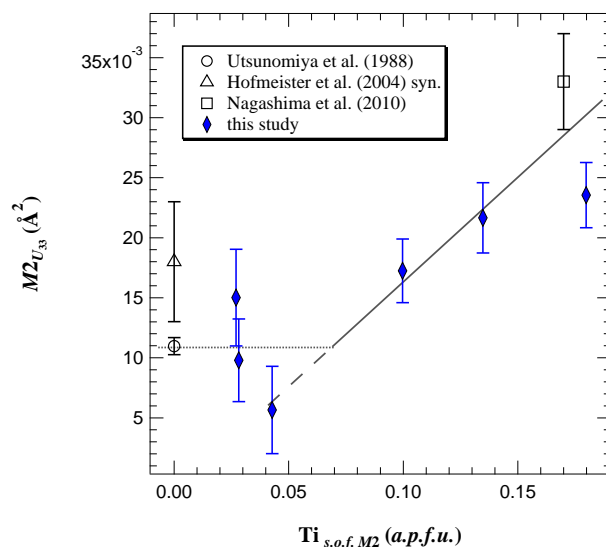


Figure 3.13: Displacement factor  $U_{33}$  for  $M2$  site as a function of the corresponding refined site occupancy factor for Ti; the available literature data are plotted with empty symbols. The solid line indicates a fit through the data points for this study, excluding gel6-3 ( $R^2 = 0.95$ ). The dotted line indicates a possible plateau of displacement factor.

This displacement factor can be interpreted as a measure of the cationic disorder and of the increased dynamic disorder in the trigonal bipyramid due to the different charge and size of the substituting cations. An increasing amount of Ti substituting for Al into the  $M2$  site corresponds to an enlargement of the displacement factor  $M2_{U_{33}}$ . The increase in disorder at the  $M2$  site can be visualised as an expansion of the thermal ellipsoid for this site as a function of  $Ti^{3+}$  and  $Ti^{4+}$  contents in representative hibonites. The samples gel4-1 and gel6-1 contain exclusively  $Ti^{4+}$  and have low and high bulk contents of Ti, respectively, while the sample gel6-3 contains high concentration of Ti in both 3+ and 4+ valence state (Fig. 3.14).

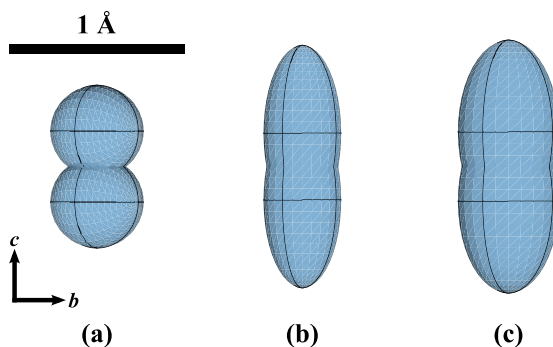


Figure 3.14: Three-dimensional visualisation of the thermal ellipsoids at the split  $M2$  site for the SCXRD data of gel4-1 (a), gel6-1 (b) and gel6-3 (c).

It appears, however, that a possible plateau of displacement factor can be identified at  $0.008(3) \text{ \AA}^2$ , which coincides with the  $M2_{U33}$  for pure hibonite (Fig. 3.13). This plateau of displacement factor is similar to the plateau of transition temperature or transition pressure (Salje et al., 1991; Hayward and Salje, 1996; Carpenter et al., 1999; Boffa Ballaran et al., 2000) that can be observed when a second component of a solid solution is added into the structure of the other end-member. Change in the transition point, or, in this case, in the displacement parameter occurs only once the microscopic strain fields around the impurity atoms start to overlap. The magnitude of the plateau is therefore a reflection of the magnitude of the local strain fields around the substituted Ti atoms. Since a visible change in  $M2_{U33}$  can be observed only for samples which have more than  $0.3 - 0.4 \text{ a.p.f.u.}$  of total Ti content (Fig. 3.13), it can be estimated that the strain fields around each Ti atoms begin to overlap at a Ti-Ti separation of about  $1 - 2$  unit cells. The significant difference of  $M2_{U33}$  between the sample gel6-3 and the terrestrial hibonite from Nagashima et al. (2010), supposedly containing only  $\text{Ti}^{4+}$ , can be interpreted as an indication of the presence of  $\text{Ti}^{3+}$  at the M2 site of synthetic hibonites. This effect can be due to the smaller microscopic strain fields around the  $\text{Ti}^{3+}$  atoms as well as to a weaker repulsion because of its smaller charge. The data from this study plotting above the plateau can be described by the empirical relationship indicated in Eq. 3.6, which has been calculated excluding gel6-3 for the reasons explained above.

$$M2_{U33} = 0.17(5) \cdot (\text{Ti}_{s.o.f.M2})_{a.p.f.u.} + 1.956(1) \quad (3.6)$$

Due to the very low difference in the scattering factors of  $\text{Al}^{3+}$  and  $\text{Mg}^{2+}$  (the two cations are isoelectronic), it was not possible to directly locate the position of Mg and thus the refinements were carried out without considering this cation. However there is a clear correlation between the concentration of Mg in hibonite and the M3-O tetragonal bond distance; in fact, an elongation of the bond distance as a function of Mg content is observed (Fig.3.15). This assignment of Mg is in agreement with what was previously reported by Bermanec et al. (1996) and Nagashima et al. (2010) who suggest that divalent cations occupy the M3 site. The variation of the average M3-O bond length as a function of divalent cations content is the following:

$$d_{M3-O} = 0.063(2) \cdot M_{a.p.f.u.}^{2+} + 1.801(1) \quad (3.7)$$

where  $1.801(1)$  is the extrapolated tetrahedral bond distance of end-member hibonite, which is in excellent agreement with the value reported by Utsunomiya et al. (1988) and Hofmeister et al. (2004) for pure hibonite.

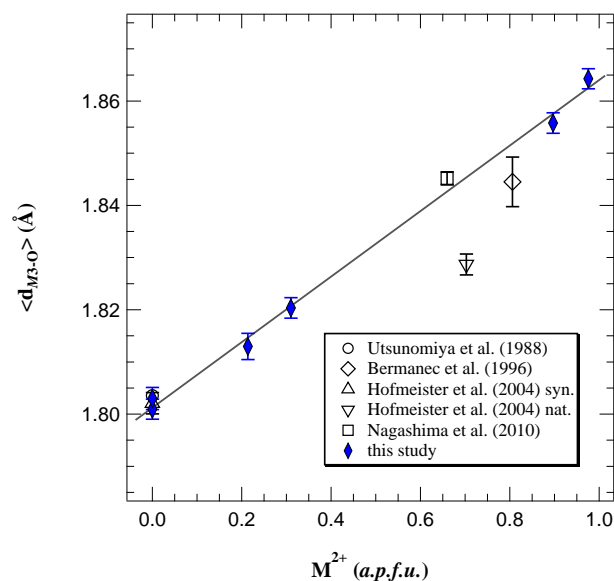


Figure 3.15: Average bond distances  $M3-O$  as a function of the sum of divalent cations substituting for Al. The solid line indicates a fit through the data points for this study ( $R^2 = 1.00$ ).

All atomic sites are influenced by the substitution of Ti and Mg into the structure of hibonite. Even for the sites fully occupied by Al, *i.e.*  $M1$  and  $M5$ , the coordination environment is modified by the movement of oxygen atoms bridging with atomic sites where substitution is occurring.

In particular the site  $M1$ , whose 6-coordinating  $O4$  oxygen are connected to the expanding tetrahedron  $M3$ , becomes more irregular as function of Ti and Mg content. This is clearly seen in the increase of the octahedral angle variance (OAV, Table 3.9), which is a measure of the distortion of the coordination environment; *i.e.* the closer the OAV is to zero, the more regular the octahedron is. This distortion is also associated with an increase in the bond distance  $M1-O4$  (Fig. 3.16-a) which is in the order of 0.5%, thus negligible since it is sensibly smaller than the corresponding increase of the unit cell volume.

The  $M5$  site is sandwiched between the layers where Ti and Mg are substituting for Al (Fig. 1.6), sharing  $O1$  and  $O2$  with  $M2$  and  $M3$ , respectively. However, as a result of the individual  $M5-O$  bond variations driven by Ti and Mg substitution in the adjacent sites, the average bond length for the  $M5$  site does not change as a function of the composition of hibonite (Fig. 3.16-b). Moreover, the  $M5$  site tends to become more regular as the substitution of Ti and Mg occurs into the structure of hibonite, *i.e.* the OAV decreases (Table 3.9).

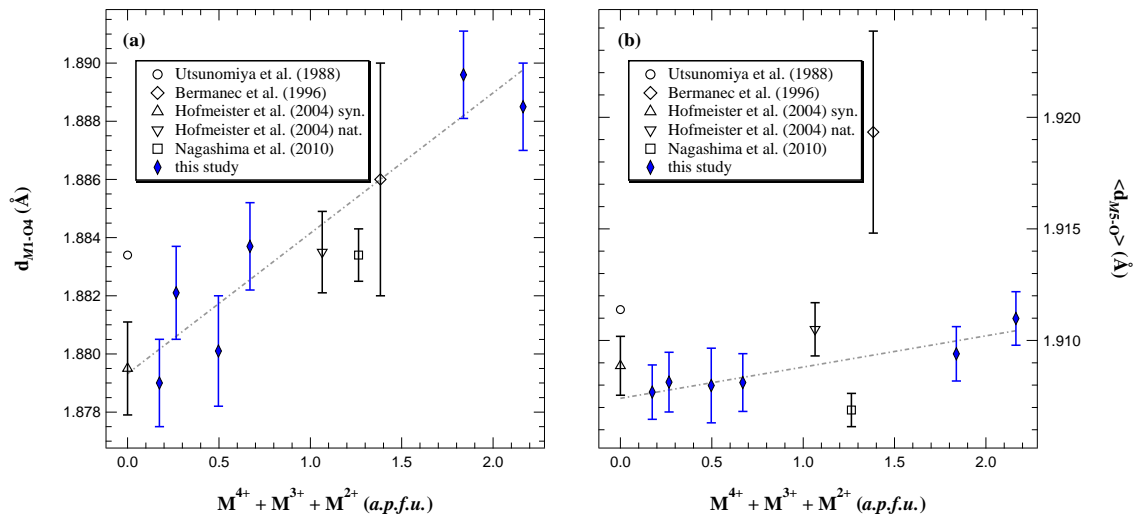


Figure 3.16: Variation of the bond length  $M1-O4$  (a) and of the average bond length  $M5-O$  (b) as a function of the sum of di-, tri- and tetra-valent cations substituting for Al; the dashed lines are guides to the eyes.

The 12-fold coordinated  $A$  site, which is where Ca is located into the structure of hibonite, is only slightly influenced by the substitution of Ti and Mg. A small increase in the average bond distance  $A-O$  as a function of Ti-Mg substitution (Fig. 3.17) is observed, however, as in the case of  $M5$  site, the variation of bond length is about 0.5 %, which is much smaller than the corresponding increase in unit cell parameters.

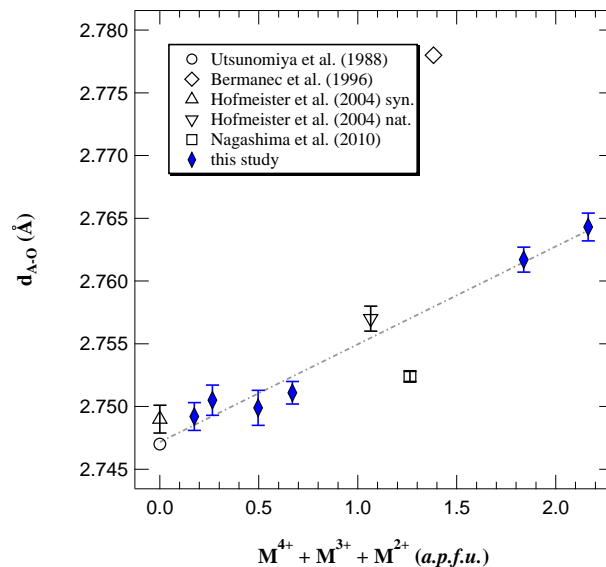


Figure 3.17: Variation of the bond distances  $A-O$  as a function of the sum of di-, tri- and tetra-valent cations substituting for Al; the dashed line is a guide to the eyes.

As already pointed out by Nagashima et al. (2010), the  $A$  site is too large for Ca, therefore, the  $Ca^{2+}$  cations are rattling inside the coordination cage, as shown by the large displacement factor at this site (Table 3.9), which even increases with increasing Ti and Mg content.

Table 3.9: Refined atomic coordinates, displacement parameters and angle variations for the analysed hibonites.

Site	Ref. <sup>‡</sup>	HBMT5_pc3	gel3-1	gel3-3	gel4-1	gel6-1	gel6-3
A	$U_{eq}$	0.0213(2)	0.0168(4)	0.0192(3)	0.0212(4)	0.0272(3)	0.0288(4)
M1	$U_{eq}$	0.0066(3)	0.0035(4)	0.0058(4)	0.0070(4)	0.0058(3)	0.0062(3)
M2	z	0.2414(2)	0.2411(2)	0.2588(3)	0.24075(21)	0.24140(18)	0.24107(16)
	$U_{33}$	0.017(3)	0.009(4)	0.015(4)	0.006(4)	0.022(3)	0.023(2)
	$U_{eq}$	0.0097(9)	0.006(1)	0.008(1)	0.006(1)	0.010(1)	0.013(1)
	Ti <sub>s.o.f.</sub>	0.10(1)	0.02(1)	0.03(2)	0.04(1)	0.13(2)	0.18(2)
M3	z	0.02785(4)	0.02792(5)	0.02792(6)	0.02783(6)	0.02731(5)	0.02727(5)
	$U_{eq}$	0.0069(2)	0.0037(3)	0.0069(3)	0.0074(3)	0.0081(2)	0.0091(3)
M4	z	0.19019(3)	0.19061(5)	0.19063(5)	0.19036(6)	0.18895(4)	0.18912(3)
	$U_{eq}$	0.0063(3)	0.0037(4)	0.0060(4)	0.0060(4)	0.0060(3)	0.0065(2)
	Ti <sub>s.o.f.</sub>	0.115(6)	0.05(1)	0.08(1)	0.07(1)	0.32(1)	0.413(8)
M5	x	0.16823(5)	0.16839(7)	0.16837(7)	0.16835(8)	0.16748(6)	0.16751(7)
	y	0.33646(9)	0.3368(1)	0.3368(2)	0.3367(2)	0.3350(1)	0.3350(1)
	z	0.89148(2)	0.89120(3)	0.89124(3)	0.89138(4)	0.89247(3)	0.89273(3)
	$U_{eq}$	0.0064(2)	0.0041(3)	0.0063(2)	0.0068(3)	0.00629(17)	0.0065(2)
O1	z	0.14956(9)	0.1489(1)	0.1490(1)	0.1493(2)	0.1503(1)	0.1504(1)
	$U_{eq}$	0.0076(4)	0.0038(5)	0.0059(6)	0.0071(7)	0.0078(4)	0.0081(5)
O2	z	0.94399(9)	0.9452(1)	0.9452(1)	0.9444(2)	0.9421(1)	0.9420(1)
	$U_{eq}$	0.0082(4)	0.0051(6)	0.0069(6)	0.0094(7)	0.0083(4)	0.0091(5)
O3	x	0.1808(2)	0.1808(2)	0.1808(3)	0.1808(3)	0.1808(2)	0.1802(2)
	y	0.3616(3)	0.3616(4)	0.3617(5)	0.3616(5)	0.3617(4)	0.3603(4)
	$U_{eq}$	0.0091(4)	0.0066(5)	0.0088(5)	0.0090(5)	0.0093(4)	0.0106(4)
O4	x	0.1542(1)	0.1551(2)	0.1550(2)	0.1545(2)	0.1524(2)	0.1518(2)
	y	0.3083(2)	0.3101(3)	0.3101(3)	0.3090(4)	0.3048(3)	0.3036(3)
	z	0.05254(6)	0.05196(7)	0.05212(7)	0.05222(9)	0.05323(6)	0.05325(6)
	$U_{eq}$	0.0083(3)	0.0074(4)	0.0050(4)	0.0085(4)	0.0092(3)	0.0094(3)
O5	x	0.50359(9)	0.5034(1)	0.5035(2)	0.5036(2)	0.5041(1)	0.5048(1)
	y	0.0072(2)	0.0069(3)	0.0071(3)	0.0072(4)	0.0082(3)	0.0096(3)
	z	0.14956(6)	0.14912(7)	0.14915(7)	0.14941(9)	0.14983(6)	0.14986(6)
	$U_{eq}$	0.0076(3)	0.0050(4)	0.0074(4)	0.0077(4)	0.0070(3)	0.0080(3)
$P_{\text{Ti}_{M4}:\text{Ti}_{M2}}$		2.3(1)	3.6(5)	4.2(4)	3.1(4)	4.8(1)	4.6(1)
Ti <sub>tot</sub>		0.32(2)	0.12(3)	0.19(3)	0.18(3)	0.77(3)	1.00(2)

<sup>‡</sup>most relevant refined and calculated parameters; the displacement factors  $U_{eq}$  and  $U_{33}$  are expressed in  $\text{\AA}^2$ . The ratio between Ti at the M4 and at the M2 sites ( $P_{\text{Ti}_{M4}:\text{Ti}_{M2}}$ ) has been calculated from the corresponding refined Ti<sub>s.o.f.</sub>; the total amount of Ti has been derived in the same way and it is expressed in atoms per formula unit of hibonite.

Table 3.10: Bond distances and geometrical parameters obtained from the structural refinements for the analysed hibonites.

Site	Par. <sup>‡</sup>	HBMT5_pc3	gel3-1	gel3-3	gel4-1	gel6-1	gel6-3
A	<A-O>	2.751(1)	2.749(1)	2.751(1)	2.750(1)	2.762(1)	2.764(1)
M1	M1-O4	1.884(2)	1.879(2)	1.882(2)	1.880(2)	1.890(2)	1.889(2)
	OAV	14.22	9.7627	10.3812	11.93	22.69	24.23
M2	M2-O1	2.010(5)	2.023(5)	2.024(6)	2.005(5)	2.010(5)	2.004(5)
	M2-O3	1.754(2)	1.753(2)	1.754(3)	1.755(3)	1.766(2)	1.764(2)
M3	M3-O2	1.837(3)	1.814(3)	1.815(3)	1.829(4)	1.880(3)	1.883(3)
	M3-O4	1.815(2)	1.797(2)	1.799(2)	1.808(2)	1.848(2)	1.858(2)
	<M3-O>	1.820(2)	1.801(2)	1.803(2)	1.813(3)	1.856(2)	1.864(2)
M4	M4-O3	1.976(2)	1.963(2)	1.964(2)	1.971(2)	2.002(2)	2.008(2)
	M4-O5	1.872(2)	1.874(2)	1.877(2)	1.874(2)	1.870(1)	1.881(1)
	<M4-O>	1.924(2)	1.919(2)	1.920(2)	1.922(2)	1.936(2)	1.945(2)
	M4-M4	2.626(2)	2.605(2)	2.605(2)	2.618(3)	2.694(2)	2.690(2)
M5	M5-O1	1.860(2)	1.845(1)	1.847(2)	1.854(2)	1.881(1)	1.888(1)
	M5-O2	1.970(2)	1.982(2)	1.982(2)	1.973(2)	1.948(2)	1.947(2)
	M5-O4	1.987(1)	1.998(1)	1.997(1)	1.993(2)	1.966(1)	1.964(1)
	M5-O5	1.822(1)	1.811(1)	1.813(1)	1.818(1)	1.848(1)	1.852(1)
	<M5-O>	1.908(1)	1.908(1)	1.908(1)	1.908(2)	1.909(1)	1.911(1)
	OAV	32.49	35.2302	34.7402	33.58	29.02	29.19

<sup>‡</sup>measured structural parameters; the bond lengths are reported in Å while the OAV are expressed in degrees.

## 4 Energy electron loss spectroscopy on synthetic hibonite

One of the principal aims of this thesis is the quantification of  $\text{Ti}^{3+}$  in hibonite by means of energy electron loss spectroscopy (EELS). This chapter focuses on the possible application to this mineral of an existing EELS calibration as well as on the development of an empirical calibration specific for hibonite which can be used to extract information about the  $\text{Ti}^{3+}$  content of natural hibonites.

### 4.1 The energy electron loss spectrum of Ti in hibonite

A typical example of energy electron loss (EEL) spectrum for the titanium  $L_{2,3}$  edge in hibonite collected for sample gel3, which contains only Ti and no Mg, synthesised at  $\log f\text{O}_2 = -11$  is shown in Fig. 4.1.

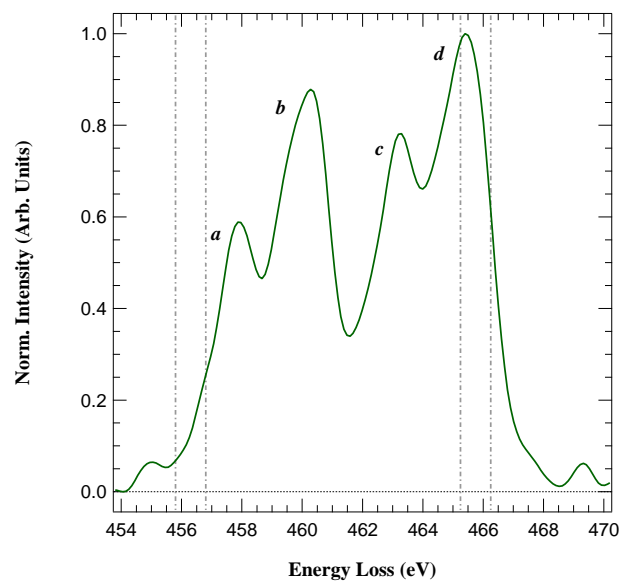


Figure 4.1: A typical EEL spectrum for the titanium  $L_{2,3}$  edge in hibonite (sample gel3-3). The vertical dashed lines indicate the integration windows for the calibration of  $\text{Ti}^{3+}/\text{Ti}^{\text{tot}}$  proposed by Stoyanov et al. (2007).

The spectrum consists of four main peaks labelled  $a, b, c$  and  $d$  that can be grouped in two pairs ( $a+b, c+d$ ) corresponding to the  $L_2$  and  $L_3$  white lines of titanium. The  $L_3$  white line appears at lower energy with respect to  $L_2$ ; their separation in energy is about 5.3 eV. The white lines are caused by the electronic transitions from the discrete  $2p$  levels to the  $3d$  band:  $2p^6d^n \rightarrow 2p^5d^{n+1}$ . In the case of  $\text{Ti}^{4+}$  ( $n = 0$ ) the  $3d$  bands are empty, while for  $\text{Ti}^{3+}$  ( $n = 1$ ) they are partially occupied. In both cases, the transitions originate from  $2p$  levels having different angular momentum  $j$ , which is equal to  $3/2$  and  $1/2$  for  $L_3$  and  $L_2$  white lines, respectively (Leapman and Grunes, 1982).

The peak splitting observed for both  $L_3$  and  $L_2$  edges can be interpreted in the frame of the Crystal Field Theory (CFT), in which the variations of local symmetry in transition metal complexes, *i.e.* Ti atoms bound to oxygen in the hibonite structure, are correlated with the changes in energy and degeneracy of the  $d$  orbitals. In CFT the coordination centres are identified by their point group symmetry using Schönflies notation, while the orbitals are named after their symmetry characters with respect to the symmetry operations of the point group. The case most commonly considered is the octahedral coordination  $O_h$  in which, as shown in Fig. 4.2, the five-fold degenerated  $d$  orbitals corresponding to a free ion ( $O$ ) are split into triply degenerated, stabilised  $t_{2g}$  and doubly degenerated, destabilised  $e_g$  levels (Cotton et al., 1999). Previous studies on the  $L_{2,3}$  edge in titanium oxides, in which the Ti atoms mostly occupy octahedrally coordinated environments, have assigned the peaks  $a$  and  $c$  to transitions to the  $t_{2g}$  energy levels, while the peaks  $b$  and  $d$  are assigned to transitions to the  $e_g$  orbitals (Brydson et al., 1987, 1989; Mitterbauer et al., 2003; Stoyanov et al., 2007; Cheynet et al., 2010). In the case of hibonite, the XRD measurements have shown that Ti occupies both a trigonally-distorted octahedral  $M4$  site and a trigonal bipyramidal  $M2$  site (Section 3.3.2), having point group symmetry  $C_{3v}$  and  $D_{3h}$ , respectively (Fig. 4.2). The octahedral distortion at the  $M4$  site is reflected by a partial loss of degeneracy from the  $t_{2g}$  orbitals, which are further split into one more stable  $a_1$  level and a slightly destabilised doubly degenerated  $e$  level, as shown in Fig. 4.2. The trigonal bipyramid coordination observed at the  $M2$  site causes the five  $d$  orbitals to split into three energy levels: two doubly degenerated non-bonding  $e''$  and  $e'$  levels as well as an anti-bonding  $a'_1$  orbital (Fig. 4.2). As a consequence of this complex coordination chemistry of Ti in hibonite, the energy difference between the peaks forming the  $L_3$  ( $a - b$ ) and  $L_2$  ( $c - d$ ) edges reflects the crystal field splitting of both octahedral and trigonal bipyramidal geometries. However, since Ti prefers the  $M4$  site with respect to the  $M2$  site, as revealed by the XRD refinements (Section 2.5, Table 3.9), the trigonally distorted octahedral crystal field splitting will dominate the EEL spectra.

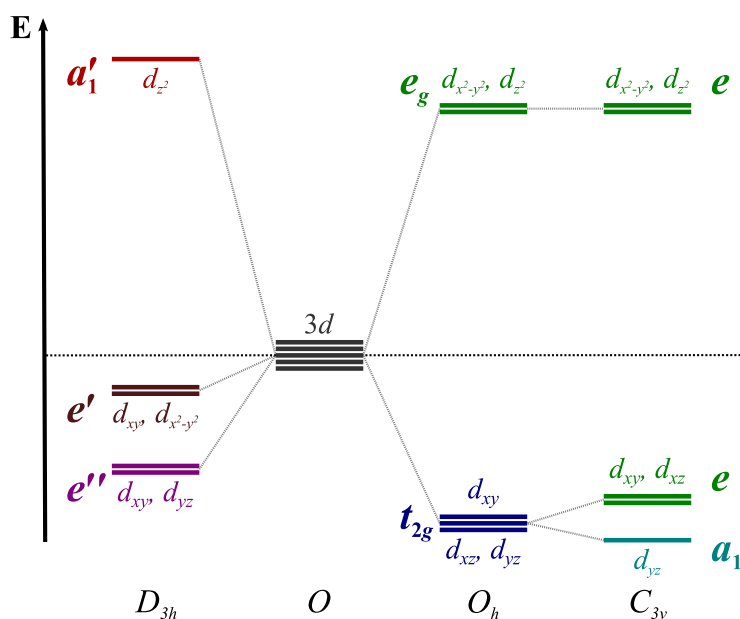


Figure 4.2: Crystal field splitting diagrams for octahedral ( $O_h$ ), trigonally-distorted octahedral ( $C_{3v}$ ) and trigonal bipyramidal ( $D_{3h}$ ) coordination environments compared to the spherical case for a free ion ( $O$ ). Ti in hibonite is present on  $C_{3v}$  and  $D_{3h}$  sites (Section 3.3.2).

## 4.2 Measurement of $Ti^{3+}$ in hibonite using energy electron loss spectroscopy

### 4.2.1 Application of a previous calibration method based on titanium oxides

In order to determine the  $Ti^{3+}/Ti^{tot}$  ratios from the EEL spectra measured in this study, firstly the method proposed by Stoyanov et al. (2007) has been considered. This calibration is based on the appreciable energy shift of the Ti  $L_{2,3}$  edge as a function of  $Ti^{3+}$  content as well as on features which are specific to the spectra of titanium oxides. The authors measured EEL spectra of titanium oxides with known  $Ti^{3+}/Ti^{tot}$  ratios in order to construct a calibration curve (Fig. 4.3).

A common phenomenon for many TEM-EELS measurements is that, due to the instabilities of the electromagnetic fields of the electron gun and of the spectrometer, the energy of the electron beam drifts with time. Despite the energy drift, the absolute energy of an EEL spectrum can be evaluated if one reference edge with known energy is simultaneously measured. Such calibration has been proposed by Stoyanov et al. (2007), who have acquired an *energy calibration spectrum* which includes the  $L$  edge of Ti, observed in the range from 454 to 469 eV, and the the  $\pi^*$  peak for the  $K$  edge of amorphous carbon, located at exactly 285 eV. In the calibration of Stoyanov et al. (2007), the core-loss spectrum is acquired with an energy dispersion of 0.05 or

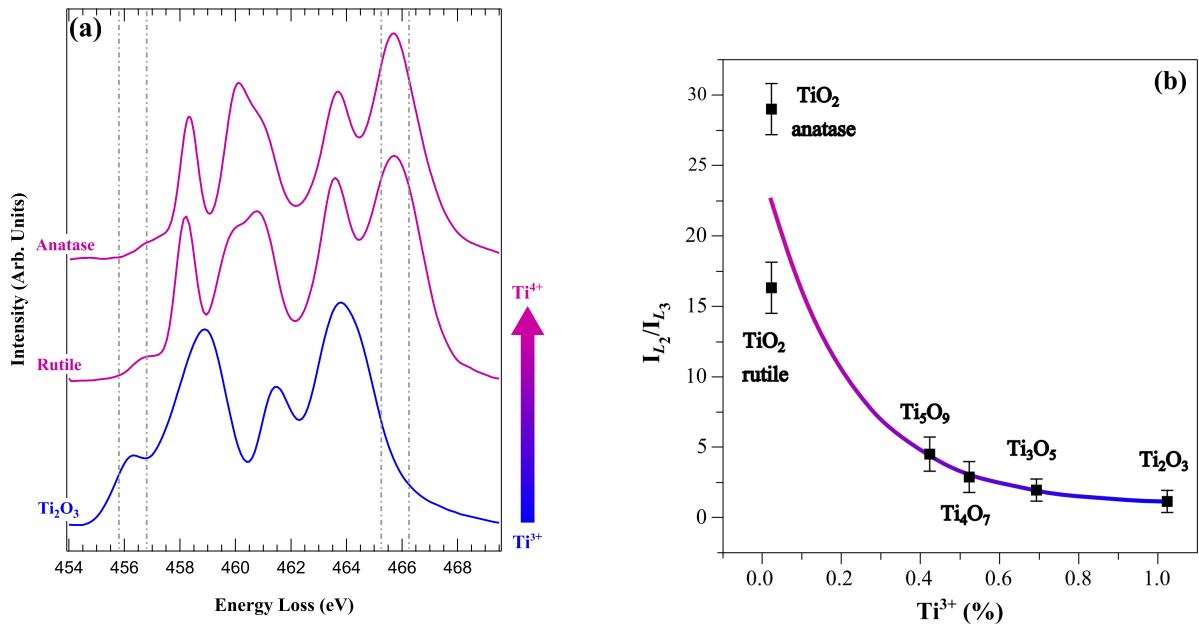


Figure 4.3: EELS calibration for the determination of  $Ti^{3+}/Ti^{tot}$  ratios, modified after Stoyanov et al. (2007). (a) Reference spectra for  $Ti^{3+}$  and  $Ti^{4+}$  standards; the dashed lines indicate the integration windows for  $L_3$  and  $L_2$  white lines of Ti. (b) Integrated intensity ratios as a function of  $Ti^{3+}$  content.

0.1 eV per channel, resulting in a resolution, measured as the FWHM of the zero-loss peak, of 0.7 to 1.0 eV. The energy calibration spectrum is measured using an energy dispersion of 0.3 eV per channel. In this configuration the zero-loss peak has a FWHM of 1.2 eV or larger, thus the peaks measured with the energy calibration spectrum appear broader and their position is more difficult to be determined accurately.

The  $Ti^{3+}/Ti^{tot}$  ratio has been estimated by Stoyanov et al. (2007) on the energy-calibrated core-loss spectrum by evaluating the intensities integrated over two windows of 1 eV width each. The first integration window is placed on the  $L_3$  edge of Ti, from 455.8 to 456.8 eV, while the second integration window is centred on the most intense peak of the  $L_2$  edge of Ti, ranging from 465.25 to 466.25 eV (Fig. 4.3-a). The intensity ratios measured for different titanium oxides have been then correlated to their  $Ti^{3+}$  content using the exponential empiric relationship illustrated in Fig. 4.3-b. The accuracy of the method, as stated by the authors, relies on the correct determination of the Ti  $L_{2,3}$  energy positions and it has been estimated to be  $\pm 10\%$  for concentrations of Ti down to 1%<sub>at</sub>.

As mentioned above, the energy calibration spectra are acquired using an energy dispersion of 0.3 eV per channel. During the evaluation of these spectra, the assignment of the position for the carbon *K* edge and subsequently for the Ti *L* edge might lead to an unavoidable arbitrary error. In the case of the Ti oxides studied by Stoyanov et al. (2007), these errors are minimised by the high count rate for the Ti *L* edge in the energy calibration spectra, making it easier to read the exact position of the peaks.

In the course of this study, the generally low signal to noise ratio in EEL spectra of hibonite was increased by repeating the measurements of each energy calibration spectrum up to six consecutive times and summing up the subsequently aligned spectra. However, for the acquisitions performed at 0.3 eV per channel, the peaks observed in the Ti *L* edge were broadened by the convolution with a large zero-loss peak (FWHM > 1.2 eV). Consequently, it was particularly difficult to determine an accurate position for the EELS peaks originating from hibonite samples with low Ti contents. In the attempt of having a better accuracy on the determination of the position of these peaks, the energy calibration spectra measured in this study were acquired using an energy dispersion of 0.2 eV per channel. An example of such a spectrum is shown in Fig. 4.4.

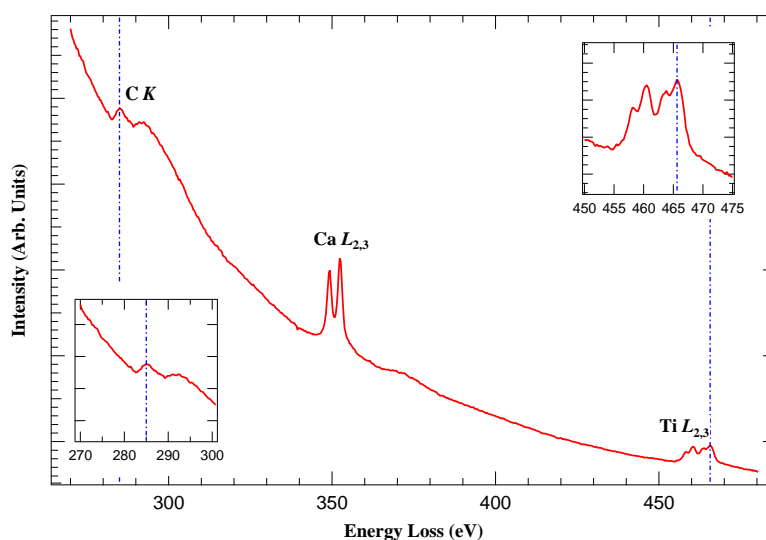


Figure 4.4: Energy calibration spectrum for sample FIB1S1B, acquired using an energy dispersion of 0.2 eV per channel. The dashed lines indicate the channels on which the position for the carbon *K* edge (inset left) was assigned to 285 eV and the energy of the peak *d* for the titanium *L*<sub>2,3</sub> (inset right) was determined.

The  $\pi^*$  peak of the C K edge, which is used as the absolute energy reference, is sometimes difficult to observe due to the fact that it precedes the broad  $\sigma^*$  peak of the C K edge and both peaks are superimposed to the intense exponential background typical of the EEL spectra, but a third, sharp and isolated signal is present at the centre of the calibration spectra of hibonite, *i.e.* the  $L_{2,3}$  edge of Ca (Fig. 4.4). The A site in the structure of the synthetic hibonites of this study (Fig. 1.6) is occupied exclusively by Ca, it is not subject to substitution and the influence of doping with Ti and Mg on the coordination environment of this cation may be considered negligible due to the large Ca-O distance (Table 3.10). Thus, the L edges of Ca can be considered to be at a constant position for different hibonites, making it a good internal reference for the position of the Ti L edges.

This assumption was verified by measuring the position of the  $L_{2,3}$  edge of Ca against the K edge of carbon, using an energy dispersion of 0.1 eV. The measurements were done on a representative wide range of samples, including the end-member pure hibonite (HB1) as well as natural and synthetic samples (Fig. 4.5).

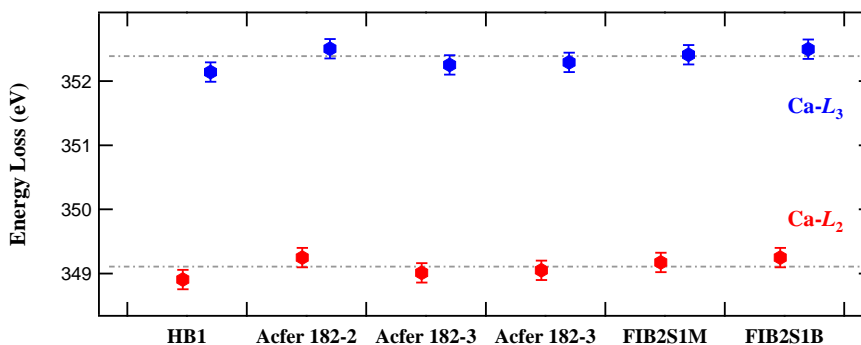


Figure 4.5: Energy calibration of the  $L_{2,3}$  edge of Ca against the reference position of the carbon K edge; the error bar for each data point is the value of energy dispersion (eV per channel) used during the acquisition of the spectrum.

According to Fig. 4.5, the position of the Ca  $L_{2,3}$  edge can indeed be considered constant within the measurement uncertainties, therefore it can be effectively used as an internal standard for the energy calibration of the Ti  $L_{2,3}$  edge in hibonite. The Ca  $L_3$  white line at 352.4(1) eV, *i.e.* the more prominent of the two peaks forming the Ca  $L_{2,3}$  edge, has been therefore chosen as the reference point for all spectra. The advantage of using the Ca  $L_{2,3}$  edge over the C K edge is that the energy calibration spectra can be acquired at higher resolution while relying on an internal standard rather than on carbon.

The  $\text{Ti}^{3+}/\text{Ti}^{\text{tot}}$  ratios obtained using the calibration reported by Stoyanov et al. (2007) and using the Ca  $L_{2,3}$  edge as energy reference are listed in Table 4.1 under the column labelled  $\text{Ti}_{\text{Ca } L_{2,3}}^{3+}$ . The variation of this quantity for the hibonite samples obtained from sol-gel precursors is shown in Fig. 4.6 as a function of oxygen fugacity at which they were prepared.

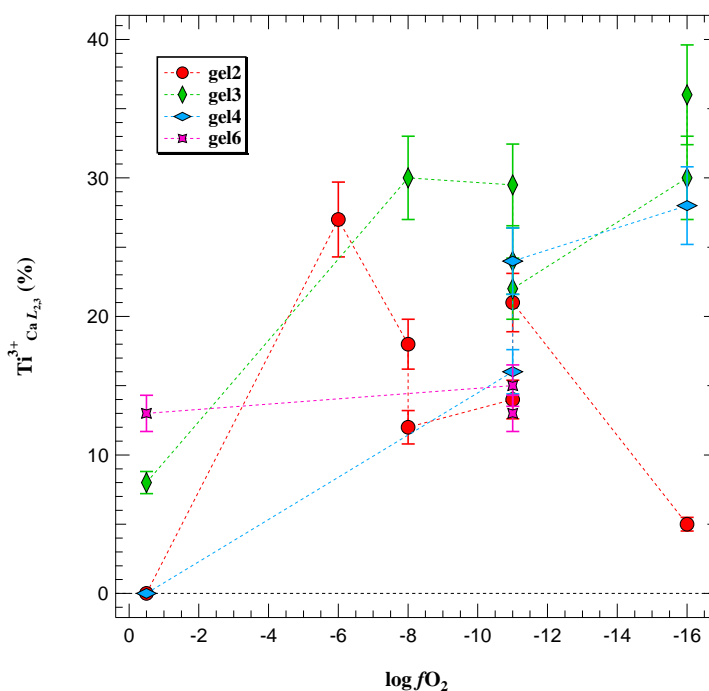


Figure 4.6:  $\text{Ti}_{\text{Ca } L_{2,3}}^{3+}$  (%) as a function of  $fO_2$  for the hibonite sample series obtained from the sol-gel precursors. The determination has been done by means of EELS according to the method proposed by Stoyanov et al. (2007), using the Ca  $L_{2,3}$  edge as energy reference.

The data show a large scatter and do not have any particular trend with respect to oxygen fugacity. For some of the samples synthesised in air the  $\text{Ti}^{3+}$  content appears to be quite significant in spite of the very oxidising conditions at which such samples have been synthesised. Moreover, for some sample series the concentration of trivalent titanium seems to decrease going towards more reducing conditions. It appears, therefore, that even after having fine-tuned the EELS calibration specifically for its use with hibonite, the calibration method does not seem to produce meaningful estimation of the  $\text{Ti}^{3+}$  content in this mineral. This is likely due to the fact that hibonite has a low bulk concentration of Ti, only a fraction of which is present as  $\text{Ti}^{3+}$ , thus generating a much weaker EEL signal for Ti and much subtle variations associated with the presence of  $\text{Ti}^{3+}$  instead of  $\text{Ti}^{4+}$ . In fact, whereas between the  $\text{TiO}_2$  and the  $\text{Ti}_2\text{O}_3$  samples presented by Stoyanov et al. (2007) there is a clear separation by 1.8 eV (Fig. 4.3), the hibonite samples synthesised at different oxygen fugacity conditions have a separation in energy which is on the order of the uncertainty deriving from the energy calibration (Fig. 4.7).

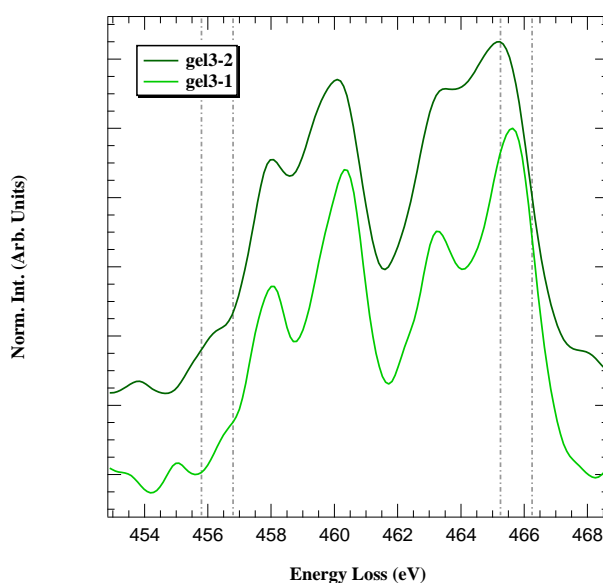


Figure 4.7: EEL spectra for the samples of gel3 series synthesised at  $\log fO_2 = -16$  and in air, which likely contain exclusively  $Ti^{3+}$  and  $Ti^{4+}$ , respectively. The dashed lines indicate the integration windows used in the calibration proposed by Stoyanov et al. (2007).

Furthermore, the variations in the spectral shape of hibonite are quite subtle (Fig. 4.7), in contrast with the large variation observed in the EEL spectra of different Ti oxides (Fig. 4.3-a), and reflect the fact that the surrounding and coordination environments of the Ti atoms vary less than in the oxides case. Finally, not all the spectral features described for the titanium oxides can be directly observed in the spectra of hibonite, either because the associated processes do not occur or the corresponding signals are convoluted into the noise, as for example the weak pre-peak observed in the spectra of rutile and anatase which is due to a spin-forbidden  $p_{3/2} \rightarrow d_{3/2}$  transition (Brydson et al., 1989; Mitterbauer et al., 2003).

Therefore, the  $Ti_{Ca}^{3+} L_{2,3}$  values obtained from this calibration method will not be further considered or discussed as they appear to do not represent trustworthy estimations for the concentration of this species in hibonite.

Table 4.1: Results for the  $\text{Ti}^{3+}$  determination by means of EELS on synthetic hibonite samples. The first column of values were calculated according to the method proposed by Stoyanov et al. (2007), using the Ca  $L_{2,3}$  edge as energy reference. The other columns represent data obtained with the new calibrations developed in this study (Section 4.2.2). The values of  $H_{peak}$  represent the *net peak heights* and are expressed in arbitrary normalised units, while  $\Gamma_0$  is the spectral width measured with the autocorrelation method.

Sample	$\text{Ti}_{\text{Ca } L_{2,3}}^{3+}$ (%)	$H_a$	$H_b$	$H_c$	$H_d$	$\Gamma_0$ (eV)	$\text{Ti}_{H_{peak}}^{3+}$ ( <i>a.p.f.u.</i> )	$\text{Ti}_{H_{peak}}^{3+}$ (%)
FIB1S1M	0.03(1)	0.257	0.580	0.195	0.484	1.655(3)	0	0
FIB1S1B2	0.08(1)	0.167	0.500	0.096	0.390	1.837(3)	0.10(1)	12(1)
FIB1S1B	0.12(1)	0.212	0.561	0.140	0.428	1.701(1)	0.06(1)	7.2(7)
FIB2S1M	0.29(3)	0.197	0.548	0.166	0.493	1.707(9)	0	0
FIB2S1B	0.39(4)	0.112	0.387	0.112	0.371	1.771(3)	0.13(1)	32(3)
FIB2S2C	0.21(2)	0.188	0.482	0.081	0.420	1.873(0)	0.08(1)	17(2)
FIB2S2D	0.01(1)	0.150	0.522	0.108	0.430	1.773(1)	0.06(1)	19(2)
HB-MT5	0.44(4)	0.171	0.503	0.133	0.431	1.740(1)	0	0
HB-MT5_pc3	0.50(5)	0.207	0.479	0.128	0.385	1.829(5)	0.05(1)	15(1)
gel2-1	0	0.199	0.534	0.116	0.445	1.751(1)	0	0
gel2-2	0.05(1)	0.158	0.464	0.089	0.362	1.885(1)	0.10(1)	26(3)
gel2-3_s1	0.21(2)	0.184	0.509	0.129	0.414	1.775(2)	0.04(1)	10(1)
gel2-3_s2	0.14(1)	0.160	0.503	0.098	0.387	1.832(3)	0.07(1)	18(2)
gel2-4_s1	0.12(1)	0.113	0.471	0.074	0.422	1.872(1)	0.03(1)	7.5(8)
gel2-4_s2	0.18(2)	0.181	0.518	0.118	0.404	1.757(2)	0.05(1)	13(1)
gel2-5	0.27(3)	0.170	0.499	0.143	0.433	1.794(6)	0.01(1)	4.2(4)
gel3-1	0.08(1)	0.162	0.508	0.112	0.417	1.779(3)	0	0
gel3-2	0.36(4)	0.047	0.279	0.001	0.137	2.284(2)	0.35(3)	93(9)
gel3-3	0.30(3)	0.132	0.400	0.093	0.312	1.987(2)	0.13(1)	51(5)
gel3-3R_s1	0.24(2)	0.069	0.361	0.071	0.207	2.137(1)	0.26(3)	100(10)
gel3-3R_s2	0.22(2)	0.097	0.365	0.052	0.268	2.104(1)	0.18(2)	76(8)
Ti3AS2B2	0.30(3)	0.053	0.199	0.026	0.111	2.352(5)	0.38(4)	100(10)
gel3-4	0.30(3)	0.159	0.471	0.092	0.330	1.794(1)	0.11(1)	48(5)
gel4-1	0	0.168	0.538	0.158	0.480	1.658(1)	0	0
gel4-2	0.28(3)	0.080	0.338	0.049	0.240	2.105(1)	0.26(3)	62(6)
gel4-3_s1	0.24(2)	0.168	0.521	0.110	0.359	1.888(2)	0.13(1)	36(4)
gel4-3_s2	0.16(2)	0.143	0.440	0.151	0.388	1.841(1)	0.10(1)	27(3)
gel6-1	0.13(1)	0.225	0.542	0.116	0.469	1.713(1)	0	0
gel6-3_s1	0.15(1)	0.046	0.375	0.024	0.286	2.283(1)	0.20(2)	17(2)
gel6-3_s2	0.13(1)	0.042	0.377	0.028	0.292	2.276(1)	0.19(2)	16(2)

#### 4.2.2 $Ti^{3+}$ in hibonite: a new calibration for energy electron loss spectroscopy

The EELS calibration proposed in this study aims at characterising the  $Ti^{3+}$  content in hibonite on the basis of fine spectral features rather than on the absolute energy position of the peaks. The observation at the base of this method is that the peaks of the EEL spectra for samples synthesised at very reducing conditions appear to be broader than the peaks of the corresponding samples synthesised in air (Fig. 4.8).

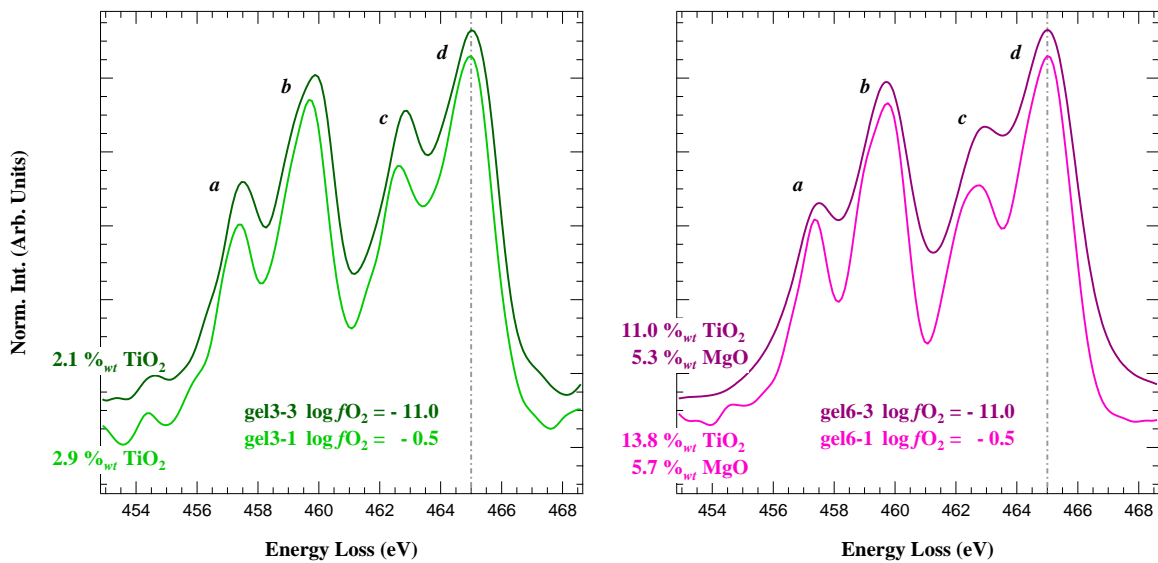


Figure 4.8: Energy electron loss spectra of the titanium  $L_{2,3}$  edge for different hibonite samples. The synthetic conditions and the EPMA analysis for Ti and Mg are reported on the plots. The dashed lines indicates the arbitrary reference point chosen to align the  $d$  peak for all spectra (465 eV).

Crystal field theory can provide the basis for rationalising the broadening of the peaks associated with the presence of  $Ti^{3+}$  by extending the consideration reported in Section 4.1 and taking into account how the local distortions of the atomic sites occupied by Ti may influence the EEL peak shapes. In general, distortion in the crystal field are associated with the removal of degeneracy from the energy levels of  $d$  orbitals, which generates more accessible levels and consequently allows a greater number of electronic transitions to take place and to contribute to the shape of the spectra. A typical cause of distortions for the coordination environments of transition metals is the (static) Jahn-Teller effect, according to which an atom lowers its crystal field energy by stabilising certain orbitals even at the cost of removing their degeneracy and lowering the symmetry of the centre (Jahn and Teller, 1937). The changes in intensity and shape of the peaks in the EEL spectra of Ti in hibonite can indeed be associated with variation in the  $Ti^{3+}$  content through the Jahn-Teller effect. In particular, the  $d^1$  electronic configuration of  $Ti^{3+}$  in  $C_{3v}$  coordination (Fig. 4.2) can increase the stabilisation of the half-occupied  $a_1$  level

driving it further apart from the  $e$  orbitals, while in the  $D_{3h}$  case the presence of  $Ti^{3+}$  can induce removal of the degeneracy from the  $e''$  orbitals. These effects can be linked to the broadening of the peaks  $a$  and  $c$  in the EEL spectra of Ti in hibonite. The Jahn-Teller effect can also be dynamic when the energy stabilisation of orbitals and the removal of degeneracy occur on the excited state for an electronic transition. For  $Ti^{3+}$  in hibonite this effect can take place as a removal of degeneracy from the anti-bonding  $e$  orbitals in the  $C_{3v}$  site, as previously reported for similar coordination environments (Cavallone et al., 1971; Brydson et al., 1989). This can be associated with the appearance of a shoulder towards lower energies of the  $b$  peak in many EEL spectra of hibonite, as shown, for example, in Fig. 4.8. This feature can be interpreted as a superposition of the peaks associated with the energy levels  $e$  and  $a'_1$  belonging to the crystal fields for  $C_{3v}$  and  $D_{3h}$  coordination environments, respectively (Fig. 4.2), and can become more prominent when the dynamic Jahn-Teller effect removes degeneracy from the  $e$  orbitals.

A well identifiable consequence of all these peak broadening effects is the relative intensity changes of the peaks forming the  $L_3$  and the  $L_2$  white lines, which can be observed as an increase of the signal corresponding to the minima in-between the peak pairs  $a - b$  and  $c - d$  (Fig. 4.8). Such intensity changes of the EEL spectra of hibonite samples can be correlated with their synthetic conditions, *i.e.* the samples exposed to more reducing conditions show higher intensities at the minimum between the peaks forming the  $L_3$  and the  $L_2$  edges.

Similar features were observed on soft X-ray absorption spectra, which are formally equivalent to EELS, of perovskite-type titanates and were qualitatively correlated to the oxidation state of titanium (Abbate et al., 1991). In analogue studies, based on EELS of  $LaTiO_3-SrTiO_3$  (Ohtomo et al., 2002) and  $LaAlO_3-SrTiO_3$  (Maurice et al., 2008) solid solutions, the  $Ti^{3+}/Ti^{tot}$  ratios have been quantified by fitting an unknown spectrum with a linear combination of two spectra corresponding to the end-members of the solid solutions, *i.e.* representing either the contribution of  $Ti^{3+}$  or  $Ti^{4+}$  on the perovskite EELS. This method is not directly applicable to the hibonite samples as they are not part of a solid solution and their bulk Ti content varies between each sample. Nevertheless, the peak heights and widths can be measured and used to calculate the  $Ti^{3+}$  content by using simple assumptions, as described in the following.

A simple way for quantifying the intensity changes observe in the EEL spectra of hibonite is to determine the relative heights of the four peaks. As shown in Fig. 4.9, for each peak the total intensity was measured from the baseline to its maximum on the normalised spectra, these quantities were labelled  $I_a$ ,  $I_b$ ,  $I_c$  and  $I_d$ . The height corresponding to the minima separating the peak pairs  $a - b$  and  $c - d$  were also measured, namely  $I_{ab}$  and  $I_{cd}$ . In order to evaluate only the peak height exceeding the corresponding peak minimum, the following quantities were calculated:

$$H_a = I_a - I_{ab} \quad H_b = I_b - I_{ab} \quad H_c = I_c - I_{cd} \quad H_d = I_d - I_{cd}. \quad (4.1)$$

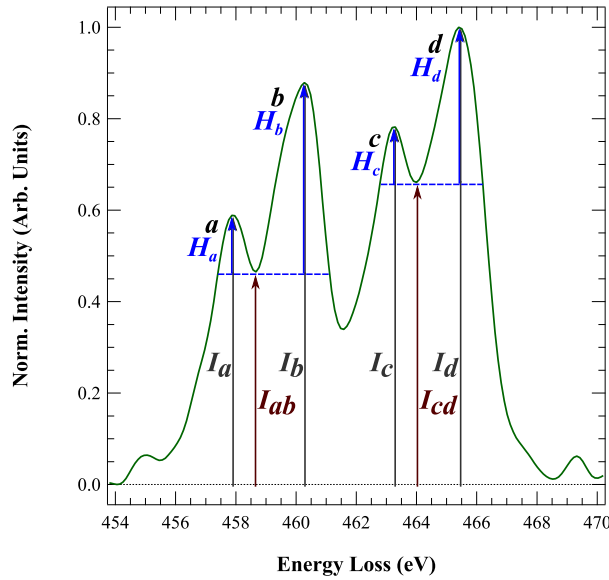


Figure 4.9: EEL spectrum for sample gel3-3 in which the heights measured on peaks and valleys are indicated by coloured arrows.

The values of  $H_{peak}$  are from this point on referred to as *net peak height*, and are reported in Table 4.1. In general, the values of  $H_a$  and  $H_c$ , corresponding to the least intense of the net peaks, are about three times smaller than  $H_b$  and  $H_d$  and hence it can be expected that they are affected by larger uncertainties. Therefore, only the net peak heights  $H_b$  and  $H_d$  have been considered for further evaluation. In Fig. 4.10 the variations of  $H_b$  and  $H_d$  for all samples from this study are reported as a function of the oxygen fugacity at which they were synthesised.

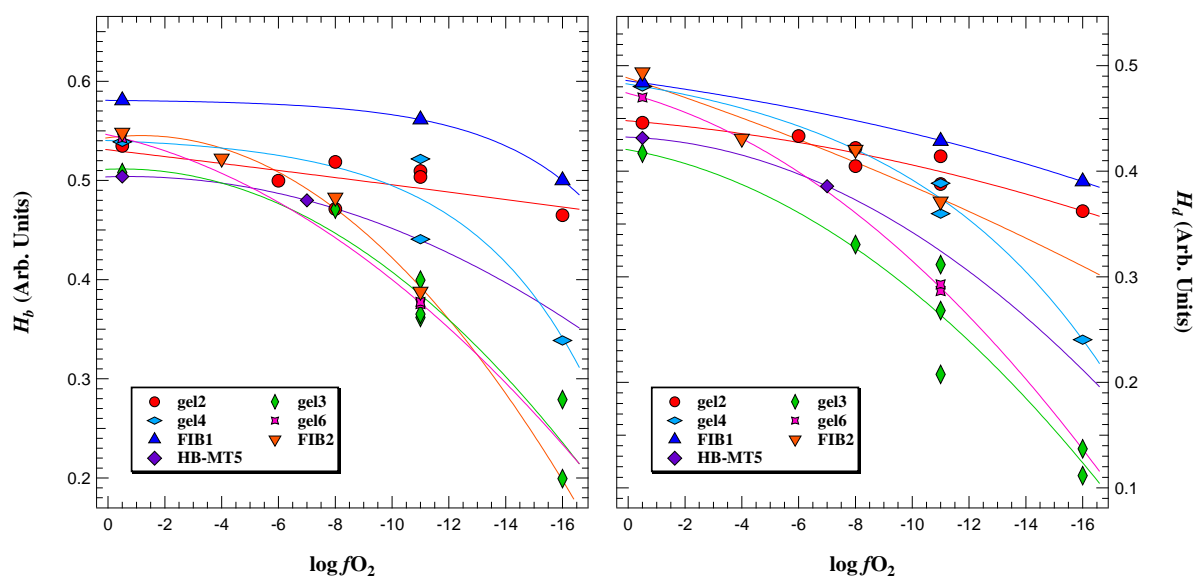
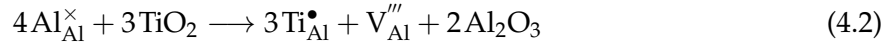


Figure 4.10: Net peak heights for the EEL spectra of synthetic hibonite plotted as a function of the  $fO_2$  conditions during their syntheses. The solid lines are guide to the eyes.

It can be observed that, for all the sample series, a decrease in oxygen fugacity, *i.e.* going towards more reducing conditions, is associated with a decrease in the values for  $H_b$  and  $H_d$ . This is consistent with the fact that the peak broadening due to the presence of  $Ti^{3+}$  causes an increase in  $I_{ab}$  and  $I_{cd}$ , with a corresponding decrease of the net peak heights. The nature of the  $H_{peak} - fO_2$  relationship is different for the various sample series due to the different amount of Ti present, however, there are some common traits. For example, over the first  $\sim 10$  log units of oxygen fugacity the variation of the net peak height from the samples in air to the corresponding reduced ones is relatively small; at the very reducing conditions, the values of  $H_b$  and  $H_d$  decrease more appreciably and the differences among the trends for the different sample series are more noticeable. The sample series in which the net peak heights, *i.e.* the  $Ti^{3+}$  content, seems to be more directly influenced by the changes in oxygen fugacity during synthesis is gel3. The samples gel4 and gel6 appear to behave similarly to gel3, even though the magnitudes of the  $H_{peak}$  changes are significantly smaller. The samples of FIB1, while following a trend similar to the other sample series, plot in a slightly higher range of  $H_{peak}$  values. For all series the value of net peak height for the samples synthesised in air are, as expected, always the largest, although the variation among the net peak height of the samples synthesised in air and belonging to different series is on the order of 0.15 arbitrary units of normalised intensity. The EEL spectra of these samples should be fairly similar in shape and width because, as demonstrated by optical absorption measurements, they contain exclusively  $Ti^{4+}$  (Section 5.1). The differences observed, therefore, can be attributed to the fact that the features of these

EEL spectra of hibonite are affected by the experimental signal/noise ratio which depends on the bulk Ti. Moreover, for the samples synthesised in air, the substitution of  $Al^{3+}$  with  $Ti^{4+}$  in absence of charge balance due to a divalent cation can result in the formation of cation vacancies, which could also affect the spectral width. The mechanism for which such vacancies can be formed is described in Eq. 4.2 using the notation proposed by Kröger and Vink (1956).



In order to take into account the differences between the EEL spectra of the various samples and allow for a direct comparison, the *normalised net peak heights*  $H_{peak_n}$  (Fig. 4.11) were calculated for each series using as normalising factors the values of  $H_{peak}$  corresponding to the samples synthesised in air. This new quantity has the advantage of bringing all the series together to a common unitary initial value of net peak height while preserving the relative changes between samples synthesised at different oxygen fugacities. An example of variation of the  $H_{peak_n}$  as a function of  $fO_2$  is reported for the peak  $d$  in Fig. 4.11.

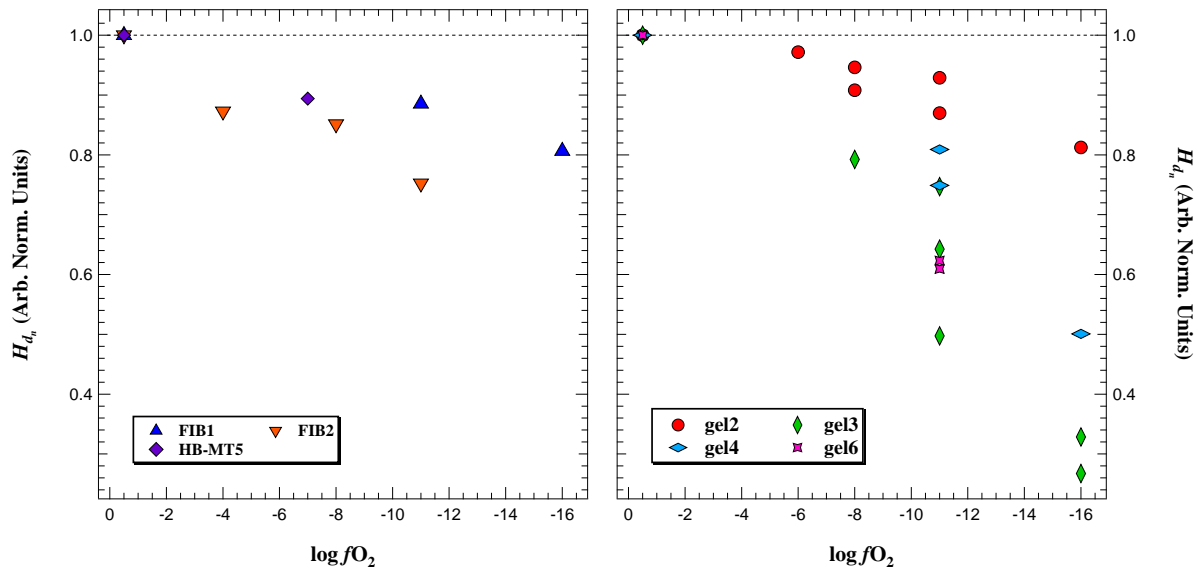


Figure 4.11: Normalised net peak  $d$  heights for the EEL spectra of hibonite obtained from oxide (left) and sol-gel (right) precursors plotted as a function of the  $fO_2$  conditions during their syntheses.

An alternative approach to the determination of the intensity changes of the EELS is the quantification of their line broadening. The direct approach would imply the determination of the spectral peak width as an average over the FWHM of a given number of Lorentzian or Gaussian profiles fitted to the EEL spectra. However, given the complexity of these spectra, this kind of deconvolution turned out to be an impractical approach and the autocorrelation method was chosen instead. This technique was introduced by Salje et al. (2000) for the analysis of peak broadening in IR spectra of mineral solid solutions and, in the present work, it has been applied to the EEL spectra of hibonite. The analysis of the spectra was carried out as follows. All the spectra, after exponential background subtraction, were subject to plural scattering deconvolution. The same value of FWHM, equal to 0.908(1) eV, was used for the Fourier-ratio processing of all the spectra, regardless of the actual width of the corresponding zero-loss peak. Forcing a core-loss spectrum to be deconvoluted with an energy resolution slightly different to the one associated with its measurement results in a change in the width of the spectrum. The effect of this variation has been estimated to be in the order of  $\pm 5\%$ , as evaluated on the final content of  $\text{Ti}^{3+}$  calculated for hibonite and it is considered to be in the range of the errors associated with the autocorrelation method. On the other hand, this approach of deconvolution allows obtaining core-loss spectra having the same resolution and file format, an essential pre-requisite for the autocorrelation analysis. The deconvoluted spectra were subsequently subtracted of the double-arctangent background and the arbitrary value of 465 eV was assigned in correspondence of the spectra maxima at the  $d$  peak.

The autocorrelation method is a very sensitive probe for the width of all the peaks contributing to an EEL spectrum, which also includes the spectral noise. Given the low content of Ti recorded in the spectra of hibonite, the process of removing plural scattering contributions through the Fourier-ratio method can introduce low intensity ripples in the spectrum, as it is possible to observe on some of the spectra reported in Fig. 4.8. This form of added noise has itself a width affecting the results of the autocorrelation method, it is hence, important to remove it. This has been done by cutting the spectrum at about 15% of its height (Fig 4.12) in order to eliminate the contribution from the Fourier transformations as well as all the low intensity processes that might take place such as  $L_1$  ( $2s \rightarrow 3d$ ) and  $d-d$  transitions. Finally, one of the requirements to apply the autocorrelation function is that the two ends of the processed signal are at zero, this was ensured by applying a linear baseline function to the cut spectrum, which was then normalised to unit.

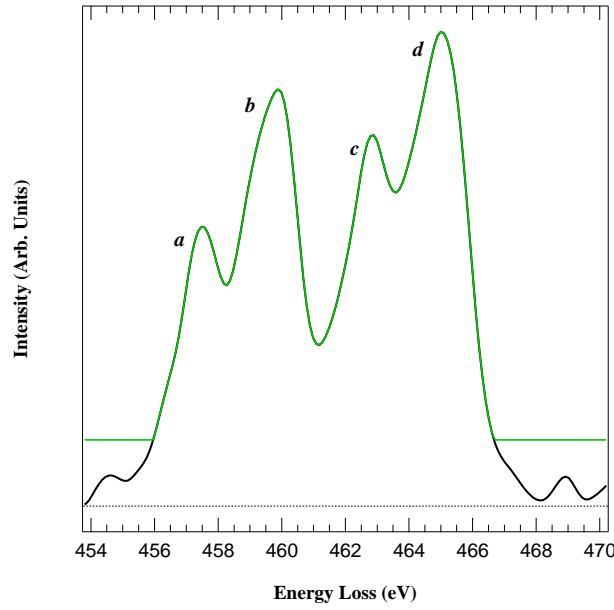


Figure 4.12: Example of noise reduction for sample gel3-3 realised by cutting the original spectrum (black curve) at  $\sim 15\%$  of its height and applying a linear baseline to obtain the spectrum actually used for the autocorrelation method (green curve).

The autocorrelation analysis consists of the convolution of a spectrum with itself, according to Eq. 4.3.

$$\text{Corr}[\mu(E, E')] = \int_{-\infty}^{+\infty} \mu(E + E') \mu(E) dE \quad (4.3)$$

where  $\mu(E)$  represents the EEL spectrum and  $\mu(E + E')$  is the same spectrum shifted by a certain energy  $E'$ . The calculated  $\text{Corr}[\mu(E, E')]$  function plotted against the energy shift  $E'$  is the so called *autocorrelation spectrum*, an example of which is shown in Fig. 4.13-a (black curve). The width of the central peak in the autocorrelation spectrum is due to the width of all the peaks in the EEL spectrum. It can be obtained by fitting a Gaussian curve of the form expressed in Eq. 4.4.

$$G_s(E') = k_0 \exp \left[ - \left( \frac{E' - k_1}{k_2} \right)^2 \right] \quad (4.4)$$

where  $k_0$  is a pre-exponential term giving the amplitude of the Gaussian curve,  $k_1$  is a zero-value offset parameter and  $k_2$  is a quantity related to the FWHM of the Gaussian curve, indicated as  $\Gamma$  (Eq. 4.5).

$$\text{FWHM}_{G_s} = \Gamma = \frac{2.354 k_2}{\sqrt{2}} \quad (4.5)$$

Given the direct proportionality between  $\Gamma$  and  $k_2$ , the latter can be used directly for the purpose of the method. Quantitative information can be extracted from the Gaussian fit of the autocorrelation spectrum in the limit of  $E' \rightarrow 0$  (Salje et al., 2000). This is realised performing a series of Gaussian fits around the central peak using a progressively smaller range of  $E'$ , as shown by the coloured curves in Fig. 4.13-a. The limit value for  $E' \rightarrow 0$ , called  $\Gamma_0$ , is extrapolated from a second order polynomial curve fitted through the values of  $k_2$  obtained from the different Gaussians, as illustrated in Fig. 4.13-b.

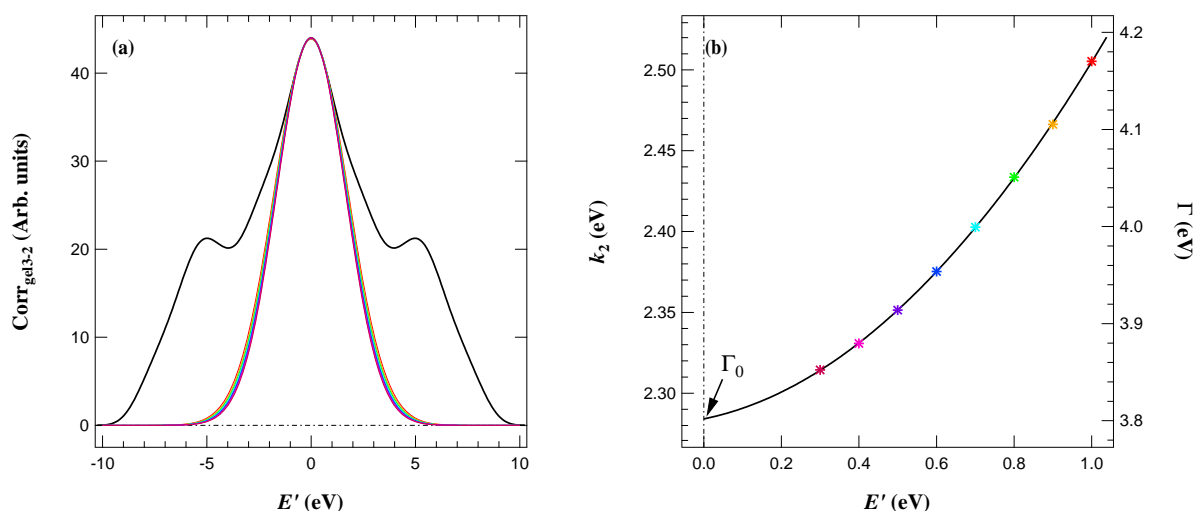


Figure 4.13: (a) Autocorrelation spectrum for sample gel3-2 (black curve) showing the Gaussian fits performed at progressively lower intervals around the spectrum maximum (coloured curves). (b) Variation of the parameter  $k_2$  and the Gaussian FWHM ( $\Gamma$ ) as a function of the fit interval (coloured stars). The black curve is a second order polynomial fit used to calculate  $\Gamma_0$ .

The values of  $\Gamma_0$  calculated with the autocorrelation method for all synthetic samples are reported in Table 4.1. As in the case of  $H_{\text{peak}}$ , the widths of the autocorrelation spectra also are influenced by the  $\text{Ti}^{3+}$  content as well as by the presence of defects, *e.g.* cation vacancies (Eq. 4.2). Therefore, in order to be able to compare the  $\Gamma_0$  for different samples, the *normalised spectral width*  $\Gamma_n$  were calculated scaling the spectral width for each sample with respect to the  $\Gamma_0$  of the corresponding sample synthesised in air (Fig. 4.14).

The  $\Gamma_n$ - $f\text{O}_2$  plot reported in Fig. 4.14 shows that a decrease in oxygen fugacity corresponds to an increase in spectral width. The variation of  $\Gamma_n$  has an opposite sign with respect to the changes in  $H_{\text{peak}}$  (Fig. 4.11), but shows a similar trend, *i.e.* most of the sample series show a little increase in spectral width over a large range of oxygen fugacity with gel3, gel4 and gel6 increasing more steeply at very reducing conditions.

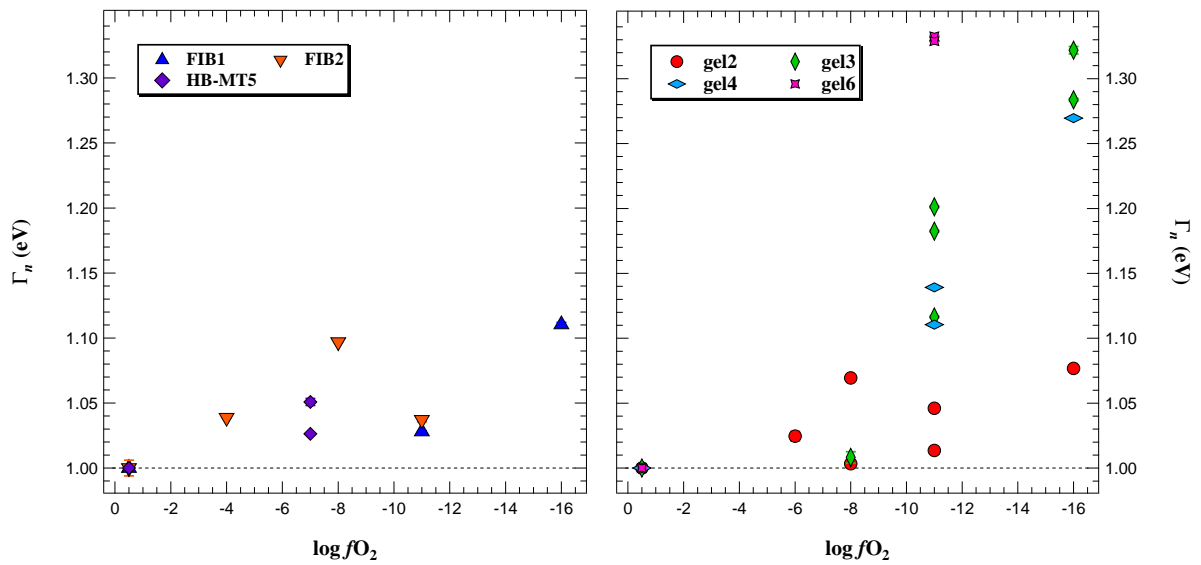


Figure 4.14: Normalised spectral width  $\Gamma_n$  for the EEL spectra of hibonites synthesised from oxide (left) and sol-gel (right) precursors plotted as a function of the  $fO_2$  conditions during their syntheses.

In Fig. 4.15 the net peak heights obtained for the hibonite samples are plotted against the corresponding measured spectral width from the autocorrelation method and it can be observed that the two quantities are linearly correlated. The solid lines reported in Fig. 4.15 are unconstrained fits through the datasets which show the direct relationship between  $\Gamma_0$  and  $H_{peak}$  as well as the equivalence between  $H_b$  and  $H_d$  (the two lines are parallel).

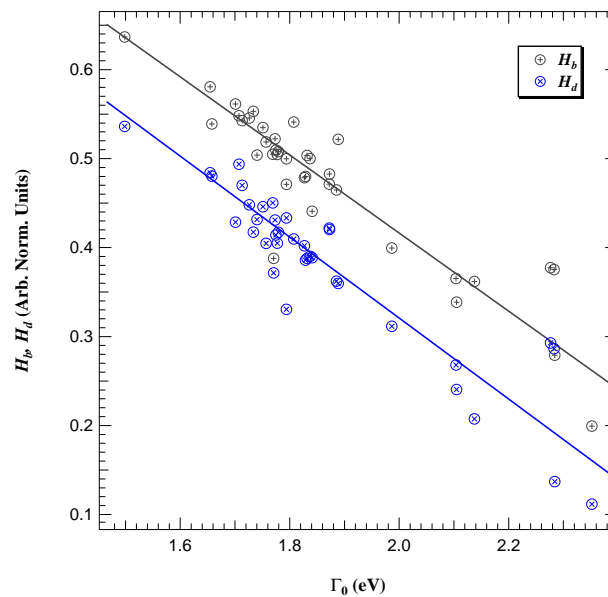


Figure 4.15: Net heights of the peaks  $b$  and  $d$  for all the EEL spectra of synthetic hibonites plotted as a function of the corresponding spectral width. The solid lines represent actual fits through the datasets ( $R^2 \approx 0.85$ ).

This corroborates the fact that both methods give equivalent results when used to evaluate the peak broadening in EEL spectra of hibonite associated with the presence of  $\text{Ti}^{3+}$ . The line broadening values expressed either as  $H_{b_n}$ ,  $H_{d_n}$  or  $\Gamma_n$  can be now used to determine the  $\text{Ti}^{3+}$  content in the different hibonite samples. Given the equivalence of these quantities, the procedure for obtaining the empirical calibration curve for  $\text{Ti}^{3+}$  is described in details only for  $H_{d_n}$ , with the understanding that the same procedure can be applied to the other line broadening measures. The advantage of using  $H_{d_n}$  resides in the fact that its application is more immediate and requires less manipulation of the EEL spectra as compared to the autocorrelation method. Moreover, the height difference between the peaks can be evaluated also for EEL spectra which are not provided as  $x$ - $y$  columns of data, *i.e.* measurements reported as plots on scientific publications or even spectra visualised during TEM-EELS sessions.

The first step for constructing a calibration curve to determine the  $\text{Ti}^{3+}$  content in hibonite is to obtain some specimens in which the  $\text{Ti}^{3+}/\text{Ti}^{\text{tot}}$  ratio is known. In the present study, the samples chosen as reference are those in which the only element substituting for Al is Ti. The absence of Mg allows making the assumption that the concentration of the  $\text{Ti}^{3+}$  which is incorporated into the structure of hibonite depends exclusively on the oxygen fugacity at which the samples were synthesised. The samples used as references are those of gel3 series, particularly gel3-1 and gel3-2 which were synthesised at 1550 °C, the former in air and the latter at the lowest oxygen fugacity,  $\log f\text{O}_2 = -16$ . Moreover, the sample Ti3AS2B2 also has been taken into consideration because it is analogous to gel3-2 but it has been synthesised from oxide precursors and at slightly lower temperature (1500 °C). The samples prepared at  $\log f\text{O}_2 = -16$  contain very similar bulk amounts of Ti. Since the synthesis conditions for gel3-2 and Ti3AS2B2 samples fall into the  $T$ - $f\text{O}_2$  stability field of  $\text{Ti}_2\text{O}_3$  (Fig. 4.16), it can be expected that all Ti present in these samples (0.37 and 0.35 *a.p.f.u.*, respectively) has an oxidation state of 3+.

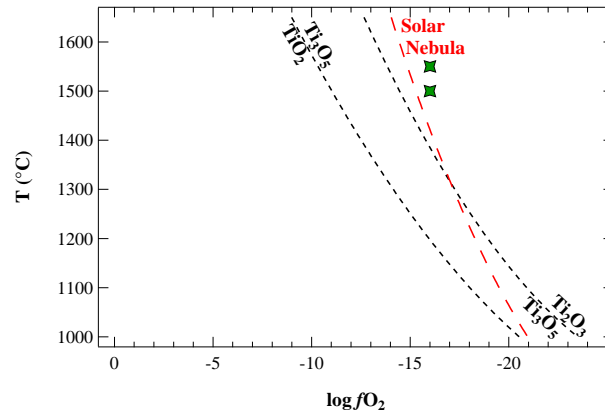


Figure 4.16: Oxygen buffer curves for titanium oxides, modified after Ihinger and Stolper (1986). The green stars represents the synthetic conditions for samples gel3-2 and Ti3AS2B2.

It has to be noted that the oxidation state of Ti incorporated into the structure of the mineral hibonite might not necessarily follow the titanium oxides buffer curves for all  $T$ - $fO_2$  conditions. However, the buffer curves are not used to finely constrain a  $Ti^{3+}/Ti^{tot}$  ratio corresponding to a single  $T$ - $fO_2$  point; they are rather used as a guide to define a range of temperatures and oxygen fugacities in which titanium is most likely to be completely reduced to  $Ti^{3+}$ . In the sample gel3-1, synthesised in air, all titanium is present as  $Ti^{4+}$ , as proven by optical absorption spectroscopy (Section 5.1). Having defined the hibonite standard samples for tetravalent and trivalent titanium, a calibration curve is obtained by plotting their  $H_{dn}$  against the estimated  $Ti^{3+}$  contents (Fig. 4.17). The simplest relationship among these three data points is expressed as a linear regression in the form of Eq. 4.6.

$$H_{dn} = 1.00(3) - 1.9(1) \cdot Ti_{a.p.f.u.}^{3+} \quad (4.6)$$

This expression has been applied to the normalised net peak height  $H_{dn}$  measured on the EEL spectra analysed in this study in order to calculate the corresponding concentrations of trivalent titanium in atoms per formula unit, which are reported in Table 4.1 under the columns labelled as  $Ti_{H_{peak}}^{3+}$ . It is important to highlight that the calibration, being essentially a two-point regression lines, assumes a linear dependence of the normalised net peak height  $H_{dn}$  on the absolute concentration of  $Ti^{3+}$ . This might not necessarily be the case and the actual  $H_{dn}$ - $Ti^{3+}$  dependence could be described by a more complex function than a simple straight line. However, the calibration has been constructed using the samples for which it is safest to assume the concentration of  $Ti^{3+}$  and given the paucity of data points, a straight line is the only possible reliable fit. Nevertheless, as it is shown in Section 5.2, the  $Ti^{3+}$  contents measured by means of

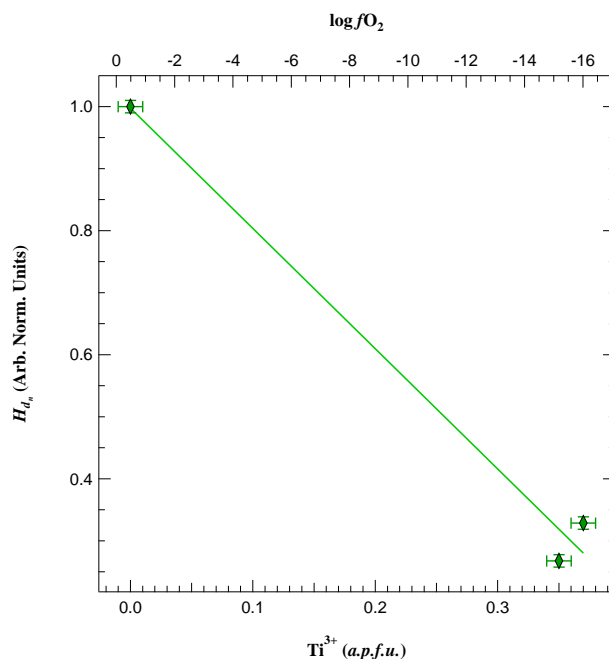


Figure 4.17: Dependency of the normalised net peak height  $H_{dn}$  on the constrained  $Ti^{3+}$  contents for the samples gel3-1, gel3-2 and Ti3AS2B2. The solid line is a fit through the data ( $R^2 = 0.98$ ) and represents the calibration used to derive the concentration of trivalent titanium from all the ELL spectra measured in this study.

this method give results consistent with the UV/Vis spectroscopic measurements, suggesting that the uncertainties introduced by this simple fit are still acceptable for determining the  $Ti^{3+}$  concentrations in hibonite.

The  $Ti^{3+}/Ti^{tot}$  ratios ( $Ti_{\%mol}^{3+}$ ) have been calculated using the  $Ti^{3+}$  content estimated from the EELS measurements and the bulk Ti concentration obtained from the EPMA, expressed both as *atom per formula unit*. The variation of this last quantity as a function of the oxygen fugacity for all hibonite samples is reported in Fig. 4.18. Based on calculation of the propagated uncertainties and on the estimation of  $Ti^{3+}$  contents for repeated EELS measurements, the error bars in Fig. 4.18 are estimated to be  $\pm 10\%$ , which also represents the estimated error for this new calibration method.

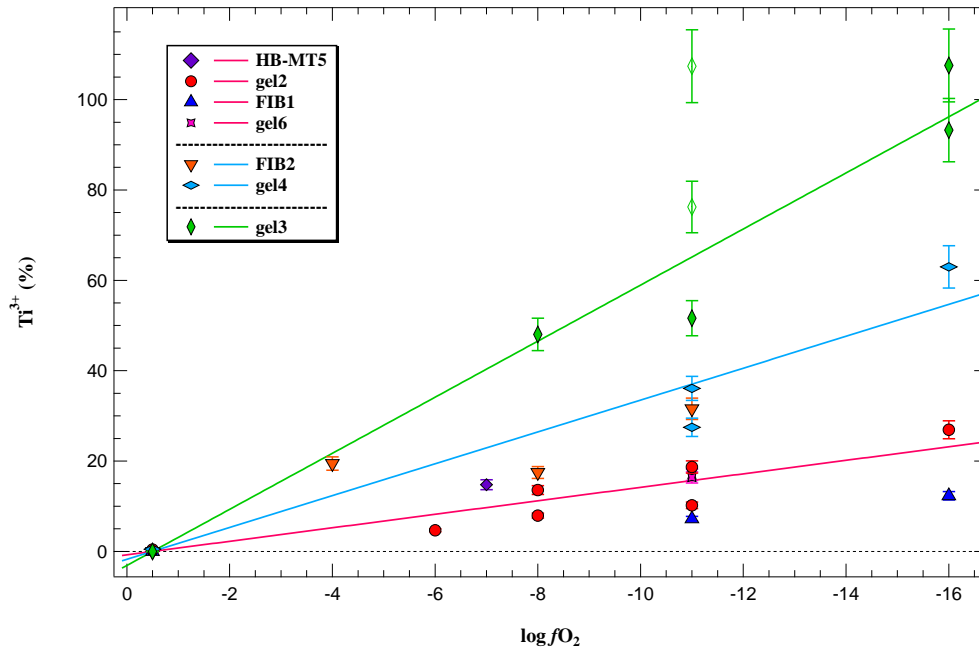


Figure 4.18: Variation of the molar percentage of  $Ti^{3+}$  as a function of  $fO_2$  for the hibonite samples analysed in this study. The solid lines represent fits performed on the groups of datasets (Table 4.2), group I is plotted in pink ( $R^2_{\text{group I}} = 0.66$ ), group II in blue ( $R^2_{\text{group II}} = 0.74$ ) and group III in green ( $R^2_{\text{group III}} = 0.83$ ).

The molar fraction of  $Ti^{3+}$  appears to correlate linearly with the oxygen fugacity, thus the datasets were fitted using the linear Eq. 4.7 which takes into account the fact that the concentration of  $Ti^{3+}$  is null for samples synthesised in air and that the origin has to be shifted by 0.5 log units to reflect the actual oxygen fugacity at such conditions.

$$Ti_{\%mol}^{3+} = \Phi_{Ti^{3+}} \cdot (\log fO_2 + 0.5) \quad (4.7)$$

The slope of the fitted lines has been indicated with  $\Phi_{Ti^{3+}}$  and the values obtained for this parameter are reported in Table 4.2.

From the analysis of Fig. 4.18 and Table 4.2 it can be observed that the various sample series are grouped into three categories according to their  $\Phi_{Ti^{3+}}$ , *i.e.* their sensitivity to oxygen fugacity variations. For each group a calibration line has been calculated performing a fit through the data from samples obtained using the sol-gel synthesis. These samples have been chosen over those synthesised from oxide precursors because they are chemically more homogeneous (Tables 3.4 and 3.5) and therefore can be considered to have been completely equilibrated synthesis conditions. Note that for the gel3 samples, the fit has been performed excluding the measurements for the specimens gel3-3R (open green diamonds). Such samples are hibonites synthesised at  $\log fO_2 = -16$  and re-equilibrated at  $\log fO_2 = -11$  for 15 h. Their  $Ti^{3+}$  content

appears clearly similar to that of gel3-2 suggesting that hibonite can maintain the imprint of the oxygen fugacity conditions at which it was formed at least for the short period used for the re-equilibration run (Section 7.2).

Table 4.2: Results obtained from the linear fits performed on the  $\text{Ti}_{\text{mol}}^{3+} - f\text{O}_2$  relationship for the hibonite sample series. The last column reports the ratio of Ti over Mg bulk contents measured by means of EPMA and averaged along the sample series.

Samples		$\Phi_{\text{Ti}^{3+}}$	$\text{Ti}_{\text{avg}}^{\text{tot}}/\text{Mg}_{\text{avg}}$
group I	HB-MT5	-1.5(1)	1.08
	gel6		1.13
	FIB1		1.14
	gel2		1.15
-----			
group II	FIB2	-3.4(3)	1.48
	gel4		1.57
-----			
group III	gel3	-6.2(4)	$\infty$

The  $\text{Ti}^{\text{tot}}/\text{Mg}$  ratios reported in Table 4.2 as an average over the EPMA for each sample series are very similar for the samples belonging to each group, suggesting that such quantity plays a major role in determining the  $\text{Ti}^{3+}$  amount in hibonite.

The first group of samples have the smallest  $\Phi_{\text{Ti}^{3+}}$  and the most balanced chemical formula, the calibration line have been calculated performing a fit through sample series of gel2 and gel6. In the case of the second group, the  $\text{Ti}^{3+}$  contents increase more steeply as a function of  $f\text{O}_2$ , these samples are characterised by a significant excess of Ti over Mg and their calibration line is based on gel4 samples. The samples of gel3 clearly form a group on their own as they show a much greater value of  $\Phi_{\text{Ti}^{3+}}$  due to the fact that they are Mg-free.

The grouping of the samples can be clearly visualised by plotting the molar percentage of  $\text{Ti}^{3+}$  as a function of  $\text{Ti}^{\text{tot}}/\text{Mg}$  for each individual sample synthesised at low oxygen fugacity, as shown in Fig. 4.19. In this plot the samples synthesised in air and the gel3 series are not reported because the former contain only  $\text{Ti}^{4+}$  (Section 5.1) and the latter does not contain Mg. It is evident that the samples of gel2 and gel6 belong to the same group despite the fact that they have very different bulk contents of Ti and Mg. Moreover, it can be seen that the samples of group I plot across a range of about 30 % of  $\text{Ti}^{3+}$  concentration, while this quantity is greater in the case of group II (up to around 60 %).

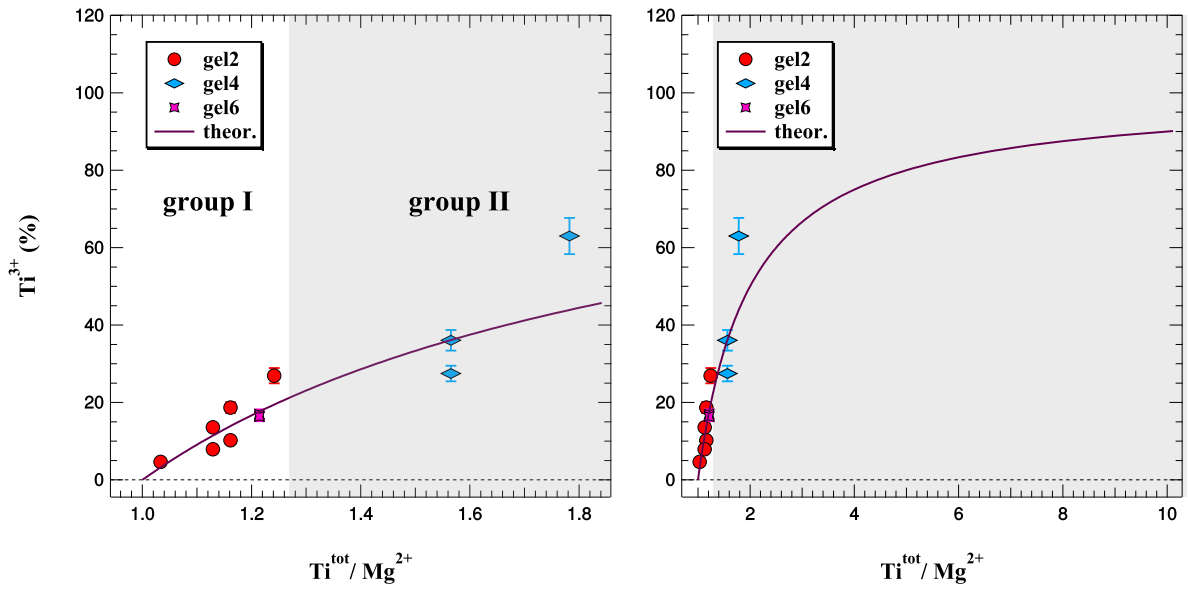


Figure 4.19: Variation of the molar percentage of  $Ti^{3+}$  as a function of  $Ti^{tot}/Mg$  for the hibonite samples analysed in this study. The purple line is a plot of Eq. 4.8. The plot on the left shows a limited range of  $Ti^{tot}/Mg$  ratio and indicates the arbitrary separation between the sample groups I and II. The plot on the right is reported with the purpose of showing the variation of Eq. 4.8 over larger values of  $Ti^{tot}/Mg$  ratio.

The purple curve shown in Fig. 4.19 corresponds to the relationship reported in Eq. 4.8, which is a theoretical function that links the  $Ti^{tot}/Mg$  ratio with the concentration of  $Ti^{3+}$ . This relationship has been derived taking into account that the  $Ti^{tot}/Mg$  ratios are always positive for synthetic hibonites, thus allowing only the amount of Ti present as 3+ to be in excess with respect to Mg.

$$\begin{aligned}
 Mg &= Ti^{4+} = Ti^{tot} - Ti^{3+} \\
 \frac{Mg}{Ti^{tot}} &= \frac{Ti^{tot} - Ti^{3+}}{Ti^{tot}} \\
 \frac{Ti^{tot}}{Mg} &= \frac{1}{1 - Ti^{3+}(\%)} \quad (4.8)
 \end{aligned}$$

The only samples that deviate from this theoretical relationship are gel4-2 and gel2-2 which were synthesised at the most reducing conditions ( $\log fO_2 = -16$ ). This indicates that the crystal chemistry of hibonite plays a major role in controlling the  $Ti^{3+}$  contents in hibonite with oxygen fugacity being an important factor only at very reducing conditions. Hence, in order to extract information regarding the oxygen fugacity conditions that natural hibonites have experienced, it is essential to consider their  $Ti^{tot}/Mg$  ratios and to apply the appropriate  $Ti^{3+}$ - $fO_2$  calibration line to the EELS results. The application of this calibration to natural samples is presented in Section 6.2.

## 5 *Optical absorption spectroscopy on hibonite*

UV/Vis spectroscopy on hibonite has been used in the literature as a qualitative estimation of  $\text{Ti}^{3+}$ - $f\text{O}_2$  relationships (Ihinger and Stolper, 1986). The UV/Vis spectra reported in this Chapter are intended to be a follow-up and an extension of these previous observations. They have been collected on single crystals rather than on polycrystalline materials, taking particular care in orienting the analysed samples. These spectra can provide quantitative information on the electronic structure for the coordination environment of transition metals in hibonite.

### 5.1 *The UV/Vis spectrum of Ti in hibonite*

Typical UV/Vis absorption spectra of Ti-Mg-bearing hibonites are shown in Fig. 5.1 and a list of the spectra acquired in this study is reported in Table 5.1 together with the intensity and position of the peak maximum. The thickness of the sections measured by means of confocal microscopy (Section 2.7) is also listed. In the case of samples for which the sizes of the synthesised crystals were large enough to allow acquiring spectra on single grains, the measurements were performed with polarised light on oriented sample. In the other cases, unpolarised light was transmitted through a polycrystalline portion of the non-oriented specimen, as done in the previous study of Ihinger and Stolper (1986).

The UV/Vis spectra of hibonite are characterised by the presence of a prominent absorption band centred around  $14000\text{ cm}^{-1}$  or  $715\text{ nm}$  (Table 5.1, Fig. 5.1) which covers a significant range of wavenumbers, having FWHM up to about  $2500\text{ cm}^{-1}$ . Moreover, the measurements are characterised by an increasing amount of noise above  $20000\text{ cm}^{-1}$  as shown, for example, on the raw spectra for the samples of gel6 series reported in Fig. 5.1-a. This noise is due to the particular light source available on the spectrometer used, hence it was not possible to resolve any feature above this spectral region. Before evaluation, the spectra were smoothed by means of a polynomial fit with 14 to 18 terms; the measurements for samples of the gel6 series are reported as raw (Fig. 5.1-a) and smoothed (Fig. 5.1-b) spectra for comparison.

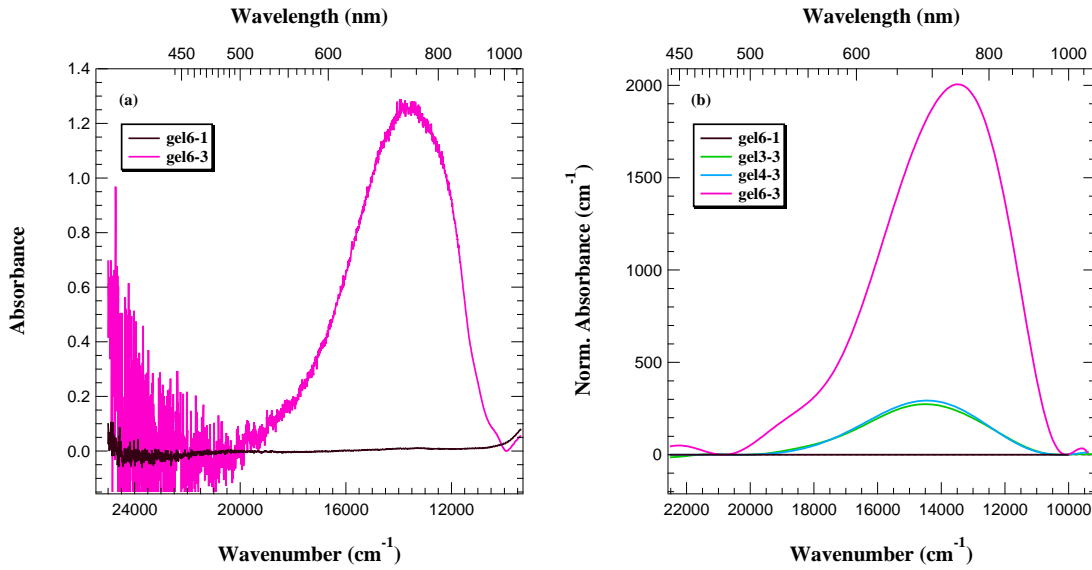


Figure 5.1: Typical UV/Vis absorption spectra of Ti-Mg-bearing hibonites synthesised at  $\log f_{\text{O}_2} = -11$  and in air. (a) Raw spectra for gel6 samples. (b) Smoothed and thickness-normalised spectra for different sample series.

The only optically active species present in the structure of the hibonites synthesised in this study is titanium, which is present with electronic configuration  $d^0$  or  $d^1$ , corresponding to  $\text{Ti}^{4+}$  and  $\text{Ti}^{3+}$ , respectively. The spectra of synthetic hibonites equilibrated in air should contain exclusively  $\text{Ti}^{4+}$  thus their UV/Vis spectra should be featureless. This is indeed confirmed by experimental measurements as it can be observed, for example, for the spectrum of sample gel6-1 reported in Fig. 5.1 (black curve).

Table 5.1: UV/Vis absorption spectra acquired in this study. The peak intensities and positions with the corresponding uncertainties (given in brackets) are referred to the average over spectra measured on different crystals for the same sample.

Sample name	Polarisation direction	Thickness (cm)	Absorbance max. position ( $\text{cm}^{-1}$ )	Absorbance max. intensity
gel2-1	unpol	0.00160	/	0
gel2-2	unpol	0.00170	14215(49)	0.201(4)
gel2-3	unpol	0.00190	14274(234)	0.234(3)
gel2-5	$c \parallel E$	0.00100	13900(0)	0.104(0)
gel3-1	$c \parallel E$	0.00170	/	0
gel3-3	$c \parallel E$	0.00170	14457(9)	0.57(2)
gel4-1	$c \parallel E$	0.00100	/	0
gel4-3	$c \parallel E$	0.00100	14480(0)	0.26(7)
gel6-1	$c \parallel E$	0.00320	/	0
gel6-3	$c \parallel E$	0.00063	13532(122)	1.4(2)
gel6-5	$c \parallel E$	0.00118	13228(5)	1.31(3)

The UV/Vis spectra collected in this study are similar to those previously reported by Ihinger and Stolper (1986) for the hibonite *Blue Angel* (Armstrong et al., 1982), having formula  $\text{Ca}_{1.01}\text{Al}_{11.17}\text{V}_{0.10}\text{Cr}_{0.01}\text{Fe}_0\text{Mg}_{0.34}\text{Ti}_{0.35}\text{O}_{19}$ , and for synthetic hibonites having similar composition to the Blue Angel (BA). The UV/Vis spectra of two of their synthetic samples, BA-2-15 and BA-VFC-2, synthesised at oxygen fugacity and temperature conditions similar to the present work and that of the natural hibonite are reported in Fig. 5.2 together with the UV/Vis spectra of gel4-3, which among all samples synthesised in this study has a Ti-Mg-content closer to that of BA. All spectra have a prominent absorption band at 715 nm, including the natural

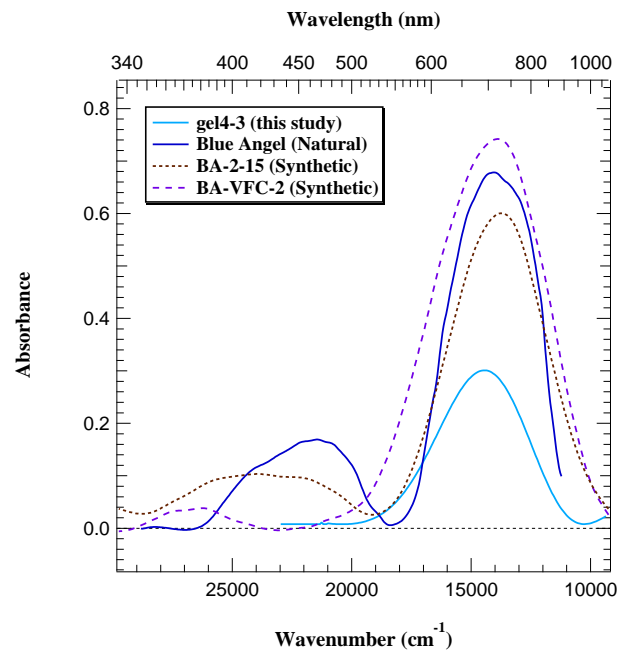


Figure 5.2: UV/Vis absorption spectra for sample gel4-3 compared with the spectra measured by Ihinger and Stolper (1986) both on natural (dark blue solid line) and synthetic (dashed lines) hibonites. The samples BA-2-15 and BA-VFC-2 have a nominal composition corresponding to BA with the latter being V, Cr and Fe free; they were synthesised at  $1430\text{ }^{\circ}\text{C}$  and at  $\log f_{\text{O}_2} = -12.7$  and  $-10.8$ , respectively. The original spectra from Ihinger and Stolper (1986) have been subtracted of a large (polynomial) background in order to be more easily compared with the spectrum from this study.

hibonite. The comparison, however, can be done only qualitatively because the spectra reported by Ihinger and Stolper (1986) were collected using unpolarised light and normalised using just rough estimations for the thickness of the thin sections.

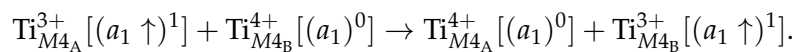
The spectra from Ihinger and Stolper (1986) reveal a second band at wavenumbers above  $20000\text{ cm}^{-1}$  whose peak maximum varies from sample to sample and which is either not present or not resolvable in the measurements of this study. This band occurs at higher wavelength and with greater intensity in the spectrum of BA and it appears broader and less intense in the spectrum of the sample BA-2-15 while it is weaker and at much larger wavenumbers in the spectrum of BA-VFC-2 which is V-, Cr- and Fe-free. Ihinger and Stolper

(1986) suggested that the band observed between 400 and 450 nm may be associated with a CF transition due to the presence of  $V^{3+}$ , but they do not give any explanation for the weak band at  $\sim 360$  nm present in the V-free BA sample. Given that all samples show a similar band at  $\sim 715$  nm, one can expect that such absorbance is due exclusively to the presence of Ti in the hibonite structure, as already pointed out by Ihinger and Stolper (1986). The origin and the nature of this absorption band can be, therefore, explained taking into account the site occupancy of Ti into the hibonite structure. In order to occur, an electronic transition has to satisfy both the spin-multiplicity rule and the Laporte or parity selection rule (Burns, 1993). The former imposes that the number of unpaired electrons must remain the same during an electronic transition; this condition is always satisfied for a  $d^1$  cation such as  $Ti^{3+}$ . The Laporte selection rules states that for centrosymmetric molecules or for transition metals in octahedral coordination, the allowed transitions are only those associated with a change in the orbital momentum quantum number  $l$ :  $\Delta l = \pm 1$ . In other words, electronic transitions which conserve parity, *i.e.* the symmetry ( $g = gerade$ , even) or antisymmetry ( $u = ungerade$ , odd) with respect to an inversion centre, are forbidden. For example, the electronic transitions  $t_{2g} \rightarrow e_g$  between the  $d$  orbitals of a perfect octahedral environment are forbidden. However, forbidden transitions can occur when distortions at the coordination centre, as in the case of Jahn-Teller effect, result in the loss of the inversion centre in the coordination environment around the transition metal's cation (Burns, 1993).

In the case of hibonite, the atoms of Ti are occupying the  $M4$  and  $M2$  sites, having  $C_{3v}$  and  $D_{3h}$  symmetry, respectively (Sections 3.3 and 4.1, and Fig. 4.2). The trigonal distortion at the octahedral  $M4$  site and the displacement of the cations from the centre of the coordination polyhedra for both sites give rise to the loss of the inversion centres for these coordination environments and allow a partial satisfaction of the Laporte rule. *Crystal field (CF)* transitions, which for hibonite can be indicated with spectroscopic terms as  ${}^2A_1, {}^2E \rightarrow {}^2E$  for the  $M4$  site and  ${}^2E \rightarrow {}^2A_1$  for the  $M2$  site, can be therefore observed.

The second typical mechanism of absorption in UV/Vis spectra involves *intervalence charge transfer (IVCT)* transitions. This phenomenon is due to magnetic interactions between neighbouring transition metal cations, which results in a paired excitation of the involved atoms. During IVCT transitions an electron is transferred from one atom to another, effectively changing the valence state of the cations during the lifetime of the transitions, which is about  $10 \times 10^{-15}$  s (Smith and Strens, 1976; Burns, 1993). In order for IVCT transitions to occur, the paired atoms have to occupy octahedral sites which are either edge- or face-sharing (Burns et al., 1980). These transitions have been observed in the spectra of different minerals and they can involve

cations of different elements (heterovalent), *e.g.* Fe<sup>2+</sup>-Ti<sup>4+</sup> in ellenbergerite (Chopin and Langer, 1988), tourmaline (Fonseca-Zang et al., 2008), garnets (Taran et al., 2007) and andalusite (Taran and Koch-Müller, 2011). Alternatively, IVCT transition can occur between atoms of the same species (homovalent), *e.g.* Ti<sup>3+</sup>-Ti<sup>4+</sup> as in fassaite (Dowty and Clark, 1973a; Burns and Huggins, 1973; Dowty and Clark, 1973b), or Fe<sup>2+</sup>-Fe<sup>3+</sup> as in tourmaline, biotite, sapphire and garnets (Smith, 1978). The case of homovalent IVCT transitions may be relevant for Ti in hibonite, since these transitions can occur across the face-sharing *M4* sites, as described by the following relationship:



In their study on the UV/Vis spectra of hibonite, Ihinger and Stolper (1986) suggested that the band at 715 nm originates from a CF transition involving Ti<sup>3+</sup> occupying the *M2* site, whereas Burns (1993) advanced the hypothesis that such band originates from a Fe<sup>2+</sup>-Ti<sup>4+</sup> IVCT transition at the *M4* site, similarly to what was observed in blue sapphire and ellenbergerite (Chopin and Langer, 1988). In particular blue sapphire, which is a gem-quality mineral having the structure of corundum ( $\alpha$ -Al<sub>2</sub>O<sub>3</sub>), owes its colour to traces of Ti and Fe involved in IVCT transitions. This mineral has a crystalline structure similar to that of hibonite, in fact the two materials contain the same hexagonal close-packed layers (Fig. 1.6), which also includes the face-sharing octahedra identified as *M4* in hibonite. A number of studies focused on the UV/Vis characterisations of synthetic Ti<sup>3+</sup>-Ti<sup>4+</sup>-bearing Al<sub>2</sub>O<sub>3</sub> have shown that the spectra of this material contain two main peaks, which are observed around 500 and 715 nm. The former has been attributed to a CF transition involving isolated Ti<sup>3+</sup> cations while the latter has been assigned to IVCT transitions occurring between Ti<sup>3+</sup>-Ti<sup>4+</sup> pairs (Peshev et al., 1988; Sanchez et al., 1988; Aggarwal et al., 1988; Yamaga et al., 1994).

As already mentioned, all the hibonite samples analysed in this study contain Ti atoms at the *M4* site and in minor quantities at the *M2* site (Section 3.3.2). Based on the studies on the optical properties of sapphire, it is reasonable to expect that the band observed at 715 nm in hibonite also may be due to a IVCT transition.

## 5.2 Quantitative analysis of the absorbance peaks in the UV/Vis spectra of hibonite

In order to test the hypotheses on the origin of the absorption peak in the UV/Vis spectra of hibonite, a quantitative analysis of the absorbance intensities was carried out by considering and evaluating different absorbance-Ti concentration relationships.

The quantitative evaluation of UV/Vis spectra is generally carried out according to Lambert-Beer's law (Eq. 2.8), which correlates the concentration of the absorbing species to the UV/Vis absorbance through the molar absorption coefficient  $\epsilon$ . CF transitions due to  $\text{Ti}^{3+}$  in hibonite are expected to follow Lambert-Beer's law and therefore a linear correlation between the absorbance normalised with respect to the thickness of the analysed crystals and the  $\text{Ti}^{3+}$  concentration of the same crystals should be observed. The  $\text{Ti}^{3+}$  content in synthetic hibonites has been determined in the previous Chapter from the EELS calibration (Section 4.2.2) and it has been reported as atoms per formula unit ( $\text{Ti}_{a.p.f.u.}^{3+}$ , Table 4.1). The Lambert-Beer law requires such concentration to be expressed in molarity ( $\text{mol l}^{-1}$ ), however. The conversion between these two quantities requires the knowledge of the density of the material, which can be calculated from the unit-cell volume ( $V_{u.c.p.}$ ) obtained by means of PXRD (Table 3.6) and can be obtained according to the following equation:

$$c_{\text{Ti}^{3+}} [\text{mol l}^{-1}] = \frac{Z \text{Ti}_{a.p.f.u.}^{3+} 10^{27}}{V_{u.c.p.} N_A} \quad (5.1)$$

where  $Z = 2$  is the number of formula units contained in the unit cell of hibonite,  $N_A$  is the Avogadro number and  $10^{27} \text{ \AA}^3 \text{ l}^{-1}$  is the volume conversion factor.

The value of normalised absorbance expressed as the peak height at its maximum normalised with respect to the thickness of the samples (Table 5.1) are plotted in Fig. 5.3 against the corresponding molar concentrations of  $\text{Ti}^{3+}$  calculated according to Eq. 5.1 and reported in Table 5.2. The normalised absorbances, as expected, are larger for the samples with greater concentrations of  $\text{Ti}^{3+}$ , however, the data do not follow a linear trend as expected for a CF transition (Fig. 5.3).

For IVCT transitions, instead, the UV/Vis absorption needs to correlate with the concentration of the  $\text{Ti}^{3+}$ - $\text{Ti}^{4+}$  pair, *i.e.* with the product of the molarity of these two species occupying the face-sharing octahedra,  $M4$ .

The total amount of Ti substituting for Al in the structure of each hibonite sample is known by the EPMA and its fraction present as  $\text{Ti}^{3+}$  is given by the EEL spectra. None of these two techniques allow determining on which site the substitution of trivalent and tetravalent

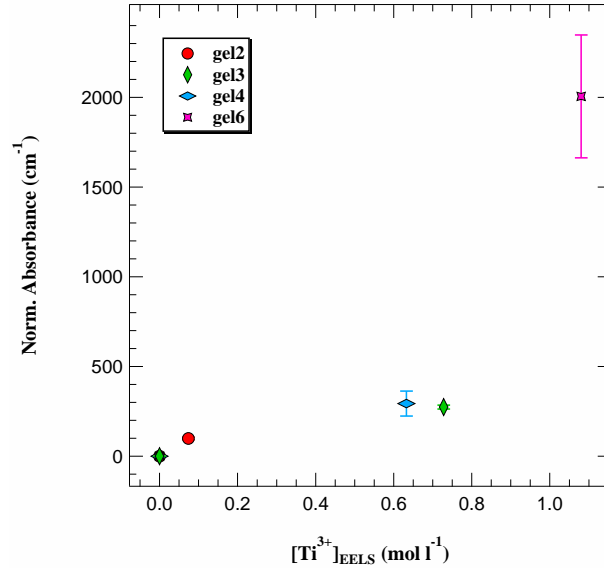


Figure 5.3: Normalised absorbance at the 715 nm band plotted as a function of molar concentration of  $\text{Ti}^{3+}$  calculated from the EELS calibration for the measured sample series.

titanium occurs. However, when considering IVCT transitions, only the concentrations of  $\text{Ti}^{3+}$  and  $\text{Ti}^{4+}$  present on the  $M4$  site (indicated as  $\text{Ti}_{M4}^{3+}$  and  $\text{Ti}_{M4}^{4+}$ , respectively) need to be taken into account. In order to estimate these quantities, two different scenarios were considered:

- (a) Single crystal XRD data presented in Section 3.3 show that Ti partitions exclusively between the  $M4$  and the  $M2$  sites with a ratio which, in average, is about 4.1 : 1. Structural refinements also indicate the presence of  $\text{Ti}^{3+}$  on both the  $M4$  and the  $M2$  sites (Section 3.3.2). Therefore a reasonable assumption is that  $\text{Ti}^{3+}$  and  $\text{Ti}^{4+}$  have the same preference for the  $M4$  site and the amount of  $\text{Ti}^{3+}$  obtained from EELS can be partitioned according to the 4.1 : 1 ratio.
- (b) According to density functional theory (DFT) calculations reported in a recent study (Doyle et al., 2014)  $\text{Ti}^{3+}$  substitutes exclusively on the  $M4$  site, whereas only  $\text{Ti}^{4+}$  is partitioned between the  $M4$  and the  $M2$  sites. In this case all  $\text{Ti}^{3+}$  obtained from EELS is considered occupying the  $M4$  site of the hibonite structure.

For case (a) the total concentration of Ti present at the  $M4$  site ( $\text{Ti}_{M4}^{\text{tot}}$ ) has been calculated according to the linear system presented in Eq. 5.2a, which is solved for  $\text{Ti}_{M4}^{\text{tot}}$  as indicated in Eq. 5.2b.

$$\begin{cases} \text{Ti}_{\text{EPMA}}^{\text{tot}} &= \text{Ti}_{M4}^{\text{tot}} + \text{Ti}_{M2}^{\text{tot}} \\ P_{\text{Ti}_{M4}:\text{Ti}_{M2}} &= \frac{\text{Ti}_{M4}^{\text{tot}}}{\text{Ti}_{M2}^{\text{tot}}} \end{cases} \quad (5.2a)$$

$$\text{Ti}_{M4}^{\text{tot}} = \frac{\text{Ti}_{\text{EPMA}}^{\text{tot}} \cdot P_{\text{Ti}_{M4}:\text{Ti}_{M2}}}{1 + P_{\text{Ti}_{M4}:\text{Ti}_{M2}}} \quad (5.2b)$$

In these equations,  $Ti_{EPMA}^{tot}$  indicates the total amount of Ti measured with microprobe (Table 3.5) and  $P_{Ti_{M4}:Ti_{M2}}$  is the partitioning ratio of Ti between the  $M4$  and the  $M2$  sites as determined by XRD (Table 3.9). For the samples in which it was possible to acquire XRD data on single crystals, the corresponding values of  $P_{Ti_{M4}:Ti_{M2}}$  reported in Table 3.9 were used, while for the other samples for which only EPMA data were obtained, the average values of  $P_{Ti_{M4}:Ti_{M2}} = 4.1(1)$  was adopted instead. Once the amount of  $Ti_{M4}^{tot}$  is known, the content of  $Ti^{3+}$  at the  $M4$  site can be calculated with the same procedure illustrated in Eqs. 5.2 where the  $Ti_{EPMA}^{tot}$  is replaced by the total quantity of  $Ti^{3+}$  determined with EELS, *i.e.*  $Ti_{H_{peak}}^{3+}$  (Table 4.1). Subsequently, the amount of  $Ti^{4+}$  present at the  $M4$  site is calculated by difference, as reported in Eqs. 5.3.

$$Ti_{M4}^{3+}(a) = \frac{Ti_{H_{peak}}^{3+} \cdot P_{Ti_{M4}:Ti_{M2}}}{1 + P_{Ti_{M4}:Ti_{M2}}}; \quad Ti_{M4}^{4+}(a) = Ti_{M4}^{tot} - Ti_{M4}^{3+}(a) \quad (5.3)$$

For case (b), the amount of  $Ti^{3+}$  determined with EELS has been subtracted from the total amount of Ti determined from EPMA, since all  $Ti^{3+}$  is assumed to be present at the  $M4$  site. The remaining Ti is then considered as all  $Ti^{4+}$  and has been partitioned as shown in Eqs. 5.4.

$$Ti^{4+}(b) = Ti_{EPMA}^{tot} - Ti_{H_{peak}}^{3+}; \quad Ti_{M4}^{4+}(b) = \frac{Ti^{4+}(b) \cdot P_{Ti_{M4}:Ti_{M2}}}{1 + P_{Ti_{M4}:Ti_{M2}}} \quad (5.4)$$

The quantities of  $Ti^{3+}$  and  $Ti^{4+}$  at the  $M4$  site obtained in both cases have been then converted to molarities using Eq. 5.1 and are reported in Table 5.2. These concentrations were then multiplied and correlated with the corresponding normalised absorptions, as presented in Fig. 5.4. It is clear that the product of  $Ti^{3+}$ - $Ti^{4+}$  concentrations correlates linearly with the intensity of the absorption peak at 715 nm, indicating that this band indeed originates from a IVCT transition. The agreement factors for the fitted lines reported in Fig. 5.4 are excellent, independently of the assumption on how the  $Ti^{3+}$  is partitioned between the  $M4$  and  $M2$  sites. It is, therefore, not possible to discriminate between the two cases, given the very small amount of Ti occupying the  $M2$  site for all hibonites.

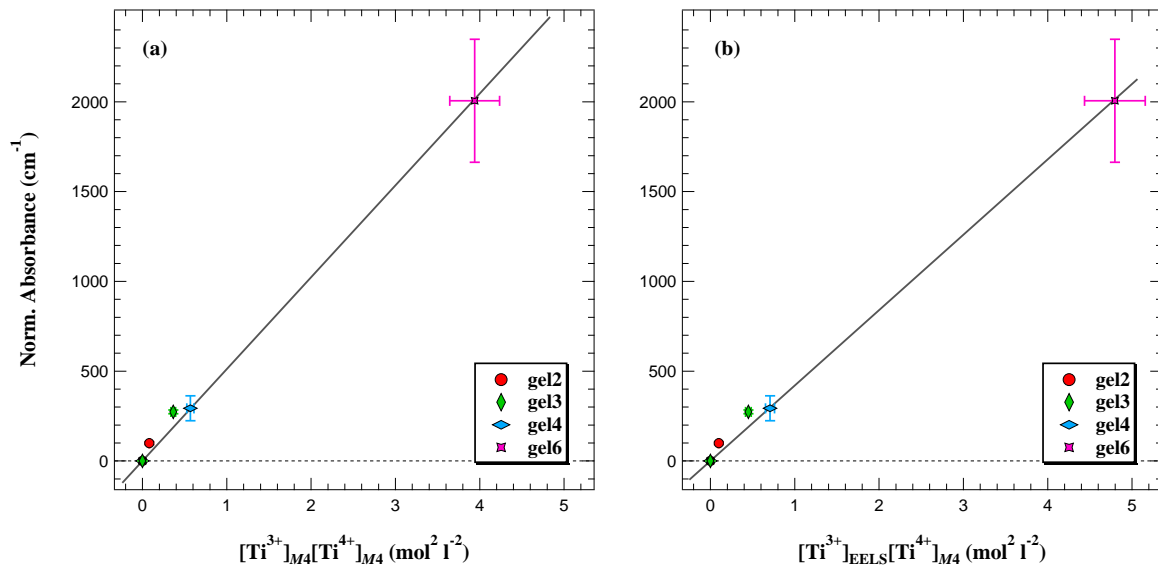


Figure 5.4: Normalised absorbance at the 715 nm peak plotted as a function of the product between the molar concentration of Ti<sup>3+</sup> and Ti<sup>4+</sup> present on the M4 site. The solid lines are fits through the data points. (a) The Ti<sup>3+</sup> calculated from EELS is assumed to partition between the M4 and M2 as determined by XRD for bulk Ti ( $R^2 = 0.98$ , slope =  $510(10) \text{ l}^2 \text{ mol}^{-2} \text{ cm}^{-1}$ ). (b) The total amount of Ti<sup>3+</sup> calculated from EELS is assumed to partition exclusively at the M4 site ( $R^2 = 0.98$ , slope =  $420(8) \text{ l}^2 \text{ mol}^{-2} \text{ cm}^{-1}$ ).

Table 5.2: Concentrations of Ti<sup>3+</sup> and Ti<sup>4+</sup> at the M4 site calculated by means of Eqs. 5.3 and 5.4. These quantities are expressed as atoms per formula unit (*a.p.f.u.*) and molarities calculated using Eq. 5.1. CF indicates the situation in which a crystal field transition is considered while (a) and (b) are referred to the cases described in the text for the IVCT transitions.

Case	Concentrations	gel2-1	gel2-5	gel3-1	gel3-3	gel4-1	gel4-3	gel6-1	gel6-3
CF	$M(\text{Ti}_{\text{tot}}^{3+})$ (mol l <sup>-1</sup> )	0	0.07(1)	0	0.73(7)	0	0.63(6)	0	1.0(1)
(a)	$\text{Ti}_{M4}^{3+}$ ( <i>a.p.f.u.</i> )	0	0.01(1)	0	0.10(1)	0	0.09(1)	0	0.16(2)
	$\text{Ti}_{M4}^{4+}$ ( <i>a.p.f.u.</i> )	0.36(4)	0.24(2)	0.17(2)	0.11(1)	0.28(3)	0.20(2)	0.9(1)	0.81(8)
	$M(\text{Ti}_{M4}^{3+})$ (mol l <sup>-1</sup> )	0	0.06(1)	0	0.59(6)	0	0.51(5)	0	0.9(1)
	$M(\text{Ti}_{M4}^{4+})$ (mol l <sup>-1</sup> )	2.0(2)	1.3(2)	0.9(1)	0.62(6)	1.6(2)	1.1(1)	5.2(5)	4.4(5)
(b)	$\text{Ti}_{M4}^{3+}$ ( <i>a.p.f.u.</i> )	0	0.01(0)	0	0.13(1)	0	0.10(1)	0	0.20(2)
	$\text{Ti}_{M4}^{4+}$ ( <i>a.p.f.u.</i> )	0.36(4)	0.24(2)	0.17(2)	0.11(1)	0.28(3)	0.20(1)	0.9(1)	0.81(7)
	$M(\text{Ti}_{M4}^{3+})$ (mol l <sup>-1</sup> )	0	0.07(1)	0	0.73(7)	0	0.63(5)	0	1.08(7)
	$M(\text{Ti}_{M4}^{4+})$ (mol l <sup>-1</sup> )	2.0(2)	1.3(1)	0.9(1)	0.6(1)	1.6(2)	1.1(1)	5.2(5)	4.4(5)

### 5.3 Assignment of the absorption bands in the UV/Vis spectra of hibonite

The considerations made so far on the UV/Vis spectra of the synthetic hibonites from this study allow commenting on the spectra published by Ihinger and Stolper (1986) and reported in Fig. 5.2. First, clearly the peak observed at 715 nm cannot originate from a CF transition as proposed by Ihinger and Stolper (1986) given the linear relationship between the normalised absorbance of the UV/vis band at 715 nm and the product of the  $\text{Ti}^{3+}$  and  $\text{Ti}^{4+}$  present at the *M4* site (Fig. 5.4). This linear relationship has been used to prove the presence of IVCT transitions associated with  $\text{Ti}^{3+}$ - $\text{Ti}^{4+}$  pairs in sapphire (Sanchez et al., 1988; Aggarwal et al., 1988) and confirm the hypothesis of IVCT transitions in hibonite previously advanced by different authors (Burns and Burns, 1984; Dyar et al., 1986; Burns, 1993). In the case of natural hibonites, the transition can involve either  $\text{Ti}^{3+}$ - $\text{Ti}^{4+}$  or  $\text{Fe}^{2+}$ - $\text{Ti}^{4+}$  pairs, however, the former is more likely to take place in natural hibonites since  $\text{Fe}^{2+}$ , being a divalent cation, is expected to occupy the tetrahedral site *M3* (Holtstam, 1996). Given the IVCT nature of the absorption band at 715 nm, the correlation between the blue colour of meteoritic hibonite and oxygen fugacity is not as straightforward as indicated by Ihinger and Stolper (1986). The colour blue in hibonite can be observed as soon as  $\text{Ti}^{3+}$  and  $\text{Ti}^{4+}$  are both present, a situation which, as shown in this study, covers a very large range of oxygen fugacities. Only at very oxidising or at very reducing conditions when only  $\text{Ti}^{4+}$  or  $\text{Ti}^{3+}$  are respectively present, hibonite is colourless. In fact, the sample gel3-3, which contains about equal quantities of  $\text{Ti}^{3+}$  and  $\text{Ti}^{4+}$  (Table 4.1), displays an intense blue colour while the sample gel3-2, supposedly containing only  $\text{Ti}^{3+}$  (Section 4.2.2), does not appear blue in colour (Fig. 5.5). The UV/Vis spectrum of sample gel3-2 is expected to do not show any absorption peak, unfortunately, due to the very small grains size of this sample it was not possible to acquire UV/Vis spectra for it.



Figure 5.5: Fragments of sintered pellets of samples gel3-3 (left) and gel3-2 (right) synthesised at  $\log f_{\text{O}_2} = -11$  and  $\log f_{\text{O}_2} = -16$ , respectively. The former sample is blue due to the presence of the  $\text{Ti}^{3+}$ - $\text{Ti}^{4+}$  pair while the latter is greyish, likely due to colourless hibonite (appearing white in the bulk sample) with minor quantities of dark blue/black corundum containing traces amounts of  $\text{Ti}^{3+}$ .

The band observed in orange hibonites around 350-450 nm by Ihinger and Stolper (1986) may be attributed to a Laporte-forbidden CF transition involving  $V^{3+}$ . In fact, the sample BA-2-15, having a complex composition similar to that of natural BA, shows a relatively intense and broad peak. It is interesting to notice, though, that in the case of the V-, Fe- and Cr-free sample BA-VFC-2 a small, but still visible band at  $\sim 350$  nm is still present (Fig. 5.2). Such band is very likely due to the CF transition in  $Ti^{3+}$ . It is, however, difficult to assess whether such band originates from  $Ti^{3+}$  occupying the *M2* or the *M4* sites or both of them, given the similar energy separation of the *d* orbitals in the two coordination environments.

The assignments of the UV/vis bands are strictly correlated to the crystal chemistry of hibonite. As mentioned in the previous section, the IVCT transitions require edge- or face-sharing coordination polyhedra between the involved centre and the only atomic position for which this condition is satisfied for hibonite is the *M4* site. This indicates that  $Ti^{3+}$  and  $Ti^{4+}$  are occupying the face-sharing octahedral site, in agreement with the XRD study presented in Section 3.3, in contrast with what was previously reported by Beckett et al. (1988) who, on the basis of electron spin resonance (ESR) suggested that  $Ti^{3+}$  occupies exclusively the trigonal bipyramid at the *M2* site.

Moreover, in a study recently published by Doyle et al. (2014), reporting results from neutron PXRD and DFT calculations performed on Ti-Mg-bearing hibonites, it has been shown that  $Ti^{3+}$  substitutes for Al exclusively at the *M4* site. The authors also re-evaluate the data published by Beckett et al. (1988) stating that the observed ESR signal corresponds to an interaction between atoms aligned along the direction of the crystallographic axis *c*, which is indeed compatible with the ESR signal originating not just from  $Ti^{3+}$  at the *M2* site but also at the *M4* site. However, the quantity of Ti substituting on the latter site is dominant (Section 3.3.2), therefore, the ESR signal generated by Ti at the *M2* site could be masked by the strongest contribution arising from the *M4* site.

Since evidences of  $Ti^{3+}$  occupying the *M4* and/or the *M2* sites have been provided by several authors using different techniques, it is more likely that, as proposed in this thesis, Ti in the 3+ and 4+ valence states is found on both structural sites.

*Part III*

*Characterisation of natural samples*

*&*

*Conclusions*

## 6 Characterisation of natural hibonites

The EELS quantification method for  $\text{Ti}^{3+}$  in hibonite and the subsequent  $\text{Ti}^{3+}$ - $f\text{O}_2$  calibration curves obtained for the synthetic samples are applied to the characterisation of natural hibonites. Since these natural samples potentially carry a record of the processes that led to their formation and of the different conditions at which they have been exposed, electron microscopy observations, SEM-EPMA and TEM-EELS, have been used to attempt revealing such information. In particular, the calibration obtained in Section 4.2.2 has been applied to quantify the  $\text{Ti}^{3+}$  content of natural samples to shed light on the oxygen fugacity conditions at which these hibonites have formed and evolved.

### 6.1 Electron microscope observation on natural hibonites

Seven Ca-Al-rich inclusions were examined in the course of this study, they were found in carbonaceous chondrites belonging to the groups CO, CH, CR and C-ung, which are further classified in the petrologic types 3 and 2 (Section 1.1.1). Given the low degree of alteration of these specimens, they represent a good example of pristine material of the Solar System. Details about the samples investigated in this study are given in Table 6.1 and typical phase assemblages of CAIs are illustrated in Fig. 6.1.

Table 6.1: Carbonaceous chondrites specimens and corresponding CAIs analysed in this study.

Chondrites			Thin section name	Diameter of CAI cross section ( $\mu\text{m}$ )	Size of hibonite grains ( $\mu\text{m}$ )
Name	Group	Type			
Dar al Gani 203	CO	3	PL96274	$\sim 110$	10 – 20
Acfer 182-2	CH	3	PL01036	$130 \times 90$	$\sim 10$
Acfer 182-3	CH	3	PL01036	$90 \times 90$	10 – 20
El Djouf 001	CR	2	PL91167	$400 \times 90$	$\sim 15$
Acfer 059	CR	2	PL90345	$390 \times 200$	15 – 20
Acfer 094-a	C-ung <sup>‡</sup>	2-3	PL93022	$390 \times 290$	40 – 50
Acfer 094-b	C-ung <sup>‡</sup>	2-3	PL93040	$\sim 170$	15 – 20

<sup>‡</sup>C-ungrouped

The sample Dar al Gani 203 consists of a small spherical CAI with a core formed of euhedral to subeuhedral crystals of hibonite intergrown with larger spinel grains. The core is surrounded by a relatively thick layer of melilite in which few occurrences of Ca-Ti-perovskite are observable (Fig. 6.1-a). This type of hibonite-spinel inclusions have been reported in numerous other CAIs from CO3 chondrites (Russell et al., 1998) and also exhibits evidences for nebular alteration, such as Wark-Lovering features (Wark and Lovering, 1977), *i.e.* the bright rim in Fig. 6.1-a.

The refractory inclusion Acfer 182-2 is mostly formed by melilite which encloses poikilitically smaller portions of spinel and hibonite intergrown with perovskite (Fig. 6.1-b). The irregular shape of this object and its very small size suggests that it may be a fragment of a once larger CAI; this idea is also supported by the presence of a Wark-Lovering sequence (spinel, melilite, Ca-clinopyroxene) which is observed on all sides of the inclusion except on the upper-left portion.

The inclusion Acfer 182-3 represents another example of CAI typical for this meteorite. The BSE image of this inclusion has been already presented in Section 2.1 and it is also shown in Fig. 6.1-c for completeness. Half of the volume of this CAI consists of grossite (or Ca-dialuminate,  $\text{CaAl}_4\text{O}_7$ ), which in other meteorites classes (for example CV3, CO3 and CM2) is just an accessory phase (Weber and Bischoff, 1994). Grossite is mostly present on the external border of the inclusion and it encloses euhedral hibonite crystals. The interstitial space between hibonite platelets is filled by perovskite and melilite.

The samples El Djouf 001 and Acfer 059, belonging to the Renazzo-type (CR) carbonaceous chondrite class, were found in two localities of the Sahara desert which are more than 500 km apart, however, these chondrites are considered as paired. Chemical, petrographic and isotopical evidences support the idea that these meteorites, together with other eight finds, are the result of a single parent meteoroid that broke-up upon contact with the Earth's atmosphere (Bischoff et al., 1993a). The refractory inclusions in El Djouf 001 and Acfer 059 are abundant and usually characterised by fine-grained materials with irregular shapes. Most of these inclusions are melilite-rich types and show incomplete Wark-Lovering rims (Wark and Lovering, 1977), indicating that they are fragments of once larger CAIs.

The samples analysed in this study make no exception; the inclusion from El Djouf 001 is dominated by melilite with small inclusions of perovskite and few occurrences of hibonite laths (Fig. 6.1-d). The CAI from Acfer 059 is melilite-rich and also contains abundant spinel which encloses small crystals of perovskite and euhedral hibonite laths; these structures are rimmed by highly porous Ca-pyroxenes (Fig. 6.1-e).

The ungrouped carbonaceous chondrite Acfer 094 is an unshocked, almost unaltered, meteorite with bulk chemical composition similar to that of CM-CO chondrites and oxygen isotopic composition and matrix modal abundance similar to those of CO chondrites (Newton et al., 1995; Weber, 1995; Krot et al., 2004; Simon and Grossman, 2011). The CAI analysed in this work from the specimen Acfer 094-a appears as a fragment of a once bigger object, having a hibonite-rich core with poikilitical enclosures of melilite and spinel; melilite also constitutes the thick rim of this inclusion (Fig. 6.1-f). The inclusion from Acfer 094-b is mineralogogically similar to Acfer 094-a, showing abundant melilite and hibonite intergrowth with spinel; perovskite is also present as an accessory phase (Fig. 6.1-g).

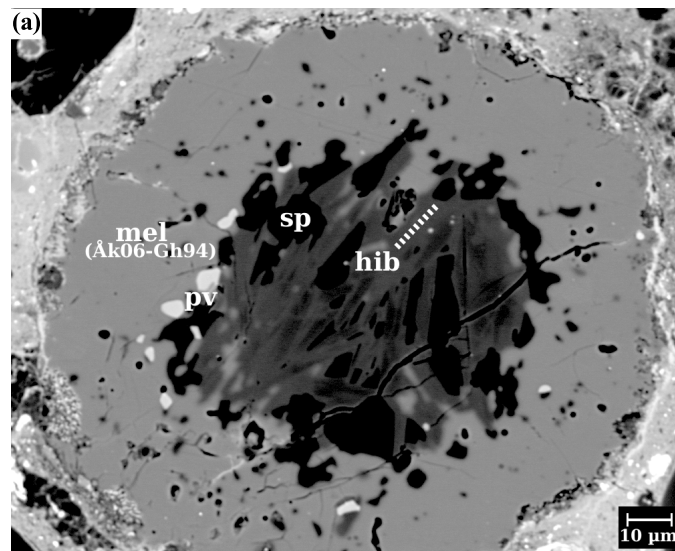


Figure 6.1: SEM-BSE images of the CAIs examined in this study. (a) Dar al Gani 203, (b) Acfer 182-2, (c) Acfer 182-3, (d) El Djouf 001, (e) Acfer 059, (f) Acfer 094-a, (g) Acfer 094-b. Hib = hibonite, sp = spinel, pv = perovskite, mel = melilite (åkermanite-gehlenite), cpx = Ca-clinopyroxene, Fe = Fe-Ni metal, gro = grossite, en = enstatite; dashed line = chosen areas for FIB preparation.

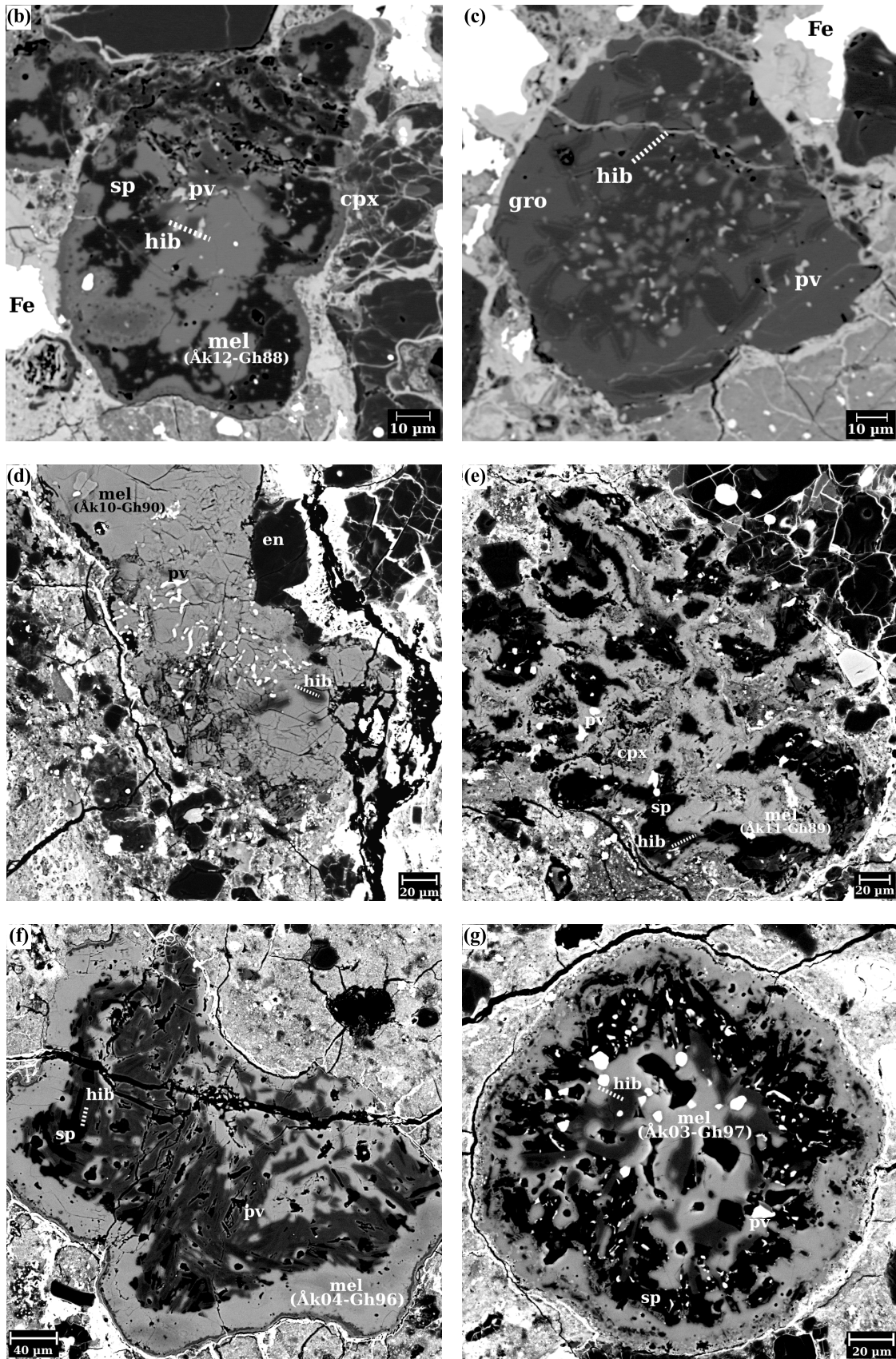


Figure 6.1: (continued)

The two CAIs from Acfer 182 are present in the same thin section prepared from this chondrite find. All the other inclusions, including those of the paired samples El Djouf 001-Acfer 059 and the ungrouped meteorite Acfer 094, are found in separate thin sections. The minerals present in the CAIs of these specimens were identified by means of EPMA (Section 2.3). Individual hibonite grains were carefully examined in order to choose the most suited for FIB preparation (Section 2.6.1.2). The selected hibonite grains had all a clear euhedral morphology with large visible area of at least  $2 \times 5 \mu\text{m}$  and they were far away from cracks or porosity in order to have FIB section more mechanically stable. Crystals among those satisfying the above requirements were selected based on their chemical compositions in the attempt to cover as much different cases as possible with respect to Ti and Mg concentration. Also, since FIB milling is a destructive preparation technique, it was given preference to grains sitting close to the edge of the CAIs versus grains inside the inclusions, with the aim of preserving as much of the inclusion as possible. This would allow further studies to be carried out on the same sample and, in case of loss of the FIB lamella, it would have given the possibility of another attempt at sample extraction and preparation.

The chemical composition determined by means of EPMA on the hibonite grains observed in the CAIs of the studied chondrites are shown in Fig. 6.2-a. The analyses performed on the individual hibonite grains which have been extracted with the FIB technique are shown in Fig. 6.2-b and listed in Table 6.2, where it is also shown that these natural hibonites contain negligible amounts of Fe and Si, and just small quantities of V.

Different analyses performed on several spots of individual hibonite grains do not indicate the presence of zoning in these crystals. However, different hibonite grains found in the same CAIs have very variable composition (Fig. 6.2-a). The occurrence of hibonite grains with such diverse composition found in the same small refractory object can be interpreted as an evidence for the heterogeneous nature of the Solar Nebula. Moreover, most of the data points in Fig. 6.2 plot very close to the line representing the coupled substitution of two  $\text{Al}^{3+}$  cations for one  $\text{Ti}^{4+}$  and one  $\text{Mg}^{2+}$ . This indicates that, in the limits of the uncertainty for individual microprobe analyses at relatively low Ti concentrations, these hibonites are likely to contain only minor amounts of  $\text{Ti}^{3+}$ .

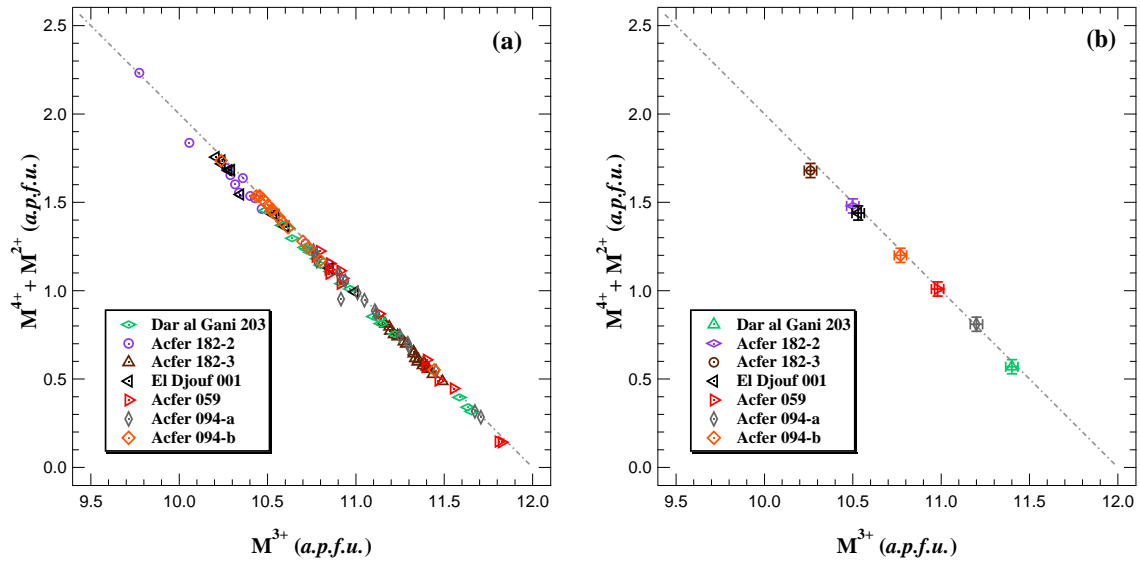


Figure 6.2: Sum of di- and tetra-valent cations plotted against the content of trivalent cations for all the EPMA performed on natural hibonites. The concentrations are given in cations per formula unit, normalised to 19 oxygen. The dashed line is a reference line representing the coupled substitution  $2\text{Al}^{3+} = \text{Ti}^{4+} + \text{Mg}^{2+}$ . (a) Individual data point measurements. (b) Average of the data points calculated only on the hibonite grains extracted by means of FIB technique.

Table 6.2: Electron microprobe analyses for the hibonite grains extracted by means of focused ion beam milling. The chemical formulæ are expressed as weight percent of oxides and as cation per formula unit, normalised to 19 oxygen atoms. The one-sigma standard deviations over different points measured on the same grain are given in brackets.

Sample	CaO	Al <sub>2</sub> O <sub>3</sub>	MgO	TiO <sub>2</sub>	V <sub>2</sub> O <sub>3</sub>	SiO <sub>2</sub>	FeO	Tot. <sup>‡</sup>
Dar al Gani 203	8.60(1)	79.8(4)	4.2(2)	8.23(8)	0.30(8)	0.35(6)	0.17(5)	101.61(1)
Acfer 182-2	8.74(4)	77.0(3)	4.54(4)	10.08(7)	0.06(2)	0.25(4)	0.14(1)	100.76(2)
Acfer 182-3	8.63(4)	86.5(3)	1.42(3)	3.31(4)	0.12(2)	0.12(3)	0.32(5)	100.37(3)
El Djouf 001	8.59(4)	78.81(4)	3.77(2)	7.35(6)	1.27(8)	0.36(4)	0.11(2)	100.26(2)
Acfer 059	8.49(1)	82.92(5)	2.73(1)	5.42(3)	0.53(4)	0.20(7)	0.25(7)	100.54(4)
Acfer 094-a	8.45(5)	84.2(3)	2.3(2)	4.1(6)	0.44(6)	0.30(1)	0.12(1)	99.8(7)
Acfer 094-b	8.56(5)	81.0(3)	3.3(2)	6.5(5)	0.79(9)	0.18(8)	0.06(3)	100.4(1)

<sup>‡</sup>the valence states of Ti, V and Fe have been assumed to be 4+, 3+ and 2+, respectively. The total weight of oxides can change if different valence states are considered.

Sample	Ca <sup>2+</sup>	Al <sup>3+</sup>	Mg <sup>2+</sup>	Ti <sup>4+</sup>	V <sup>3+</sup>	Si <sup>4+</sup>	Fe <sup>2+</sup>	Tot.
Dar al Gani 203	1.03(1)	10.50(4)	0.70(4)	0.69(1)	0.03(1)	0.04(1)	0.02(1)	13.01(2)
Acfer 182-2	1.06(1)	10.26(3)	0.77(4)	0.86(5)	0.01(1)	0.03(1)	0.01(1)	12.98(1)
Acfer 182-3	1.04(1)	11.40(4)	0.24(2)	0.28(3)	0.01(1)	0.01(1)	0.03(1)	13.00(2)
El Djouf 001	1.04(1)	10.53(3)	0.64(2)	0.63(3)	0.12(2)	0.04(1)	0.01(1)	12.97(1)
Acfer 059	1.02(2)	10.98(4)	0.46(2)	0.46(3)	0.05(1)	0.02(1)	0.02(1)	12.99(2)
Acfer 094-a	1.02(1)	11.2(1)	0.38(4)	0.35(5)	0.04(1)	0.03(1)	0.01(1)	12.98(1)
Acfer 094-b	1.03(1)	10.77(5)	0.55(3)	0.55(4)	0.07(1)	0.02(1)	0.01(1)	12.99(1)

As already described for synthetic hibonites the natural samples do not show particular defect structures. Bright field (BF) images taken along diverse zone axes on different grains showed uniform diffraction contrasts, as illustrated, for example, in Fig. 6.3. The contrast features observed in the images of the sample Acfer 182-3 are due to the different thickness of the specimen (Fig. 6.3-a). Similar variations in contrast are visible for El Djouf 001, but in this case there are also few isolated dislocations (Fig. 6.3-b).

The sample Acfer 182-2 comprises a hibonite lath which, when observed under the zone axis  $[100]$  shows a very strong diffraction contrast (Fig. 6.4-a). This specimen shows the presence of a twin, which is observed as the dark grey grain on the left side of Fig. 6.4-a and it is also associated with misfit dislocations. A high-resolution (HR) image of the subgrain boundary between the two twin individuals is shown in Fig. 6.4-b. The observed  $(001)$  twinning is compatible with what determined on synthetic samples by means of electron microscopy and X-ray diffraction analyses (Sections 3.1.2 and 3.3.2, respectively).

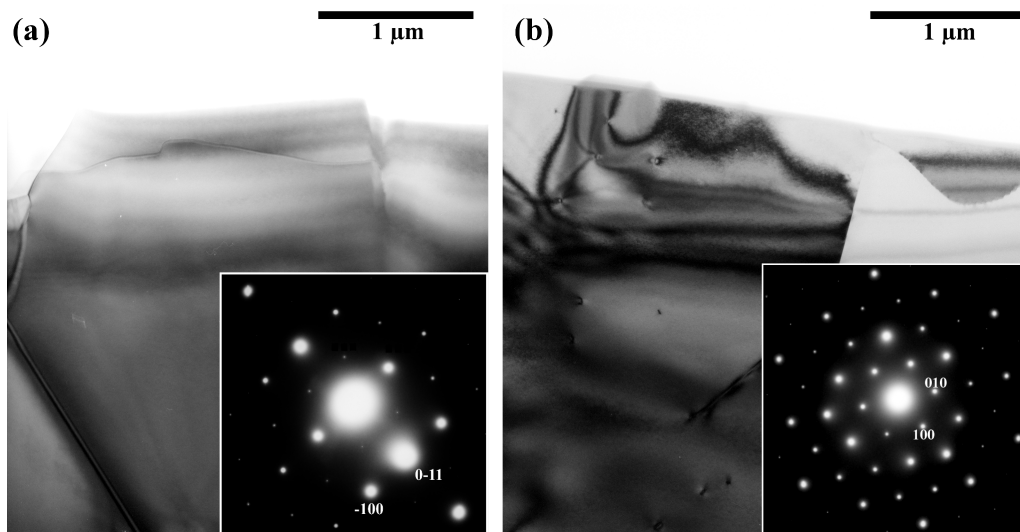


Figure 6.3: TEM-BF images of chondritic hibonites; the insets show the electron diffraction patterns used during imaging. (a) Acfer 182-3 under the zone axis  $[011]$ . (b) El Djouf 001 under the zone axis  $[001]$ .

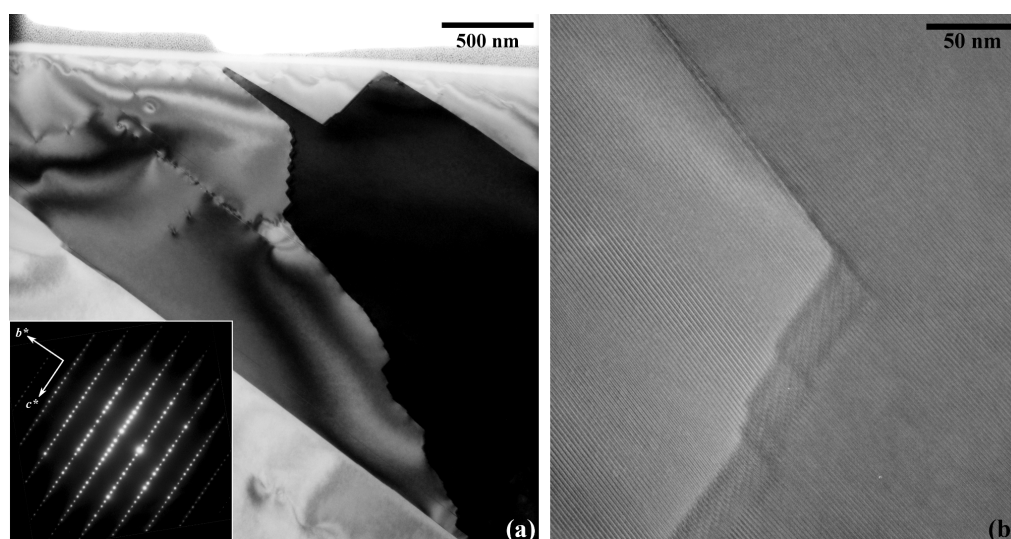


Figure 6.4: TEM images of Acfer 182-2 hibonites. (a) Bright field (b) High resolution. The inset shows the diffraction pattern corresponding to the zone axis  $[100]$  which has been used to acquire both images.

## 6.2 Quantification of $Ti^{3+}$ in natural hibonites

EEL spectra were measured on the thinnest areas of the FIB lamellæ of the natural hibonites and from locations as close as possible to the spots where the microprobe analyses (Table 6.2) were performed. This procedure was chosen to obtain Ti  $L_{2,3}$  edge EEL spectra with the highest possible signal/noise ratio and originating from an area with well known Ti bulk content. The acquisition of the spectra was carried out as described in Section 2.6.2 and the  $Ti^{3+}$  concentrations have been quantified adopting the hibonite-specific calibration developed in this study and presented in Section 4.2.2. The Ti EEL spectra measured on the natural hibonites from this study are shown in Fig. 6.5. The spectrum of the synthetic sample gel6-1, which has a similar  $Ti^{tot}/Mg$  ratio to that of these hibonites, also is shown for comparison.

The EEL spectra of the natural hibonites are very similar to those of the synthetic samples, showing four main peaks with variable fine features. The main difference between the spectra shown in Fig. 6.5 is the width of the peaks and consequently their relative intensity ratios, as already observed for the synthetic samples. It follows that the shape of these spectra can be rationalised in terms of  $Ti^{3+}$ - $Ti^{4+}$  contents using the same arguments adopted to interpret the EEL spectra of synthetic hibonites (Section 4.1). The similarities between the spectra of natural and synthetic hibonite justifies the use of the calibration based on the measurements described in Section 4.2.2 in order to determine their  $Ti^{3+}$  concentrations. As for synthetic hibonites, the spectra are considered independently of their absolute energy and thus the position of the  $d$  peak is aligned at the arbitrary value of 465 eV, as shown in Fig. 6.5. Moreover, during the Fourier-ratio deconvolution (Section 2.6.2) of the spectra of natural samples the FWHM

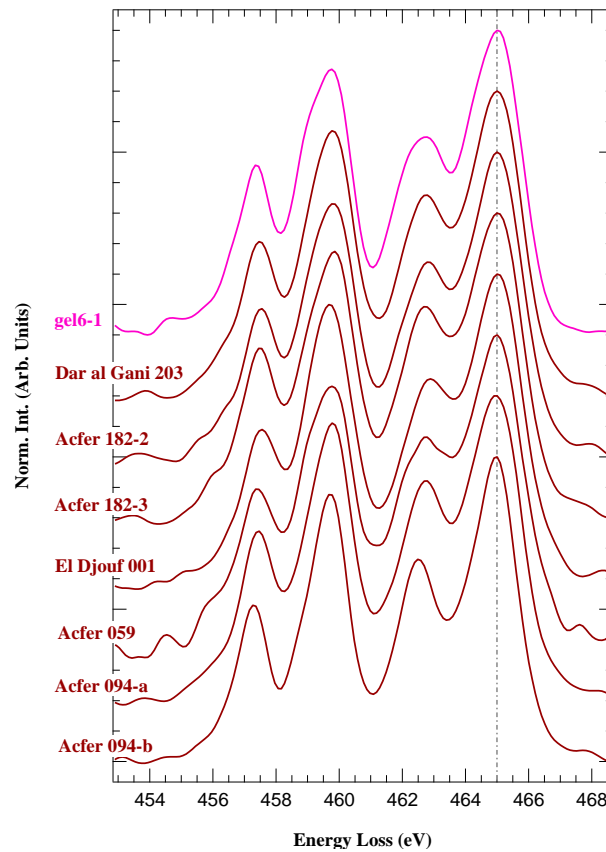


Figure 6.5: EEL spectra for the natural samples measured in this study. The spectrum of the synthetic sample gel6-1 synthesised in air also is reported for comparison. The dashed lines indicate the arbitrary value of energy (465 eV) at which the spectra were aligned for the  $\text{Ti}^{3+}$  determination.

of the zero-loss peak was set to the value of 0.908(1) eV, the same value previously adopted for processing the EELS of synthetic hibonites. Once satisfied these conditions, the net peak heights  $H_{peak}$  has been measured for the EEL spectra of natural hibonites; such values are reported in Table 6.3.

The calculation of  $\text{Ti}^{3+}$  concentration from the net peak heights, in particular that of  $H_d$ , requires the application of the calibration line reported in Eq. 4.6 which, however, is based on normalised values of  $H_d$ . In the case of the synthetic samples, the EEL spectra of each sample series were normalised with respect to the  $H_d$  value of the corresponding sample synthesised in air. This procedure was followed in order to take into account any defect or non-stoichiometry present in the hibonite samples which may give rise to line broadening of the EEL spectra and therefore affects the  $\text{Ti}^{3+}$  determination. For the natural samples, normalisation of the EEL spectra is not straightforward, since there is no corresponding oxidised sample. However, given the large amount of available data obtained from EELS measurement conducted in this study, a fairly good estimation for a common normalising factor can be calculated taking the average of the net peak height  $H_d$  for all synthetic samples equilibrated in air. Such normalising factor

has the value of 0.465(8) normalised intensity units. The normalised net peak height  $H_{d_n}$  and the corresponding  $Ti^{3+}$  estimations for natural hibonites, also are reported in Table 6.3.

Table 6.3: Net peak heights and corresponding  $Ti^{3+}$  concentrations (Section 4.2.2) obtained from the EELS measurements performed on natural hibonites. The lettering of the samples corresponds to the bullets plotted in Fig. 6.6.

Sample	$H_a$	$H_b$	$H_c$	$H_d$	$H_{d_n}$	$Ti^{3+}$ (a.p.f.u.)	$Ti^{3+}$ (%)	$Ti^{tot}/Mg$
(a) Dar al Gani 203	0.274	0.637	0.200	0.483	1.043	0	0	0.99
(b) Acfer 182-2	0.198	0.553	0.138	0.417	0.897	0.05(1)	6.0(6)	1.12
(c) Acfer 182-3	0.141	0.479	0.067	0.402	0.864	0.06(1)	21(2)	1.17
(d) El Djouf 001	0.131	0.541	0.065	0.410	0.881	0.06(1)	9.6(9)	0.98
(e) Acfer 059	0.186	0.505	0.098	0.405	0.870	0.07(1)	14(1)	1.00
(f) Acfer 094-a	0.161	0.505	0.089	0.450	0.968	0.02(1)	4.3(4)	0.92
(g) Acfer 094-b	0.182	0.546	0.106	0.448	0.963	0.02(1)	2.9(3)	1.00

The determination of  $Ti^{3+}$  contents in the selected natural hibonites can be used to obtain information on the oxygen fugacity conditions that these hibonites experienced during the formation and evolution of the CAIs in which they were included. However, it has been shown in Section 4.2.2 that the  $Ti^{3+}$  contents in hibonite also depends on the  $Ti^{tot}/Mg$  ratios and not simply on the oxygen fugacity. Therefore such ratios have to be taken into account in order to apply the appropriate  $Ti^{3+}-fO_2$  relationship. The values of  $Ti^{tot}/Mg$  ratio observed for the chondritic hibonites do not exceed 1.17 (Table 6.3) and are comparable to those of the synthetic samples series gel2 and gel6, which form the group I described in Table 4.2. The molar percentage of  $Ti^{3+}$  of the natural samples are hence reported on the  $Ti^{3+}-fO_2$  relationship obtained for the synthetic hibonites of group I (Fig. 6.6).

The corresponding oxygen fugacities obtained from these natural samples cover a range between  $\log fO_2 = -14$  and  $\log fO_2 = -0.5$ , *i.e.* the hibonite grain from Dar al Gani 203 experienced complete oxidation. These quantitative estimations of  $fO_2$  are much more oxidising than those expected for samples exposed to the Solar Nebula, however, they are in agreement with previous qualitative estimations (Ihinger and Stolper, 1986).

The results can be interpreted taking in consideration a recent study presented by Paque et al. (2013). The authors have determined the valence state of Ti in minerals of CAIs from Allende meteorite (CV3) by means of XANES and found the remarkable occurrence of a spinel grain having a  $Ti^{4+}$ -rich core,  $Ti^{3+}$ -rich rim, and coexisting with a  $Ti^{3+}$ -rich clinopyroxene. They also have determined the valence state of Ti on run products from previously published CAI crystallisation experimental studies (Stolper, 1982; Stolper and Paque, 1986; Connolly Jr. and

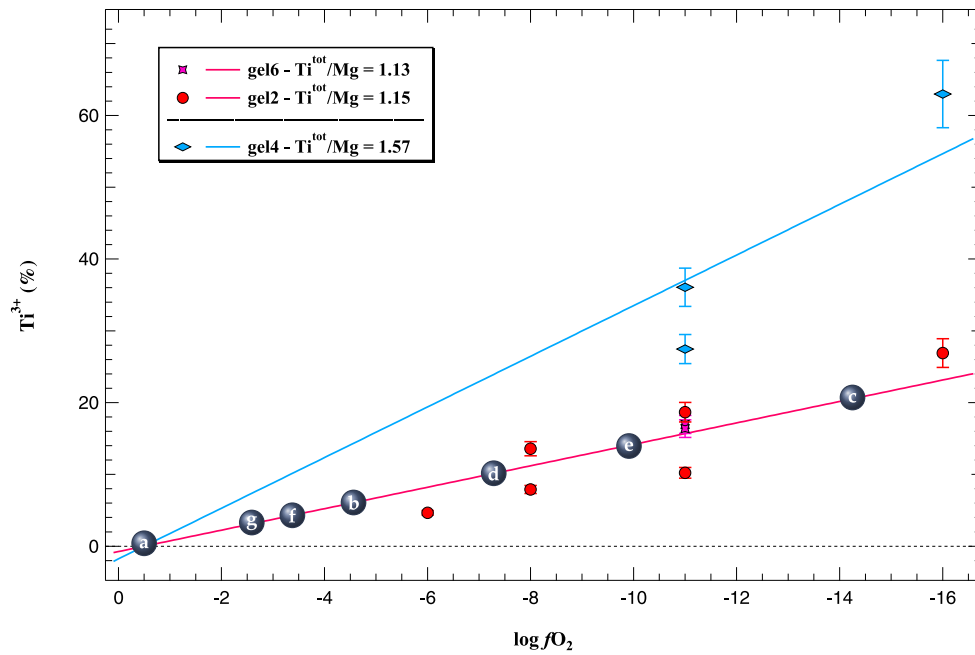


Figure 6.6: Variation of the molar percentage of  $Ti^{3+}$  as a function of  $fO_2$  for the hibonite samples of groups I and II together with the measurements carried out on natural hibonites. The lettering of the samples is that reported in Table 6.3.

Burnett, 2003) and found that both spinels and clinopyroxenes had  $Ti^{3+}$  contents directly correlated with the  $fO_2$  imposed during experiments. The models proposed by Paque et al. (2013) to explain the redox paradox observed on the natural samples involve either *relict spinel-perovskite equilibria* or *low pressure evaporation*. These models require the occurrence of transient heating events that melted and vaporised already existing CAIs or nebular dust. In the relict spinel-perovskite model a spinel grains survives the remelting of the hosting CAI and rapidly equilibrates with a  $Ti^{4+}$ -rich liquid environment due, for example, to melting of neighbouring perovskite, which typically contains prevalent amounts of tetravalent Ti. On the other hand, the low-pressure evaporation model considers that the complete vaporisation of nebular precursors at typically low pressures can result in localised regions of highly oxidising conditions due to the dissociation of, for example, lithophile elements oxides:  $MgO = Mg + O$ ,  $SiO_2 = SiO + O$ .

Both models proposed by Paque et al. (2013) for explaining high  $Ti^{4+}$  contents in natural spinel can be extended to hibonite. In fact, also in the case of this mineral there is a discrepancy between the  $fO_2$  estimated using  $Ti^{3+}$  in clinopyroxenes (Grossman et al., 2008) and in hibonite (Fig. 6.6; Ihinger and Stolper, 1986).

Hibonite-perovskite associations are common petrographic features of CAI and are also observed in the natural samples analysed in this study (Fig. 6.1), thus the relict spinel-perovskite

model can be reinterpreted as a *hibonite-perovskite model*. Moreover, the CAIs analysed in this study also contain spinel-perovskite associations, therefore further studies on these samples could be performed by means of XANES in order to determine the valence state of Ti in spinel and test the observations made by Paque et al. (2013).

The low pressure evaporation model can be applied to hibonite as such, in fact, this mineral condenses at temperatures higher with respect to spinel; these hotter conditions can provide an environment in which oxides are dissociated at higher rates thus providing even more O-rich, *i.e.* oxidising, conditions.

The fact that clinopyroxenes are more  $Ti^{3+}$  rich can be explained, as pointed out by Paque et al. (2013), considering that this mineral condenses at lower temperatures thus in conditions where the transient event that generated oxidising conditions are no longer active and normal, *i.e.* reducing, nebular conditions are restored. Moreover, the spinel analysed by Paque et al. (2013) shows a core-to-rim  $Ti^{3+}$  enrichment due to later re-equilibration at reducing conditions. For the hibonites analysed in this study by means of TEM-EELS it was not possible to perform  $Ti^{3+}$  profiling due to the limited availability of thin areas in the FIB lamellæ. It can be assumed, however, that given the strong effect exerted by the hibonite crystal chemistry in stabilising  $Ti^{4+}$ - $Mg^{2+}$  couples, hibonite might retain the high valence state of Ti once more reducing conditions were re-established.

## 7 Concluding remarks

The aim of this thesis is to better understand the cation distribution and the crystal chemistry of hibonite as well as to determine the valence state of Ti in order to correlate it to the oxygen fugacity at which hibonite formed. The results obtained for hibonites synthesised at different oxygen fugacity and with different Ti/Mg ratios have been used to interpret TEM-EELS analyses performed on natural hibonites (Chapter 6) and to shed new light on the measurements performed on hibonite by previous authors.

This final chapter is a summary of the result obtained using a collection of techniques such as SEM-EPMA and XRD (Chapter 3), TEM-EELS (Chapter 4) and UV/Vis spectroscopy (Chapter 5).

### 7.1 Site distribution and valence state of Ti in hibonite

Polycrystalline and single crystal hibonite samples were synthesised at variable oxygen fugacities and with a range of composition in Ti and Mg relevant for natural hibonites. To date this is the first report of synthesis of  $\text{Ti}^{3+}$ - $\text{Ti}^{4+}$ -Mg-bearing hibonites single crystals. These innovative syntheses were carried out by hot-pressing polycrystalline hibonites in a piston-cylinder apparatus and by using Ti-Mg-doped citrate-based sol-gel precursors for high temperature sintering under controlled oxygen fugacities. X-ray diffraction investigations on hibonite single crystals have shown that Ti atoms occupy two sites in the structure of hibonite, a trigonally distorted octahedral site occurring in face-sharing pairs, *M4*, and a trigonal bipyramid, *M2*. Moreover, the refined occupancy factors on these two sites clearly indicated that the amount of Ti partitioning on the *M4* site is four time larger than that on the *M2* site. The analysis of bond distances and thermal displacement parameters also suggests that  $\text{Ti}^{3+}$  may be present at both the *M4* and *M2* sites; it is also confirmed that divalent species such as  $\text{Mg}^{2+}$  occupy the tetrahedral *M3* site.

These findings are in disagreement with previous determinations of  $\text{Ti}^{3+}$  in hibonite based on ESR, which indicated the presence of this cation exclusively on the *M2* site (Beckett et al., 1988). However, the ESR data have been recently reinterpreted as originating from  $\text{Ti}^{3+}$  being present only on the *M4* site, in agreement with the results of DFT calculations on Ti-Mg-bearing hibonites (Doyle et al., 2014). Nevertheless, the data presented in this study show that  $\text{Ti}^{3+}$  substitutes for Al neither only on the *M4* site nor only on the *M2* site but rather on both sites.

This study also provides the first titanium  $L_{2,3}$  edge characterisation on synthetic and natural hibonites, as well as the most accurate UV/Vis spectroscopy determination carried out so far. Fine-grained specimens do not constitute a limitation for a technique with high spatial resolution such EELS in a TEM, however, they are problematic for UV/Vis spectroscopy. The synthesis of large hibonite single crystals have enabled acquiring UV/Vis spectra with polarised light on oriented hibonite samples. Moreover, the structural information obtained from single crystal XRD, such as cation distribution, site geometry and site distortions, have allowed characterising the coordination environment of the Ti species present in the structure of hibonite. These information have been used to describe the electronic configuration of  $\text{Ti}^{3+}$  in terms of relative energy of the *d* orbitals involved in its coordination thus bringing a great contribution to the interpretation of EEL and UV/Vis spectra.

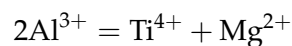
In EELS the fine-structure of the Ti  $L_{2,3}$  edge have been linked to site distortions due to (dynamic) Jahn-Teller effect and have been used to quantify  $\text{Ti}^{3+}$  in synthetic samples. The valence state of Ti was then correlated to the oxygen fugacity at which the samples were synthesised. These information were subsequently use to interpret the  $\text{Ti}^{3+}$  concentration measured on natural samples in terms of  $f\text{O}_2$  conditions. The application of this technique on natural hibonites, not only provides the first direct measure of  $\text{Ti}^{3+}$  in these samples, but also implies that the chemical and structural properties observed on synthetic hibonites are also valid for natural ones. In particular, it is assumed that Ti occupy the *M4* and the *M2* sites with a significant preference for the former and that the changes in the EEL spectra of natural samples are also due to Jahn-Teller effect. This assumption is supported by the similarities between the EELS and UV/Vis spectra of natural and synthetic hibonites.

In UV/Vis spectroscopy the intensity of the most prominent absorption band at 715 nm has been found to linearly correlate with the product between the concentrations of  $\text{Ti}^{3+}$  and  $\text{Ti}^{4+}$  determined from EEL spectra, indicating that this absorption band originates from a  $\text{Ti}^{3+}$ - $\text{Ti}^{4+}$  intervalence charge transfer (IVCT) transition. The occurrence of this type of transition in hibonite has been proposed before, although preference was given to the hypothesis that this

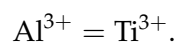
bands was due simply to absorption of  $\text{Ti}^{3+}$  atoms. This study, therefore represents the first experimental evidence for IVCT in hibonite. This results supports the evidences obtained from XRD of Ti mostly occupying the face-sharing octahedra  $M4$  as this is the only site in which IVCT transitions can occur. Moreover, since the absorbance-Ti concentration relationship were based on the  $\text{Ti}^{3+}$  contents obtained with EELS, the analysis of UV/Vis spectra indicates that the EELS measurements provide reasonably good estimates of  $\text{Ti}^{3+}$  concentrations in hibonite. Lastly, the comparison of the UV/Vis spectra of V-free samples from this study with those of V-bearing hibonites from Ihinger and Stolper (1986) supports the idea that the orange colour in hibonite is due to a crystal field band observed between 350 and 450 nm and attributed to V, whereas the blue colour originates from the  $\text{Ti}^{3+}$ - $\text{Ti}^{4+}$  IVCT transition. It is not clear, however, from which site the transition involving V occurs, in fact titanium and vanadium are likely to compete for the occupation of the same sites. How this competition takes place and what is the reciprocal effect of Ti and V on their valence states, however, still remains an open question and subject of future investigations.

## 7.2 *The crystal chemistry of hibonite*

The analysis of electron microprobe measurements on both synthetic and natural hibonites have indicated that the coupled substitution mechanism presented in Eq. 3.1,

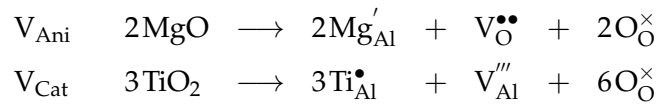


is the major incorporation mechanism for Ti and Mg in hibonite. In fact, these two element occupy sites which are found in neighbouring layers on the structure of hibonite, thus the local charge balance becomes important when substituting for Al. Only at very reducing conditions or when the amount of Mg is deficient with respect to that of Ti, the substitution of  $\text{Ti}^{3+}$  for  $\text{Al}^{3+}$  can take place, Eq. 3.2,



The EELS measurements have confirmed that the amount of  $\text{Ti}^{3+}$  substituting into the structure of hibonite is a function of the  $\text{Ti}^{\text{tot}}/\text{Mg}$  ratio; for ratios close to one, the incorporation of  $\text{Ti}^{3+}$  is very limited, whereas for Mg-free hibonites the  $f\text{O}_2$  fully controls the trivalent titanium intake. Further considerations on these substitution mechanisms in hibonite can be made combining the data from EPMA and from EELS in order to consider the chemical formula of hibonite

distinguishing the two valence state of Ti. The ternary plot presented in Fig. 7.1 shows on each corner the sum of di-, tri- and tetra-valent cations and indicates the possible substitution mechanisms in hibonite. These mechanisms are tagged in Fig. 7.1 as No V,  $V_{\text{Ani}}$  and  $V_{\text{Cat}}$  indicating substitution mechanisms occurring without the formation of defects, with the formation of anion vacancies and with the formation of cation vacancies, respectively. The first case is realised according to Eqs. 3.1 and 3.2 while the latter two are expressed using Kröger-Vink's notation (Kröger and Vink, 1956) as follows:



The data shown in Fig. 7.1-a correspond to the synthetic hibonites obtained from sol-gel precursors. In the limit of EPMA uncertainties, the data plot along the direction indicated with No V for gel2 and gel6 sample series which, according to their  $\text{Ti}^{\text{tot}}/\text{Mg}$  ratio, belong to group I (Table 4.2), indicating that these samples follow the coupled substitution of Eqs. 3.1 and 3.2. The data of samples from gel4 series that, given their excess of Ti over Mg, belong to series II, would be expected to plot off from the No V trend. However, probably due to the relatively low concentration of bulk Ti, they can not be assigned to any deficiency mechanism. On the other hand, the Mg-free samples of gel3 series (group III), clearly plot in the direction of cation vacancy indicating that at oxidising conditions the incorporation of  $\text{Ti}^{4+}$  is charge balanced by cation vacancies.

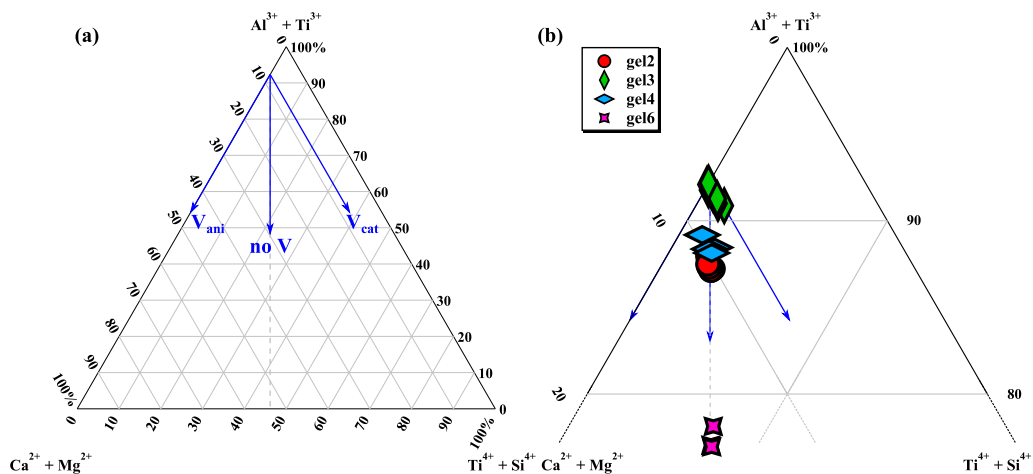


Figure 7.1: Ternary plot showing the sum di-, tri- and tetra-valent cations plotted against each other. (a) Full-range plot indicating the expected data trends for different substitution mechanisms (blue arrows). (b) Enlargement of the top portion of the ternary plot showing the data for the EPMA performed on synthetic samples obtained from sol-gel precursors.

It is important to consider the kinetic of  $\text{Ti}^{3+}$  and  $\text{Ti}^{4+}$  equilibration in hibonite. In order to promote faster kinetics of reaction and growth of larger crystals, the synthesis of most of the hibonite samples were performed at temperatures between 1500 and 1550 °C even though the temperature of condensation of hibonite in nebular condition is about 1450 °C. The samples FIB2S2C and gel2-4 have similar compositions (Table 3.5) and were synthesised both at  $\log f\text{O}_2 = -8$  for comparable times (Tables 3.2 and 3.3) at 1450 and 1550 °C, respectively. The EELS measurements reveal that these samples have similar  $\text{Ti}^{3+}$  contents (17 and 13%), indicating that the temperature effects seems to be negligible. This allows extending at lower temperatures the observations made on samples synthesised at temperatures above those considered in thermodynamic models for predicting the condensation sequence of minerals in the Solar Nebula, *i.e.* 1450 °C. On the other hand, the shock-wave model implies that for short periods of time the temperatures in the region where condensation took place were high enough to induce vaporisation of the nebular dust, thus even higher than 1550 °C.

The sample gel3 synthesised at  $\log f\text{O}_2 = -16$  and 1550 °C (gel3-2) has also been re-equilibrated at  $\log f\text{O}_2 = -11$  and 1550 °C for 15 h (gel3-3R). The sample gel3-2 was considered to exclusively contain  $\text{Ti}^{3+}$  while after re-equilibration the EELS measurements on two different grains give discordant results. This sample seems to have changed only slightly the  $\text{Ti}^{3+}$  content once uncertainties are taken into account (Table 4.1). As a consequence, sample gel3-3R is more reduced than the corresponding sample gel3-3 synthesised directly at  $\log f\text{O}_2 = -11$ . Note that repeated EELS measurements on different samples show more consistent  $\text{Ti}^{3+}$  contents for similar equilibration times. This indicates that the crystal chemistry not only controls the valence state of titanium at the moment of crystallisation of hibonite, but also makes later changes of  $\text{Ti}^{3+}$  concentrations more sluggish, at least at the experimental time scale in the laboratory.

### 7.3 *The oxygen fugacity in the Solar Nebula*

EPMA and EELS measurements performed on hibonite samples can be used to quantify  $\text{Ti}^{3+}$  if the effects of crystal chemistry on the Ti valence state and their  $\text{Ti}^{\text{tot}}/\text{Mg}$  ratio are taken into account. Moreover, it has been observed that the valence state of Ti correlates linearly with oxygen fugacity at which hibonites are exposed. The proportionality factor between  $\text{Ti}^{3+}$  and  $f\text{O}_2$ , however, are small for samples having  $\text{Ti}^{\text{tot}}/\text{Mg}$  ratios close to one, which is a typical value for natural hibonites.

The application of the  $\text{Ti}^{3+}$ - $f\text{O}_2$  relationship to the EELS measurements performed on the

natural samples analysed in this study indicates that these hibonites were exposed in the Solar Nebula to oxygen fugacities several order of magnitude more oxidising than expected, confirming what suggested, though not quantified, in the pioneering study on the  $\text{Ti}^{3+}$ - $f\text{O}_2$  relationship in hibonite (Ihinger and Stolper, 1986).

Finally, the discrepancy between  $f\text{O}_2$  of the Solar Nebula derived from  $\text{Ti}^{3+}$  determinations on hibonite and on clinopyroxenes (Grossman et al., 2008) has been interpreted considering that the transient heating events that triggered the condensation of CAIs were also associated with locally oxidising environments (Paque et al., 2013). Consequently, the oxygen fugacity recorded by a refractory phase such as hibonite is that of the heating event that led to its formations, while clinopyroxenes, condensing at lower temperatures, have likely sensed the re-established reducing conditions typical of the Solar Nebula, *i.e.*  $\log f\text{O}_2 = -19.8$  at  $\sim 1503$  K (Grossman et al., 2008).

## References

- M. Abbate, F. M. F. de Groot, J. C. Fuggle, A. Fujimori, Y. Tokura, Y. Fujishima, O. Strebel, M. Domke, G. Kaindl, J. van Elp, B. T. Thole, G. A. Sawatzky, M. Sacchi, and N. Tsuda. Soft-X-ray-absorption studies of the location of extra charges induced by substitution in controlled-valence materials. *Physical Review B*, 44(11):5419–5422, 1991. doi:10.1103/PhysRevB.44.5419. 88
- B. L. Adams, S. I. Wright, and K. Kunze. Orientation imaging: The emergence of a new microscopy. *Metallurgical Transactions A*, 24(4):819–831, 1993. doi:10.1007/BF02656503. 46
- R. Aggarwal, A. Sanchez, M. M. Stuppi, R. Fahey, A. Strauss, W. Rapoport, and C. P. Khattak. Residual infrared absorption in as-grown and annealed crystals of  $\text{Ti:Al}_2\text{O}_3$ . *IEEE Journal of Quantum Electronics*, 24(6):1003–1008, 1988. doi:10.1109/3.221. 106, 111
- Agilent Technologies. CrysAlisPro Software system, 2012. 33
- J. M. Allen, L. Grossman, A. M. Davis, and I. D. Hutcheon. Mineralogy, textures and mode of formation of a hibonite-bearing Allende inclusion. In *Proceedings Lunar Planetary Science Conference 9th*, pages 1209–1233, 1978. 10
- Y. Amelin, A. N. Krot, I. D. Hutcheon, and A. A. Ulyanov. Lead isotopic ages of chondrules and Calcium-Aluminum-rich inclusions. *Science*, 297(5587):1678–1683, 2002. doi:10.1126/science.1073950. 9
- L. An, H. M. Chan, and K. K. Soni. Control of calcium hexaluminate grain morphology in in-situ toughened ceramic composites. *Journal of Materials Science*, 31(12):3223–3229, 1996. doi:10.1007/BF00354672. 21, 55
- J. D. Anderson, E. L. Lau, M. K. Bird, B. C. Clark, G. Giampieri, and M. Pätzold. Dynamic science on the Stardust mission. *Journal of Geophysical Research: Planets*, 108(E10):8117, 2003. doi:10.1029/2003JE002092. 3
- R. J. Angel and L. W. Finger. SINGLE: a program to control single-crystal diffractometers. *Journal of Applied Crystallography*, 44(1):247–251, 2010. doi:10.1107/S0021889810042305. 32
- J. T. Armstrong, G. P. Meeker, J. C. Huneke, and G. J. Wasserburg. The blue angel: I. The mineralogy and petrogenesis of a hibonite inclusion from Murchison meteorite. *Geochimica et Cosmochimica Acta*, 46(4):575–595, 1982. 11, 104
- A. Audétat. *Personal communication*. Bayerisches Geoinstitut, University of Bayreuth, Germany., 2011. 27
- J. Bally, J. Morse, and B. Reipurth. The birth of stars: Herbig-Haro jets, accretion and proto-planetary disks. In *Science with the Hubble Space Telescope - II*, pages 491–502, 1996. 2
- J. Beckett, D. Live, F. Tsay, L. Grossman, and E. Stolper.  $\text{Ti}^{3+}$  in meteoritic and synthetic hibonite. *Geochimica et Cosmochimica Acta*, 52(6):1479–1495, 1988. doi:10.1016/0016-7037(88)90219-0. 11, 12, 17, 112, 127
- J. R. Beckett and L. Grossman. Oxygen fugacities in the Solar nebula during crystallization of fassaite in Allende inclusions. In *Proceedings Lunar Planetary Science Conference 17th*, pages 36–37, 1986. 11, 13, 19
- V. Bermanec, D. Holtstam, D. Sturman, A. J. Criddle, M. E. Back, and S. Scavnicar. Nezilovite, a new member of the magnetoplumbite group, and the crystal chemistry of magnetoplumbite and hibonite. *Canadian Mineralogist*, 34(6):1287–1297, 1996. 14, 16, 30, 33, 66, 67, 70, 73
- A. Bischoff, H. Palme, R. Ash, R. Clayton, L. Schultz, U. Herpers, D. Stöffler, M. Grady, C. Pillinger, B. Spettel, H. Weber, T. Grund, M. Endress, and D. Weber. Paired Renazzo-type (CR) carbonaceous chondrites from the Sahara. *Geochimica et Cosmochimica Acta*, 57(7):1587–1603, 1993a. doi:10.1016/0016-7037(93)90014-N. 20, 115

- A. Bischoff, H. Palme, L. Schultz, D. Weber, H. Weber, and B. Spettel. Acfer 182 and paired samples, an iron-rich carbonaceous chondrite: Similarities with ALH85085 and relationship to CR chondrites. *Geochimica et Cosmochimica Acta*, 57(11):2631–2648, 1993b. doi:10.1016/0016-7037(93)90422-S. 9
- M. Blander and L. H. Fuchs. Calcium-aluminum-rich inclusions in the Allende meteorite: evidence for a liquid origin. *Geochimica et Cosmochimica Acta*, 39(12):1605–1619, 1975. doi:10.1016/0016-7037(75)90083-6. 10
- T. Boffa Ballaran, R. J. Angel, and M. A. Carpenter. High-pressure transformation behaviour of the cummingtonite-grunerite solid solution. *European Journal of Mineralogy*, 12(6):1195–1213, 2000. doi:10.1127/0935-1221/2000/0012-1195. 73
- F. R. Boyd and J. L. England. Apparatus for phase-equilibrium measurements at pressures up to 50 kilobar and temperatures up to 1750 °C. *Journal of Geophysical Research*, 65(2):741–748, 1960. doi:10.1029/JZ065i002p00741. 25
- W. L. Bragg. The diffraction of short electromagnetic waves by a crystal. *Mathematical Proceedings of the Cambridge Philosophical Society*, 17:43–57, 1913. 30
- R. Brydson, B. Williams, W. Engel, H. Sauer, E. Zeitler, and J. Thomas. Electron energy-loss spectroscopy (EELS) and the electronic structure of titanium dioxide. *Solid State Communications*, 64(4):609–612, 1987. doi:10.1016/0038-1098(87)90792-7. 79
- R. Brydson, H. Sauer, W. Engel, J. Thomas, E. Zeitler, N. Kosugi, and H. Kuroda. Electron energy loss and X-Ray absorption spectroscopy of rutile and anatase - a test of structural sensitivity. *Journal of Physics: Condensed Matter*, 1(4):797–812, 1989. doi:10.1088/0953-8984/1/4/012. 79, 85, 88
- R. G. Burns. *Mineralogical Applications of Crystal Field Theory*. Cambridge University Press, 1993. ISBN 9780521430777. 105, 106, 111
- R. G. Burns and V. M. Burns. Crystal chemistry of meteoritic hibonites. *Journal of Geophysical Research: Solid Earth*, 89(Supplement):C313–C321, 1984. 111
- R. G. Burns and F. E. Huggins. Visible-region absorption spectra of a  $\text{Ti}^{3+}$  fassaite from the Allende meteorite: a discussion. *American Mineralogist*, 58:955–961, 1973. 106
- R. G. Burns, D. A. Nolet, K. M. Parkin, C. A. McCammon, and K. B. Schwartz. Mixed-valence minerals of iron and titanium: Correlations of structural, mössbauer and electronic spectral data. In *Mixed-Valence Compounds*, volume 58 of *NATO Advanced Study Institutes Series*, pages 295–336. Springer Netherlands, 1980. ISBN 978-94-009-9078-4, 978-94-009-9076-0. 105
- M. A. Carpenter, T. Boffa Ballaran, and A. J. Atkinson. Microscopic strain, local structural heterogeneity and the energetics of silicate solid solutions. *Phase Transitions*, 69(1):95–109, 1999. doi:10.1080/01411599908208011. 73
- F. Cavallone, I. Pollini, and G. Spinolo. Optical Properties of  $\alpha\text{-TiCl}_3$  at the Magnetic Transition Temperature. *Physica Status Solidi (b)*, 45(2):405–410, 1971. doi:10.1002/pssb.2220450204. 88
- E. J. Chaisson and R. Villard. The science mission of the Hubble Space Telescope. *Vistas in Astronomy*, 33(2):105–141, 1990. doi:10.1016/0083-6656(90)90018-4. 2
- A. K. Chatterjee and G. I. Zhmoidin. The phase equilibrium diagram of the system  $\text{CaO-Al}_2\text{O}_3\text{-CaF}_2$ . *Journal of Materials Science*, 7(1):93–97, 1972. doi:10.1007/BF00549555. 49
- M. Cheynet, S. Pokrant, S. Irsen, and P. Krüger. New fine structures resolved at the ELNES  $\text{Ti-L}_{2,3}$  edge spectra of anatase and rutile: Comparison between experiment and calculation. *Ultramicroscopy*, 110(8):1046–1053, 2010. doi:10.1016/j.ultramic.2010.03.001. 79
- C. Chopin and K. Langer.  $\text{Fe}^{2+}\text{-Ti}^{4+}$  Charge-transfer between face-sharing octahedra - Polarized absorption-spectra and crystal-chemistry of Ellenbergerite. *Bulletin De Mineralogie*, 111(1):17–27, 1988. 106
- M. K. Cinibulk. Effect of precursors and dopants on the synthesis and grain growth of calcium hexaluminate. *Journal of the American Ceramic Society*, 81(12):3157–3168, 1998. 22, 23, 54
- R. C. Clark and J. S. Reid. The analytical calculation of absorption in multifaceted crystals. *Acta Crystallographica Section A*, 51:887–897, 1995. 9, 33

- J. N. Connelly, M. Bizzarro, A. N. Krot, Å. Nordlund, D. Wielandt, and M. A. Ivanova. The absolute chronology and thermal processing of solids in the Solar protoplanetary disk. *Science*, 338(6107):651–655, 2012. doi:10.1126/science.1226919. 7
- H. C. Connolly Jr. and D. S. Burnett. On type B CAI formation: experimental constraints on  $fO_2$  variations in spinel minor element partitioning and reequilibration effects. *Geochimica et Cosmochimica Acta*, 67(22):4429–4434, 2003. doi:10.1016/S0016-7037(03)00271-0. 123
- F. A. Cotton, G. Wilkinson, A. C. Murillo, and M. Bochmann. *Advanced inorganic chemistry*. John Wiley & Sons, 6th edition, 1999. ISBN 0471199575 978-0471199571. 79
- A. M. Davis and F. M. Richter. Condensation and evaporation of solar system materials. In *Treatise on Geochemistry, Vol. 1: Meteorites, Comets and Planets*, pages 407–430. Elsevier, Oxford, 2003. ISBN 978-0-08-043751-4. 6
- S. J. Desch, F. J. Ciesla, L. L. Hood, and T. Nakamoto. Heating of chondritic materials in Solar nebula shocks. In *Chondrites and the Protoplanetary Disk ASP Conference Series*, volume 341, pages 849–872, 2005. ISBN 1050-3390. 6
- R. T. Downs and M. Hall-Wallace. The American Mineralogist crystal structure database. *American Mineralogist*, 88(1):247–250, 2003. 33
- E. Dowty and J. R. Clark. Crystal structure refinement and optical properties of a  $Ti^{3+}$  fassaite from the Allende meteorite. *American Mineralogist*, 58:230–242, 1973a. 106
- E. Dowty and J. R. Clark. Crystal structure refinement and optical properties of a  $Ti^{3+}$  fassaite from the Allende meteorite: Reply. *American Mineralogist*, 58:962–964, 1973b. 106
- P. M. Doyle, P. F. Schofield, A. J. Berry, A. M. Walker, and K. S. Knight. Substitution of  $Ti^{3+}$  and  $Ti^{4+}$  in hibonite ( $CaAl_{12}O_{19}$ ). *American Mineralogist*, 99:1369–1382, 2014. doi:10.2138/am.2014.4532. 17, 108, 112, 127
- M. D. Dyar, T. C. Solberg, and R. G. Burns. The effects of composition, oxygen fugacity, and crystal structure on the color of hibonite. In *Proceedings Lunar Planetary Science Conference 17th*, pages 194–195, 1986. 111
- K. A. Dyl, J. I. Simon, and E. D. Young. Valence state of titanium in the Wark–Lovering rim of a Leoville CAI as a record of progressive oxidation in the early Solar nebula. *Geochimica et Cosmochimica Acta*, 75(3):937–949, 2011. doi:10.1016/j.gca.2010.09.042. 13
- R. F. Egerton. *Electron energy-loss spectroscopy in the electron microscope*. Springer, 1996. ISBN 9780306452239. 39, 42
- L. Farrugia. WinGX suite for small-molecule single-crystal crystallography. *Journal of Applied Crystallography*, 32(4):837–838, 1999. 33
- B. Fegley Jr. and H. Palme. Evidence for oxidizing conditions in the solar nebula from Mo and W depletions in refractory inclusions in carbonaceous chondrites. *Earth and Planetary Science Letters*, 72(4):311–326, 1985. doi:10.1016/0012-821X(85)90055-X. 10, 11
- W. A. d. Fonseca-Zang, J. W. Zang, and W. Hofmeister. The Ti-influence on the tourmaline color. *Journal of the Brazilian Chemical Society*, 19(6):1186–1192, 2008. doi:10.1590/S0103-50532008000600020. 106
- B. R. Frost. Introduction to oxygen fugacity and its petrologic importance. *Reviews in Mineralogy & Geochemistry*, 25(1):1–9, 1991. 10, 51
- D. J. Frost, C. Liebske, F. Langenhorst, C. A. McCammon, R. G. Trønnes, and D. C. Rubie. Experimental evidence for the existence of iron-rich metal in the Earth’s lower mantle. *Nature*, 428(6981):409–412, 2004. doi:10.1038/nature02413. 18
- L. A. J. Garvie. From the editor of the meteoritical bulletin. *Meteoritics & Planetary Science*, 47(11):1887–1887, 2012. doi:10.1111/maps.12057. 3
- T. Gasparik. Experimental study of subsolidus phase relations and mixing properties of pyroxene in the system  $CaO-Al_2O_3-SiO_2$ . *Geochimica et Cosmochimica Acta*, 48(12):2537–2545, 1984. doi:10.1016/0016-7037(84)90304-1. 27, 49
- C. Geiger, O. Kleppa, B. Mysen, J. Lattimer, and L. Grossman. Enthalpies of formation of  $CaAl_4O_7$  and  $CaAl_{12}O_{19}$  (hibonite) by high temperature, alkali borate solution calorimetry. *Geochimica et Cosmochimica Acta*, 52(6):1729–1736, 1988. doi:10.1016/0016-7037(88)90241-4. 17, 25

- C. Giacovazzo. *Fundamentals of Crystallography*. Oxford University Press, 2002. ISBN 9780198509585. 29, 32, 54
- R. C. Greenwood and I. A. Franchi. Alteration and metamorphism of CO<sub>3</sub> chondrites: Evidence from oxygen and carbon isotopes. *Meteoritics & Planetary Science*, 39(11):1823–1838, 2004. 9
- N. W. Grimes, P. Thompson, and H. F. Kay. New symmetry and structure for spinel. *Proceedings of the Royal Society of London. Series A - Mathematical and Physical Sciences*, 386(1791):333–345, 1983. doi:10.1098/rspa.1983.0039. 30
- L. Grossman. Condensation in the primitive solar nebula. *Geochimica et Cosmochimica Acta*, 36(5):597–619, 1972. doi:10.1016/0016-7037(72)90078-6. 6, 15
- L. Grossman and S. Clark Jr. High-temperature condensates in chondrites and the environment in which they formed. *Geochimica et Cosmochimica Acta*, 37(3):635–649, 1973. doi:10.1016/0016-7037(73)90224-X. 9
- L. Grossman and J. W. Larimer. Early chemical history of the solar system. *Reviews of Geophysics*, 12(1):71–101, 1974. doi:10.1029/RG012i001p00071. 4, 6
- L. Grossman and E. Olsen. Origin of the high-temperature fraction of C2 chondrites. *Geochimica et Cosmochimica Acta*, 38(1):173–187, 1974. doi:10.1016/0016-7037(74)90202-6. 9, 10
- L. Grossman, J. R. Beckett, A. V. Fedkin, S. B. Simon, and F. J. Ciesla. Redox conditions in the solar nebula: Observational, experimental, and theoretical constraints. *Reviews in Mineralogy & Geochemistry*, 68:93–140, 2008. 13, 19, 124, 131
- T. Hahn. *International tables for crystallography, space-group symmetry*. John Wiley & Sons, 2005. ISBN 9780792365907. 33
- S. A. Hayward and E. K. H. Salje. Displacive phase transition in anorthoclase; the "plateau effect" and the effect of T1-T2 ordering on the transition temperature. *American Mineralogist*, 81(11-12):1332–1336, 1996. 73
- M. Hechler. ROSETTA mission design. *Advances in Space Research*, 19(1):127–136, 1997. doi:10.1016/S0273-1177(96)00125-1. 3
- D. C. Hezel and H. Palme. The chemical relationship between chondrules and matrix and the chondrule matrix complementarity. *Earth and Planetary Science Letters*, 294(1–2):85–93, 2010. doi:10.1016/j.epsl.2010.03.008. 5
- R. Hinton, A. Davis, D. Scatenawachel, L. Grossman, and R. Ddraus. A chemical and isotopic study of hibonite-rich refractory inclusions in primitive meteorites. *Geochimica et Cosmochimica Acta*, 52(11):2573–2598, 1988. doi:10.1016/0016-7037(88)90028-2. 9
- A. M. Hofmeister, B. Wopenka, and A. J. Locock. Spectroscopy and structure of hibonite, grossite, and CaAl<sub>2</sub>O<sub>4</sub>: Implications for astronomical environments. *Geochimica et Cosmochimica Acta*, 68(21):4485–4503, 2004. doi:10.1016/j.gca.2004.03.011. 16, 18, 66, 70, 73
- D. Holtstam. Iron in hibonite: a spectroscopic study. *Physics and Chemistry of Minerals*, 23(7):452–460, 1996. doi:10.1007/BF00202031. 16, 111
- C. B. Hübschle, G. M. Sheldrick, and B. Dittrich. ShelXle: a Qt graphical user interface for SHELXL. *Journal of Applied Crystallography*, 44(6):1281–1284, 2011. doi:10.1107/S0021889811043202. 33
- G. R. Huss, C. M. O. Alexander, H. Palme, P. A. Bland, and J. T. Wasson. Genetic relationships between chondrules, fine-grained rims, and interchondrule matrix. In *Chondrites and the Protoplanetary Disk ASP Conference Series*, volume 341, pages 701–731, 2005. ISBN 1050-3390. 5
- G. R. Huss, A. E. Rubin, and J. N. Grossman. Thermal metamorphism in chondrites. In *Meteorites and the Early Solar System II*, pages 567–586. 2006. ISBN 978-0-8165-2562-1. 7
- I. D. Hutcheon and R. C. Newton. Mg Isotopes, mineralogy and mode of formation of secondary phases in C3 refractory inclusions. In *Proceedings Lunar Planetary Science Conference 12th*, pages 491–493, 1981. 10
- P. D. Ihinger and E. Stolper. The color of meteoritic hibonite: an indicator of oxygen fugacity. *Earth and Planetary Science Letters*, 78(1):67–79, 1986. doi:10.1016/0012-821X(86)90173-1. 11, 12, 17, 19, 28, 97, 102, 104, 105, 106, 111, 112, 123, 124, 128, 131

- T. R. Ireland. Presolar isotopic and chemical signatures in hibonite-bearing refractory inclusions from the Murchison carbonaceous chondrite. *Geochimica et Cosmochimica Acta*, 54(11):3219–3237, 1990. doi:10.1016/0016-7037(90)90136-9. 9
- H. A. Jahn and E. Teller. Stability of polyatomic molecules in degenerate electronic states. I. Orbital degeneracy. *Proceedings of the Royal Society of London. Series A - Mathematical and Physical Sciences*, 161(905):220–235, 1937. doi:10.1098/rspa.1937.0142. 87
- S. Jakobsson and N. Oskarsson. The system C-O in equilibrium with graphite at high pressure and temperature: An experimental study. *Geochimica et Cosmochimica Acta*, 58(1):9–17, 1994. doi:10.1016/0016-7037(94)90442-1. 51
- R. A. Kerr. A meteoriticist speaks out, his rocks remain mute. *Science*, 293(5535):1581–1584, 2001. doi:10.1126/science.293.5535.1581. 4
- H. E. King and L. W. Finger. Diffracted beam crystal centering and its application to high-pressure crystallography. *Journal of Applied Crystallography*, 12(AUG):374–378, 1979. 32
- N. T. Kita, G. R. Huss, S. Tachibana, Y. Amelin, L. E. Nyquist, and I. D. Hutcheon. Constraints on the origin of chondrules and CAIs from short-lived and long-lived radionuclides. In *Chondrites and the Protoplanetary Disk ASP Conference Series*, volume 341, pages 558–587, 2005. ISBN 1050-3390. 7, 9
- F. A. Kröger and H. J. Vink. Relations between the concentrations of imperfections in crystalline solids. *Solid State Physics*, 3:307–435, 1956. doi:10.1016/S0081-1947(08)60135-6. 91, 129
- A. Krot, Y. Amelin, P. Bland, F. Ciesla, J. Connelly, A. Davis, G. Huss, I. Hutcheon, K. Makide, K. Nagashima, L. Nyquist, S. Russell, E. Scott, K. Thrane, H. Yurimoto, and Q.-Z. Yin. Origin and chronology of chondritic components: A review. *Geochimica et Cosmochimica Acta*, 73(17):4963–4997, 2009. doi:10.1016/j.gca.2008.09.039. 7
- A. N. Krot, T. J. Fagan, K. Keil, K. D. McKeegan, S. Sahijpal, I. D. Hutcheon, M. I. Petaev, and H. Yurimoto. Ca,Al-rich inclusions, amoeboid olivine aggregates, and Al-rich chondrules from the unique carbonaceous chondrite Acfer 094: I. mineralogy and petrology. *Geochimica et Cosmochimica Acta*, 68(9):2167–2184, 2004. doi:10.1016/j.gca.2003.10.025. 116
- Larson, A. C. and Von Dreele, R. B. General Structure Analysis System (GSAS), 2004. 30
- R. Leapman and L. Grunes. Study of the  $L_{2,3}$  edges in the  $3d$  transition metals and their oxides by electron-energy-loss spectroscopy with comparisons to theory. *Physical Review B*, 26(2):614–636, 1982. 79
- P. Lessing. Mixed-cation oxide powders via polymeric precursors. *American Ceramic Society Bulletin*, 68(5):1002–1007, 1989. 22
- K. Lodders. Solar system abundances and condensation temperatures of the elements. *The Astrophysical Journal*, 591:1220–1247, 2003. 8
- G. J. MacPherson. Calcium-aluminum-rich inclusions in chondritic meteorites. In *Treatise on Geochemistry, Vol. 1: Meteorites, Comets and Planets*, pages 201–246. Elsevier, Oxford, 2003. ISBN 978-0-08-043751-4. 10
- G. J. Macpherson and L. Grossman. "Fluffy" type A Ca-, Al-rich inclusions in the Allende meteorite. *Geochimica et Cosmochimica Acta*, 48(1):29–46, 1984. doi:10.1016/0016-7037(84)90347-8. 10
- C. Marcilly, P. Courty, and B. Delmon. Preparation of highly dispersed mixed oxides and oxide solid solutions. *Journal of the American Ceramic Society*, 53(1):56, 1970. doi:10.1111/j.1151-2916.1970.tb12003.x. 46
- D. Mateika and H. Laudan. Czochralski growth of barium hexaaluminate single crystals. *Journal of Crystal Growth*, 46(1):85–90, 1979. doi:10.1016/0022-0248(79)90113-1. 17
- J.-L. Maurice, G. Herranz, C. Colliex, I. Devos, C. Carrétero, A. Barthélémy, K. Bouzehouane, S. Fusil, D. Imhoff, E. Jacquet, F. Jomard, D. Ballutaud, and M. Basletic. Electron energy loss spectroscopy determination of Ti oxidation state at the (001)  $\text{LaAlO}_3/\text{SrTiO}_3$  interface as a function of  $\text{LaAlO}_3$  growth conditions. *Europhysics Letters*, 82(1):17003, 2008. doi:10.1209/0295-5075/82/17003. 88
- C. McCammon. The Paradox of mantle redox. *Science*, 308(5723):807–808, 2005. doi:10.1126/science.1110532. 18

- E. Médard, C. A. McCammon, J. A. Barr, and T. L. Grove. Oxygen fugacity, temperature reproducibility, and H<sub>2</sub>O contents of nominally anhydrous piston-cylinder experiments using graphite capsules. *American Mineralogist*, 93(11-12):1838–1844, 2008. doi:10.2138/am.2008.2842. 51
- A. Meibom, M. I. Petaev, A. N. Krot, J. A. Wood, and K. Keil. Primitive FeNi metal grains in CH carbonaceous chondrites formed by condensation from a gas of solar composition. *Journal of Geophysical Research: Planets*, 104(E9):22053–22059, 1999. doi:10.1029/1999JE001052. 9
- C. Mitterbauer, G. Kothleitner, W. Grogger, H. Zandbergen, B. Freitag, P. Tiemeijer, and F. Hofer. Electron energy-loss near-edge structures of 3d transition metal oxides recorded at high-energy resolution. *Ultramicroscopy*, 96(3-4):469–480, 2003. doi:10.1016/S0304-3991(03)00109-8. 79, 85
- C. Moutou, M. Deleuil, T. Guillot, A. Baglin, P. Bordé, F. Bouchy, J. Cabrera, S. Csizmadia, and H. J. Deeg. CoRoT: Harvest of the exoplanet program. *Icarus*, 226(2):1625–1634, 2013. doi:10.1016/j.icarus.2013.03.022. 2
- M. Nagashima, T. Armbruster, and T. Hainschwang. A temperature-dependent structure study of gem-quality hibonite from Myanmar. *Mineralogical Magazine*, 74(5):871–885, 2010. doi:10.1180/minmag.2010.074.5.871. 16, 17, 66, 67, 70, 71, 73, 75
- J. Newton, A. Bischoff, J. W. Arden, I. A. Franchi, T. Geiger, A. Greshake, and C. T. Pillinger. Acfer 094, a uniquely primitive carbonaceous chondrite from the Sahara. *Meteoritics*, 30:47–56, 1995. doi:10.1111/j.1945-5100.1995.tb01211.x. 116
- A. O. Nier, R. W. Thompson, and B. F. Murphey. The isotopic constitution of lead and the measurement of geological time. III. *Physical Review*, 60(2):112–116, 1941. doi:10.1103/PhysRev.60.112. 9
- S. Nishikawa and S. Kikuchi. Diffraction of cathode rays by mica. *Nature*, 121(3061):1019–1020, 1928. doi:10.1038/1211019a0. 47
- M. Oetzel and G. Heger. Laboratory X-ray powder diffraction: a comparison of different geometries with special attention to the usage of the Cu K $\alpha$  doublet. *Journal of Applied Crystallography*, 32(4):799–807, 1999. doi:10.1107/S0021889899005737. 30
- A. Ohtomo, D. A. Muller, J. L. Grazul, and H. Y. Hwang. Artificial charge-modulation in atomic-scale perovskite titanate superlattices. *Nature*, 419(6905):378–380, 2002. doi:10.1038/nature00977. 88
- H. Palme and A. Jones. Solar system abundances of the elements. In *Treatise on Geochemistry, Vol. 1: Meteorites, Comets and Planets*, pages 41–61. Pergamon, Oxford, 2003. ISBN 978-0-08-043751-4. 8
- J. M. Paque, S. R. Sutton, S. B. Simon, J. R. Beckett, D. S. Burnett, L. Grossman, H. Yurimoto, S. Itoh, and H. C. Connolly. XANES and Mg isotopic analyses of spinels in Ca-Al-rich inclusions: Evidence for formation under oxidizing conditions. *Meteoritics & Planetary Science*, 48(10):2015–2043, 2013. doi:10.1111/maps.12216. 13, 123, 124, 125, 131
- P. Peshev, S. Delineshev, V. Petrov, N. Manuilov, P. Yankov, and I. Bachvarov. Bridgman-stockbarger growth and spectral characteristics of Al<sub>2</sub>O<sub>3</sub>:Ti<sup>3+</sup> single crystals. *Crystal Research and Technology*, 23(5):641–645, 1988. doi:10.1002/crat.2170230512. 106
- M. Planck. Ueber das gesetz der energieverteilung im normalspectrum. *Annalen der Physik*, 309(3):553–563, 1901. doi:10.1002/andp.19013090310. 44
- C. Prescher. EELSA - EELS Analysis software (Personal communication), 2011. 43
- D. J. Prior, A. P. Boyle, F. Brenker, M. C. Cheadle, A. Day, G. Lopez, L. Peruzzi, G. Potts, S. Reddy, R. Spiess, N. E. Timms, P. Trimby, J. Wheeler, and L. Zetterstrom. The application of electron backscatter diffraction and orientation contrast imaging in the SEM to textural problems in rocks. *American Mineralogist*, 84(11-12):1741–1759, 1999. 46
- M. M. Raith, P. Raase, and J. Reinhardt. *Guide to thin section microscopy*. Mineralogical Society of America, 2nd edition, 2012. ISBN 978-3-00-037671-9. 45, 46, 54
- M. D. Rayman, T. C. Fraschetti, C. A. Raymond, and C. T. Russell. Dawn: A mission in development for exploration of main belt asteroids Vesta and Ceres. *Acta Astronautica*, 58:605–616, 2006. doi:10.1016/j.actaastro.2006.01.014. 3

- S. J. B. Reed. *Electron microprobe analysis and scanning electron microscopy in geology*. Cambridge University Press, Cambridge, 2010. ISBN 9780521142304 052114230X. 28
- K. Robinson, G. V. Gibbs, and P. H. Ribbe. Quadratic elongation: a quantitative measure of distortion in coordination polyhedra. *Science*, 172(3983):567–570, 1971. doi:10.1126/science.172.3983.567. 33
- A. E. Rubin. Petrologic, geochemical and experimental constraints on models of chondrule formation. *Earth Science Reviews*, 50:3–27, 2000. doi:10.1016/S0012-8252(99)00067-7. 4
- S. S. Russell, G. R. Huss, A. J. Fahey, R. C. Greenwood, R. Hutchison, and G. J. Wasserburg. An isotopic and petrologic study of Calcium-Aluminum-rich Inclusions from CO3 meteorites. *Geochimica et Cosmochimica Acta*, 62(4):689–714, 1998. doi:10.1016/S0016-7037(97)00374-8. 115
- E. Salje, U. Bismayer, B. Wruck, and J. Hensler. Influence of lattice imperfections on the transition temperatures of structural phase transitions: The plateau effect. *Phase Transitions*, 35(2):61–74, 1991. doi:10.1080/01411599108203423. 73
- E. K. H. Salje, M. A. Carpenter, T. Malcherek, and T. Boffa Ballaran. Autocorrelation analysis of infrared spectra from minerals. *European Journal of Mineralogy*, 12(3):503–519, 2000. 92, 94
- A. Sanchez, A. Strauss, R. Aggarwal, and R. Fahey. Crystal growth, spectroscopy, and laser characteristics of Ti:Al<sub>2</sub>O<sub>3</sub>. *IEEE Journal of Quantum Electronics*, 24(6):995–1002, 1988. doi:10.1109/3.220. 106, 111
- S. Sasaki, C. T. Prewitt, J. D. Bass, and W. A. Schulze. Orthorhombic perovskite CaTiO<sub>3</sub> and CdTiO<sub>3</sub>: structure and space group. *Acta Crystallographica Section C Crystal Structure Communications*, 43(9):1668–1674, 1987. doi:10.1107/S0108270187090620. 30
- H. Schmid and L. C. De Jonghe. Structure and non-stoichiometry of calcium aluminates. *Philosophical Magazine A*, 48(2):287–297, 1983. doi:10.1080/01418618308244316. 54
- D. L. Schrader, I. A. Franchi, H. C. Connolly Jr., R. C. Greenwood, D. S. Lauretta, and J. M. Gibson. The formation and alteration of the Renazzo-like carbonaceous chondrites I: Implications of bulk-oxygen isotopic composition. *Geochimica et Cosmochimica Acta*, 75(1):308–325, 2011. doi:10.1016/j.gca.2010.09.028. 9
- E. R. Scott and A. N. Krot. Thermal processing of silicate dust in the solar nebula: clues from primitive chondrite matrices. *The Astrophysical Journal*, 623(1):571, 2005a. 6, 7
- E. R. D. Scott and R. H. Jones. Disentangling nebular and asteroidal features of CO3 carbonaceous chondrite meteorites. *Geochimica et Cosmochimica Acta*, 54(9):2485–2502, 1990. doi:10.1016/0016-7037(90)90235-D. 9
- E. R. D. Scott and A. N. Krot. Chondrites and their components. In *Treatise on Geochemistry, Vol. 1: Meteorites, Comets and Planets*, pages 143–200. Elsevier, Oxford, 2003. ISBN 978-0-08-043751-4. 5
- E. R. D. Scott and A. N. Krot. Chondritic meteorites and the high-temperature nebular origins of their components. In *Chondrites and the Protoplanetary Disk ASP Conference Series*, volume 341, pages 15–53, 2005b. ISBN 1050-3390. 4, 6
- R. D. Shannon. Revised effective ionic radii and systematic studies of interatomic distances in halides and chalcogenides. *Acta Crystallographica Section A*, 32(5):751–767, 1976. doi:10.1107/S0567739476001551. 67
- G. M. Sheldrick. A short history of SHELX. *Acta Crystallographica Section A*, 64(1):112–122, 2008. doi:10.1107/S0108767307043930. 33
- J. I. Simon, E. D. Young, S. S. Russell, E. K. Tonui, K. A. Dyl, and C. E. Manning. A short timescale for changing oxygen fugacity in the solar nebula revealed by high-resolution <sup>26</sup>Al-<sup>26</sup>Mg dating of CAI rims. *Earth and Planetary Science Letters*, 238(3–4):272–283, 2005. doi:10.1016/j.epsl.2005.08.004. 7
- S. B. Simon and L. Grossman. Refractory inclusions in the unique carbonaceous chondrite Acfer 094. *Meteoritics & Planetary Science*, 46(8):1197–1216, 2011. doi:10.1111/j.1945-5100.2011.01224.x. 116
- S. B. Simon, S. Sutton, and L. Grossman. Valence of titanium and vanadium in pyroxene in refractory inclusion interiors and rims. *Geochimica et Cosmochimica Acta*, 71(12):3098–3118, 2007a. doi:10.1016/j.gca.2007.03.027. 13

- S. B. Simon, S. R. Sutton, and L. Grossman. The valence of titanium in refractory forsterite. In *Proceedings Lunar Planetary Science Conference 38th*, page 1892, 2007b. 13
- S. B. Simon, S. R. Sutton, and L. Grossman. First Ti-XANES analyses of refractory inclusions from Murchison. In *Proceedings Lunar Planetary Science Conference 40th*, page 1626, 2009. 13
- S. B. Simon, S. R. Sutton, and L. Grossman. Ti-XANES analyses of spinel in coarse-grained refractory inclusions from Allende. In *Proceedings Lunar Planetary Science Conference 41st*, page 1459, 2010a. 13
- S. B. Simon, S. R. Sutton, and L. Grossman. First Ti-XANES analyses of olivine in amoeboid olivine aggregates. *Meteoritics and Planetary Science Supplement*, 73:5123, 2010b. 13
- S. B. Simon, L. Grossman, and S. R. Sutton. Comment on "Valence state of titanium in the Wark–Lovering rim of a Leoville CAI as a record of progressive oxidation in the early Solar Nebula" by K.A. Dyl, J.I. Simon and E.D. Young. *Geochimica et Cosmochimica Acta*, 85:373–376, 2012. doi:10.1016/j.gca.2012.01.041. 13
- G. Smith. Evidence for absorption by exchange-coupled  $\text{Fe}^{2+}$ - $\text{Fe}^{3+}$  pairs in the near infra-red spectra of minerals. *Physics and Chemistry of Minerals*, 3(4):375–383, 1978. doi:10.1007/BF00311848. 106
- G. Smith and R. G. J. Strens. Intervalence transfer absorption in some silicate, oxide and phosphate minerals. In *The Physics and Chemistry of Minerals and Rocks*, pages 583–612. John Wiley & Sons, 1976. ISBN 9780471833680. 105
- E. Stolper. Crystallization sequences of Ca-Al-rich inclusions from Allende: An experimental study. *Geochimica et Cosmochimica Acta*, 46(11):2159–2180, 1982. doi:10.1016/0016-7037(82)90192-2. 10, 11, 12, 13, 19, 123
- E. Stolper and J. M. Paque. Crystallization sequences of Ca-Al-rich inclusions from Allende: The effects of cooling rate and maximum temperature. *Geochimica et Cosmochimica Acta*, 50(8):1785–1806, 1986. doi:10.1016/0016-7037(86)90139-0. 123
- E. Stoyanov, F. Langenhorst, and G. Steinle-Neumann. The effect of valence state and site geometry on Ti  $L_{2,3}$  and O K electron energy-loss spectra of  $\text{Ti}_x\text{O}_y$  phases. *American Mineralogist*, 92(4):577–586, 2007. doi:10.2138/am.2007.2344. 19, 43, 78, 79, 80, 81, 82, 84, 85, 86
- M. N. Taran and M. Koch-Müller. Optical absorption of electronic Fe–Ti charge-transfer transition in natural andalusite: the thermal stability of the charge-transfer band. *Physics and Chemistry of Minerals*, 38(3):215–222, 2011. doi:10.1007/s00269-010-0397-9. 106
- M. N. Taran, M. D. Dyar, and S. S. Matsyuk. Optical absorption study of natural garnets of almandine-skiagite composition showing intervalence  $\text{Fe}^{2+} + \text{Fe}^{3+} \rightarrow \text{Fe}^{3+} + \text{Fe}^{2+}$  charge-transfer transition. *American Mineralogist*, 92(5-6):753–760, 2007. doi:10.2138/am.2007.2163. 106
- B. H. Toby. EXPGUI, a graphical user interface for GSAS. *Journal of Applied Crystallography*, 34(2):210–213, 2001. doi:10.1107/S0021889801002242. 30
- A. Utsunomiya, K. Tanaka, H. Morikawa, F. Marumo, and H. Kojima. Structure refinement of  $\text{CaO} \cdot 6\text{Al}_2\text{O}_3$ . *Journal of Solid State Chemistry*, 75(1):197–200, 1988. doi:10.1016/0022-4596(88)90317-9. 14, 16, 17, 66, 73
- W. R. Van Schmus and J. A. Wood. A chemical-petrologic classification for the chondritic meteorites. *Geochimica et Cosmochimica Acta*, 31(5):747–765, 1967. doi:10.1016/S0016-7037(67)80030-9. 8
- C. A. Volkert and A. M. Minor. Focused ion beam microscopy and micromachining. *MRS Bulletin*, 32(05):389–399, 2007. doi:10.1557/mrs2007.62. 36
- D. A. Wark and J. F. Lovering. Marker events in the early evolution of the solar system - Evidence from rims on Ca-Al-rich inclusions in carbonaceous chondrites. In *Proceedings Lunar Planetary Science Conference 8th*, pages 95–112, 1977. 10, 13, 115
- J. T. Wasson, A. N. Krot, M. S. Lee, and A. E. Rubin. Compound chondrules. *Geochimica et Cosmochimica Acta*, 59: 1847–1869, 1995. doi:10.1016/0016-7037(95)00087-G. 4
- D. Weber. Refractory inclusions from the carbonaceous chondrite Acfer-094. *Meteoritics & Planetary Science*, 30(5): 595–596, 1995. 20, 116

- D. Weber and A. Bischoff. The occurrence of grossite ( $\text{CaAl}_4\text{O}_7$ ) in chondrites. *Geochimica et Cosmochimica Acta*, 58 (18):3855–3877, 1994. doi:10.1016/0016-7037(94)90368-9. 20, 115
- D. Weber, E. Zinner, and A. Bischoff. Trace element abundances and magnesium, calcium, and titanium isotopic compositions of grossite-containing inclusions from the carbonaceous chondrite Acfer 182. *Geochimica et Cosmochimica Acta*, 59(4):803–823, 1995. doi:10.1016/0016-7037(94)00366-T. 20
- M. K. Weisberg, T. J. McCoy, and A. N. Krot. Systematics and evaluation of meteorite classification. In *Meteorites and the Early Solar System II*, pages 19–52. 2006. ISBN 978-0-8165-2562-1. 3, 4
- M. Wildner, M. Andrut, and C. Z. Rudowicz. Optical absorption spectroscopy in geosciences. Part I: Basic concepts of crystal field theory. In *Spectroscopic Methods in Mineralogy*, volume 6 of *EMU Notes in Mineralogy*, pages 93–143. Eötvös University Press, Budapest, 2004. 44, 46
- D. B. Williams and C. B. Carter. *Transmission electron microscopy: a textbook for materials science*. Springer, 1996. ISBN 9780306452475. 34, 39, 40, 41, 42
- T. Wilson and C. Sheppard. *Theory and practice of scanning optical microscopy*. 1984. 46
- J. A. Wood. On the origin of chondrules and chondrites. *Icarus*, 2:152–180, 1963. doi:10.1016/0019-1035(63)90013-7. 4
- J. A. Wood. Chondritic meteorites and the Solar nebula. *Annual Review of Earth and Planetary Sciences*, 16(1):53–72, 1988. doi:10.1146/annurev.ea.16.050188.000413. 4, 6
- J. T. Wright, O. Fakhouri, G. W. Marcy, E. Han, Y. Feng, J. A. Johnson, A. W. Howard, D. A. Fischer, J. A. Valenti, J. Anderson, and N. Piskunov. The exoplanet orbit database. *Publications of the Astronomical Society of the Pacific*, 123:412–422, 2011. doi:10.1086/659427. 2
- M. Yamaga, T. Yosida, S. Hara, N. Kodama, and B. Henderson. Optical and electron spin resonance spectroscopy of  $\text{Ti}^{3+}$  and  $\text{Ti}^{4+}$  in  $\text{Al}_2\text{O}_3$ . *Journal of Applied Physics*, 75(2):1111–1117, 1994. doi:10.1063/1.356494. 106
- B. E. Yoldas. Hydrolysis of titanium alkoxide and effects of hydrolytic polycondensation parameters. *Journal of Materials Science*, 21(3):1087–1092, 1986. doi:10.1007/BF01117399. 24
- S. Yoneda and L. Grossman. Condensation of  $\text{CaO-MgO-Al}_2\text{O}_3\text{-SiO}_2$  liquids from cosmic gases. *Geochimica et Cosmochimica Acta*, 59(16):3413–3444, 1995. doi:10.1016/0016-7037(95)00214-K. 6
- E. D. Young, K. A. Dyl, and J. I. Simon. Response to the Comment by S.B. Simon, L. Grossman, and S.R. Sutton on "Valence state of titanium in the Wark-Lovering rim of a Leoville CAI as a record of progressive oxidation in the early Solar Nebula". *Geochimica et Cosmochimica Acta*, 85:377–382, 2012. doi:10.1016/j.gca.2012.01.029. 13

## *(Eidesstattliche) Versicherungen und Erklärungen*

(§ 8 S. 2 Nr. 6 PromO)

*Hiermit erkläre ich mich damit einverstanden, dass die elektronische Fassung meiner Dissertation unter Wahrung meiner Urheberrechte und des Datenschutzes einer gesonderten Überprüfung hinsichtlich der eigenständigen Anfertigung der Dissertation unterzogen werden kann.*

(§ 8 S. 2 Nr. 8 PromO)

*Hiermit erkläre ich eidesstattlich, dass ich die Dissertation selbständig verfasst und keine anderen als die von mir angegebenen Quellen und Hilfsmittel benutzt habe.*

(§ 8 S. 2 Nr. 9 PromO)

*Ich habe die Dissertation nicht bereits zur Erlangung eines akademischen Grades anderweitig eingereicht und habe auch nicht bereits diese oder eine gleichartige Doktorprüfung endgültig nicht bestanden.*

(§ 8 S. 2 Nr. 10 PromO)

*Hiermit erkläre ich, dass ich keine Hilfe von gewerbliche Promotionsberatern bzw. -vermittlern in Anspruch genommen habe und auch künftig nicht nehmen werde.*

Bayreuth, September 2014

Mattia Giannini